PORPHYRIN-APPENDED RU(II) TERPYRIDYL COMPLEXES: TOWARDS UNDERSTANDING ELECTRON TRANSFER PROCESSES IN BIOMIMETIC SYSTEMS

By

Shenshen Li

A DISSERTATION

Submitted to
Michigan State University
in partial fulfillment of the requirements
for the degree of

DOCTOR OF PHILSOPHY

Chemistry

2011

ABSTRACT

PORPHYRIN-APPENDED RU(II) TERPYRIDYL COMPLEXES: TOWARDS UNDERSTANDING ELECTRON TRANSFER PROCESSES IN BIOMIMETIC SYSTEMS

By

Shenshen Li

Electron and energy transfer processes represent fundamentally important chemical reactions. They are critical components of many biological processes, including respiration, redox enzymatic processes and photosynthesis. I have designed molecular systems that will allow me to probe the electron transfer process within the context of the sulfite reductase active site model complex, *i.e.* iron porphyrin-iron sulfur cluster dyad. For this purpose, a third component, a ruthenium bisterpyridine, was incorporated into the system to act as a phototrigger to initiate a cascade of thermally driven events; and a fourth component, a modified pyridinium moiety, was attached as an internal oxidant to ensure the correct direction of these intercomponent processes. Due to the intrinsic complexity of this Donor-Acceptor-Trigger-Oxidant system, a stepwise research protocol was adopted. A series of control molecules resembling different components of the system have been synthesized and fully characterized prior to the investigation on the full assembly. This dissertation details the synthesis and photophysical characterization of the Acceptor-Trigger dyad, *i.e.* porphyrin-appended ruthenium bisterpyridyl complexes. These studies lay the foundation for future studies on the entire assembly.

ACKNOWLEDGEMENTS

I would like to thank my advisor Professor James K. McCusker most sincerely for his guidance and help during my time at Michigan State University. I learned tremendous amount from him, the correct way of tackling scientific problems, the highest standard towards data accuracy and numerous more! These are the wealth of a lifetime.

Further, I would like to thank Professor Chi-Kwong Chang for his advices on porphyrin syntheses; Professor Gary Blanchard, who kindly helped me with all my TCSPC measurements; Professor Gavin Reid, who generously helped with ESI-MS data for my Ru heteroleptic complexes; as well as Professor Milton Smith and Professor Aaron Odom who offered valuable scientific suggestions and comments throughout my PhD career.

I would also like to thank my fellow McCusker group members who helped in one way or another in the past years.

Last but not least, I want to devote my biggest thanks to family members, especially my parents, who supported me so much in my whole life. I am here because of them and to them I owe everything I have and will have in my life.

Thank you all!

TABLE OF CONTENTS

LIST OF TABLES

LIST OF FIGURES

Chapter 1. Ultimate Research Goal and Roadmap

1.1 Background and Research Goal

Electron transfer reactions represent some of the most interesting yet complicated reactions in nature[1-3]. In biology especially, electron transfer is essential to a variety of life phenomena including photosynthesis, respiration, and enzymatic catalysis. Moreover, many frontier chemical research fields have their roots and inspirations based in such biological processes[4, 5], which includes, among others, solar energy conversion and a number of catalysis reactions[6, 7]. A better understanding of these biological processes within the native system will be beneficial for the improvement of such artificial systems. As a result of global climate change and a potential energy crisis, many researchers have been working hard in this field in an attempt to determine an electronic structure-function relationship that will lead to more efficient artificial designs. Current understanding of the electronic structure-function relationship[8] for these types of reactions is still not complete; still yet to be determined is the specific contribution of the spin effect. This is especially relevant for electron transfer systems involving multi-metal clusters. As Holm, Kennepohl and Soloman pointed out, “far less is presently known about the relation of cluster electronic structure to electron transfer properties”[8]. The project described in this dissertation is targeted at ultimately addressing the importance of spin structure to biological electron transfer processes by photophysical

means. A supramolecular system which mimics the active site of the sulfite reductase protein will be the context of this research.

1.2 Research Platform

Sulfite reductase[9] catalyzes the overall reaction of $SO_3^{2-}+7H^++6e^-\rightarrow HS^-+3H_2O$ without releasing intermediate substrate oxidation states to the environment. This reaction is responsible for the fundamental chemical transformation of sulfur for biogeochemical cycling. The active site of this protein has been identified as an Fe_4S_4 cubane-type cluster juxtaposed with a siroheme by a cysteinate sulfur atom (Figure 1-1 left)[9]. A very similar motif is also found in the nitrite reductase[10] protein active site, which catalyzes the reduction of nitrite to ammonia, its function being crucial to early and contemporary life. The function of both proteins involve the electron transfer (ET) process between an Fe_4S_4 cluster and iron porphyrin. Although there has been a limited number of studies on the structure-function relationship in this protein from a biological standpoint[11, 12], no chemical investigation has been performed addressing its effects on the molecular level, which is expected to be critically important for applications such as catalyst designs.

The artificial analogue of this biological system is well suited for the current research goal because 1) the complex spin structure within the Fe_4S_4 cubane cluster allows for the comprehensive investigation of spin-reactivity correlations in biological electron transfer; 2) the active site of this protein is among the few explicitly characterized by X-

ray crystallography[9]; and a synthetic model complex ($[Fe_4S_4$-S-FeP$]^{2-}$)[13] has been prepared by the Holm group at Harvard University, allowing the research findings to be directly relevant to the real system; 3) the two cofactors within the active sites represent two of the most commonly seen cofactors in biology, *i.e.* the heme and iron-sulfur cluster, making it possible for the findings to be extended to other similar biotic systems. Further, the multi-electron nature of this catalytic reaction is not only a ubiquitous phenomena in biology, but also a common problem for artificial systems including those with the two-electron hydrogen production, four-electron oxygen evolution and the four-electron carbon dioxide reduction. Therefore, the progress in this project will also lend insights to the contemporary energy-related research as well.

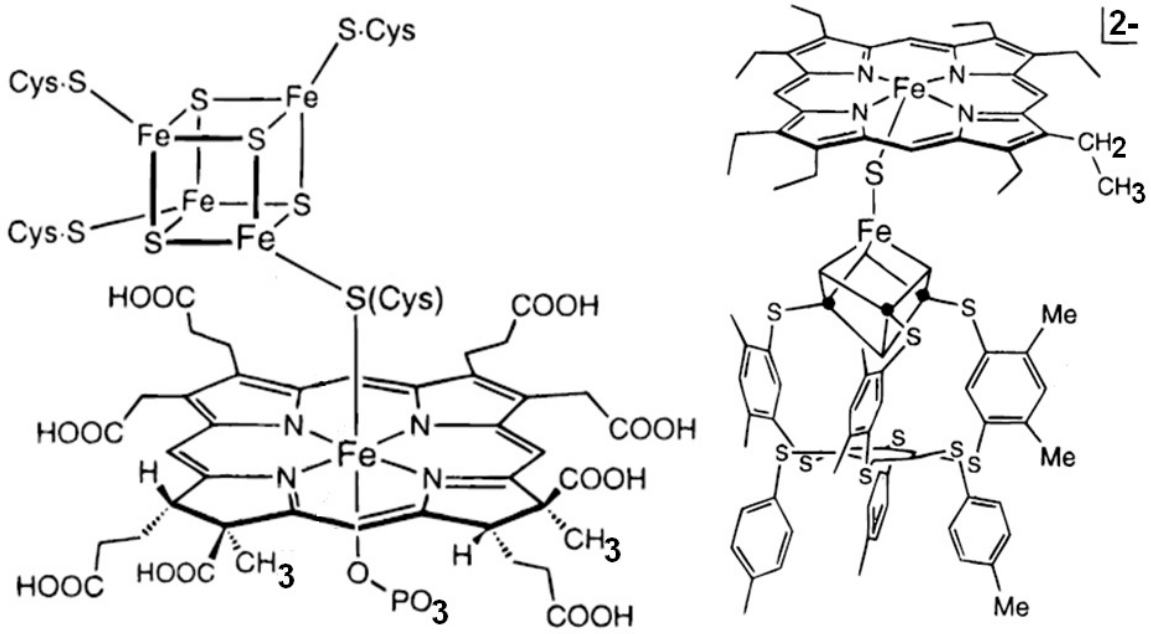

Figure 1-1. Left: structure of the E. coli sulfite reductase hemoprotein active site in the phosphate-bound form. Right: the model complex[13] of the sulfite reductase active site $[Fe_4S_4$-S-FeP$]^{2-}$, synthesize at R. H. Holm's group. Schematics reproduced from reference (13).

The current research project intends to adopt photophysical and photochemical means, with steady-state, nanosecond, and ultrafast laser instruments, to directly monitor the ET processes between these two biologically important cofactors and understand the various factors impacting the reactivity. The greatest foreseeable challenge lies in the separation of spin contribution from a number of other complex effects. A model-to-assembly approach will be used to extract out such desired information.

It needs to be pointed out that one key component of the structure-function relationship is the effect of the protein environment. Unfortunately, this is something too complex to address until the active site itself is unequivocally understood. Therefore, the research described here will only involve studies carried out in a solution environment. Follow-up research is expected to adopt site-directed mutant studies, as suggested by Crane et al.[11], or use the apoenzyme reconstitution methodology[14, 15] to investigate the change in reactivities within the protein.

1.3 Molecular System Design

In nature, the protein active site is activated once the substrate is bound to the vacant axial coordination site of the heme cofactor, preparing a thermally unstable redox state which subsequently undergoes sequential electron transfer steps and perform catalytic functions[11]. This unstable redox state, in the absence of a substrate, can also be prepared *in situ* by photophysical means, *i.e.* laser excitation. It is important,

however, to isolate the photo-triggering process from the subsequent electron transfer process, so that these later ET processes could faithfully represent the thermal events occurring in the natural system. For this purpose, appropriate phototrigger needs to be incorporated into the system. Based on our group's experience in ruthenium polypyridyl chemistry, ruthenium/rhenium complexes were selected as the initial candidate, as shown in Figure 1-2.

Two systems have been designed in order to investigate the electron transfer processes between Fe_4S_4 and porphyrin components in both directions, *i.e.* the *forward ET* from $[Fe_4S_4]^+$ component to iron(III) porphyrin ($Fe^{III}P$), and the *back ET* from $Fe^{II}P$ to $[Fe_4S_4]^{2+}$. The back ET design (Figure 1-2, left panel) is simpler and uses Holm's complex as the ET couple with the extra chromophore attached (Figure 1-2). Photoexcitation on the chromophore produces a charge transfer state where Ru^{II} is formally oxidized and the electron travels to the bridging ligand. Once this excited state is formed, the extra electron on the bridging ligand can either go back to reduce the oxidized metal center or go forward and reduce the Fe^{III} to Fe^{II}. Provided that charge recombination process is slow enough, the latter process will occur, leading to the formation of a Fe^{II} species. If the produced ferrous porphyrin has a redox potential lower than the $[Fe_4S_4]^{2+}$ component, the electron transfer process from $Fe^{II}P$ to $[Fe_4S_4]^{2+}$ will be initiated.

In the forward ET scenario (Figure 1-2, right panel), the system is slightly modified so that both the iron sulfur cluster and iron porphyrin will be prepared in their reduced

forms. The resting state will be $[Fe_4S_4\text{-S-FeP}]^{4-}$. In this design, a sacrificial acceptor will be incorporated into the system either as another covalently linked component or as a free additional molecule. After photoexcitation, the excited state Ru^{II*} will be oxidatively quenched by the sacrificial acceptor to produce a Ru^{III} state. The Ru^{III} ion thus produced should be able to oxidize the Fe^{II} porphyrin to Fe^{III} porphyrin. The electron transfer process from $[Fe_4S_4]^{+}$ to the resultant $Fe^{III}P$ is expected to be thermodynamically attainable, and photophysical characterizations can follow. A similar example of the usage of a sacrificial acceptor is provided by Hamachi and coworkers[16] in investigating photo-triggered oxidation of a ferri-heme to a ferryl-heme.

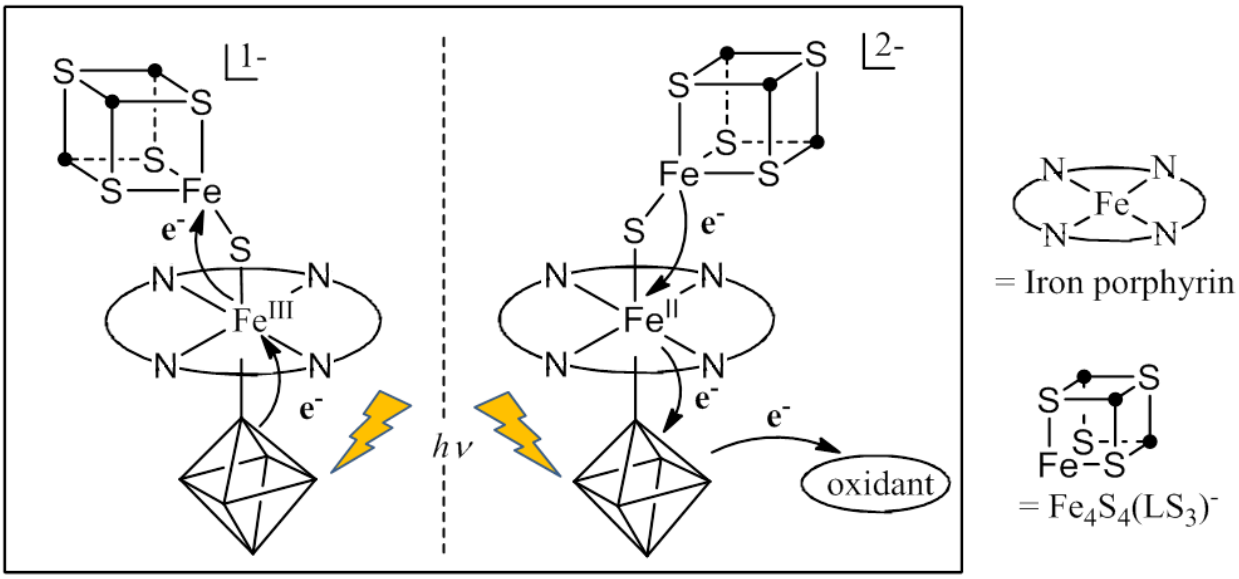

Figure 1-2. A scheme of back ET (left) and forward (right) from iron porphyrin to $[Fe_4S_4]^{2+/+}$, as triggered by the excitation of the chromophore. LS_3=1,3,5-tris[(4,6-dimethyl-3-mercaptophenyl)thio]-2,4,6-tris(p-tolylthio)benzene(3-). For interpretation of the references to the color in this and all other figures, the reader is referred to the electronic version of this dissertation.

In the forward ET (Figure 1-2, right panel), the system is slightly modified so that both the iron sulfur cluster and iron porphyrin will be prepared in their reduced forms. The resting state will be $[Fe_4S_4\text{-}S\text{-}FeP]^{4-}$. In this design, a sacrificial acceptor will be incorporated into the system either as another covalently linked component or as a free additional molecule. After photoexcitation, the excited state Ru^{II*} will be oxidatively quenched by the sacrificial acceptor to produce a Ru^{III} state before the $Ru^{III}\text{-}py^{-}$ MLCT excited state forms. A similar example of the usage of a sacrificial acceptor is provided by Hamachi and coworkers[16] in investigating photo-triggered oxidation of a ferri-heme to a ferryl-heme. The Ru^{III} ion thus produced should be able to oxidize the Fe^{II} porphyrin to Fe^{III} porphyrin. The electron transfer process from $[Fe_4S_4]^{+}$ to the resultant $Fe^{III}P$ is expected to be thermodynamically attainable, and photophysical characterizations can follow.

The appropriate choice of a photo-trigger is essential for the overall success of the project. This chromophore can be achieved by attaching a chromophore to either the axial position of the iron porphyrin, the porphyrin ring or the cubane cluster. Several major criteria need to be satisfied, however: the chromophore has to be stable and do not undergo any chemical reactions on the time scale of electron transfer; it has to have a large absorption cross-section to harvest light energy; and it has to have a monodentate site to bind to the iron porphyrin. Additionally, to investigate the electron transfer reaction, the lowest energy excited state has to be charge transfer in nature. This charge transfer excited state also needs to have sufficient reducing or oxidizing

power to push an electron into, or pull an electron out of the iron sulfur cluster-iron porphyrin assembly. Since the reduction potential of $[Fe_4S_4\text{-}S\text{-}FeP]^{2-}$ is on the order of 1 eV[13], the redox potential of the charge transfer excited state of the chromophore should be in the same region or higher. Therefore, my choice of ruthenium and rhenium polypyridyl complexes seems to be appropriate. In Chapter 5, details of the various chromophores prepared and attempted to attach to the iron porphyrin axial site will be discussed, although focuses will be given to Ru bisterpyridyl chromophore in the other chapters. This study discussed here also represents the first attempt to attach a chemically synthesized iron porphyrin to ruthenium polypyridyls.

Following a detailed understanding of the porphyrin excited state decay pathways and kinetics in the presence of the phototrigger, the iron sulfur cluster moiety will be incorporated into the system to construct the trimer, which is capable of performing a similar electron transfer process to that occurring in the active site of sulfite reductase, nitrite reductase and the respiratory chain. This will be the first attempt to experimentally monitor electron transfer processes in a protein active site model complex. It has to be clarified that, at least initially, it is not my intention to make the exact model complex of sulfite reductase and reproduce its catalytic behaviors. Rather, I desire to achieve progress toward fundamentally understanding the electron transfer processes in bio-relevant systems in detail. This will be an essential step preceding the construction of a protein active site mimic with similar complex catalytic behavior.

1.4 Dissertation Outline

The work described in this dissertation summarizes the majority of my work up-to-date towards the preparation and characterization of the iron porphyrin-chromophore assembly outlined in Figure 1-3. The $[Fe_4S_4]^{2+/+}$ can either be incorporated into the system by its reaction with the FeP-chromophore assembly, or by reacting $[Fe_4S_4$-FeP$]^{2-/4-}$ with the appropriate chromophore. This latter step is a work in progress in collaboration with the Holm group and is not covered in this dissertation.

Due to the intrinsic complexity of the whole system, a component-to-assembly protocol has been followed throughout the research. Briefly, to understand the properties of the assembly, all of the following has to be achieved: 1) synthesis of every relevant component as an individual complex to serve as reference compounds; 2) complete understanding of the properties of all these references molecules; and 3) detailed understanding of the inter-component interactions between each pair of components. In characterizing the multi-component assemblies, the spectra features of the assembly will be compared against those of the individual components. Focus will be given to the changes in the behaviors for the purpose of understanding inter-component interactions. Naturally, progress toward the final research goal has been made in several parallel pathways as shown in Figure 1-3. Listed below is a brief outline for the chapters to follow:

Chapter 2 is a brief review on relevant literature reports on the topic of porphyrin sensitized by transition metal complexes.

Chapter 3 describes the synthetic effort to prepare heteroleptic Ru bisterpyridyl complexes where complications from purity issue and photodecompositions were involved. Unique photophysical properties will be analyzed carefully.

Chapter 4 describes the synthesis and properties of two free-base porphyrin-ruthenium terpyridine complexes. The focus will be given to elucidating the effects of the presence of charge-separated states.

Chapter 5 describes alternative system designs and various attempts to prepare iron porphyrin-chromophore dyads with different transition metal complexes. Preliminary characterizations will be discussed as well.

Chapter 6 discusses the future work of this project and how it fits into our research interest in investigating spin effects on chemical reactivities.

Figure 1-3 Road map towards synthesis of the target molecular system.

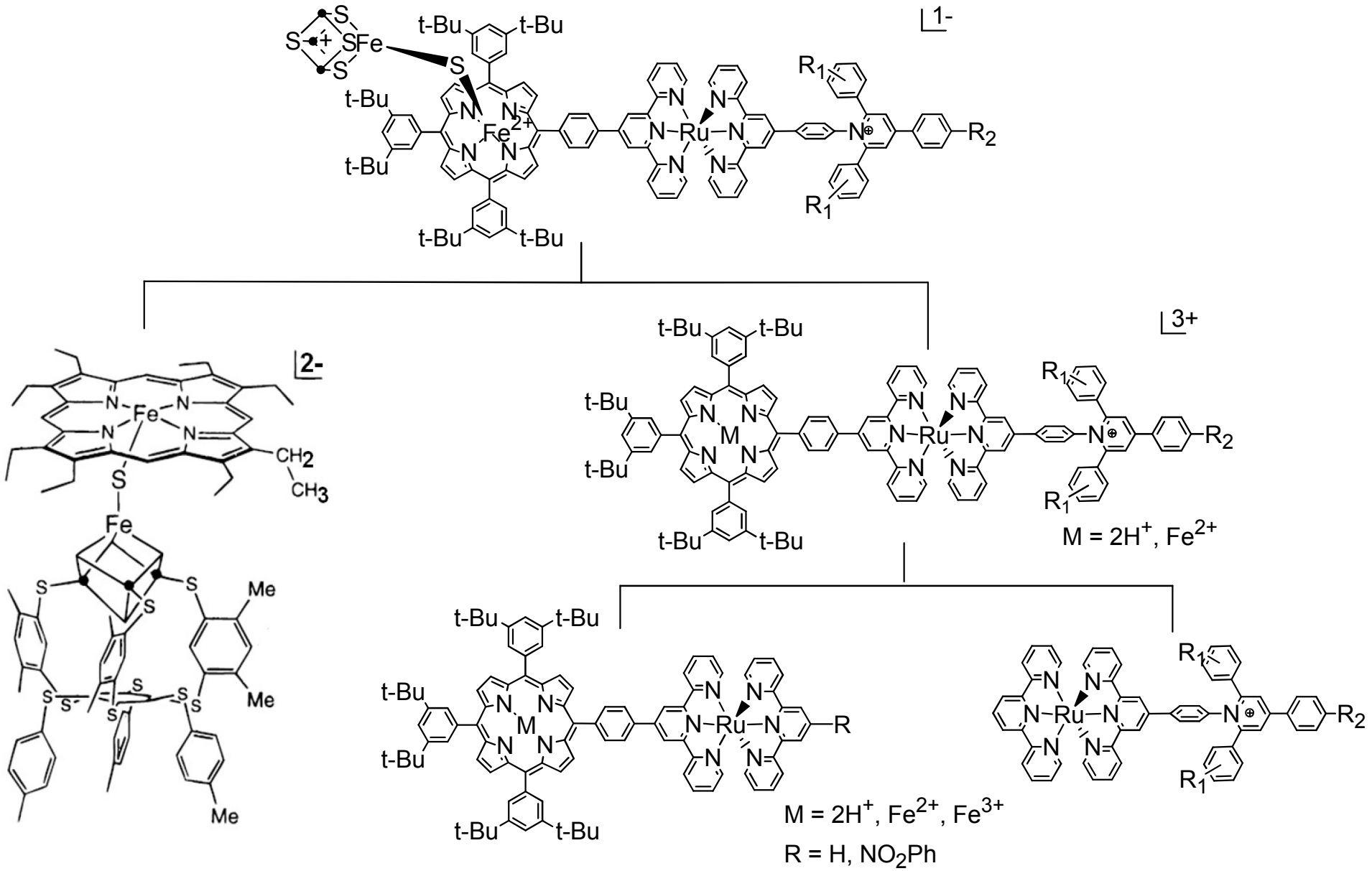

REFERENCES

REFERENCES

[1] Moser, C. C.; Keske, J. M.; Warncke, K.; Farid, R. S.; Dutton, P. L., *Nature*, (1992) **355**, 796.

[2] MARCUS; A., R.; SUTIN; N., *Electron transfers in chemistry and biology*, Elsevier: Amsterdam, PAYS-BAS, (1985); Vol. 811.

[3] Müller, A.; Ratajczak, H.; Junge, W.; Diemann, E. Eds., *Electron and proton transfer in chemistry and biology*, Elsevier Science Publishers: Amsterdam, Netherlands, (1992); Vol. p 394.

[4] Wasielewski, M. R., *Chem Rev*, (1992) **92**, 435.

[5] Wasielewski, M. R., *The Journal of Organic Chemistry*, (2006) **71**, 5051.

[6] Gamez, P.; Aubel, P. G.; Driessen, W. L.; Reedijk, J., *Chem Soc Rev*, (2001) **30**, 376.

[7] Enthaler, S.; Junge, K.; Beller, M., *Angewandte Chemie International Edition*, (2008) **47**, 3317.

[8] Holm, R. H.; Kennepohl, P.; Solomon, E. I., *Chem Rev*, (1996) **96**, 2239.

[9] Crane, B. R.; Siegel, L. M.; Getzoff, E. D., *Science*, (1995) **270**, 59.

[10] Ida, S.; Mikami, B., *Biochimica et Biophysica Acta (BBA) - Protein Structure and Molecular Enzymology*, (1986) **871**, 167.

[11] Crane, B. R.; Getzoff, E. D., *Current Opinion in Structural Biology*, (1996) **6**, 744.

[12] Keesey, R. L., Dissertation Marquette University (1999).

[13] Cai, L.; Holm, R. H., *J Am Chem Soc*, (1994) **116**, 7177.

[14] Hamachi, I.; Tanaka, S.; Tsukiji, S.; Shinkai, S.; Oishi, S., *Inorg Chem*, (1998) **37**, 4380.

[15] Fruk, L.; Kuo, C.-H.; Torres, E.; Niemeyer, C. M., *Angewandte Chemie International Edition*, (2009) **48**, 1550.

[16] Hamachi, I.; Tsukiji, S.; Shinkai, S.; Oishi, S., *J Am Chem Soc*, (1999) **121**, 5500.

Chapter 2. Porphyrin Sensitized by Transition Metal Complexes

2.1 Introduction

In the rapid development of chemical sciences, porphyrin[1-3] and metalloporphyrins occupy a prominent role. Their well-established synthetic methodologies, versatile derivatizations, multiple binding motifs, superb photophysical and photochemical[4], electrochemical[5], biochemical[6, 7] properties, among others, have lend them to various applications, varying from artificial photosynthesis[8-11] to optoelectronics[12], from photodynamic therapy[13-16] to quantum computing[17, 18], from catalysis[19-23] to photovoltaic cells[24-29], from ion sensing[30] to molecular devices[31]. For the purpose of further improving the various functions, transition metal components have been commonly incorporated into the system. Although enormous amount of effort has been dedicated to such systems, limited number of comprehensive reviews are in place to guide the further investigations. Relevant reviews targeting at specific systems or specific applications are published. For example, Alessio and coworkers discussed the design and control of the supramolecular assemblies[32]; Hiroto and coworkers reviewed porphyrin derivatives with carbon-metal bonds[33]; Scandola et al. reviewed the photophysical properties of multi-porphyrin arrays mediated with transition metal components[34]; Harriman and coworkers discussed the porphyrin-transition metal complexes as photosynthetic model systems[35]; Gray and coworkers[36], as well as

Ramasarma[37], reviewed the methodology of studying electron transfer within heme enzymes by incorporating ruthenium components, and so on. This current chapter targets at complementing these reviews by adopting a broader methodological perspective. Rather than addressing specific applications or specific systems, this account attempts to provide a starting point in considering *how* a specific property of porphyrin could be enhanced, by *which* transition metal complex, under *what* conditions for a specific application.

Although a number of bichromic systems have been designed to utilize porphyrins as a supporting role for the transition metal complexes, for example, use the porphyrin as scaffold to understand long-range electronic coupling between multiple ferrocene units[17, 18], majority of the systems utilize transition metal components to enhance the function of porphyrin-based reactivities. Therefore, porphyrin component will be taken as the standing point of this chapter and focuses will be given to the discussions on how transition metal component is able to enhance the performances of porphyrin active sites. In order to keep the discussion to a manageable size, the following molecular systems will be excluded: any systems involving photodecompositions[38] (despite of their relevance to catalysis applications), interfaces between porphyrins and solid materials (like those based-on metal[39, 40], metal oxide[41-44], metal sulfide[45] and quantum dot[46], etc.), macrocyclic non-porphyrin components[47] (phthalocyanine, corroles, and so on), multi-porphyrin arrays[48-50] (unless transition metal complexes are involved as a role beyond simple building blocks), components like fullerene[51-60],

carbon nanotubes[59], and oligopeptides[61-63] (due to the additional complexities involved in such systems). On the other hand, papers on different systems with significant relevancy to the subject discussed will be briefly mentioned.

2.2 Porphyrins: a brief overview:

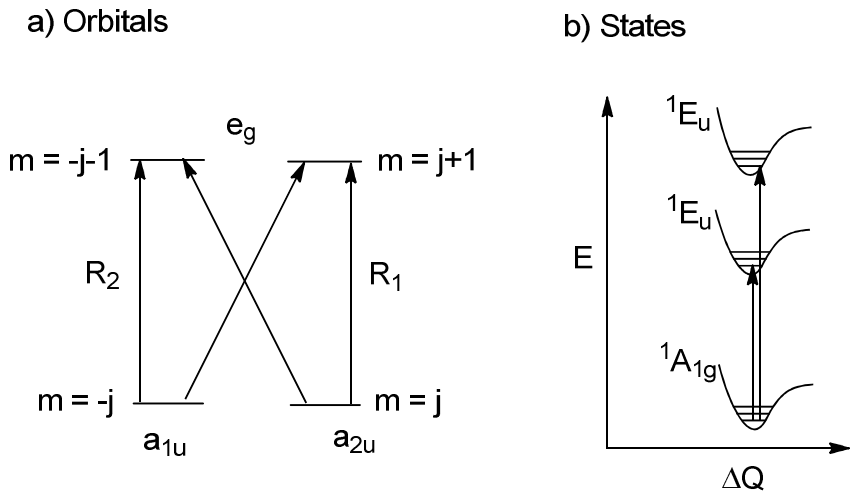

Figure 2-1 Illustration of porphyrin orbitals and states[64].

Porphyrin and its derivatives are a class of molecules with extraordinarily rich chemistry. These molecules can be categorized into *regular*, *hypso* and *hyper* types. *Regular* porphyrins have their optical properties majorly determined from the π electrons on the porphyrin ring with only very limited effects from the central metal ion, if present. Typically *regular* porphyrins will have either no metal ion in the ring or have closed-shell metal ion like Zn(II), Mg(II), Al(III), etc. *Hypso* porphyrins have blue-shifted

absorption features due to strong metal perturbations. Examples include Co(II)TPP and Cu(II)OEP (refer to a list of abbreviations in the appendix). *Hyper* porphyrin, for example Mn(III)TPP, possess new features as a result of the presence of metal ion.

Porphyrins have very rich photophysical properties. For example, it possess very strong absorption features, consisted of a feature at around 400 nm, known as Soret band with typical extinction coefficient on the order of 10^5 $L \cdot mol^{-1} cm^{-1}$, and two or four bands at lower energy known as Q bands. Gouterman's *four-orbital model,* as shown in Figure 2-1, is commonly used to explain these spectroscopic features. This model considers two highest occupied molecular orbitals of π symmetry, a_{1u} and a_{2u}, along with the two-fold degenerate unoccupied e_g orbital (in D_{4h} symmetry), and explains majority of the spectral features reasonably well. Since the first two excited states are both singlet in nature, the mixing of transition dipoles leads to one higher energy transition (Soret, B band) with very high oscillator strength, as well as another lower energy state (Q bands) of low oscillator strength. The Q band also has a vibronic overtone a few thousand wavenumbers to the red. In the case of free-base porphyrin, two protons replace the central metal in the ring and occupy two of the four nitrogen coordination sites, reducing the symmetry to D_{2h}. In this case, the degeneracy of the e_g orbital is lifted, leading to a split in the Q bands into Q_x and Q_y bands separated by approximately 3,000 cm^{-1}. With their individual vibronic overtones, four peaks are present on the absorption spectra of free base porphyrins. Effect of different

substituents, central metal ion coordinations as well as other various affecting factors may be reasonably accounted for within this model.

The excited state manifold of a *regular* porphyrin is typically consisted of a singlet S_2 state, majorly responsible for the very intense Soret band absorption, a lower lying singlet S_1 state, responsible for the Q bands in the visible region, and a very long-lived triplet T state, which is transparent to room temperature optical spectroscopic measurements.

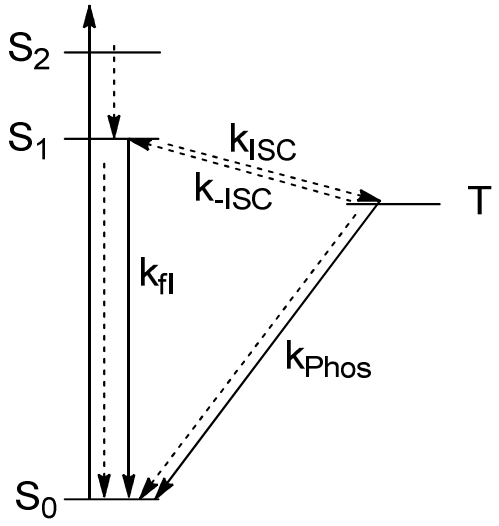

Figure 2-2 Simplified energy level diagram for regular porphyrins. When S_2-S_1 energy gap is sufficiently large, S_2->S_0 emission pathway could be present.

The dynamics of these states are summarized in Figure 2-2. The S_2 state decays very rapidly via internal conversion to the S_1 state. The lifetime of S_2 state has been estimated to be on the order of a few tens of femtoseconds[65]. Occasionally, however,

S_2 emission can also be observed[66] as a result of large energy gap (0.7 ~ 1.0 eV) between S_1 and S_2 states which leads to a sufficiently slow internal conversion, allowing the S_2-to-S_0 process to compete and be manifested as a second emission component. The formed S_1 state can go through both radiative and nonradiative decay processes to reform the ground state S_0. Or, it can go through intersystem crossing pathway to form the longer-lived triplet excited state. The S_1 state typically has lifetimes on the order of a few tens of nanoseconds and can be detected by fluorescence measurements as two peaks in the range of 600-750 nm. The T state possess weak phosphorescence which can only be detected to the red of 800 nm in low-temperature glasses. Interestingly, due to its extremely long lifetime as compared to all other states within the compound, this state may also thermally repopulate into the singlet S_1 state and produce emissions, a unique phenomenon called “delayed fluorescence”[1].

The absorption features for these excited states are quite complicated. As expected, the singlet and triplet state absorption features are quite similar due to identical orbital compositions. They are both characterized by a strong absorption in the region in between the ground state Soret peak and Q bands, as well as a broad weaker band tailing into the near-IR region. These absorption features are overlaid on top of bleach features at positions of ground state absorptions. The differences between the singlet and triplet states majorly exist in the near-infrared region between 700 nm and 900 nm, where new absorption features could be detected between 820-850 nm for TPP or between 710-800 nm for OEP complexes. For *meso*-tetraphenyl substituted porphyrins,

another new absorption feature in the region of 450 nm-500 nm are also distinct and characteristic for the T state.

For the purpose of designing, properties of porphyrin molecules can be modulated by different modifications on the porphyrin ring, either at meso- (or β-) positions or α-positions. Alternatively, metal ions could be introduced into the ring as well. In general, the lifetimes of the S_1 state can only be slightly tweaked via substituents and/or central metal coordination. The incorporation of the central metal ion also results in an increase in the symmetry of the system as well as lowered energy level. Depending on the type of the porphyrin, solvent may have either very limited (for free base porphyrin, for example) or pronounced (for ZnTPP, for example) effects on the excited state properties[1].

Some key photophysical parameters for the porphyrins discussed in this review are listed in Table 2-1 and common redox potentials are seen in Table 2-2.

Last but not least, porphyrins are prone to intermolecular interactions because of the large flat morphology. These interactions leads to additional features, different from those in monomers. Such phenomena are especially clear in solid state materials or films[67] which is important for a variety of applications. These additional complications will not be discussed in this chapter.

It needs to be noted that porphyrin molecules with transition metal ions in the ring share a lot of common features with transition metal complexes. For example, Ru(II) porphyrin has very fast intersystem crossing processes due to the heavy atom effect,

therefore, most reactions involve the longest-lived T state only, a situation similar to that of ruthenium polypyridyls. Au(III) porphyrin possess an optically forbidden ligand (porphyrin)-to-metal charge transfer state, like many other transition metal complexes, which couples the porphyrin-based S_1 state to T state and ground state with high efficiency[68]. Further, the richness of metalloporphyrin chemistry in part comes from the possibility of redox reactions on the central metal ion in the ring[69], which is similar to other transition metal complexes as well.

Table 2-1 Photophysical Parameters for Common Regular Porphyrins

	S_2 state		S_1 state			T state		
				Fluorescence		Phosphorescence		
	Absorption, nm	Lifetime (benzene)	Absorption,nm	Emission, nm (Φ)	Lifetimes	Φ_f	Emission, 77K nm (Φ)	Lifetime (RT) μs
H_2TPP		68±15 fs[100]		667 (0.13)	13.6	0.82	865 ($4x10^{-5}$)	1380
H_2OEP				(0.14)	18	0.86		
ZnTPP	423	0.2 ps, 1.45 ps[101]	587	645 (0.03)	2.54	0.88	779 (0.0012)	1200
ZnOEP	405	< 20 fs[102]	569	625 (0.04)	2.3		705	

Table 2-2 Ground State Redox Potentials for Common Regular Porphyrins[70], $E_{1/2}$ volts versus SCE (aq.)

	$P^{2+/+}$	$P^{+/0}$	$P^{0/-}$	$P^{-/2-}$
H_2TPP	1.28	0.95	-1.05	-1.47
ZnTPP	1.03	0.71	-1.35	-1.80
H_2OEP	1.30	0.81	-1.46	-1.86
ZnOEP	1.02	0.63	-1.65	

Table 2-3 Excited State Redox Potentials for Common Regular Porphyrins, $E_{1/2}$ volts versus NHE (aq.)[1]

	P^+/S_1	S_1/ P^-	P^+/T	T/ P^-
H_2TPP	-0.67	1.05	-0.24	0.62
ZnTPP	-1.10	0.94	-0.64	0.48
H_2OEP	-0.95	0.78	-0.56	0.39
ZnOEP	-1.27	0.77	-0.89	0.39

2.3 Transition metal-porphyrin supramolecular assemblies

Transition metal complex is another large class of molecule possessing very interesting properties in both the ground state and the excited states. A number of contemporary field of sciences and technology relies on these molecules.[71, 72] Transition metal complexes, which share a number of similar properties as

metalloporphyrins have a few additional advantages, among which, the multiple redox states, ability to form multinuclei clusters are notable ones. These properties can often be complementary to the function of porphyrins. These complexes possess excited states of different orbital origins, including metal-centered (MC) excited state, charge-transfer (CT) states and ligand-centered (LC) states. Metal-centered states, or also commonly called ligand field (LF) states or d-d states, are characterized by weak-to-moderate absorption bands and weak, broad, featureless emission bands. The lifetimes of these states are quite temperature dependent and are typically on the order of a few tens to a few hundreds of microseconds. As these excited states are of anti-bonding in character, excitation into these states may incur photodissociations. Charge-transfer (CT, metal-to-ligand or ligand-to-metal) states exist in various complexes with redox active metal centers, for example, Fe(II), Ru(II), Os(II), Re(I), Ir(III) and others. These CT states are responsible for the typically stronger, broad and solvent-sensitive absorption bands in the visible region with extinction coefficient on the order of a few thousands. Their corresponding emission bands are usually intense with quantum yields exceeding 10% and structured with vibrational progressions. The lifetime of these states are usually on the order of microseconds in low temperature glass and picoseconds or nanoseconds at room temperature. Due to their electron transfer nature, these states are most commonly involved in the photo-redox chemistry in functional supramolecular system. Ligand centered (LC) states have similar absorption features like those of the charge-transfer bands, although commonly occur in the UV region. The emission from

LC state typically can only be detected in low temperature glass and exhibits lifetimes on the order of milliseconds. Further, heavier transition metal ions are able to relax the spin-selection rule, thereby bring in pathways forbidden in pure organic systems. This large variety of excited states and pathways lead to a plethora of possibilities for them to be applied in molecular electronics, biomimetic systems and others.

Supramolecular systems incorporating both these two moieties can potentially display even more diverse and useful features, in the meantime, commonly intimidating complexities as well, which is especially true for photo-induced processes. While details in regards to their interactions and applications will be discussed in detail in the sections to come, it is worthwhile to point out that a couple of interesting papers[73, 74] reported on the synthesis of porphyrins with transition metal-based catalyst. Although this is not the focus of this review, it demonstrates one other important connection between these two class of molecules.

2.3.1. Constructing the system:

The incorporation of features of both transition metal and porphyrin chemistry can be done either intermolecularly or intramolecularly. In the formal case, the two components can either be simply premixed[75], complexed via columbic interactions or via hydrogen bodings[76]. These bimolecular systems are commonly limited, in terms of reactivity, by the diffusion limit as well as significant solvent interferences. Such a diffusion limit is

manifested in, for example, the plateau in quenching rate in Itou's system[77]. These factors bring in additional complexity for the purpose of fundamental research as well as difficulty in controlling reactivities in practical applications. An alternative method is to utilize coordination bonds and form supramolecules, which although commonly suffer from significant synthetic difficulties, are envisioned to possess better properties towards a number of applications.

For these covalently bound assemblies, various bridging motifs can be incorporated. There have been reports on using 1) aliphatic bridges, like a -OCH2CH2O-[78] linker studied by Poddutoori, 2) conjugated aromatic bridges including phenylenes, acetylenes, etc. 3) bridges containing metal moieties[79], and so on. These studies on intramolecular systems, *i.e.* dyads, triads or higher-order supramolecular structures, have been expanded enormously in the past two decades. The most critical aspect of the problem in such supramolecules is the extent to which the bridging group affects the chemical reactivities of the donor-acceptor couple. This is largely determined by the electronic coupling strength between the couple mediated by the bridge.

There is also a unique type of system between the extremes of bimolecular and intramolecular situations, *i.e.* the mechanically linked complexes like rotaxanes and catenanes. The incorporation of transition metals converts such mechanical linkage into coordination bonds[80].

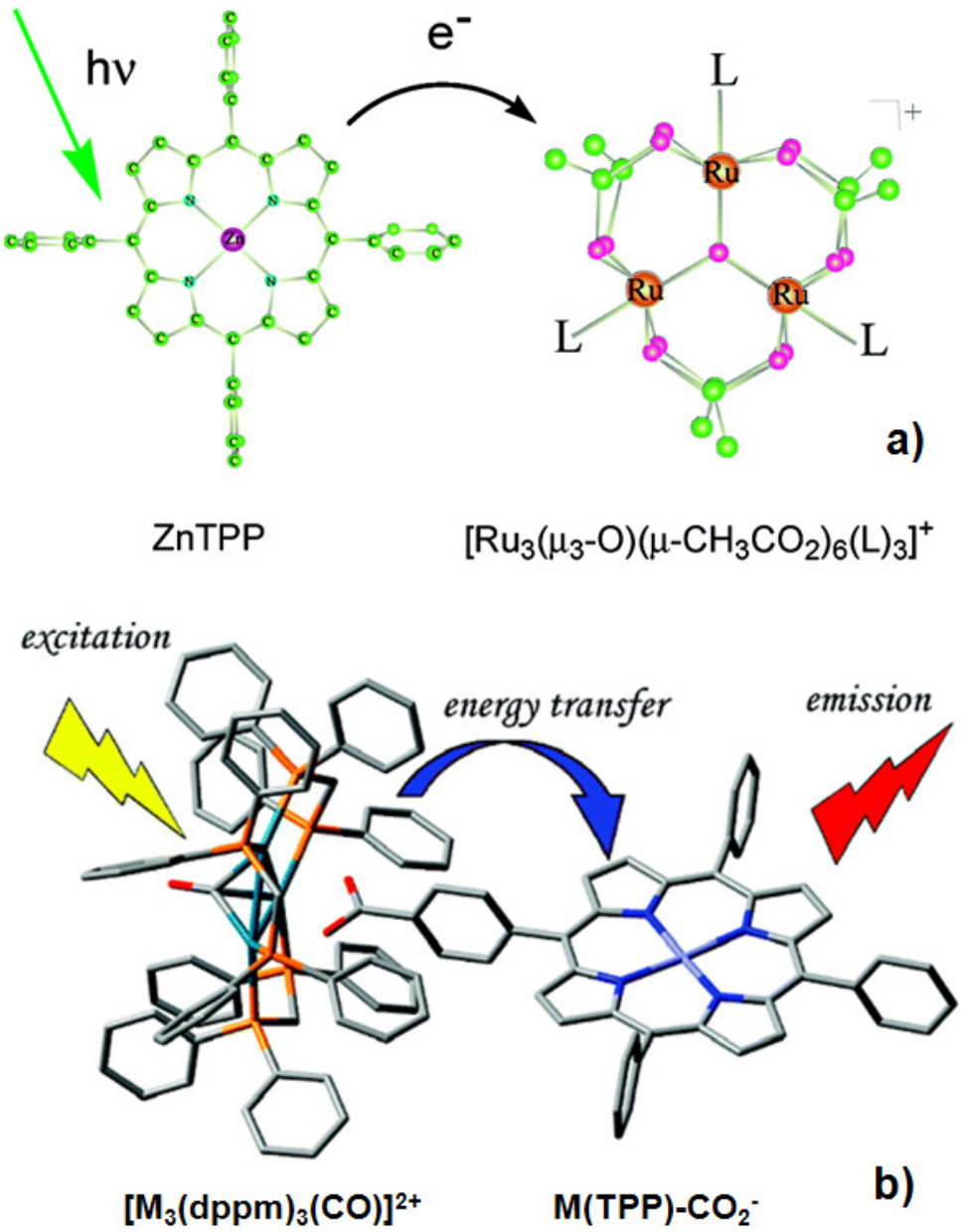

Figure 2-3 Representative examples of binary porphyrin-transition metal systems which demonstrate efficient intermolecular electron transfer (a)[77] and energy transfer (b)[81] processes.

There are also other motifs to construct such porphyrin-transition metal complexes. For example, Berry et al. synthesized a trinuclear complex[82] composed of a Ru(IV) porphyrin which connects the central metal ion through two oxo- bridges to two terminal transition metal complexes, where strong spin interaction was observed. Vahrenkamp and coworkers reported a highly redox-active tetranuclear complex with a nearly linear Fe-CN-Mn-O-Mn-NC-Fe backbone[83] where electronic coupling among all four metallic components were manifested in electrochemical characterizations.

2.3.2. Characterizations and dynamics investigations

To fully characterize the properties of excited states in these supramolecules, it typically starts from establishing a basic energy level diagram via studies with electrochemistry and steady-state spectroscopic measurements, followed by time-resolved laser spectroscopy measurements, including time-resolved pump-probe absorption, luminescence, infrared[84], resonance Raman, electron paramagnetic resonance (EPR) spectroscopy, etc to evaluate the dynamics involved amongst all these states.

Perturbations can be introduced to the system for the purpose of understanding various factors affecting the energetics and dynamics of the systems. Other than synthetically tuning the substitutions, conformation and other structural aspect of the system, solvent, temperature, excitation wavelengths can also be used. These factors will be discussed in more detail in the following sections.

2.4 Transition Metal-Sensitized Porphyrins: Dynamics of Inter-component processes.

The excited states of porphyrin are relatively reactive species. Provided that thermodynamic requirements are fulfilled, various processes may in principle occur in either covalently-bound supramolecules, ionically formed charge complexes, or simple binary system. The quenching processes can be categorized into either energy transfer:

$$D^{*} + A \rightarrow D + A^{*}$$

or electron transfers:

$$D^{*} + A \rightarrow D^{+} + A^{-}$$

$$D + A^{*} \rightarrow D^{+} + A^{-}$$

where D stands for the energy / electron donor and A represents the energy / electron acceptor.

The energy transfer quenching can occur in one of the two ways, either by dipole-dipole resonance (Förster) mechanism or by exchange interaction (Dexter) mechanism. In general, resonance energy transfer requires significant overlap between the emission profile of the energy donor and the absorption profile of the energy acceptor. This mechanism allows interactions between donor-acceptor couples separated by long distances; exchange energy transfer occurs through direct electronic exchange interactions and does not require spectral overlap, yet is traditionally considered to be only efficient within 10 Å or shorter distances. It is generally considered that triplet-to-triplet energy transfer occurs only in Dexter mechanism while singlet-to-singlet energy

transfer occurs commonly via Förster mechanism. This distance limitation of Dexter mechanism, however, is less stringent in systems where extended conjugations exist. Examples of triplet-triplet energy transfer over a distance of 21 Å has been observed in a bisporphyrinic Ru(II) terpyridyl complex[85] at low temperature, where electronic communications were maintained throughout the assembly via aromatic rings as well as the orbitals on the Ru component.

The availability of electron transfer pathway is determined by the redox chemistry of the excited states. These parameters can be estimated according to the following equations:

$$E(P^*/P^+) = E(P/P^+) - E_{00}$$

$$E(P^-/P^*) = E(P^-/P) - E_{00}$$

where $E(P^-/P)$ and $E(P/P^+)$ are the ground state porphyrin redox parameters while E_{00} is the (0, 0) energy gap between the ground state and excited state involved. Redox potentials for representative porphyrin excited states are listed in Table 2-3. With these data, the free energy change for a photo-induced redox process involving porphyrin S_1 or T state can be estimated. As electron transfer takes electron exchange mechanism, the same distance dependence discussed above for Dexter mechanism exists. An efficient ET over a distance of as long as 17 Å has been observed[86] via a sequential electron transfer mechanism.

The S_1 state of porphyrin lives reasonably long and has decent redox powers (Table 2-3), which allows for a range of photophysical and photochemical processes. The T

state, while lower in energy and redox potentials, could also be involved in a variety of interactions due to its long lifetimes on the order of a few hundred microseconds.

2.4.1. Theoretical Considerations:

Typically, for covalently-bound supramolecules, depending on the strengths of the electronic coupling between the different components, they can be categorized into either so-called *weak coupling limit* or *strong coupling limit.* In the formal situation, all the major properties of each individual component within the complex are preserved despite of the covalent bonding. These properties, among others, include absorption features, redox chemistry, NMR chemical shifts, etc. If the assembly absorption spectra overlays reasonably well with the calculated sum spectra between all the consisting components, with only slightly variations in peak intensities, positions or broadness, and no new features[87-89], a weak coupling limit case can be established. Additional evidence for weak coupling can also be obtained via observing invariant chemical shits and redox potentials[78, 87, 89] as compared to the relevant individual components, or from small stoke shifts (< 300 cm^{-1})[90, 91]. For systems in this limit, model-to-assembly study method is usually adopted, where a series of model complexes resembling different components of the system are separately probed in the same condition as the assemblies, producing a combined picture of energetic states as well as dynamics which differ from the assembly only by intercomponent-related processes. The

comparison between this picture and that obtained for the assemblies leads to a comprehensive understanding of the assembly properties.

For the strong coupling limit case, such a protocol is not applicable. These properties in the assembly are significantly altered due to the different interactions between the components. Manifestations[92] of such interactions are usually evident in absorption spectra, which differ from the models by either new spectra features, loss of component features, or significant amount of shift in peak positions or variations in peak intensities. In this situation, the distinctions between feature origins are usually vague or completely inappropriate. The properties of the model complexes can be used at best as an indication rather than basis for analyzing the assembly behaviors. Therefore, it is more reasonable to consider the whole complex as one module. In practice however, even when the spectra features can no longer be assigned definitively to a certain component, they can be considered to be *majorly* originated from one of the components with significant modulations from the others. This provides some convenience in understanding these assemblies. This chapter will majorly focus on systems in the weak coupling limit. One example of strong coupling situation[93] will be given in the last section.

Both porphyrins and transition metal complexes possess very rich excited state reactivities and are both involved in many useful photophysical and photochemical applications. A series of energy transfer and electron transfer (*i.e.* photoinduced redox reactions) can be envisioned when these components are brought together. In the limit

of weak coupling, these processes can be discussed in the context of free energy change (ΔG°), reorganization energy (λ) and electronic coupling (V).

Fermi's Golden Rule says that the probability of radiationless transitions between two states can be expressed in the following equation, provided that the electronic coupling term is not too large:

$$k=\frac{2\pi}{\hbar}H_{if}^{2}\,FCWD$$

where H_{if} is the electronic coupling term between the initial and final states involved, *FCWD* is the Frank-Condon weighted density of states (or commonly referred to as Frank-Condon factor).

The Frank-Condon factor contains a sum of overlap integrals between the isoenergetic vibrational state wave functions of the initial and final states, which is considered as the nuclear factor and can be evaluated in different ways based on the type of excited state processes involved. For electronic transitions originated from electronic coupling, *i.e.* electron transfer[94] and Dexter energy transfer, the *FCWD* expression can be reduced to the following form with a few approximations:

$$FCWD=\left(\frac{1}{4\pi\lambda k_{B}T}\right)^{1/2}exp\left[-\frac{(\Delta G^{\circ}+\lambda)^{2}}{4\lambda k_{B}T}\right]$$

where T is the temperature. The exponential term resembles that for Marcus's parabola curve, where the electron transfer rate is predicted to increase with increasing driving force in the normal region ($-\lambda < \Delta G^{\circ} < 0$), to decrease with increasing driving force in the inverted region ($-\lambda > \Delta G^{\circ}$) and stays relatively independent of driving force in barrierless region when ($-\lambda \approx \Delta G^{\circ}$). This classical treatment of Fermi's Golden Rule is

consistent with the Jortner's quantum mechanical treatment[95] which gives *energy gap law*.

The reorganization energy is defined as the energy required to change the geometry of the reactants to that of the products without leaving its own potential surface. It is composed of the sum of inner sphere reorganization energy and the outer sphere reorganization energy. The former is associated with the structural change of the first coordination sphere of the donor-acceptor couple in response to the photoinduced reaction, and typically can only be determined indirectly. Inner sphere reorganization energy for an electron transfer reaction involving ruthenium bisterpyridine is typically smaller than that of the same reaction involving ruthenium trisbipyridine, for the simple reason that the addition or removal of one electron in the terpyridyl ligand as a result of intercomponent reactions, has smaller structural consequences due to the larger extent of delocalization. Likewise, inner-sphere reorganization energy involving porphyrin components is typically small for the same reason. This term is usually much larger in systems with flexible bridging motifs, where large structural or conformational changes are allowed.[61, 96]

The outer sphere reorganization energy is determined by the change in solvent orientation coordinates between the initial and final states and can be calculated as follows[97]:

$$\lambda_o=(\Delta e)^2\left\{\frac{1}{2\alpha_D}+\frac{1}{2\alpha_A}-\frac{1}{r_{DA}}\right\}\left\{\frac{1}{\varepsilon\infty}-\frac{1}{\varepsilon_0}\right\}$$

where α_D and α_A are the radii of the donor and acceptor respectively, r_{DA} is the distance between donor and acceptor, and ε_∞ and ε_0 are the optical frequency and zero frequency dielectric constants of the solvents, and Δe is the amount of charge transferred. For electron transfers, as it involves redistribution of the charge around the redox couple, the solvent response will be significant leading to a larger outer sphere reorganization energy than that in energy transfer reactions, which do not involve net charge redistributions. Therefore, all other factors being equal, a lower reorganization energy generally favors Dexter-type energy transfer over electron transfer in the context of a less favorable driving force. It has also been shown that such solvent effect is typically more pronounced in intermolecular electron transfers than intramolecular processes[77].

For Förster energy transfer, the Frank Condon factor can be evaluated in the form of experimental observables as follows:

$$FCWD \propto J = \int_0^\infty I_D(\nu)\varepsilon_A(\nu)d\nu$$

where J is the spectra overlap integral between the partners of the resonance energy transfer; $I_D(\nu)$ and $\varepsilon_A(\nu)$ are normalized luminescence ($D^* \rightarrow D$) and absorption ($A \rightarrow A^*$) spectra.

The H_{if} term, referred to as electronic factor, depends on the nature of the components involved, their coupling mechanism, their bridging group, geometries and their spatial distance. Gamow[98, 99] and McConnell[100] both predicted that the H_{if} term depends on the energy gap and decreases approximately exponentially with

distance. Albinsson, in a couple of separate papers[101, 102], reviewed the dependence of electronic coupling term on energy gap and bridge conformation. Although most of the papers reviewed did not involve transition metal complexes, these principles shall be generalizable to such systems as well.

2.4.2. Electronic Coupling:

The electronic coupling is majorly dependent upon the natures of the donor/acceptor excited states. If the state is charge-transfer or ligand-based in nature, the electron density is more localized on the periphery of the component, thereby its interaction with other component can be strong, manifested as a large electronic coupling strength. If the state is metal-based d-d transition in nature, the electron density will be mostly localized on the metal center, buried under the ligands around, making it harder to communicate with other components in the system, thus typically a smaller electronic coupling strength. Further modulation of the electronic coupling strength can be achieved with a few factors:

A. Identity of the bridging motif:

The bridging motifs should be the most important factor affecting the electronic coupling, only after the donor-accepter couple themselves. A number of different bridging motifs have been utilized to construct porphyrin-transition metal systems. These bridges affects the electronic coupling by modulating the energetic of the system.

From a theoretical standing point, Jortner and coworkers[103] presented a quantum mechanical treatment of the electron transfer on energetics of the bridges. Practically, these bridging motifs include direct ring connection without a spacer[85], amide[50] and oxo[104, 105] connections, or more frequently a spacer based on either aliphatic or aromatic carbon-carbon linkages.

Intuitively, aliphatic bridges do not promote the intercomponent electronic coupling to any significant extent due to the low efficiency in mixing their higher-energy states with the donor-acceptor couple. Their roles are majorly structural in defining a donor-acceptor distance. Rigid aliphatic bridges have been investigated in the porphyrin dimer context[106]. When these bridges are also flexible, donor-acceptor distance could vary within a range, leading to additional complexity. Therefore, if the purpose is to increase electronic coupling, conjugated bridges are more desirable in that they can facilitate the interaction much more efficiently by providing either direct orbital overlap between the two components or mediate such by superexchange mechanism.

It has been shown that when the bridge is able to facilitate electron delocalization throughout the whole supramolecular system, the electronic coupling can be maintained efficiently through a long distance. Effective electronic coupling was maintained in a porphyrin-transition metal oligomer of 120 Å[107], where full conjugation was achieved via fused aromatic rings. This type of situation, however, is rather rare and less convenient due to the limited possibility of chemical modifications. More commonly used conjugated bridges include phenylenes and acetylenes. Although systematic studies on

the various affects of these bridges are not present in porphyrin-transition metal assemblies, insights can be obtained from those well-established in the context of porphyrin oligomers and transition metal oligomers[108-110].

In the case of acetylene bridge**[111]** between porphyrin *meso*- position and ruthenium polypyridyl ligand, for example, the highest occupied molecular orbital (HOMO) of the bridge is directly mixed with that of both components, resulting in very high electronic communications and produces a picture better considered to be in the strong-coupling limit, where the processes should be considered more appropriately as that happening between different energy levels of the same component. Phenylene bridges lies in between the above two extremes due to their relatively low energy yet commonly canted plane angles between components, restricting the donor-acceptor interactions.

Counter-intuitively, it has been shown that hydrogen bonding can be efficient bridging mechanism, and is more efficient than saturated aliphatic bridges in facilitating electron transfer between two porphyrins.[76, 112]

B. Distance between the donor and acceptor

For the purpose of isolating the various effects on electronic coupling strength by different bridges, distance dependence of electronic coupling in a porphyrin dimer with partly saturated bridges[106] has been studied. Surprisingly, the fall off of the electronic coupling thus the electron transfer rate with increased distance is slow where only a 165-fold decrease in electron transfer rate is observed when the bridge length increased

from 14.4 to 27.3 Å. Similar distance dependence[113] was also discussed in biological systems. This relatively small distance dependence is expected to be further obscured when conjugated bridges were used, where the presence of the low bridge-based state asserts additional mediating effect on the electronic coupling. It needs to be pointed out, however, that due to the intrinsic complexity of these systems, with various energy levels, the determining factor for the electronic coupling element is actually a delicate balance between all factors. A change of distance is usually accompanied with a change of other factors, for example, dihedral angles, leading to a less-than-obvious situation. Small perturbations like the addition of one more spacer may still cause significant reactivity changes.[114, 115]

Interestingly, other than changing the number of bridging spacers used in between the donor and acceptor, this distance can also be modulated by changing the conformations of the assembly when appropriate bridging groups are present. Lehn and coworkers synthesized and investigated a butterfly-shaped molecular assembly consisted of two metalloporhyrins connected by a terpyridine bridge[116]. In its natural state, the two side pyridyl rings adopts the trans- configuration as compared to the central ring. In this state, the two porphyrins on the extremes have limited communication. However, when metal ion is incorporated, the pyridyl rings rotate to form metal-pyridyl chelates, which brings the two porphyrin rings to close proximity. As expected, a strong interaction is observed as evidenced in the efficient electron transfer process.

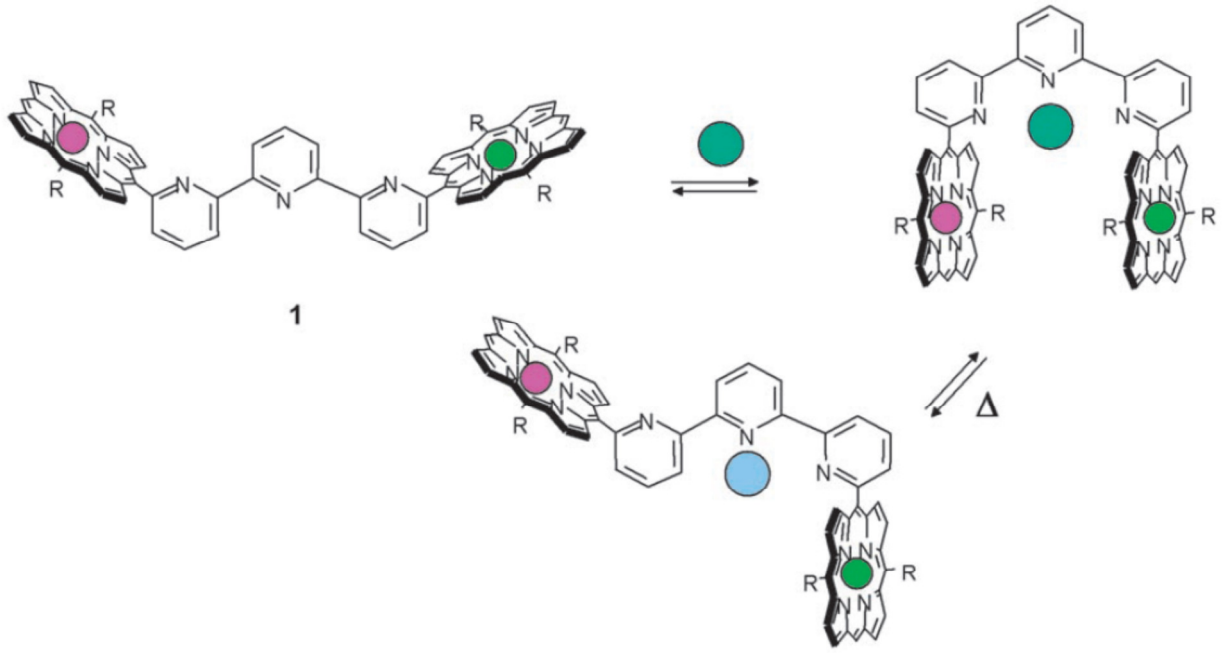

Figure 2-4 Metal-induced conformation change in a bisporphyrin system[116].

C. Coordination site of the bridge

Not only the identity of the bridge, but also the coordination site[117] of the bridge affects the electronic coupling. In a comparison study between two porphyrin-ruthenium cluster pentads, the electronic coupling was found to be significantly larger in the 4-position linked complex than that in its 2-position linked counterpart. This is due to broken π-electron coupling in the latter system. This effect was manifested as a smaller soret band broadening when comparing the supramolecule to the porphyrin component itself, as well as a smaller ring current shielding effect observed from in NMR data. Apparently, there are other minor factors accompanying this binding site change, for example, the slight change in the distance between donor and acceptor (*vide supra*),

and the dihedral angle of the bridge segment plane[104] with the donor and acceptor (*vide infra*), which may have some additional effects. Similar binding site effect was also observed in a Mo-porphyrin dyad[118, 119], where the charge separation process is affected by the extent of electronic coupling as a result of the substitution site, *i.e. para-*, *meta-*, *ortho-*.

While most reported porphyrin-transition metal complexes have the two moieties connected at either the *meso-* positions or the axial positions of the porphyrin, other connection motifs exist, for example, simple double bond has been used to connect to the β-position of the porphyrin pyrrole ring [88, 120]. Such motifs, however, are quite rare.

D. Dihedral angle of the bridging component plane with the donor and acceptor

It has be shown[102] that not only the bridge length and energy have significant roles in determining electronic coupling, dihedral angles between individual bridge-segment planes have crucial effects as well. The bridging segment plane can take different dihedral angle with regard to the donor-acceptor couple it connects. Such conformational differences have been carefully studied in ruthenium bisterpyridine-pyridinium systems by Laine and coworkers[121], as well as by Albinsson and coworkers[102], and were proposed to significantly affect the electronic coupling strength and bring in differences in the reactivity[121]. Similar effect is also proposed in a porphyrin-rhenium dyad[84] as well as porphyrin-Mo triad[104], where the multi-

conformation model was the only explanation to be able to reconcile all the photophysical data. Such a dihedral angle affect was also seen in binary porphyrin dimers.[122]

Further modulations of electronic coupling can be achieved by means of pH controls[107], additional small molecules[116], and so on.

2.4.3. Thermodynamic and energetic requirements.

The nature of the excited state not only affects the electronic coupling, but is also very important in determining the excited state energy dissipation pathways. For example, the energy of ligand-based excited states, other than those for highly conjugated molecules with strong aromatic stabilization energies (porphyrin, phthalocyanine, perelyene, etc.), are usually high in the UV or near-UV region and do not participate in photophysical and/or photochemical processes of interest here with meaningful efficiency. Charge-transfer states, however, typically resides in the visible region and are commonly responsible for the reactivity observed. As the absorption feature peak positions are directly linked to the energies of these states, such energetic parameters translate directly into the thermodynamic driving forces from which certain reaction pathways can either be favored or ruled out.

From the basic thermodynamic point of view, the free energy change has to be negative for a process to occur. This rule applies to the photoinduced processes as well

when the initial photon excitation energy input was taken into account. The free energy change can be calculated according to the following equations:

$$\Delta G^0_{EnTr} = E_f - E_i$$

$$\Delta G^0_{ET} = E_{red} - E_{ox} + E^{00}$$

where ΔG^0_{EnTr} and ΔG^0_{ET} are the free energy changes for energy transfer and electron transfer respectively, the E_f and E_i are the energies for the final and initial states of the energy transfer respectively, while E_{red}, E_{ox} and E^{00} are the ground/excited state redox potentials and the 0-0 energy gap between the initial excited state and the ground state respectively. The exogonicity can be used to predict the feasibility of the interested processes[123].

The driving force determines the direction of the intercomponent processes. When the porphyrin energy level is close to the transition metal complex, such processes can be reverted with simple modulations. For example, energy transfers in the opposite directions at the same time are not rare in ruthenium polypyridyl-porphyrin assemblies[124]. Also, electron transfer can occur in both directions in closely related systems[124] by simply changing the stoichiometric ratio between the donor and acceptor, which indirectly changed the energy levels, hence the driving forces.

From the designing point of view, the energetics of the states can be tuned by derivatizing the donor and/or acceptor moieties thereby altering the redox potential of the relevant couples, ultimately changing the driving force. Therefore, in order to increase the chance of electron transfer, electron–donating substituents on the donor

and/or electron withdrawing group on the acceptor will be helpful. In Itou's binary system[77], the electron-withdrawing ability of the substituents on the electron-accepting cluster directly affects the intermolecular electron transfer rate. Alternatively, increasing the electronic delocalization on the acceptor group will also increase the rate of electron transfer to acceptor as well.[125]

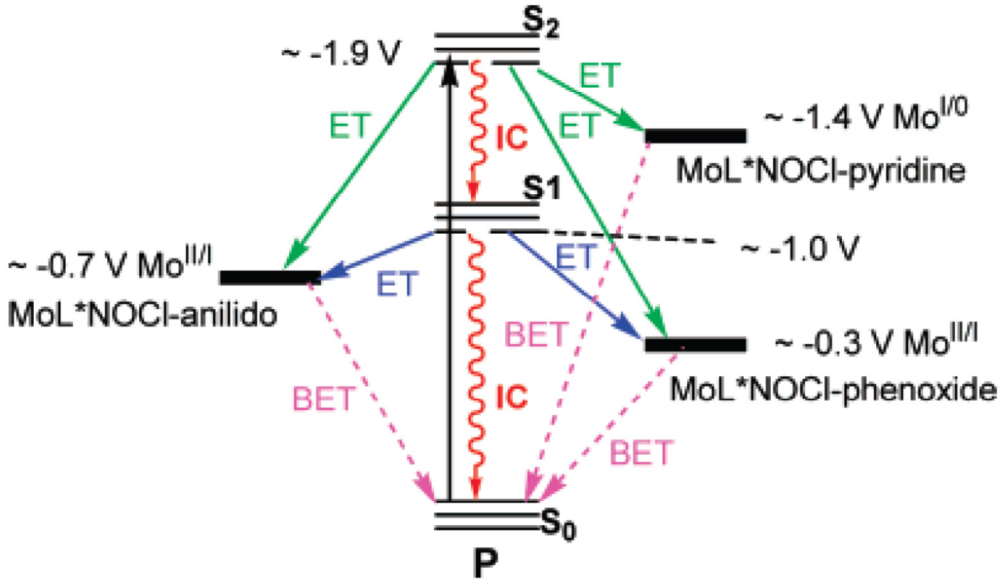

Figure 2-5 Probable relaxation channel and electron transfer processes[104] between photoexcited porphyrin (P) fragment and Mo-based acceptor orbitals.

This driving force effect is especially clear in the system of porphyrin-bismolybdenum complex[104], where the two different redox states of the Mo center allow switching on and off of electron transfer from S_1 state of porphyrin to the Mo moiety. Therien and coworkers put different substituents onto the ruthenium terpyridine

complex which enabled them to swap the relative energies between the charge-transfer state and that of the porphyrin T state hence the energy transfer rates (*vide infra*).

The coordination of different metal ions into the porphyrin ring also alters the energy of porphyrin states significantly. For example, Zn porphyrin and free base porphyrins commonly serve as the energy/electron donor although Au(III) porphyrin typically serve as energy/electron acceptor because the only[68] long-lived excited state is of T in nature, which is relatively low in energy. For metalloporphyrins, another way to modulate the energetics is by axial coordinations, which has been shown to effectively change the redox potential thereby control the electron transfer directions[124, 126].

Similar to the electronic coupling parameter, the driving force can also be tuned by external perturbations. Additional metal ions[127] has been shown by Okamoto in a Zn porphyrin-Naphthalenediimide system to affect the electron transfer rates. In this example, the forward and reverse electron transfer rates have different sensitivities towards the metal ions, and were therefore modulated differently.

For binary donor-acceptor couples, this driving force parameter folds directly into the rate of quenching processes or into the quenching efficiency term Φ in diffusion-limited binary systems[77]. Energy transfer[81] rates on the orders of 10^4 s^{-1} (porphyrin triplet) and 10^9 s^{-1} (porphyrin singlet)[81] and electron transfer rate[128] of as high as 10^{11} s^{-1} were observed. Considering that these systems are not connected via covalent bonds, these rates are surprisingly large.

It needs to be emphasized that the driving force and reorganization energy are more than often entangled with each other. Based on Marcus theory, it is the combination of these two factors that comprises the energetic consideration in determining the rates. In Mo-porphyrin dyads, it has been shown that the electron transfer rate is slower with an amide-bridge[118] than that with an oxo-bridge[105], which was a consequence of combined large driving force as well as a small reorganization energy situating the process in the Marcus inverted region. It is the consideration of both factors that enables researchers to make rational designs.

2.4.4. Spin-selection rule and heavy atom effect

Whenever heavy atom is incorporated into the system, the spin will no longer be a good quantum number and spin-selection rule will be relaxed. This phenomenon, however, cannot always be readily distinguished from that of intercomponent processes. Scandola and coworkers systematically investigated this effect by studying the photophysics of a series of pyridylporphyrin Ru(II)[129] and Re(I)[130] adducts. They were able to separate such an effect from the intercomponent energy transfer effect, and found that the relative importance between the two quenching mechanism relies on the relative energy of the Ru-based triplet state, which is ultimately determined by the ligand field strength around the Ru center. Such heavy atom effect has been observed in more complicate systems, such as a molecular box[129] based-on the same building

blocks. Heavy atom effect on porphyrin as a result of central metal ion coordination was also studied by Harriman and coworkers. [131]

2.4.5. Solvent and matrix effect.

The solvent[112] modulates the energy of the excited states, for example, Ru-based charge-transfer state is varied in nonpolar solvent (toluene) by 0.07 eV as compared to polar solvents in an aliphatically bridged porphyrin-ruthenium dyads[78], which resulted in the change of the quenching efficiency via energy transfer mechanism. These researchers also found that the spectroscopic and electrochemical properties of these assemblies were also significantly altered in nonpolar solvents like cyclohexane and toluene as compared to their relevant components, yet are only insignificantly-perturbed in CH_2Cl_2. Such a phenomenon was attributed to the difference in excitonic coupling strength as a result of the solvent-induced conformational changes.

In a tetraferrocenylporphyrin[17, 18, 132] system investigated by Nemykin et al for the purpose of potential application as nanomeric size multinuclear molecular electronics, the authors found that the electrochemical behavior of this assembly was significantly dependent upon the solvent/electrolyte combination. While a single four-electron oxidation process was present in DMF, THF or MeCN with TBAP (refer to Appendix for abbreviations) as a supporing electrolyte, which involves simultaneous oxidation of all four ferrocene components, two two-electron oxidation processes were observed with

1,2-dochlorobenzene/TBAP. When TFAB is used along with either dichloromethane or 1,2-dochlorobenzene as solvent, four single-electron oxidation processes occurred instead.

At sufficiently low temperatures, the solvent freezes into a solid matrix. As electron transfer reactions form charge-separated states, which are relatively high in energy without the presence of solvent stabilizations, these processes are commonly disfavored in solid matrices. It has been estimated that the same charge separated state will be destabilized by at least 0.25 eV[86] in a solid matrix as compared to the solution. Therefore, multi-temperature study is a good way to differentiate electron transfer versus energy transfer. For example, Kon et al. was able to observe the shut-down of a electron transfer quenching mechanism in a pyridylporphyrin-ruthenium complex[124] evidenced by the presence of ruthenium emission in solid matrix at low temperature, which is absent at ambient temperature due to efficient electron transfer processes.

Solvent has significant impacts not only in simple chemical systems, but also in protein folding and unfolding dynamics. The quenching effect with external transition metal complexes was studied by Winkler and coworkers.[133, 134] Interestingly, protein structures by themselves also have similar effects on the chemical reactivity. Hamachi and coworkers[10] studied an artificial photosynthetic system composed of a triad molecule in protein environment which showed that protein structure regulates the electron transfer pathway and, contrary to the solid matrix effect discussed above,

stabilizes the charge separated state leading to a long-live state, similar to those desired for artificial photosynthesis applications.

Solvent has significant impacts not only in simple chemical systems, but also in protein folding and unfolding dynamics. The quenching effect with external transition metal complexes was studied by Winkler and coworkers.[133, 134] Interestingly, protein structures by themselves also have similar effects on the chemical reactivity. Hamachi and coworkers[10] studied an artificial photosynthetic system composed of a triad molecule in protein environment which showed that protein structure regulates the electron transfer pathway and, contrary to the solid matrix effect discussed above, stabilizes the charge separated state leading to a long-live state, similar to those desired for artificial photosynthesis applications.

It is important to realize that all of energy gap, reorganization energy and electronic coupling term are involved here. From a fundamental point of view, to identify the effect of a single factor, it is always very important to make sure that the other factors are not changing significantly at the same time. Control-molecule characterizations are essential in this regard. Such a protocol will be demonstrated in both Chapter 3 and 4 to be followed.

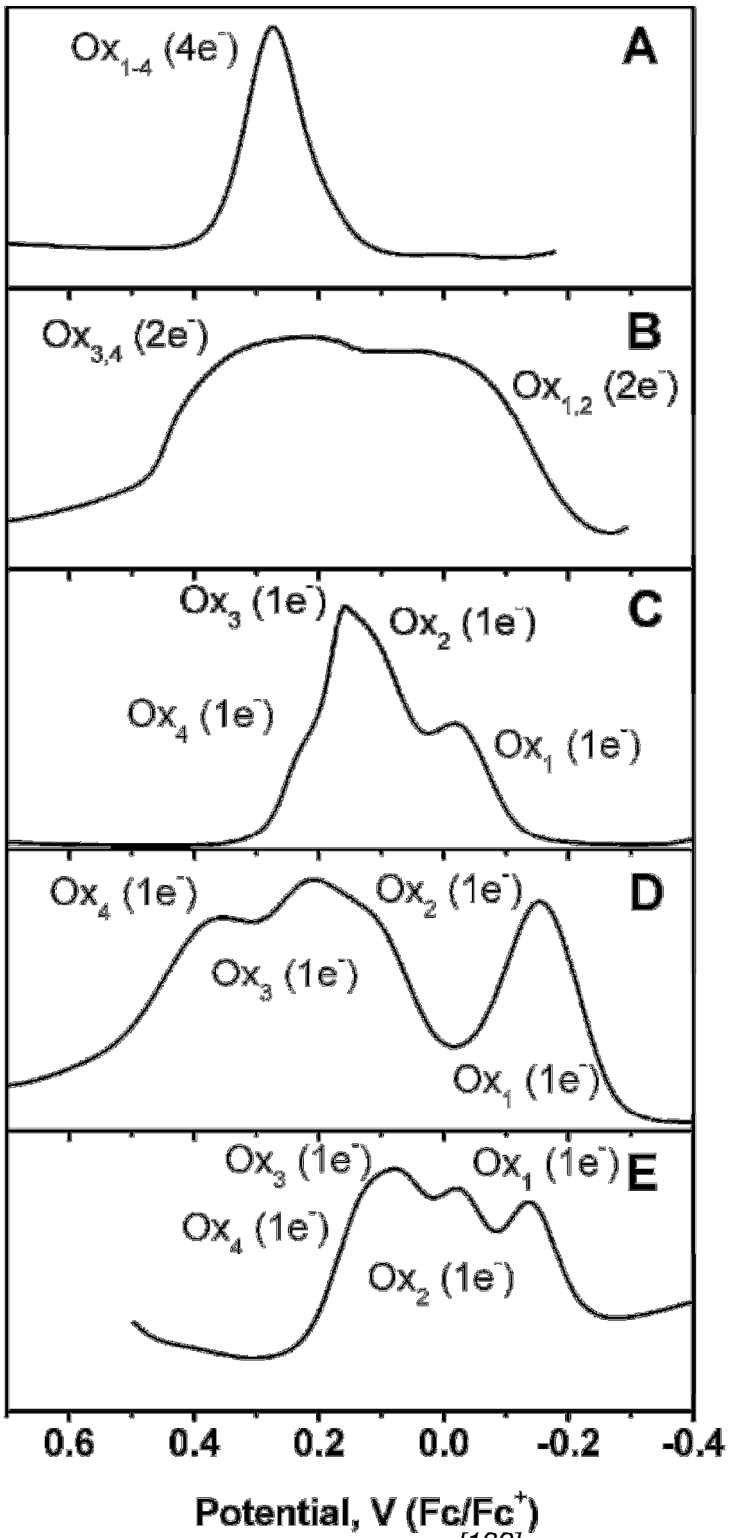

Figure 2-6 Comparison of DPV results of H_2TFcP[132] in (A) MeCN with TBAP, (B) o-DCB with TBAP, (C) DCM with TBAP, (D) o-DCB with TFAB, and (E) (bmim)Tf_2N ionic liquid.

2.5 Porphyrins sensitized by transition metal complex – A case study

2.5.1 Geometric control of supramolecules:

In nature, the change of molecular shape can result in electrochemical and/or photochemical processes which lead to mechanical or electrochemical energy change. This is best demonstrated by the butterfly-type supramolecular constructs[135] example shown earlier, where electronic communications between the two remote groups, controlled by the metallation and demetallation of a terpyridyl bridge can be rationally tuned. New electron transfer pathway could be opened or removed as shown by the different emission property of the system.

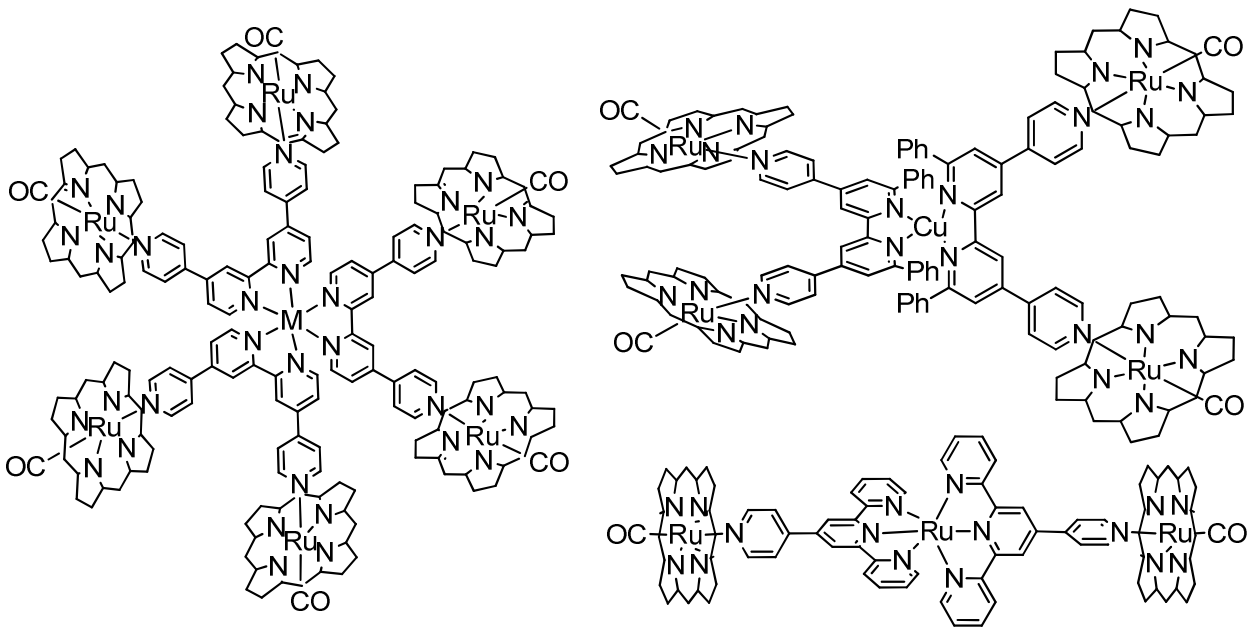

Figure 2-7 Porphyrin-transition metal adducts[136] with controlled spatial arrangements and nuclearity.

More examples of geometric designing can be seen in Figure 2-7. One-dimentional bisporphyrinic complex utilizing the linear arrangement of $[M(tpy)_2]^{n+}$ motif has been prepared by Chambron et al.[137] They also prepared similar complexes with different spatial arrangements with bipyridyl and phen motifs. Utilizing a pyridyl axial-coordination to Ru porphyrins, Branda and coworkers[136] were able to make a series of transition metal complex-templated porphyrin adducts of different nuclearity and spatial arrangement, from linear to octahedral, via self-assembling. These complexes show a combination of steady-state photophysical and redox properties of the individual components indicating very limited ground state electronic coupling, as well as new inter-component processes upon photoexcitations. Interestingly, the direction of such inter-component processes changes according to the nature of transition metal core (Ru vs. Os). Similar motif is also utilized by other groups[138, 139] who, instead of constructing with electronically isolated groups as Branda did, these authors targets at extending the conjugation of the porphyrin into the metal complex thus uses aromatic linkers directed fused onto the β-pyrrole positions of the porphyrin.

Another very unique category of supramolecules based on geometric properties is porphyrin-based rotaxanes and catenanes[140] molecules pioneered by Sauvage and coworkers. An excellent review[80] on this exact topic has been published recently. Representative structures are seen in Figure 2-8, where the structural control effect of the metal moiety is clear.

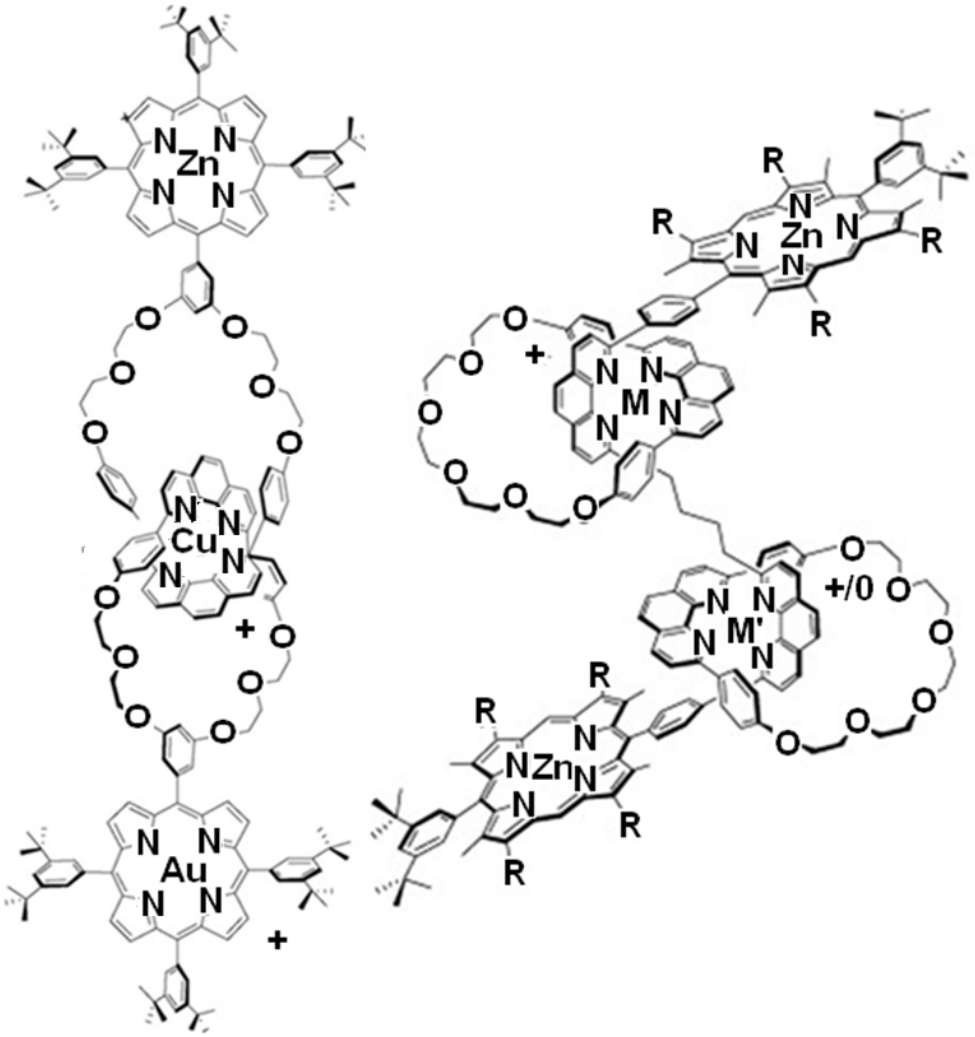

Figure 2-8 Representative rotaxanes involving porphyrin and transition metal components[80].

Alternative to the transition metal-based multi-porphyrin systems, porphyrins have also been used as structural templates to build tetranuclear metal complexes as well. The native D_{4h} symmetry of porphyrin core allows up to four-armed structures to be synthesized and probed. For example, a number of ruthenium polypyridyl, ferrocenyls[141]35,36,174, Mo cluster[105, 142] components have been attached to the porphyrin core. Further, various synthesis methods have been developed to allow either

2:2 substitution pattern or 3:1 substitution patterns. This allows a significant amount of controlling capacity from the perspective of designing.

The structural function of porphyrin is more clearly manifested in the preparation of supramolecular architectures. For example, the porphyrin-rhenium molecular square[143], molecular squares of different sizes with Pd(II) or Pt(II) components[144], porphyrin-rhodium molecular box[145], 1-D or 2-D molecular arrays with Hg(II) or Pb(IV), Cd(IV) components[146], two-ring threaded system with Cu(I) component[140] or even molecular organic frameworks[22]. A more delicate example of the geometric control is reported by Yamaguchi and coworkers[147], who prepared monomeric and polymeric porphyrin compartments utilizing a Pd(II) component with chiral twisting ligand BINAP (Figure 2-9). Marzilli reported a mixed-metal building block composed of pyridyl porphyrin with a ruthenium peripheral component.[148]

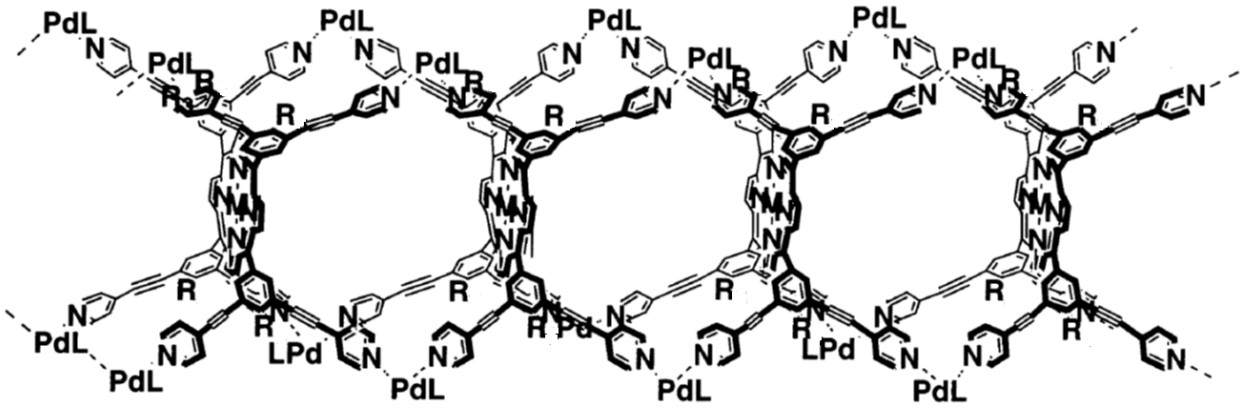

Figure 2-9 Polymeric porphyrin compartments[147] utilizing a Pd(II) component with chiral twisting ligand BINAP.

There have been a few works on the electronic coupling between peripheral metal components covalently linked to a porphyrin core. Das and coworkers[104] have shown that such electronic communication is dependent upon the spatial orientation of the bridging phenyl group which breaks electronic communication between the two extreme metal components, manifested most clearly in EPR measurements. In a bisferrocenylporphyrin system[141] studied by Burrell et al, a long-range electronic coupling at over 10 Å distance across a porphyrin ring was seen. Ferrocene-based molecular orbitals were found between the HOMO and LUMO of the porphyrin orbitals. It was proposed that a restricted rotational freedom is required in order for the ferrocene orbitals to communicate effectively through the mediating porphyrin orbitals. Other factor affecting such over-porphyrin electronic couplings include the planarity of the porphyrin plane, which could be altered by either changing the central metal ion[17, 18, 132], or by changing the coordination sites[117] of the metal clusters, where steric effects force the ring to be ruffled. Spectroelectrochemistry experiment allowed characterization of the spectral signatures of all relevant intervalence species. Intervalence charge transfer bands are also observed in the near-IR region.

While this current review is majorly on transition metal complex-porphyrin adducts, it is worthwhile to point out that some lanthanides have also being linked to porphyrin moieties in similar constructs and studied for their photophysical properties for various photonic applications[149, 150]. For example, Er (III)-terpyridine has been linked to Pt(II) porphyrin dendrimers where energy transfer from the T state of peripheral porphyrin to

the Er (III) core was observed. The near-IR emission intensity of Er (III) complex is significantly enhanced as a result of such Light-Harvesting (LH) effect as well as the site-isolation effect of the dendrons.

2.5.2 (Metallo-)porphyrin with multiple peripheral metal components --utilizing the redox properties for catalysis applications.

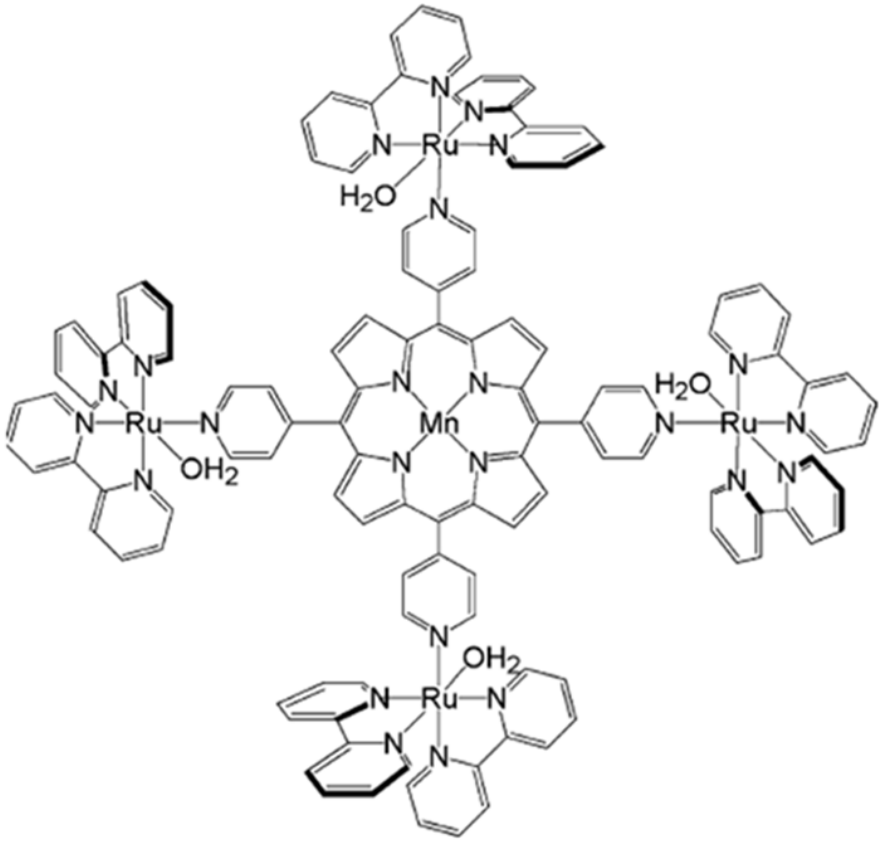

Figure 2-10 Example of catalysis systems[117, 151] based on transition metal-sensitized porphyrins.

One of the most important applications of porphyrins, especially those *irregular* porphyrins incorporating open-shell transition metal ions, is in the biomimetic catalysis field. In this regard, it has been found that the binding of selective metal complexes on

the periphery of the porphyrin enhances its activity as a catalyst[152-155], where the metal complexes serves as cofactors. These processes can either be ground state[30, 156] events or photo-induced[157] processes. Ru components are most often incorporated for this purpose, including [Ru(bpy)$_2$Cl] moieties[158], μ_3-oxo-triruthenium[117, 159] clusters, and so on. Other metals, like mollybodum[120] could be used as well due to its remarkable electrochemical properties. Representative electrochemistry and spectroelectrochemistry assignments in these systems were discussed by Marek[158] et al.

In the context of a MnTPP appended with four μ_3-oxo-triruthenium acetate clusters, Toma[151, 159-163] and coworkers observed increased selectivity in the oxidation reaction of cycloctene and cyclohexane. The transition metal complex is specifically selected due to their up to-five sequential monoelectronic processes in the range between -1.5 to +2.5 V. These cluster of oxidation states affects the properties of the porphyrin core, leading to enhanced catalysis performance. The porphyrin-transition metal component binding site difference discussed above was used to explain the different electroactivities between two isomeric H_2TPP-μ_3-oxo-triruthenium clusters[117, 159] system. A related Mn porphyrin-Ru supramolecule was studied by Prasad et al.[120] who saw two reversible two-electron oxidation waves at significantly lower oxidation potentials than the ruthenium reference complexes.

In pursue of electrochemical catalytic reduction of O_2 into water, a similar Co-based porphyrin-tetra-Ru pentad was exploited[164]. With the incorporation of the four

ruthenium components, the catalytic activity was greatly enhanced at a high current density of 2.8 mA cm^{-2}. Detailed electrochemical and spectroelectrochemical measurements showed that the oxidation potential of the Co(III) porphyrin is shifted to more positive potentials, yet it remains to be the only active species in reducing oxygen. Rotating Ring Disk Experiement (RRDE) was used to confirm that all O_2 was reduced tetraelectronically to water. The enhancement was due to the existence of the Ru components as well as their strong electronic coupling with the cobalt porphyrin active site, yet they only serve a supportive role. Similar enhancement in O_2 reduction activity was also found in a porphyrin- $SiW_{12}O_{40}$ cluster ion pair complex[165].

Note that some transition metal complexes themselves possess good catalysis efficiencies towards certain reactions. The presence of the porphyrin may also in turn enhance their activity. This is demonstrated by Reek and coworkers[166] where the rhodium catalyst was encapsulated into a phosphine ligand-directed multi-porphyrin assembly. The catalysis efficiency towards selected product was observed to be enhanced as a result of such encapsulation. Dynamics were observed to be modulated by structural changes.

Apparently, for the transition metal component to enhance the electroactivity of porphyrin or *vice versa*, there has to be significant electronic communications between them. In systems where such a communication is minimized, modulation of the activities will be small[105, 118, 119]. However, the lack of communication in the ground state does not necessarily mean a lack of communication in the excited states. Photoinduced

redox processes, or electron transfer processes (*vide infra*) actually has been widely observed in porphyrin-transition metal complexes, which displays only minimal ground state couplings. Such reactivities may be designed based on ground state photophysical and electrochemical data as discussed above.

2.5.3 Porphyrin-M(tpy)2 supramolecules under weak coupling limit: creating new excited state pathways

The incorporation of transition metal complexes into porphyrin systems bring in the possibility of new excited state decay pathways. These pathways can either be energy transfer or electron transfer[31] processes or both. Such photoinduced pathways are critically important for a number of applications, for example, as photoswitch[167], photosynthetic mimics, photovoltaic, photocatalyst, etc.

It needs to be kept in mind that identifying one pathway as an excited state decay mechanism does not necessarily exclude the others as valid components of a complicated picture. In fact, these pathways commonly coexist[77, 130, 168]. Depending on the specific applications designed for, one of these pathways can be selectively enhanced or suppressed. For example, to build photosynthetic mimic systems, electron transfer should be the dominating pathway. Other processes like energy transfer has to be minimized. Careful designs are required to ensure such desired pathway to be the most efficient process.

A. Excited states involved in intercomponent processes

In order to fully understand the processes in the excited states, it is necessary to understand which states are involved in such processes. Although typically any higher excited states in porphyrin will decay to S_1 state rapidly, with the existence of appropriate acceptor, energy or electron transfer can out-compete the internal conversion[159]131,178 and lead to S_2 reactivity.

In a ZnTPP appended with a (μ-alkoxo)bis(μ-carboxylato)diruthenium complex[168], the S_2 state fluorescence was observed to be quenched by a factor of 76% along with its lifetime reducing from 2 ps in the model porphyrin model complex to 300-500 fs. The quenching rate constant is calculated to be on the order of 10^{12} s^{-1}. This large rate is explained by the fact that the reorganization energy being very close to the free energy change of the electron transfer process, situating the system on the top of the Marcus's parabola in the barrier-less region. Hammarström and coworkers reported a similar fast electron transfer rate from S_2 state of porphyrin to the appended ruthenium *tris*-bipyridine moiety[169]. Another fast electron transfer process[97] was reported by Kito and coworkers although they assigned it, instead to the S_2-derived process, a hot-S_1-derived event, due to the excessive vibrational energy. Electron transfer from S_2 state to the appended Mo clusters[104] was found to occur at a rate of as fast as 150 fs.

Similarly, exciting into transition metal components, for example, Ru components, the high-lying excited state may play a role as well. While limited number of previous examples exist in literature, Chapter 4 gives a clear example of such reactivity. Such

"hot" processes from non-thermalized states are expected to be important towards applications requiring high-energy inputs, for example, solar cells. However, convincing proofs for such ultrafast processes are still comparatively rare. More commonly involved in the photoinduced processes are the lowest energy excited states of each given spin-multiplicity, *i.e.* S_1 and T for porphyrin and ^{3}MLCT for Ru polypyridyl components. Charge-separated states may exist depending on the redox chemistry of the components involved, as discussed previously. These processes will be evaluated in more detail below.

It needs to be clarified that in this type of systems, researchers typically use two excitation wavelengths in order to specifically excite either transition metal or porphyrin components. It is very important to note that due to the broad spectral coverage of porphyrin, selective excitation of transition metal component may not be always possible. Small amount of porphyrin absorptions may lead to dominating emission as well as non-negligible absorption signals (see Chapter 4 for an example). Such a detail could lead to misassignments in the observed photophysical features considering the level of intrinsic complexities involved in such systems. This is especially true whenever luminescence spectroscopic data are heavily relied upon. In the following discussions, I simply rely on the models presented in the literature. But in referencing to the original paper, this issue should be carefully considered and re-evaluated where necessary.

B. Selective enhancing electron transfer vs. energy transfer

Transition metal complex can serve as energy donor[170], energy acceptor[171], electron relay[172] or energy relay[85, 115, 173]. By selecting different components, reactions of different nature can be enhanced. For example, metal bis(dipyrrinato) complexes[170] has been shown as an effective secondary light harvesting moiety which absorbs photon energy in the valley region of porphyrins, *i.e.* 460 nm – 490 nm. This system is superior than other transition metal complexes in terms of light harvesting due to its single direction energy transfer from the metal component to the porphyrin, rather than those complicated by reverse energy transfer and electron transfer processes. Yet more commonly observed are situations involving multiple parallel pathways as discussed above.

The identity of the transition metal component also affects the rate of intercomponent processes. In a porphyrin-$[Os(tpy)_2]^{2+}$ assembly, the energy transfer from porphyrin to the Os component was so fast (~4 x 10^{12} s^{-1}) that no residual porphyrin emission was detected. With Ru component in the same setup, however, such rate was reduced by a few orders. Such reactivity difference was attributed to an Förster energy transfer pathway, available only in the Os –component.

An excellent example of rational designing was presented by Flamigni[85, 123, 125, 172, 174-176], where for the purpose of designing artificial photosynthesis systems, a number of different components were linked to porphyrin and their properties evaluated carefully against the research goal, which leads to optimized designs. It was found that

by incorporating a large conjugated ligand, 2,6-bis(4′-phenyl-2′-quinolyl)pyridine, into the Ru component, the previously non-existing electron transfer pathway was able to account for approximately 30% of the total excited state decay. This was attributed to the introduction of a low-energy charge-separated state, which allows electron transfer to compete with the intrinsically efficient energy transfer processes.[125] Further increase of electron transfer performance, however, was considered to be impossible for this specific application due to the low oxidation potential of Ru(II), which leads to an unavoidable energy drain pathway. A $[Ir(tpy)_2]^{3+}$ component[172], therefore, was later employed in such applications. This application was well served by the $[Ir(tpy)_2]^{3+}$ moiety due to its higher oxidation state, easier reduction (-0.78 eV vs. SCE in CH_3CN as compared to -1.2 eV for Ru(II) and Os(II) counterparts) as well as strong photophysical signatures. The possible interligand electron transfer pathway in Ir (III) complexes, when appropriate substitutions attached also facilitates efficient long range electron transfers.

Further selection of excited state pathways can also utilize different excitation wavelength. Flamigni was able to show that a switching between electron transfer and energy transfer mechanism can be achieved by exciting either porphyrin or Ir component.[86, 175]

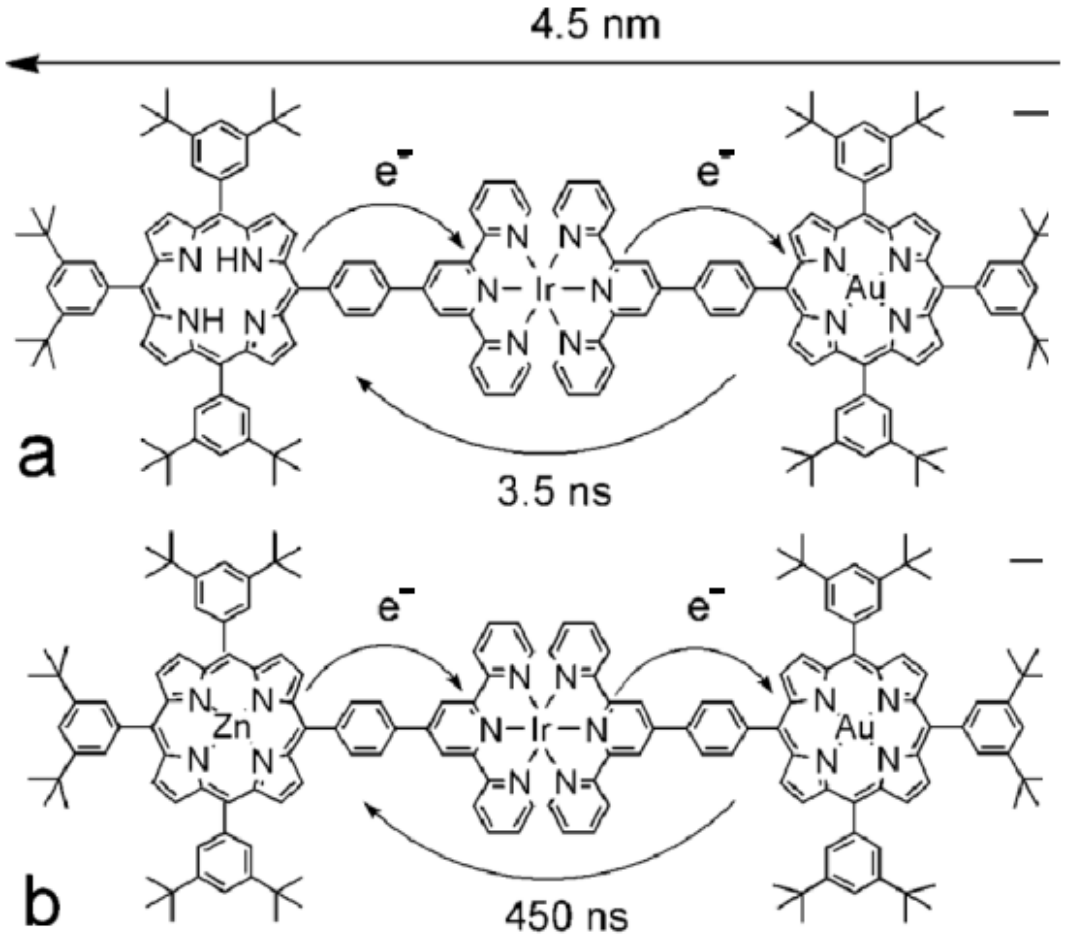

Figure 2-11 Structure and energy level diagram[172] for artificial photosynthesis system with $[Ir(tpy)_2]^{3+}$ as electron relay.

C. Long-lived charge-separated (CS) states: reducing the back electron transfer

A long-lived CS states is highly desirable in a number of contemporary applications, among which is artificial photosynthesis. In order to achieve a long lifetime, back-electron transfer rate has to be limited while forward electron transfer be enhanced, which means a decoupling between these two closely related events. Albinsson and coworkers looked at the ratio of charge separation versus charge recombination in the context of Zn porphyrin-Au/Fe porphyrin system[177]. Although it does not involve

transition metal component in this study, the results are quite relevant: the exponential distance dependence of these two reactions are different as a result of the different tunneling barrier height, which is critically dependent on the identity of the donor and acceptor components.

An example of such separate control of forward and back electron transfers was shown by Das and coworkers, where by careful designing of the system[104], the rate of forward electron transfer can be tuned without affecting the back electron transfer rate. Another example was in the porphyrin-$Ir(tpy)_2$ system discussed above, (Figure 2-11), where the lifetime of the P^+-Ir^- CS state was increased when an energy drain based of free-base porphyrin T state was replaced by a higher-energy Zn porphyrin T state, which makes it inaccessible from the CS state.

Other methods of lowering the charge recombination rate was realized by Collin and coworkers who showed that by inserting a phenyl spacer[114], the back electron transfer process could be put into the Marcus inverted region so that the decrease in rate is much larger than that in the forward process, so as to decouple the two processes. Such a lengthening of lifetime also allowed a sequential electron transfer to occur in this system.

D. Additional points to note

Several subtle points are commonly neglected in the literature. While this does not indicate those models being incorrect, more rigorous proofs are needed to better support their arguments. To name a few, while the close match between the sum of

component absorption spectra with that of the assembly suggest weak coupling, it does not preclude electronic communications hence the Dexter energy transfer or electron transfer pathways[168]; excluding Forster mechanism as a valid decay pathway based on the absence of spectral overlap does not mean energy transfer could not occur, as Dexter mechanism could still be in effect[178]; the lack of electron transfer[92] or energy transfer[178] product signatures does not necessarily rule out the role of these processes, since it may simply be due to the transient nature of such states where the population could not be accumulated to an extent they could be detected; although S_2 state of porphyrin typically internally converts to S_1 state quickly, it should not be excluded from the discussion without additional proof, as precedence exist in literature indicating such state being involved when excitation wavelength is in the soret region[168].

2.5.4 Porphyrin-acetylene-Ru(tpy)2 under strong coupling limit: Utilizing the strong absorption of the system

Since both porphyrin and a number of transition metal complexes are both good chromophores, rational combination of both in one supramolecular complex can effectively broaden the spectrum coverage. Of particular interest is the coverage in the near-IR region for the purpose of enhancing solar cell performances as well as potential applications in fields like near-IR sensing, etc. A couple of different directions have been

investigated. One of them is to utilize energy transfer to sensitize an already existing near-IR absorption of, for example, cluster complexes. In this regard, porphyrin can serve as the secondary light harvesting to achieve such sensitization. Toma and coworkers[117] observed a Ru cluster-to-porphyrin charge transfer band in the near IR region at around 720 nm. Das, Ghosh and their coworkers[92] incorporated a semi-quinone fragment into the porphyrin-ruthenium dyad and realized a reversible redox switchable near-IR dye with an extinction coefficient of (59,000 - 83,500 $M^{-1}cm^{-1}$), which is among the highest for inorganic complexes, a 6-9 fold increase compared to Ru reference complex.

Therien and coworkers, in their exploration for ways to achieve optical limiting materials in the near-IR region, pioneered in the methods of utilizing strong excitonic coupling for the purpose of creating new long-lived absorptive states with high extinction coefficients in the near IR region.[93] Such a goal is intrinsically hard to reach, because a near-IR absorption means a small energy gap, which facilitates internal conversion to the ground state. Such processes often outcompetes the spin-forbidden processes to form the triplet state (which in this case is a mixture of ^{3}MLCT of the Ru component and the T state of porphyrin) required for a long-lived absorbing state. Further complications come from the need for high extinction coefficients for this same T state.

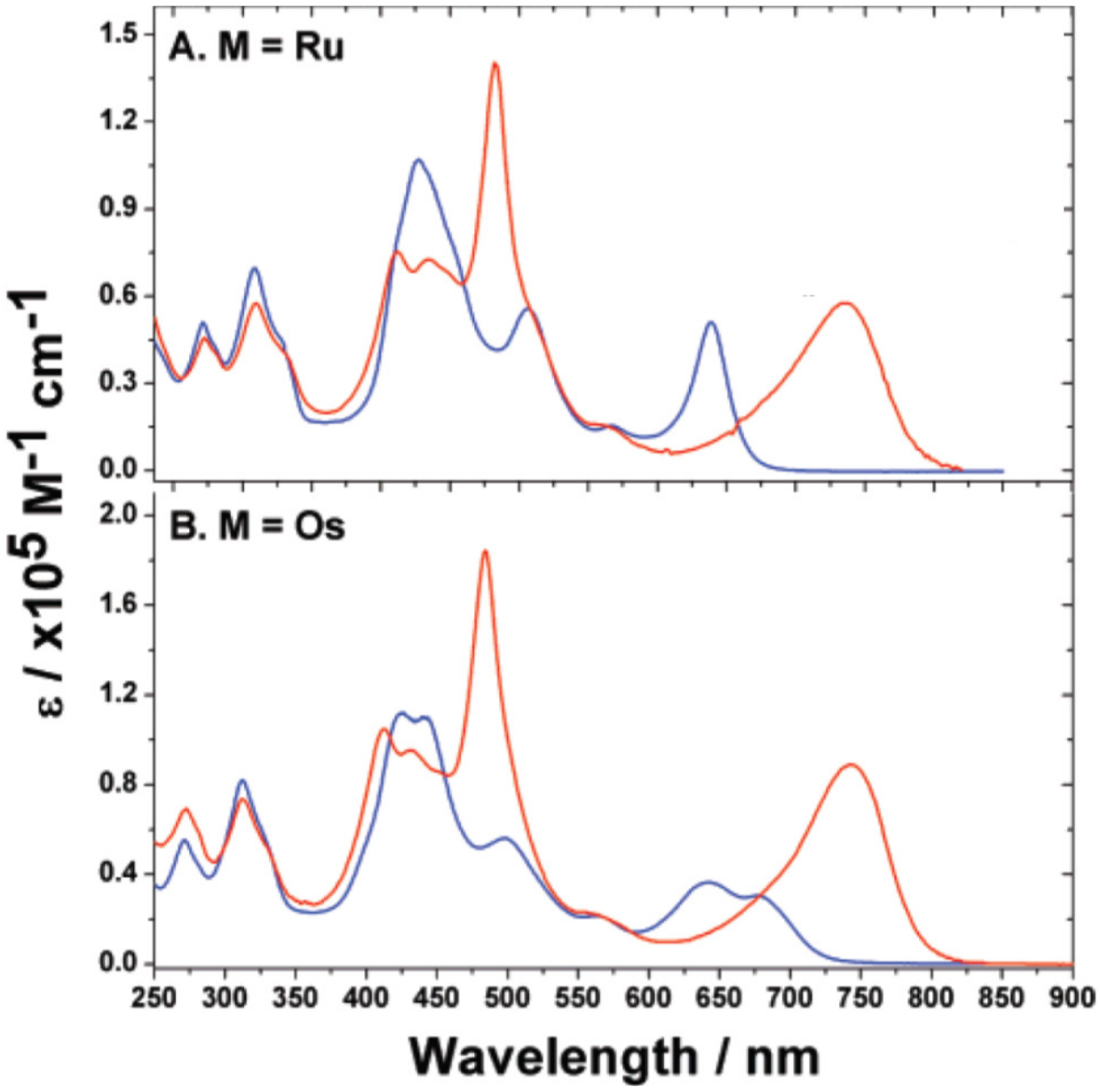

Figure 2-12 Enhanced near-IR absorptions of $MPZn_n$ systems[93], where M is either Ru (A) or Os (B). For interpretation of the references to color in this and all other figures, the reader is referred to the electronic version of this dissertation.

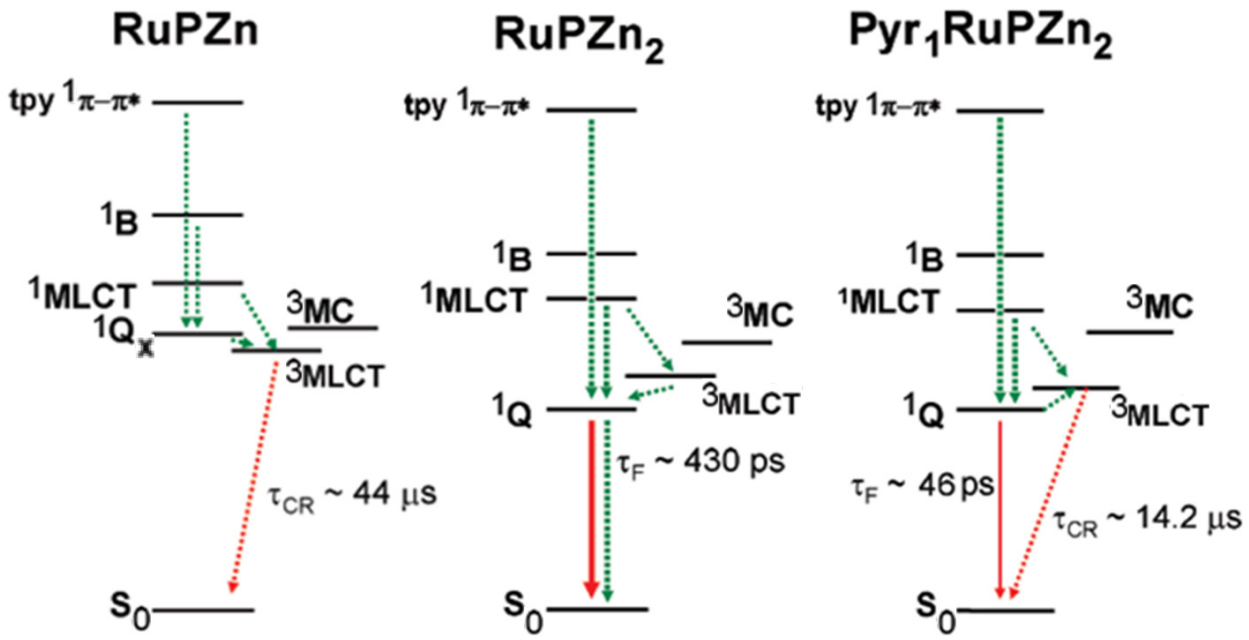

Figure 2-13 Molecular structure, energy level diagrams and triplet lifetimes of $MPZn_n$ system[93].

For the purpose of achieving high extinction coefficient in the near-IR region, Therien and coworkers utilized a 5, 15-diethynl(porphinato)zinc (II) core as well as a transition metal complex coupled by a novel acetylene bridge to yield a series of low energy electronic transitions, mainly in the near-IR region[179-181]. This choice of acetylene component was critical in this design in that its intrinsic cylindrical π-symmetry aligns the two transition dipoles on its two ends in a head-to-tail motif, leading to a strong excitonic coupling and energy splitting which resulted in the optimized near-IR features. The performance was further enhanced when a secondary porphyrin component was introduced via acetylene linkage, although the lifetime of the absorptive state shortened significantly. This was assigned to the lowering of S_1-based state due to stabilization effect caused by larger delocalizations, which essentially serves as a deactivating

pathway for the T state, resulting in a reduced lifetime (430 ps). To solve this issue, electron donating groups were attached to the periphery terpyridine and therefore lowering the redox potential of metal center. As the relevant reduction occurs on the proximal terpyridine (relative to the porphyrin moiety), this reduction in metal oxidation potential leads to a net reduction in the energy of ^{3}MLCT state, without altering the porphyrin moiety or its Q_x state. Therefore, the ^{3}MLCT state in Pyr_1RuPZn_2 and Pyr_3RuPZn_2 show $3x10^4$ and $1.5x10^4$ fold increase in lifetimes respectively as compared to $RuPZn_2$ reference compound.

2.6 Summary:

Porphyrin systems with transition metal components attached are very intricate and complicated systems. While they are potentially very useful for a number of applications, the intrinsic complexity is enormous as well. More than often, these assemblies undergo a combination of various reaction pathways. Understanding the underlying determining factors for such pathways will hopefully lead to more rational designs.

Built upon the understandings discussed in this chapter, porphyrin-Ru bisterpyridyl dyads will be explored in detail in Chapter 4.

APPENDIX

APPENDIX

Table 2-4 List of Abbreviations

TPP	5,10,15,20-Tetraphenyl-21H,23H-porphin, H_2TPP
OEP	2,3,7,8,12,13,17,18-octaethyl-21H,23H-porphin, H_2OEP
DMF	Dimethylformaldehyde
BINAP	2,2'-bis(diphenylphosphino)-1,1'-binaphthyl
$TFcP^{2-}$	5,10,15,20-tetraferrocenylporphyrin(2–)

REFERENCES

REFERENCES

[1] Kalyanasundaram, K., *Photochemistry of Polypyridines and Porphyrin Complexes*, Academic Press: London: (1992).

[2] Gouterman, M. I., *The Porphyrins*, Academic Press: New York: (1978); Vol. III.

[3] D'Souza, F., *J Porphyr Phthalocya*, (2002) **6**, 285.

[4] Odobel, F.; Blart, E.; Lagree, M.; Villieras, M.; Boujtita, H.; El Murr, N.; Caramori, S.; Alberto Bignozzi, C., *J Mater Chem*, (2003) **13**, 502.

[5] Fish, J. R.; Kubaszewski, E.; Peat, A.; Malinski, T.; Kaczor, J.; Kus, P.; Czuchajowski, L., *Chem Mater*, (1992) **4**, 795.

[6] Feng, Y.; Pilbrow, J. R., *Biophys Chem*, (1990) **36**, 117.

[7] Kuroda, R.; Takahashi, E.; Austin, C. A.; Fisher, L. M., *FEBS Letters*, (1990) **262**, 293.

[8] Alstrum-Acevedo, J. H.; Brennaman, M. K.; Meyer, T. J., *Inorg Chem*, (2005) **44**, 6802.

[9] Wasielewski, M. R., *Chem Rev*, (1992) **92**, 435.

[10] Hu, Y. Z.; Tsukiji, S.; Shinkai, S.; Oishi, S.; Hamachi, I., *J Am Chem Soc*, (2000) **122**, 241.

[11] *Canadian Journal of Chemistry*, (2011) **89**, 152.

[12] Ambroise, A.; Wagner, R. W.; Rao, P. D.; Riggs, J. A.; Hascoat, P.; Diers, J. R.; Seth, J.; Lammi, R. K.; Bocian, D. F.; Holten, D.; Lindsey, J. S., *Chem Mater*, (2001) **13**, 1023.

[13] Cunningham, M.; McCrate, A.; Nielsen, M.; Swavey, S., *Eur J Inorg Chem*, (2009), 1521.

[14] Rani-Beeram, S.; Meyer, K.; McCrate, A.; Hong, Y. L.; Nielsen, M.; Swavey, S., *Inorg Chem*, (2008) **47**, 11278.

[15] Ha, J. H.; Kim, M. S.; Park, Y. I.; Ryu, S.; Park, M.; Shin, K.; Kim, Y. R., *B Korean Chem Soc*, (2002) **23**, 281.

[16] Ha, J. H.; Jung, G. Y.; Kim, M. S.; Lee, Y. H.; Shin, K.; Kim, Y. R., *B Korean Chem Soc*, (2001) **22**, 63.

[17] Nemykin, V. N.; Barrett, C. D.; Hadt, R. G.; Subbotin, R. I.; Maximov, A. Y.; Polshin, E. V.; Koposov, A. Y., *Dalton Transactions*, (2007), 3378.

[18] Nemykin, V. N.; Galloni, P.; Floris, B.; Barrett, C. D.; Hadt, R. G.; Subbotin, R. I.; Marrani, A. G.; Zanoni, R.; Loim, N. M., *Dalton T*, (2008), 4233.

[19] Bedioui, F.; Devynck, J.; Bied-Charreton, C., *Accounts Chem Res*, (1995) **28**, 30.

[20] Sheldon, R. A. Ed. *Metalloporphyrins in catalytic oxidations*, M. Dekker: New York, (1994); Vol.

[21] Younathan, J. N.; Wood, K. S.; Meyer, T. J., *Inorg Chem*, (1992) **31**, 3280.

[22] Shultz, A. M.; Farha, O. K.; Hupp, J. T.; Nguyen, S. T., *J Am Chem Soc*, (2009) **131**, 4204.

[23] Smejkalova, D.; Piccolo, A., *Environ Sci Technol*, (2006) **40**, 1644.

[24] Cho, T. J.; Shreiner, C. D.; Hwang, S. H.; Moorefield, C. N.; Courneya, B.; Godinez, L. A.; Manriquez, J.; Jeong, K. U.; Cheng, S. Z. D.; Newkome, G. R., *Chem Commun*, (2007), 4456.

[25] Hagemann, O.; Jørgensen, M.; Krebs, F. C., *The Journal of Organic Chemistry*, (2006) **71**, 5546.

[26] Nogueira, A. F.; Formiga, A. L. B.; Winnischofer, H.; Nakamura, M.; Engelmann, F. M.; Araki, K.; Toma, H. E., *Photoch Photobio Sci*, (2004) **3**, 56.

[27] Nogueira, A. F.; Furtado, L. F. O.; Formiga, A. L. B.; Nakamura, M.; Araki, K.; Toma, H. E., *Inorganic Chemistry*, (2003) **43**, 396.

[28] Martinson, A. B. F.; Hamann, T. W.; Pellin, M. J.; Hupp, J. T., *Chemistry – A European Journal*, (2008) **14**, 4458.

[29] Winnischofer, H.; Formiga, A. L. B.; Nakamura, M.; Toma, H. E.; Araki, K.; Nogueira, A. F., *Photoch Photobio Sci*, (2005) **4**, 359.

[30] da Rocha, J. R. C.; Angnes, L.; Bertotti, M.; Araki, K.; Toma, H. E., *Anal Chim Acta*, (2002) **452**, 23.

[31] Adams, D. M.; Brus, L.; Chidsey, C. E. D.; Creager, S.; Creutz, C.; Kagan, C. R.; Kamat, P. V.; Lieberman, M.; Lindsay, S.; Marcus, R. A.; Metzger, R. M.; Michel-Beyerle, M. E.; Miller, J. R.; Newton, M. D.; Rolison, D. R.; Sankey, O.; Schanze, K. S.; Yardley, J.; Zhu, X., *The Journal of Physical Chemistry B*, (2003) **107**, 6668.

[32] Iengo, E.; Zangrando, E.; Alessio, E., *Eur J Inorg Chem*, (2003), 2371.

[33] Hiroto, S.; Yamaguchi, S.; Shinokubo, H.; Osuka, A., *J Syn Org Chem Jpn*, (2009) **67**, 688.

[34] Scandola, F.; Chiorboli, C.; Prodi, A.; Iengo, E.; Alessio, E., *Coordin Chem Rev*, (2006) **250**, 1471.

[35] Harriman, A.; Sauvage, J. P., *Chem Soc Rev*, (1996) **25**, 41.

[36] Winkler, J. R.; Malmstrom, B. G.; Gray, H. B., *Biophys Chem*, (1995) **54**, 199.

[37] Ramasarma, T., *Indian J Biochem Bio*, (1999) **36**, 379.

[38] Gabrielsson, A.; Hartl, F.; Smith, J. R. L.; Perutz, R. N., *Chem Commun*, (2002), 950.

[39] Buchner, F.; Warnick, K. G.; Wolfle, T.; Gorling, A.; Steinruck, H. P.; Hieringer, W.; Marbach, H., *J Phys Chem C*, (2009) **113**, 16450.

[40] Sathyapalan, A.; Lohani, A.; Santra, S.; Goyal, S.; Ravikanth, M.; Mukherji, S.; Rao, V. R., *Aust J Chem*, (2005) **58**, 810.

[41] Hayashi, S.; Tanaka, M.; Hayashi, H.; Eu, S.; Umeyama, T.; Matano, Y.; Araki, Y.; Imahori, H., *J Phys Chem C*, (2008) **112**, 15576.

[42] Marczak, R.; Werner, F.; Gnichwitz, J. F.; Hirsch, A.; Guldi, D. M.; Peukert, W., *J Phys Chem C*, (2009) **113**, 4669.

[43] Odobel, F.; Blart, E.; Lagree, M.; Villieras, M.; Boujtita, H.; El Murr, N.; Caramori, S.; Bignozzi, C. A., *J Mater Chem*, (2003) **13**, 502.

[44] Kerisit, S.; Rosso, K. M.; Dupuis, M.; Valiev, M., *J Phys Chem C*, (2007) **111**, 11363.

[45] de Jong, M. P.; Friedlein, R.; Sorensen, S. L.; Ohrwall, G.; Osikowicz, W.; Tengsted, C.; Jonsson, S. K. M.; Fahlman, M.; Salaneck, W. R., *Phys Rev B*, (2005) **72**,

[46] Kilin, D. S.; Tsemekhman, K.; Prezhdo, O. V.; Zenkevich, E. I.; von Borczyskowski, C., *J Photoch Photobio A*, (2007) **190**, 342.

[47] Gonzalez-Cabello, A.; Vazquez, P.; Torres, T.; Guldi, D. M., *J Org Chem*, (2003) **68**, 8635.

[48] Prodi, A.; Chiorboli, C.; Scandola, F.; Iengo, E.; Alessio, E., *Chemphyschem*, (2006) **7**, 1514.

[49] Reimers, J. R.; Lu, T. X.; Crossley, M. J.; Hush, N. S., *Nanotechnology*, (1996) **7**, 424.

[50] Reimers, J. R.; Lu, T. X.; Crossley, M. J.; Hush, N. S., *Chem Phys Lett*, (1996) **256**, 353.

[51] Spanig, F.; Ruppert, M.; Dannhauser, J.; Hirsch, A.; Guldi, D. M., *J Am Chem Soc*, (2009) **131**, 9378.

[52] Hasobe, T.; Imahori, H.; Kamat, P. V.; Ahn, T. K.; Kim, S. K.; Kim, D.; Fujimoto, A.; Hirakawa, T.; Fukuzumi, S., *J Am Chem Soc*, (2005) **127**, 1216.

[53] Imahori, H.; Kashiwagi, Y.; Endo, Y.; Hanada, T.; Nishimura, Y.; Yamazaki, I.; Araki, Y.; Ito, O.; Fukuzumi, S., *Langmuir*, (2004) **20**, 73.

[54] Imahori, H., *Org Biomol Chem*, (2004) **2**, 1425.

[55] Imahori, H.; Norieda, H.; Yamada, H.; Nishimura, Y.; Yamazaki, I.; Sakata, Y.; Fukuzumi, S., *J Am Chem Soc*, (2001) **123**, 100.

[56] Kahnt, A.; Kärnbratt, J.; Esdaile, L. J.; Hutin, M.; Sawada, K.; Anderson, H. L.; Albinsson, B., *J Am Chem Soc*, (2011), null.

[57] Kobori, Y.; Yamauchi, S.; Akiyama, K.; Tero-Kubota, S.; Imahori, H.; Fukuzumi, S.; Norris, J. R., *P Natl Acad Sci USA*, (2005) **102**, 10017.

[58] Schuster, D. I.; Cheng, P.; Jarowski, P. D.; Guldi, D. M.; Luo, C. P.; Echegoyen, L.; Pyo, S.; Holzwarth, A. R.; Braslavsky, S. E.; Williams, R. M.; Klihm, G., *J Am Chem Soc*, (2004) **126**, 7257.

[59] Chitta, R.; D'Souza, F., *J Mater Chem*, (2008) **18**, 1440.

[60] Humbert, C.; Caudano, Y.; Dreesen, L.; Sartenaer, Y.; Mani, A. A.; Silien, C.; Lemaire, J. J.; Thiry, P. A.; Peremans, A., *Appl Surf Sci*, (2004) **237**, 462.

[61] Jasuja, R.; Hazlett, T. L.; Helms, M. K.; Lee, S. H.; Jameson, D. M.; Larsen, R. W., *Chem Phys Lett*, (2001) **350**, 515.

[62] Williamson, D. A.; Bowler, B. E., *J Am Chem Soc*, (1998) **120**, 10902.

[63] Aoudia, M.; Guliaev, A. B.; Leontis, N. B.; Rodgers, M. A. J., *Biophys Chem*, (2000) **83**, 121.

[64] Spellane, P. J.; Gouterman, M.; Antipas, A.; Kim, S.; Liu, Y. C., *Inorg Chem*, (1980) **19**, 386.

[65] Zhong, Q.; Wang, Z.; Liu, Y.; Zhu, Q.; Kong, F., *The Journal of Chemical Physics*, (1996) **105**, 5377.

[66] Gurzadyan, G. G.; Tran-Thi, T. H.; Gustavsson, T., *The Journal of Chemical Physics*, (1998) **108**, 385.

[67] Goletti, C.; Paolesse, R.; Dalcanale, E.; Berzina, T.; Di Natale, C.; Bussetti, G.; Chiaradia, P.; Froiio, A.; Cristofolini, L.; Costa, M.; D'Amico, A., *Langmuir*, (2002) **18**, 6881.

[68] Eng, M. P.; Ljungdahl, T.; Andréasson, J.; Mårtensson, J.; Albinsson, B., *The Journal of Physical Chemistry A*, (2005) **109**, 1776.

[69] Ou, Z.; Kadish, K. M.; E, W.; Shao, J.; Sintic, P. J.; Ohkubo, K.; Fukuzumi, S.; Crossley, M. J., *Inorg Chem*, (2004) **43**, 2078.

[70] Felton, R. H., In *The Porphyrins*, Dolphin, D. Ed. Academic Press: New York, Vol. 5.

[71] Furtado, L. F. O.; Alexiou, A. D. P.; Gonçalves, L.; Toma, H. E.; Araki, K., *Angewandte Chemie International Edition*, (2006) **45**, 3143.

[72] Wilkins, R. G., *Kinetics and Mechanism of Reactions of Transition Metal Complexes*, Wiley-VCH Verlag GmbH & Co. KGaA: (2003).

[73] Shinokubo, H.; Osuka, A., *Chem Commun*, (2009), 1011.

[74] Shinokubo, H., *Organometallic News*, (2010),

[75] Labarre, M. J.; Pacheco, A.; Enemark, J. H., *Inorg Chim Acta*, (1994) **226**, 259.

[76] Derege, P. J. F.; Williams, S. A.; Therien, M. J., *Science*, (1995) **269**, 1409.

[77] Itou, M.; Otake, M.; Araki, Y.; Ito, O.; Kido, H., *Inorg Chem*, (2005) **44**, 1580.

[78] Poddutoori, P. K.; Poddutoori, P.; Maiya, B. G., *J Porphyr Phthalocya*, (2006) **10**, 1049.

[79] Harriman, A.; Hissler, M.; Trompette, O.; Ziessel, R., *J Am Chem Soc*, (1999) **121**, 2516.

[80] Flamigni, L., *J Photoch Photobio C*, (2007) **8**, 191.

[81] Aly, S. M.; Ayed, C.; Stern, C.; Guilard, R.; Abd-El-Aziz, A. S.; Harvey, P. D., *Inorg Chem*, (2008) **47**, 9930.

[82] Berry, K. J.; Moubaraki, B.; Murray, K. S.; Nichols, P. J.; Schulz, L. D.; West, B. O., *Inorg Chem*, (1995) **34**, 4123.

[83] Geiss, A.; Keller, M.; Vahrenkamp, H., *J Organomet Chem*, (1997) **541**, 441.

[84] Gabrielsson, A.; Hartl, F.; Zhang, H.; Smith, J. R. L.; Towrie, M.; Vlcek, A.; Perutz, R. N., *J Am Chem Soc*, (2006) **128**, 4253.

[85] Flamigni, L.; Barigelletti, F.; Armaroli, N.; Ventura, B.; Collin, J.-P.; Sauvage, J.-P.; Williams, J. A. G., *Inorg Chem*, (1999) **38**, 661.

[86] Harriman, A.; Odobel, F.; Sauvage, J. P., *Journal of the American Chemical Society*, (1995) **117**, 9461.

[87] Liu, X.; Liu, J.; Pan, J.; Chen, R.; Na, Y.; Gao, W.; Sun, L., *Tetrahedron*, (2006) **62**, 3674.

[88] Allwood, J. L.; Burrell, A. K.; Officer, D. L.; Scott, S. M.; Wild, K. Y.; Gordon, K. C., *Chem Commun*, (2000), 747.

[89] Liu, X.; Liu, J.; Pan, J.; Andersson, S.; Sun, L., *Tetrahedron*, (2007) **63**, 9195.

[90] Zhang, T.-G.; Zhao, Y.; Song, K.; Asselberghs, I.; Persoons, A.; Clays, K.; Therien, M. J., *Inorg Chem*, (2006) **45**, 9703.

[91] Zhang, T.-G.; Zhao, Y.; Asselberghs, I.; Persoons, A.; Clays, K.; Therien, M. J., *J Am Chem Soc*, (2005) **127**, 9710.

[92] Jose, D. A.; Shukla, A. D.; Kumar, D. K.; Ganguly, B.; Das, A.; Ramakrishna, G.; Palit, D. K.; Ghosh, H. N., *Inorg Chem*, (2005) **44**, 2414.

[93] Duncan, T. V.; Ishizuka, T.; Therien, M. J., *J Am Chem Soc*, (2007) **129**, 9691.

[94] Balzani, V. Ed. *Electron Transfer in Chemistry*, Wiley-VCH Verlag GmbH, Weinheim: (2008); Vol.

[95] Jortner, J., *The Journal of Chemical Physics*, (1976) **64**, 4860.

[96] Croney, J. C.; Helms, M. K.; Jameson, D. M.; Larsen, R. W., *J Phys Chem B*, (2000) **104**, 973.

[97] Wall, J. M. H.; Akimoto, S.; Yamazaki, T.; Ohta, N.; Yamazaki, I.; Sakuma, T.; Kido, H., *B Chem Soc Jpn*, (1999) **72**, 1475.

[98] Gamow, G., *Nature*, (1928) **122**,

[99] Gamow, G., *Z. Phys. A*, (1928) **51**,

[100] McConnell, H. M., *The Journal of Chemical Physics*, (1961) **35**, 508.

[101] Eng, M. P.; Albinsson, B., *Chem Phys*, (2009) **357**, 132.

[102] Albinsson, B.; Eng, M. P.; Pettersson, K.; Winters, M. U., *Phys Chem Chem Phys*, (2007) **9**, 5847.

[103] Bixon, M.; Jortner, J., *J Chem Phys*, (1997) **107**, 5154.

[104] Jose, D. A.; Shukla, A. D.; Ramakrishna, G.; Palit, D. K.; Ghosh, H. N.; Das, A., *J Phys Chem B*, (2007) **111**, 9078.

[105] Rowley, N. M.; Kurek, S. S.; Foulon, J.-D.; Hamor, T. A.; Jones, C. J.; McCleverty, J. A.; Hubig, S. M.; McInnes, E. J. L.; Payne, N. N.; Yellowlees, L. J., *Inorg Chem*, (1995) **34**, 4414.

[106] Portela, C. F.; Brunckova, J.; Richards, J. L.; Schollhorn, B.; Iamamoto, Y.; Magde, D.; Traylor, T. G.; Perrin, C. L., *J Phys Chem A*, (1999) **103**, 10540.

[107] Hush, N. S.; Reimers, J. R.; Hall, L. E.; Johnston, L. A.; Crossley, M. J., *Ann Ny Acad Sci*, (1998) **852**, 1.

[108] Albinsson, B.; Martensson, J., *J Photoch Photobio C*, (2008) **9**, 138.

[109] Kilsa, K.; Kajanus, J.; Macpherson, A. N.; Martensson, J.; Albinsson, B., *J Am Chem Soc*, (2001) **123**, 3069.

[110] Odobel, F.; Fortage, J., *Cr Chim*, (2009) **12**, 437.

[111] Duncan, T. V.; Ishizuka, T.; Therien, M. J., *Journal of the American Chemical Society*, (2007) **129**, 9691.

[112] Bolton, J. R.; Schmidt, J. A.; Ho, T. F.; Liu, J. Y.; Roach, K. J.; Weedon, A. C.; Archer, M. D.; Wilford, J. H.; Gadzekpo, V. P. Y., *Adv Chem Ser*, (1991), 117.

[113] Gruschus, J. M.; Kuki, A., *J Phys Chem B*, (1999) **103**, 11407.

[114] Collin, J. P.; Harriman, A.; Heitz, V.; Odobel, F.; Sauvage, J. P., *J Am Chem Soc*, (1994) **116**, 5679.

[115] Benniston, A. C.; Harriman, A.; Pariani, C.; Sams, C. A., *Phys Chem Chem Phys*, (2006) **8**, 2051.

[116] Linke-Schaetzel, M.; Anson, C. E.; Powell, A. K.; Buth, G.; Palomares, E.; Durrant, J. D.; Balaban, T. S.; Lehn, J. M., *Chem-Eur J*, (2006) **12**, 1931.

[117] Formiga, A. L. B.; Nogueira, A. F.; Araki, K.; Toma, H. E., *New J Chem*, (2008) **32**, 1167.

[118] Rowley, N. M.; Kurek, S. S.; Ashton, P. R.; Hamor, T. A.; Jones, C. J.; Spencer, N.; McCleverty, J. A.; Beddard, G. S.; Feehan, T. M.; White, N. T. H.; McInnes, E. J. L.; Payne, N. N.; Yellowlees, L. J., *Inorg Chem*, (1996) **35**, 7526.

[119] Rowley, N. M.; Kurek, S. S.; George, M. W.; Hubig, S. M.; Beer, P. D.; Jones, C. J.; Kelly, J. M.; McCleverty, J. A., *Journal of the Chemical Society, Chemical Communications*, (1992), 497.

[120] Prasad, R.; Kumar, A., *Supramol Chem*, (2006) **18**, 77.

[121] LAINE; #160; P., P.; CAMPAGNA; Sebastiano; LOISEAU; Fr; #233; rique, *Conformationally gated photoinduced processes within photosensitizer-acceptor dyads based on ruthenium(II) and osmium(II) polypyridyl complexes with an appended pyridinium group*, Elsevier: Kidlington, ROYAUME-UNI, (2008); Vol. 252, p 20.

[122] Smith, D. M. A.; Rosso, K. M.; Dupuis, M.; Valiev, M.; Straatsma, T. P., *J Phys Chem B*, (2006) **110**, 15582.

[123] Collin, J.-P.; Dalbavie, J.-O.; Heitz, V.; Sauvage, J.-P.; Flamigni, L.; et al., *B Soc Chim Fr*, (1996) **133**, 749

[124] Kon, H.; Tsuge, K.; Imamura, T.; Sasaki, Y.; Ishizaka, S.; Kitamura, N., *Inorg Chem*, (2006) **45**, 6875.

[125] Flamigni, L.; Armaroli, N.; Barigelletti, F.; Balzani, V.; Collin, J.-P.; et al., *Journal of Physical Chemistry B: Condensed Matter, Materials, Surfaces, Interfaces, & Biophysical Chemistry*, (1997) **101**, 5936

[126] Liu, J.; Huang, J.-W.; Shen, H.; Wang, H.; Yu, H.-C.; Ji, L.-N., *Dyes Pigments*, (2008) **77**, 374.

[127] Okamoto, K.; Mori, Y.; Yamada, H.; Imahori, H.; Fukuzumi, S., *Chemistry--A European Journal*, (2004) **10**, 474

[128] Larsen, R. W.; Jasuja, R.; Niu, S.-L.; Dwivedi, K., *Journal of Photochemistry and Photobiology A: Chemistry*, (1997) **107**, 71.

[129] Prodi, A.; Kleverlaan, C. J.; Indelli, M. T.; Scnadola, F.; Alessio, E.; Iengo, E., *Inorg Chem*, (2001) **40**, 3498.

[130] Ghirotti, M.; Chiorboli, C.; Indelli, M. T.; Scandola, F.; Casanova, M.; Iengo, E.; Alessio, E., *Inorg Chim Acta*, (2007) **360**, 1121.

[131] Harriman, A., *Journal of the Chemical Society, Faraday Transactions 2: Molecular and Chemical Physics*, (1981) **77**, 1281.

[132] Nemykin, V. N.; Rohde, G. T.; Barrett, C. D.; Hadt, R. G.; Bizzarri, C.; Galloni, P.; Floris, B.; Nowik, I.; Herber, R. H.; Marrani, A. G.; Zanoni, R.; Loim, N. M., *J Am Chem Soc*, (2009) **131**, 14969.

[133] Kim, J. E.; Pribisko, M. A.; Gray, H. B.; Winkler, J. R., *Inorg Chem*, (2004) **43**, 7953.

[134] Lee, J. C.; Chang, I. J.; Gray, H. B.; Winkler, J. R., *J Mol Biol*, (2002) **320**, 159.

[135] Linke-Schaetzel, M.; Anson, C. E.; Powell, A. K.; Buth, G.; Palomares, E.; Durrant, J. D.; Balaban, T. S.; Lehn, J.-M., *Chemistry – A European Journal*, (2006) **12**, 1931.

[136] de Biani, F. F.; Grigiotti, E.; Laschi, F.; Zanello, P.; Juris, A.; Prodi, L.; Chichak, K. S.; Branda, N. R., *Inorg Chem*, (2008) **47**, 5425.

[137] Chambron, J. C.; Collin, J. P.; Dixon, I.; Heitz, V.; Salom-Roig, X. J.; Sauvage, J. P., *J Porphyr Phthalocya*, (2004) **8**, 82.

[138] Vannelli, T. A.; Karpishin, T. B., *Inorg Chem*, (2000) **39**, 340.

[139] Vannelli, T. A.; Karpishin, T. B., *Inorg Chem*, (1999) **38**, 2246.

[140] Linke, M.; Chambron, J. C.; Heitz, V.; Sauvage, J. P., *Chem Commun*, (1999), 2419.

[141] K. Burrell, A.; M. Campbell, W.; B. Jameson, G.; L. Officer, D.; D. W. Boyd, P.; Zhao, Z.; A. Cocks, P.; C. Gordon, K., *Chem Commun*, (1999), 637.

[142] Basu, P.; Raitsimring, A. M.; Labarre, M. J.; Dhawan, I. K.; Weibrecht, J. L.; Enemark, J. H., *J Am Chem Soc*, (1994) **116**, 7166.

[143] Splan, K. E.; Keefe, M. H.; Massari, A. M.; Walters, K. A.; Hupp, J. T., *Inorg Chem*, (2002) **41**, 619.

[144] Fan, J.; Whiteford, J. A.; Olenyuk, B.; Levin, M. D.; Stang, P. J.; Fleischer, E. B., *J Am Chem Soc*, (1999) **121**, 2741.

[145] Lo Schiavo, S.; Serroni, S.; Puntoriero, F.; Tresoldi, G.; Piraino, P., *Eur J Inorg Chem*, (2002), 79.

[146] Sharma, C. V. K.; Broker, G. A.; Huddleston, J. G.; Baldwin, J. W.; Metzger, R. M.; Rogers, R. D., *J Am Chem Soc*, (1999) **121**, 1137.

[147] Ayabe, M.; Yamashita, K.; Sada, K.; Shinkai, S.; Ikeda, A.; Sakamoto, S.; Yamaguchi, K., *J Org Chem*, (2003) **68**, 1059.

[148] Alessio, E.; Macchi, M.; Heath, S. L.; Marzilli, L. G., *Inorg Chem*, (1997) **36**, 5614.

[149] Oh, J. B.; Nah, M. K.; Kim, Y. H.; Kang, M. S.; Ka, J. W.; Kim, H. K., *Adv Funct Mater*, (2007) **17**, 413.

[150] Oh, J. B.; Kim, Y. H.; Nah, M. K.; Kim, H. K., *Journal of Luminescence*, (2005) **111**, 255.

[151] Araki, K.; Dovidauskas, S.; Winnischofer, H.; Alexiou, A. D. P.; Toma, H. E., *J Electroanal Chem*, (2001) **498**, 152.

[152] Araki, K.; Toma, H. E., *Inorg Chim Acta*, (1991) **179**, 293.

[153] Alexiou, A. D. P.; Toma, H. E., *J. Chem. Res.-S*, (1997), 338.

[154] Araujo, J.; Nikolaou, S.; Alexiou, A. D. P.; Toma, H. E., *Mon. Chem.*, (1997) **128**, 759.

[155] Araki, k., *J Chem Res M*, (1994),

[156] Rea, N.; Loock, B.; Lexa, D., *Inorg Chim Acta*, (2001) **312**, 53.

[157] Onuki, J.; Ribas, A. V.; Medeiros, M. H. G.; Araki, K.; Toma, H. E.; Catalani, L. H.; Di Mascio, P., *Photochem Photobiol*, (1996) **63**, 272.

[158] Marek, D.; Narra, M.; Schneider, A.; Swavey, S., *Inorg Chim Acta*, (2006) **359**, 789.

[159] Dovidauskas, S.; Toma, H. E.; Araki, K.; Sacco, H. C.; Iamamoto, Y., *Inorg Chim Acta*, (2000) **305**, 206.

[160] Toma, H. E.; Araki, K.; Silva, E. O., *Monatshefte für Chemie / Chemical Monthly*, (1998) **129**, 975.

[161] Araki, K.; Winnischofer, H.; Viana, H. E. B.; Toyama, M. M.; Engelmann, F. M.; Mayer, I.; Formiga, A. L. B.; Toma, H. E., *J Electroanal Chem*, (2004) **562**, 145.

[162] Nunes, G. S.; Mayer, I.; Toma, H. E.; Araki, K., *Journal of Catalysis*, (2005) **236**, 55.

[163] Winnischofer, H.; Otake, V. Y.; Dovidauskas, S.; Nakamura, M.; Toma, H. E.; Araki, K., *Electrochimica Acta*, (2004) **49**, 3711.

[164] Araki, K.; Dovidauskas, S.; Winnischofer, H.; Alexiou, A. D. P.; Toma, H. E., *J Electroanal Chem*, (2001) **498**, 152.

[165] Liu, S.-Q.; Xu, J.-Q.; Sun, H.-R.; Li, D.-M., *Inorg Chim Acta*, (2000) **306**, 87.

[166] Slagt, V. F.; Kamer, P. C. J.; van Leeuwen, P. W. N. M.; Reek, J. N. H., *J Am Chem Soc*, (2004) **126**, 1526.

[167] Zhou, Z. C.; Zhu, Y. Z.; Zheng, J. Y., *Chem J Chinese U*, (2008) **29**, 1153.

[168] Obata, M.; Tanihara, N.; Nakai, M.; Harada, M.; Akimoto, S.; Yamazaki, I.; Ichimura, A.; Kinoshita, I.; Mikuriya, M.; Hoshino, M.; Yano, S., *Dalton T*, (2004), 3283.

[169] LeGourriérec, D.; Andersson, M.; Davidsson, J.; Mukhtar, E.; Sun, L.; Hammarström, L., *The Journal of Physical Chemistry A*, (1999) **103**, 557.

[170] Yu, L. H.; Muthukumaran, K.; Sazanovich, I. V.; Kirmaier, C.; Hindin, E.; Diers, J. R.; Boyle, P. D.; Bocian, D. F.; Holten, D.; Lindsey, J. S., *Inorg Chem*, (2003) **42**, 6629.

[171] Aly, S. M.; Ayed, C.; Stern, C.; Guilard, R.; Abd-El-Aziz, A. S.; Harvey, P. D., *Inorg. Chem. (Washington, DC, U. S.)*, (2008) **47**, 9930.

[172] Flamigni, L.; Collin, J. P.; Sauvage, J. P., *Accounts Chem Res*, (2008) **41**, 857.

[173] Benniston, A. C.; Chapman, G. M.; Harriman, A.; Mehrabi, M., *J Phys Chem A*, (2004) **108**, 9026.

[174] Dixon, I. M.; Collin, J.-P.; Sauvage, J.-P.; Flamigni, L., *Inorg Chem*, (2001) **40**, 5507.

[175] Flamigni, L.; Marconi, G.; Dixon, I. M.; Collin, J.-P.; Sauvage, J.-P., *The Journal of Physical Chemistry B*, (2002) **106**, 6663.

[176] Baranoff, E.; Barigelletti, F.; Bonnet, S.; Collin, J. P.; Flamigni, L.; Mobian, P.; Sauvage, J. P., *Struct Bond*, (2007) **123**, 41.

[177] Wiberg, J.; Guo, L. J.; Pettersson, K.; Nilsson, D.; Ljungdahl, T.; Martensson, J.; Albinsson, B., *J Am Chem Soc*, (2007) **129**, 155.

[178] D'Souza, F.; Chitta, R.; Gadde, S.; Islam, D. M. S.; Schumacher, A. L.; Zandler, M. E.; Araki, Y.; Ito, O., *J Phys Chem B*, (2006) **110**, 25240.

[179] Lin, V.; DiMagno, S.; Therien, M., *Science*, (1994) **264**, 1105.

[180] Uyeda, H. T.; Zhao, Y. X.; Wostyn, K.; Asselberghs, I.; Clays, K.; Persoons, A.; Therien, M. J., *Journal of the American Chemical Society*, (2002) **124**, 13806.

[181] Zhang, T. G.; Zhao, Y. X.; Song, K.; Asselberghs, I.; Persoons, A.; Clays, K.; Therien, M. J., *Inorg Chem*, (2006) **45**, 9703.

Chapter 3. Heteroleptic Ru Bisterpyridine Complexes: Understanding the Interligand Electronic Communications

3.1. Introduction

In spirit of the model-to-assembly approach to investigate a multi-component system incorporating a $[Ru(tpy)_2]^{2+}$ moiety, where tpy stands for 2,2':6':2''-terpyridyl, a complete understanding of this moiety will be essential towards elucidating the properties of the full target system. One key component of such understanding is the effect of asymmetric substitutions on the excited state behaviors of the molecule. Indeed, the global system design described in Chapter 1 requires asymmetric substitutions on the $[Ru(tpy)_2]^{2+}$ core.

While a detailed picture of substitution effects was presented by Thompson and coworkers[1] more than a decade ago, the dynamic consequences of asymmetric substitution were not systematically investigated to the best of my knowledge. In the context of $[Ru(R_1\text{-tpy})\ (R_2\text{-tpy})]^{2+}$ heteroleptic complex, following excitation in the region of the metal-to-ligand charge transfer (MLCT) absorption, two possible excited species will be produced:

$$[Ru^{II}(R_1 - tpy)(R_2 - tpy)]^{2+} \xrightarrow{h\nu} [Ru^{III}(R_1 - tpy^{-})(R_2 - tpy)]^{2+}$$

$$[Ru^{II}(R_1 - tpy)(R_2 - tpy)]^{2+} \xrightarrow{h\nu} [Ru^{III}(R_1 - tpy)(R_2 - tpy^{-})]^{2+}$$

where an electron is transferred from a nominally metal-based orbital to a ligand-based π* orbital on either of the ligands. Unless R_1 and R_2 are the same, the final states in the

two equations above represent the lowest and the second-lowest MLCT states, differing only by the localization of the negative charge. As the light absorption event can be reasonably approximated to be an instantaneous Frank-Condon process, the populations of these two MLCT states depend solely on their extinction coefficients at the excitation wavelength. The higher-energy state of these two will then go through interligand electron transfer (ILET) to form the lowest MLCT state:

$$[Ru^{III}(R_1 - tpy)(R_2 - tpy^-)]^{2+} \xrightarrow{ILET} [Ru^{III}(R_1 - tpy^-)(R_2 - tpy)]^{2+}$$

at the same time as it decays via intrinsic radiative (luminescence) and nonradiative processes. When the ILET rate is sufficiently fast and dominates all other processes, only the lowest-energy MLCT state is relevant for the subsequent photophysical and photochemical reactivities, *i.e.* Kasha's rule. When this criterion is not satisfied, however, the second-lowest MLCT state will have a significant role in determining the Ru reactivities. While this issue is not commonly discussed in plain Ru polypyridyl complexes, it is a crucial aspect of the early-time dynamics of excited molecule, and has to be addressed carefully. This becomes especially important in supramolecular systems, where the intrinsic geometry of the molecule results in different donor-acceptor distances associated with the two terpyridyl ligands, thus different reactivities. In these situations, the ILET rate becomes a critical parameter in analyzing the dynamic data, an example of which will be shown in Chapter 4.

The ILET process in $[Ru(tpy)_2]^{2+}$ complex has not yet been characterized to the best of my knowledge. The most relevant rate constant is that for its bipyridyl analogue

$[Ru(bpy)_3]^{2+}$, which is in the sub-50 ps time domain in acetonitrile[2, 3]. This suggests that Kasha's rule will not be a good approximation when any chemical/physical processes with a time constant on the order of 50 ps or less are considered: more than one MLCT excited states need to be invoked. Although the local ligand environment is similar between $[Ru(tpy)_2]^{2+}$ and $[Ru(bpy)_3]^{2+}$, topologies are distinctly different. $[Ru(tpy)_2]^{2+}$ has two terpyridyl ligands lying in orthogonal planes, suggesting a much different (presumably smaller) inter-ligand electronic coupling strength. A different ILET rate may logically follow. Definitive understandings in the reactivities of the second-lowest MLCT state and its role in subsequent processes require a better characterization of ILET in $[Ru(tpy)_2]^{2+}$-based complexes.

The detection of ILET process can be achieved either indirectly by measuring the lifetime of the higher-lying MLCT state in the asymmetric compound and compare to that of the relevant homoleptic complex, or directly by looking at the conversion of the absorptive signature between the initial and final states. The dilemma is that neither luminescence nor absorption data alone gave convincing data due to the intrinsic nature of this type of complex: the Ru-terpy based luminescence are typically extremely weak with quantum yields on the order of 10^{-5}, which makes accurate determination of lifetimes difficult and ILET rate obtained this way unreliable; and the absorption features of the MLCT states associated with terpyridine radical anions are commonly quite similar, which leads to a very small detectable signal in difference absorption (TA) measurements, resulting in inconclusive data as well. In order to address these issues,

a new heteroleptic complex, *i.e.* (4'-phenyl-2,2':6':2”-terpyridyl)(4'-(4-nitro)phenyl-2,2':6':2”-terpyridyl) ruthenium(II) hexafluorophosphate ($[Ru(NO_2Phtpy)(Phtpy)]^{2+}\cdot 2PF_6^-$, or **RuNPh**, Figure 3-1) was synthesized and investigated carefully, where the combined electronic withdrawing and delocalization effect of the nitro- substituent results in a red shift of the terpyridyl radical anion absorption signature, allowing a clear differentiation between the two MLCT states with transient absorption technique.

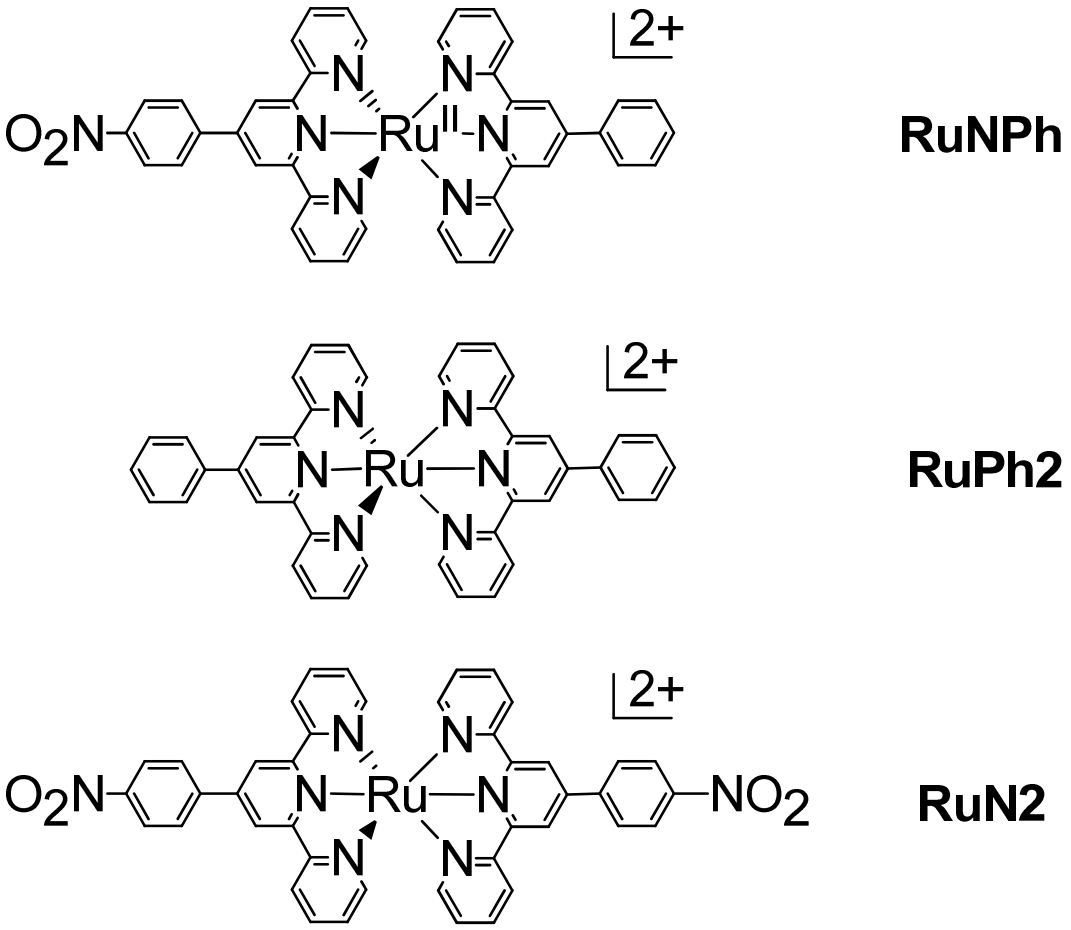

Figure 3-1 $[Ru(R_1\text{-tpy})(R_2\text{-tpy})](PF_6)_2$ complexes discussed in this chapter.

In this chapter, a detailed investigation of the photophysical properties of **RuNPh** will be presented in the first part of the discussion, along with its two homoleptic reference

complexes, **RuPh2** and **RuN2**, each resembling one half of the target molecule. Interestingly, complications from purity and photodecomposition arose during my synthesis, separation and initial characterization efforts, which revealed some crucial, yet commonly disregarded issues in handling these heteroleptic Ru bisterpyridyl complexes. These considerations will be addressed separately in detail in the second part of the discussion. To the best of my knowledge, this represents the first systematic study on such details and could add on not only to the scientific understandings of the excited state processes in these heteroleptic Ru bisterpyridyl complexes for applications like the one to be discussed in Chapter 4, but also to establishing the methodological protocols to be followed when handling this class of molecules.

3.2. Experimental Section

General. All reagents and materials were purchased from Aldrich Chemical Co. and used as received without further purification unless otherwise stated. The ligands 4'-phenyl-2,2':6':2''-terpyridine[4] (Phtpy) and 4'-nitrophenyl-2,2':6':2''-terpyridine[5] (NO_2Phtpy) were synthesized according to literature methods respectively. $RuCl_3 \cdot xH_2O$ were purchased from Strem Chemicals, Inc. All syntheses were performed under N_2 inert atmosphere. ^{1}H NMR spectra were recorded on either Varian UnityPlus-500 (500 MHz) or Varian Inova-300 (300 MHz) spectrometers.

Bis-(4'-phenyl-2,2':6':2''-terpyridyl) ruthenium (II) Hexafluorophosphate ($[Ru(Phtpy)_2]^{2+}\cdot 2PF_6^-$, RuPh2). 4'-phenyl-2,2':6':2''-terpyridyl (680 mg, 2.2 mmol) and $RuCl_3\cdot 3H_2O$ (262 mg, 1 mmol) were dissolved in a strictly deaerated 1:1 solvent mixture of freshly distilled ethylene glycol and absolute ethanol (50 mL) and heated under reflux condition for 3 hours with magnetic stirring maintained. The red brown solution was cooled to room temperature and diluted with water (20 mL) and filtered to remove the fine black precipitate. The solution was the treated with $NaPF_6$ (3 eq.), which resulted in the precipitation of a red-brown solid, which was collected on a frit, washed with water (2 × 20 mL) and diethyl ether (2 × 20 mL) and air dried. The crude product was dissolved in minimal amount of acetonitrile and recrystalized by slow ether diffusion. The yield was 70%. ESI-MS: 360.1 ([**RuPh2**-$2PF_6$]$^{2+}$).

Bis-(4'-(4-nitro)phenyl-2,2':6':2''-terpyridyl) ruthenium (II) Hexafluorophosphate ($[Ru(NO_2Phtpy)_2]^{2+}\cdot 2PF_6^-$, RuN2). 4'-(4-nitro)phenyl-2,2':6':2''-terpyridyl (780 mg, 2.2 mmol) and $RuCl_3\cdot 3H_2O$ (262 mg, 1 mmol) were dissolved in a strictly deaerated 1:1 solvent mixture of freshly distilled ethylene glycol and absolute ethanol (50 mL) and heated under refluxing condition for 3 hours with magnetic stirring maintained. The red brown solution was cooled to room temperature and diluted with water (20 mL) and filtered to remove the fine black precipitate. The solution was the treated with $NaPF_6$ (3 eq.), which resulted in the precipitation of a red-brown solid, which was collected on a frit, washed with water (2 × 20 mL) and diethyl ether (2 × 20 mL) and air dried. The crude product was dissolved in acetonitrile (4 mL) and chromatographed on silica eluted

with 7:1 acetonitrile–H_2O/KNO_3 (sat.). The main red-brown band containing the product was reduced in volume to 5 mL, and treated with $NaPF_6$ to precipitate the product. The precipitate was filtered, washed with water (2 × 20 mL), diethyl ether (2 × 20 mL) and dried *in vacuo* before it was re-dissolved in minimal amount of acetonitrile and recrystallized by slow ether diffusion. The yield was 50%. ESI-MS: 405.1 ([**RuN2**-$2PF_6$]$^{2+}$).

(4'-phenyl-2,2':6':2”-terpyridyl)(4'-(4-nitro)phenyl-2,2':6':2”-terpyridyl) ruthenium(II) Hexafluorophosphate ([Ru(NO_2Phtpy)(Phtpy)]$^{2+}$·$2PF_6^-$, RuNPh). Ru(Phtpy)Cl_3 (258 mg, 0.5 mmol), and NO_2phtpy (354 mg, 1 mmol) were heated to reflux in a 1:1 solvent mixture of freshly distilled ethylene glycol and absolute ethanol (30 mL) for 2 hours with magnetic stirring maintained. The purple solution was cooled to room temperature and diluted with water (30 mL) and filtered to remove the fine black precipitate. The solution was the treated with $NaPF_6$ (3 eq.), which resulted in the precipitation of a red-brown solid. The solid was collected on a frit, washed with water (2 × 20 mL) and diethyl ether (2 × 20 mL) and air dried. The crude product was dissolved in acetonitrile (2 mL) and chromatographed on silica eluted with 7:1 acetonitrile–H_2O/KNO_3 (sat.). The main red-brown band containing the product was reduced in volume to 5 mL, and treated with $NaPF_6$ to precipitate the product. The precipitate was filtered, washed with water (2 × 20 mL), diethyl ether (2 × 20 mL) and dried *in vacuo*. This product was subjected to high-performance liquid chromatography separations with a Supelcosil™ LC-18 semi-preparative reverse-phase silica gel (C18) column with the

dimensions of 25 cm x 10 mm and a 5 μm particle size. The eluent used was composed of spectrometric grade acetonitrile and 0.1 M KNO_3 aqueous solution with a ratio of 5:2. The middle band was collected and crystallized to yield pure product. ESI-MS: 382.6 ([**RuNPh**-2PF_6]$^{2+}$). Yield: 10%.

Physical Measurements. Electrochemistry. Electrochemical measurements were performed with a CHI 630B electrochemical analyzer under Ar atmosphere in a glove box. A standard three-electrode electrochemical setup, consisted of a Pt working electrode, a graphite counter electrode and a Ag/AgCl reference electrode (from Cypress Systems) were used. Solutions of the compounds were dissolved in distilled spectrometric grade acetonitrile, which was degassed by freeze-pump-thaw method prior to the experiment. Tetrabutylammonium hexafluorophosphate ([TBA]PF_6, ca. 0.1 M) was used as supporting electrolyte.

Steady State Electronic Absorption and Emission Spectroscopy. Steady state electronic absorption and extinction coefficients measurements were done with a Cary 50 UV-Visible Spectrometer in spectro-grade acetonitrile solutions unless otherwise noted. Steady-state emission spectroscopy was obtained on a Spex Fluoromax fluorimeter with instrumental response corrected against a NIST standard of spectral irradiance[2]. All samples were dissolved in spectro-grade solvents distilled over CaH_2 and thoroughly degassed via standard freeze-pump-thaw method. Emission spectra were acquired in argon-filled air-free 1 cm-path length quartz cuvettes under optical dilute condition with absorbance values between 0.1 and 0.15. The excitation slits on

the fluorimeter were set at 7 mm in order to obtain reasonable signal intensity, while emission slit widths were set at 0.5 mm.

Variable Temperature Time-correlated Single Photon Counting (TCSPC) Spectroscopy.

All fluorescence lifetime data were acquired using a time-correlated single photon counting (TCPSC) instrument. The instrumental setup will be described in detail in Chapter 4. For variable temperature measurements described in this section, the sample temperature (-5℃ ~ 45℃) was regulated with a coolant-circulating bath (Neslab RTE-110) where the coolant was a 1:1 ethylene glycol-water mixture, connected via a well-wrapped (with cotton) hose to a temperature-controlled brass cell jacket which held the sample cuvette. For sub-room temperature measurements, a house nitrogen line was used to blow cold N_2 onto the cuvette to prevent water condensation. This nitrogen stream was chilled first by going through a low-temperature flask, kept in an acetone/dry ice bath of -75 ℃, before hitting the cuvette. The temperatures of the sample reported were the mathematical average of that measured before and after each data point measurement, by replacing the sample with a cuvette filled with acetonitrile, and read the temperature of that directly with a thermometer. The temperatures were regulated to be within ± 1 ℃ throughout the extended period of time of 1-3 hrs per data point. All samples were allowed to equilibrate thermally for 10 minutes prior to data acquisition. The sample condition is the same as that described for the steady-state emission measurements.

Transient Absorption (TA) Spectroscopy and flow setup.

The transient absorption instrument setup with laser pulses in the regime of femtoseconds and a 13 ns long delay line will be described in detail in Chapter 4. The sample was made in glove-box filled with argon atmosphere. For the femtosecond TA measurements on a *flow setup*, the spectra were taken on a constantly flowing sample in a home-made flow-cell setup composed of a 250 ml round bottom flask with its bottom opened and connected via a Teflon tube to a 1 mm path length quartz cuvette. Both the opening of the round bottom flask and the outlet of the cuvette were closed with appropriate rubber septa. The flask was held on a clamp above the cuvette sample holder on the laser table. The flow started when the capping septa on the outlet of the cuvette was poked with a needle and allowed to flow out as a result of gravity. The pressure inside the flask was maintained to be minimally larger than atmosphere using the combination of a N_2–filled balloon connected to a needle, which could be plugged into the septa on the top of the flask to increase the pressure, and an empty syringe, which could be used to reduce the pressure inside the flask without it being opened to air. The flow was maintained at minimal, yet non-negligible pace. The estimated flow rate was 10 mL/h.

Mass Spectrometry. Samples dissolved in acetonitrile were introduced to an ultra-high resolution / accurate mass Thermo Scientific model LTQ Orbitrap Velos mass spectrometer (Thermo Scientific, San Jose, CA) using either a Advion Nanomate Triversa (Advion BioSciences, Ithaca, NY, USA) nano-electrospray ionization (nESI)

source operating in infusion mode. Chipsoft version 7.1 software (Advion, Ithaca, NY) was used to set the NanoMate spray voltage to 1.5 kV, gas pressure to 0.3 psi, and post-aspiration air gap of 3 µL. Alternatively, samples were introduced by infusion using a syringe pump at a flow rate of 5 µL min^{-1}. Mass spectra were acquired for one minute using a mass resolving power of 100,000.

3.3. Results and Discussions

Due to the complications in the synthesis, separation as well as photolability issue, section 3.3.2 will be devoted exclusively to these considerations. The discussions presented in 3.3.1 will be based on purified samples under an instrumental setup, detailed in the experimental section, which does not induce decomposition reactions.

3.3.1. Photophysical Properties of Ruthenium Bisterpyridyl Complexes

3.3.1.1 Photophysical Properties of Ruthenium Bisterpyridyl Complexes in General: RuPh2 and RuN2

In order to comprehensively understand the heteroleptic **RuNPh** complex, it is necessary to review the photophysical properties of its two homoleptic reference complexes. It has been found that ruthenium bisterpyridyls have quite similar photophysical properties as $[Ru(bpy)_3]^{2+}$ systems due to the very similar local ligand environment around the metal center. However, a few distinct spectroscopic features

are notable: the features in UV-Vis absorption spectra are usually evidently sharper and stronger than $[Ru(bpy)_3]^{2+}$ systems; the emission quantum yield is a few hundred fold weaker and the lifetimes much shorter. All these differences can be rationalized in the context of energy level diagrams of these systems (Figure 3-2).

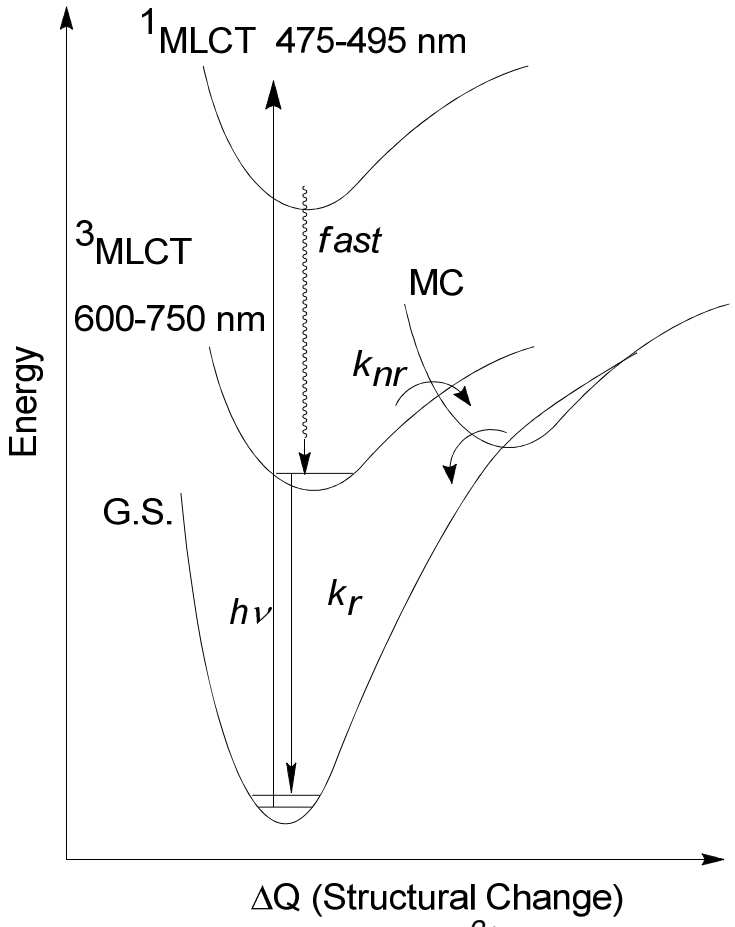

Figure 3-2 Energy level diagram for typical $[Ru(tpy)_2]^{2+}$ complexes

The ground state absorption spectra of this series of complexes are shown in Figure 3-3. The absorption peak around 490 nm was assigned to ^{1}MLCT absorption based on the magnitude of extinction coefficients (Table 3-1). The lower energy of absorption maxima as compared to that of the parent $[Ru(tpy)_2]^{2+}$ compound can be explained by

a weak electron-donating effect of the phenyl substituent which lowers the reduction potential of the complex while leaving the oxidation potential of Ru metal relatively unperturbed. The sharpness of these bands as compared to their $[Ru(bpy)_3]^{2+}$ counterparts is a result of increased electron delocalization effect associated with the terpyridine ligands, where the additional electron in the ligand being spread over all three pyridyl rings leads to a diluted effect on the structural change of the molecule. This translates into a small shift of excited state potential energy surface along the ΔQ coordinate (Figure 3-2), as compared to that of the ground state. As a result, the much nested potential surfaces lead to well matched wave function distributions, hence the sharp and intense band as direct spectroscopic consequences. The additional phenyl ring on the back of the terpyridine ligand, however, is shown by DFT calculations to be canted by an angle between 35 to 39 degrees, depending on peripheral substitutions. On the time scale of light absorption (~ fs), the ring cannot respond sufficiently quick via rotation to allow electron delocalization onto the back phenyl ring, hence unable to exert any significant stabilization effect on the absorption spectra other than the weak electron-donating effect. As a result, in the Frank-Condon-type ^{1}MLCT state, the electronic structures are almost identical across the series of **RuNPh**, **RuN2**, **RuPh2** and are very similar to that of $[Ru(tpy)_2]^{2+}$ reported earlier.[6] In other words, the absorption feature shall be controlled majorly by the $[Ru(tpy)_2]^{2+}$ core rather than any substituents attached. This was confirmed in this series via the absorption spectra, where the peak maxima span a range of merely 5 nm.

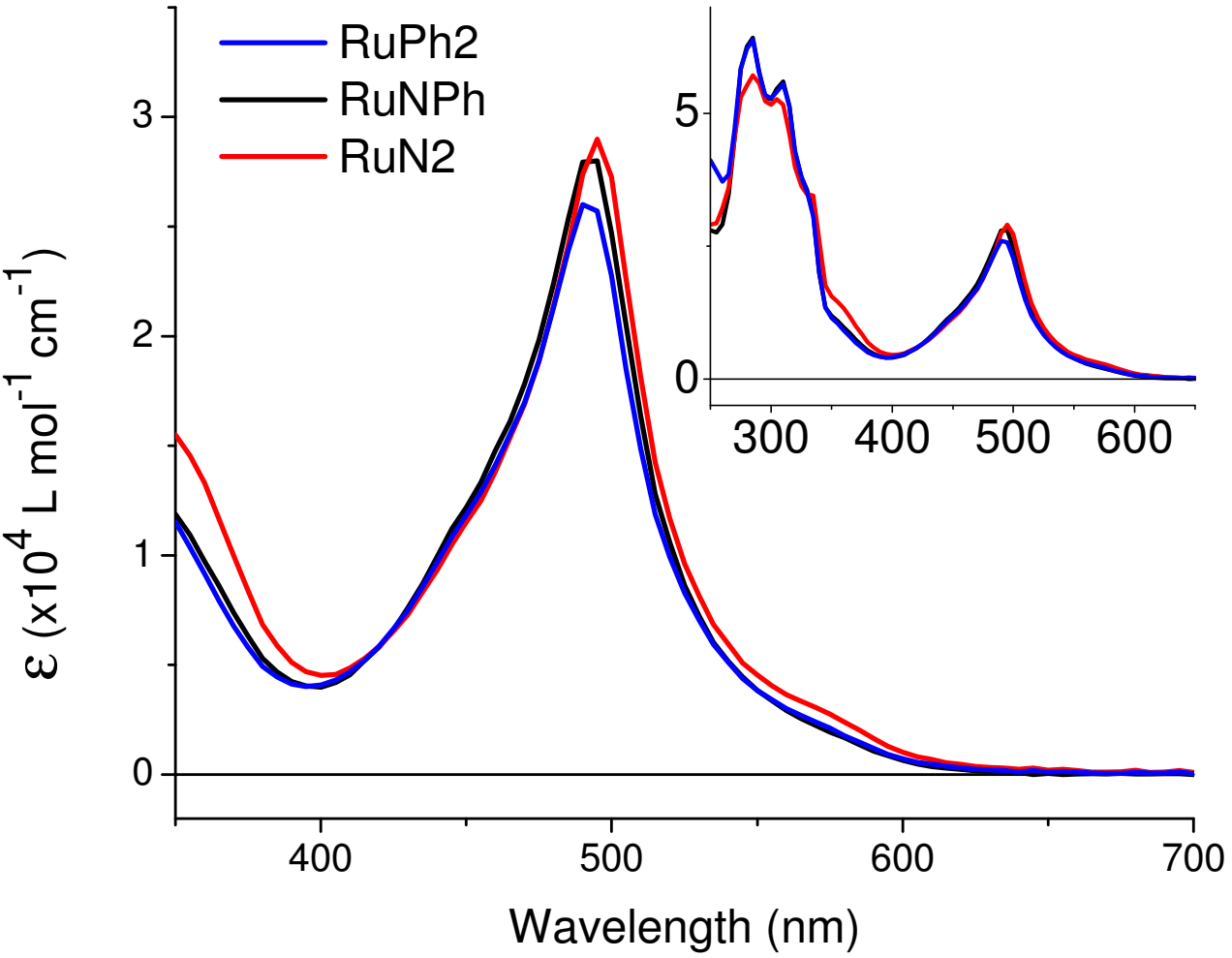

*Figure 3-2 UV-Vis absorption spectra of **RuNPh** (black), **RuPh2** (blue) and **RuN2** (red). The spectra were recorded in a spectro-grade acetonitrile solution. The extinction coefficients are listed in Table 3-2.*

The two peaks in the UV region were assigned to the two π to π* absorption features based on terpyridine ligands. The smaller intensity in **RuN2** can be rationalized with the electronic withdrawing effect of nitro- substitution reducing the population on the terpyridine ring; while the unchanged peak positions across the three complexes again confirm that the energy of the absorption is not affected to any significant extent by the nature of the substituents attached.

The lowest excited states in these $[Ru(R\text{-}tpy)]^{2+}$ complexes have been identified to be ^{3}MLCT in nature. Since the electronic difference between this state and the Frank-Condon ^{1}MLCT state is merely a spin flip, it is expected to possess the same electronic structures and can be placed at the same ΔQ coordinate on the energy level diagram (Figure 3-2). This excited state, typically with lifetimes on the order of a few hundred picoseconds and a few orders of magnitude shorter than $[Ru(bpy)_3]^{2+}$, is the longest-lived excited state in this type of complexes. Its quantum yield on the order of 10^{-5} is commonly considered non-emissive in literature. This is the result of the presence of a thermally-accessible metal-centered ligand-field state (MC) above the emitting ^{3}MLCT state. Such a difference with that for $[Ru(bpy)_3]^{2+}$ complex can be explained by the much larger deviation of local ligand environment from the ideal octahedral geometry, leading to a weaker ligand field and a low-in-energy metal-centered excited state. As this state is known to couple efficiently to the ground state, it serves as an efficient nonradiative decay pathway for the emissive ^{3}MLCT state.

The emission peak positions of **RuN2** and **RuPh2** (Table 3-1) are quite similar to each other and can be explained by the cancelling effects on energy gap (ΔE) between a smaller structural change (ΔQ) in **RuN2** and a lower energy position on the energy axis, leading to the close emission maxima.[1] The lifetime of this ^{3}MLCT state can be obtained via time-resolved luminescence measurements. The decay traces could be fit to a single-exponential decay model to give the time constants as shown below:

$$y = y_0 + Ae^{-x/\tau}$$

where *y* is the emission intensity, *x* is the time, and *τ* is the lifetime constant. It has been reported[1] that $[Ru(tpy)_2]^{2+}$ possess a ^{3}MLCT state with a lifetime of 250 ps and that for $[Ru(Ph\text{-}tpy)_2]^{2+}$ (or **RuPh2**) is 1 ns. My TCSPC measurements on **RuPh2** shows a lifetime of 800 ± 50 ps, reasonably consistent with the literature results within experimental error.

Table 3-1 Absorption and Luminescence Data

	λ_{abs}, nm (ε, x 10^4 $M^{-1}cm^{-1}$)	λ_{em}[a], nm (Φ, x 10^{-5})	τ_{RT}[b], ns
RuPh2	490 (2.6)	670 (4)	0.7 ± 0.01
RuNPh	493 (2.8)	685 (6)	9.6 ± 0.4
RuN2	495 (2.9)	685 (7)	9.6 ± 0.4

[a] The large excitation slit (7 mm) settings in the steady-state emission instrument restricted the accuracy of the quantum yield.

[b] Lifetime based on TCSPC measurements.

The fact that $[Ru(Ph\text{-}tpy)_2]^{2+}$ has a longer lifetime as compared to $[Ru(tpy)]^{2+}$ results from its increased delocalization into the additional phenyl ring in the long-lived excited state. Unlike ^{1}MLCT state, where the molecule can be considered to be frozen in the ground state geometry on the time scale of absorption event, the lifetime measurement is conducted on a thermalized ^{3}MLCT excited state which has vibrationally-cooled to its

lowest energy. This means that the fourth phenyl ring in $[Ru(Ph\text{-}tpy)_2]^{2+}$ has sufficient time to rotate and become more coplanar with the terpyridyl plane thereby allowing the electron density to be delocalized onto a larger extent and lowering the energy of ^{3}MLCT state as compared to $[Ru(H\text{-}tpy)_2]^{2+}$. The ruthenium core, however, is expected to only be slightly affected by the already-diluted delocalization effect on the ligand. Thus the ligand field strength is only minimally changed, leaving the higher-lying MC state relatively non-perturbed in energy[7]. This, in effect, decouples the emissive state from the deactivating upper state, thereby lengthening the ^{3}MLCT lifetime. The lifetime of $[Ru(NO_2Ph\text{-}tpy)_2]^{2+}$ (**RuN2**) was found to be 10 ns at room temperature (see Table 3-1), which is also consistent within the above framework: both the delocalization as well as the electronic withdrawing effect of nitro- substituent lower the energy of ^{3}MLCT state, reducing the effectiveness of this decay pathway[8], hence the much longer lifetime.

Transient absorption spectroscopy is another important characterization tool to understand the properties of the lowest energy ^{3}MLCT excited state(s). The spectra profiles of the two reference complexes **RuN2** and **RuPh2** are quite similar in general, with relatively small variation in the shapes of the two peaks in the blue and red regions (see Figure 3-4). Representative single wavelength decay traces, are shown in Figure 3-8. The lifetime of ligand radical absorption signature decay in **RuPh2** was fit to be 700 ± 10 ps while that for **RuN2** was fit to be approximately 10 ns, consistent with TCSPC results (see Table 3-1). It needs to be pointed out that due to the limitation of

instruments, longer lifetimes are more accurately determined from time-resolved luminescence instrument where the time window available was 50 ns; while the shorter time component can be more accurately determined in femtosecond time-resolved absorption spectra as the instaneous instrument response function allows better time resolutions.

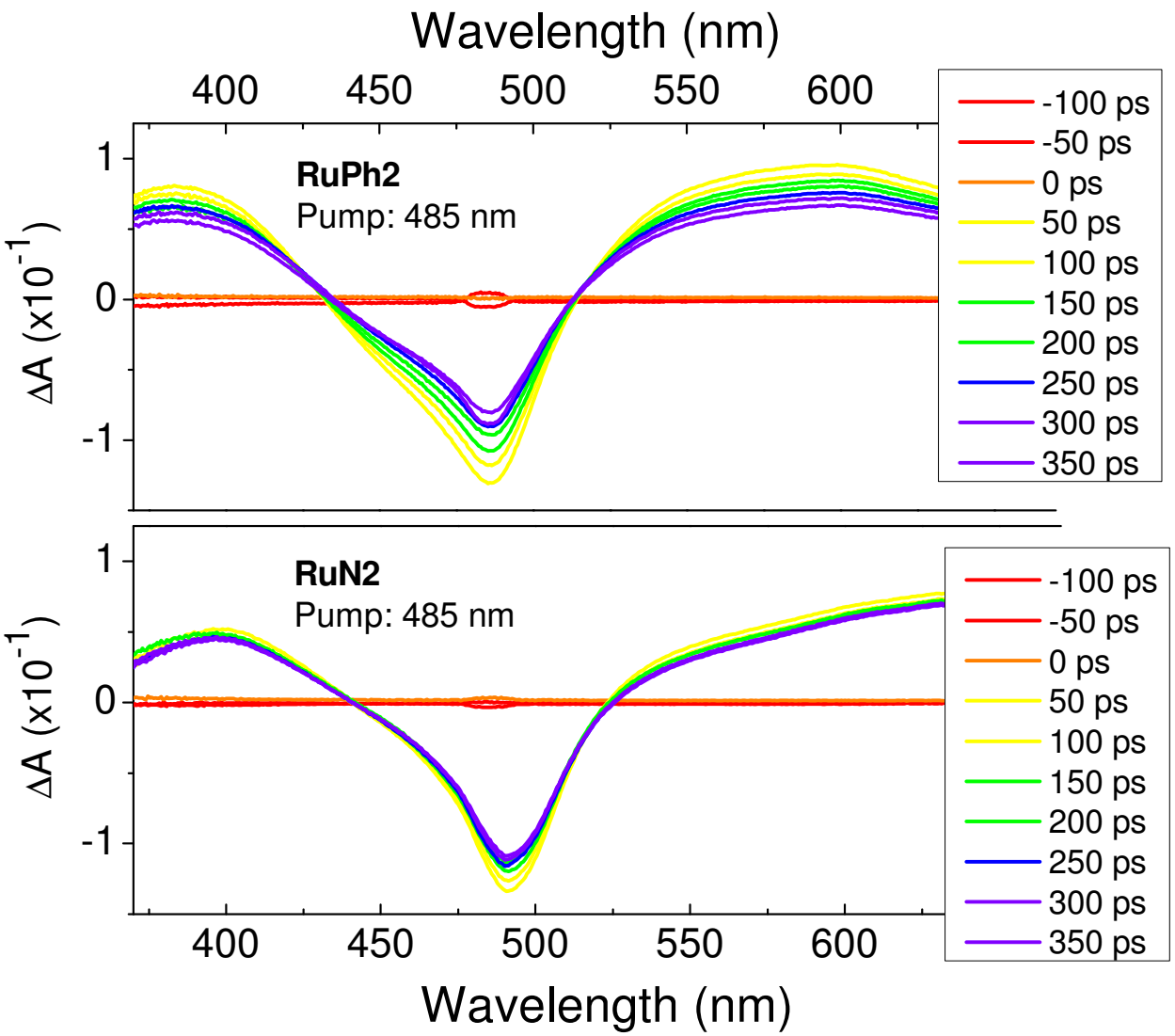

*Figure 3-3 Femtosecond transient absorption (TA) spectra for **RuPh2** (top) and **RuN2** (bottom) following excitation at 485 nm.*

3.3.1.2 RuNPh: Steady-State Absorption and Emission Spectroscopy.

The ground state absorption spectrum of **RuNPh** is shown in Figure (3-2) along with those for the two reference complexes. Clearly, all the features are very similar to each other. This, while expected as both halves of the **RuNPh** shall absorb light with similar extinction coefficients (Table 3-1) at the same time, also indicates that the electronic communication between these two halves of the molecule is weak, despite that they are coupled to the same Ru metal center. As discussed above, this supports the notion that the orthogonal meridinal binding motif of the two terpyridyl ligands limits the interligand electronic communications. The steady-state emission spectroscopy of **RuNPh** shows similar peak position to the homoleptic complexes. The quantum yields is calculated to be 6×10^{-5} based on a comparison to that of $[Os(bpy)_3](PF_6)_2$ as a standard.

3.3.1.3 Femtosecond TA on a flowing RuNPh sample: Identification of Interligand Electron Transfer.

Starting with a HPLC-purified **RuNPh** sample in a flow setup as described above, femtosecond TA spectra were recorded following excitation at 485 nm. Both full spectra and representative single wavelength dynamic data are seen in Figure 3-5.

Single wavelength dynamic traces show that on top of the expected long component with approximately 8.5 ± 1.5 ns lifetime, which is attributed to the intrinsic decay of $[Ru(NO_2Phtpy)]$ fragment referenced to the homoleptic $[Ru(NO_2Phtpy)]_2^{2+}$ complex (see Table 3-1), a short rise with a time constant smaller than 100 ps is also present.

Although the signal-to-noise ratio (S/N) of this measurement does not allow an accurate time constant to be determined, the presence of a short process is clear. Considering the facts that 1) the intrinsic lifetime for the [Ru(Phtpy)] fragment is on the order of 700 ps (see Table 3-1), 2) both intersystem crossing from ^{1}MLCT state and the vibrational cooling of a hot ^{3}MLCT state are expected to be completed within the first 10 ps, and 3) the solvent contribution should not be manifested due to the laser polarization being situated at magic angle position, this observed new component is tentatively assigned to the interligand electron transfer, that from the higher-lying ^{3}MLCT localized on the Phtpy ligand to the lowest ^{3}MLCT localized on the NO_2Phtpy ligand. The rise feature and the small amplitude change are consistent with the slightly-higher extinction coefficient associated with the NO_2Phtpy radical anion versus that of Phtpy.

This model is further supported by the full spectra profile change of this complex as a function of time, seen Figure 3-5 bottom panel. While the spectral profile of this complex is quite similar to those of the two reference homoleptic complexes (Figure 3-4), differences are notable. The absorptive feature in the red region for **RuPh2** peaks at approximately 600 nm, while that for **RuN2** shows a continuous growth going from 550 nm beyond 630 nm. While **RuNPh** mostly resembles the profile of **RuN2** closely, the trace collected 200 ps after laser excitation is distinctly different with a peak value of 650 nm. It appears to be a mixture between that of **RuPh2** and **RuN2**. This supports the model presented here that a higher ^{3}MLCT state based on the Phtpy ligand exists briefly following the excitation, and quickly goes through interligand electron transfer to

form the lowest ^{3}MLCT state on NO_2Phtpy. Recollection of the same data with a shorter time-step of 1 ps is under progress in order to fill in the detailed profile change indicative of the proposed ILET.

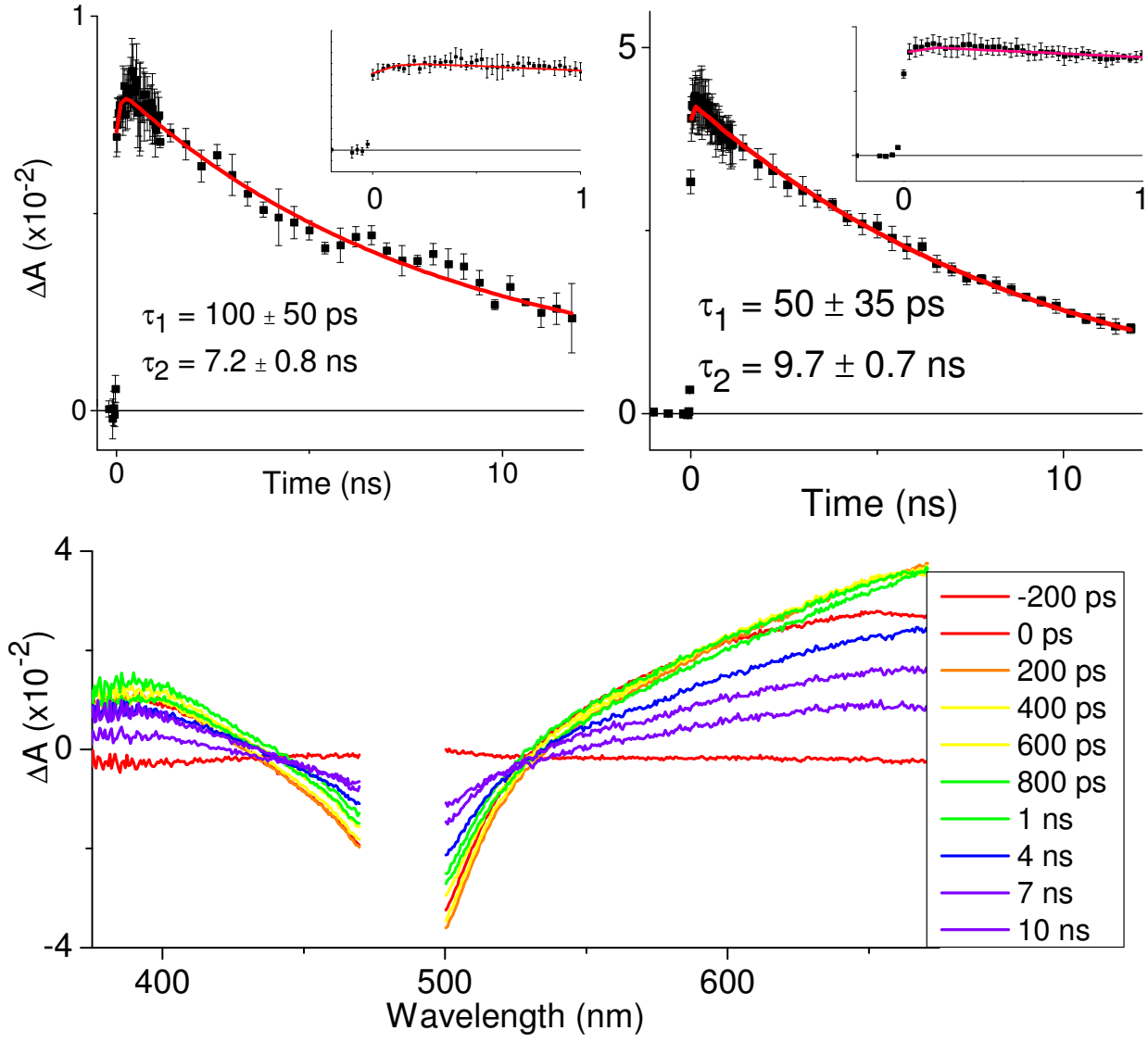

Figure 3-5 Femtosecond TA spectra for **RuNPh** following 485 nm excitation: Full spectra (bottom) and single wavelength dynamics probed at 570 nm (top left) and 650 nm (top right). The 470 nm - 495 nm region in full spectra was affected by the presence of laser scatter, thus removed for clarity.

To summarize this section, a fast process (< 100 ps) was observed on transient absorption spectra of the newly synthesized **RuNPh** complex. This process is tentatively assigned to the interligand electron transfer from the second-lowest ^{3}MLCT state to the lowest ^{3}MLCT state. This process has not been subjected to close scrutiny in the community, is crucial to understanding subsequent photophysical/photochemical processes correctly. The fact that this rate is comparable to that of $[Ru(bpy)_3]^{2+}$ suggests that the dominant interligand electron transfer process involves a pathway not sensitive to topology. A reasonable possibility is that via the hole created on the metal-based orbitals. DFT-calculations are being pursued to verify such assumption.

3.3.2. Handling Ru Bisterpyridyl Complexes: Complications and Precautions.

3.3.2.1. Consideration of Synthesis.

The syntheses of the ruthenium bisterpyridyl complexes have been well documented, and that of the homoleptic complexes **RuPh2**, **RuN2** were straightforward. The reported synthesis of heteroleptic Ru complexes typically starts with the preparation of Ru (III) terpyridyl trichloride, a black power insoluble in most solvents, followed by its reaction with excess amount of the other terpyridine ligand as a suspension at elevated temperatures. Different procedures were reported for this second step, where reducing

agents like *N*-ethylmorpholine can be added to assist in the reduction of Ru (III) to Ru (II). Alternatively, the solvent itself may serve as the reducing agents. My previous efforts in synthesizing similar complexes typically utilized a 1:1 mixture of ethanol and ethylene glycol. As compared to the literature method, the presence of ethanol allows easier reduction of the Ru (III) to Ru (II), due to the fact that oxidation of ethanol does not produce a cation adjacent to an electropositive carbon as it does in the ethylene glycol case. Yet the ethylene glycol was required for the solubility reason. The yield was usually reasonably high in the range of 70%.

Attempts to synthesize **RuNPh** following this same route, however, suffered from very low yield. When Ru(Phtpy)Cl_3 was first prepared followed by its reaction with NO_2Phtpy ligand, a mixture of the desired product along with significant amount of two homoleptic complexes was produced. When Ru(NO_2Phtpy)Cl_3 was reacted with Phtpy ligand, the only product obtained was $[Ru(Phtpy)_2]^{2+}$ with no significant presence of the desired heteroleptic complex. These observations point to the possibility of scrambling during the heating process. Scrambling of ruthenium polypyridyl complexes at higher temperatures was known in the community and observed in our previous attempts to prepare similar complexes. Chromatographic separations, however, usually affords pure product readily. Unfortunately, similar separation treatments on **RuNPh** turned out to be ineffective. Contrary to the intuitions that complexes bearing different numbers of nitro-substituents shall have sufficiently different retention times on the column, they turned out to be rather similar. My best column chromatography separation results were

obtained using neutral alumina 150 mesh (58 Å) from Aldrich as stationary phase and an eluent consisted of acetonitrile with 0%-5% methanol. The orange band containing all three complexes smeared out on the whole column. **RuPh2** mostly occupied the lower half of the column, with its concentration decreasing slowly from the solvent front to pass-the-middle point of the column. **RuN2** stayed at the very top of the column although significant amount started to appear from before-the-middle point of the column with slowly increasing percentage moving up the column. **RuNPh** band peaked right at the middle of the band although extended throughout the whole column. In other words, the **RuNPh** sample was always polluted with one homoleptic complex or the other, and more frequently, with both. While repetitive column chromatography did remove a significant amount of homoleptic impurities, it did not yield a pure product, and suffer from huge yield loss to give only a speck of product of ~95% purity. The identities of the complexes in the various column fractions were monitored with ^{1}H NMR (Table 3-2) and ESI-MS spectrometry. Trials with alternative solvent mixtures as well as different stationary phases (normal or reverse-phase Si gel) failed to provide any improvements on the separation.

The final pure product of **RuNPh** was obtained via High Performance Liquid Chromatography (HPLC) *after* one regular alumina column as describe above to remove non-Ru impurities, using a Shimadzu LC-8A preparative liquid chromatograph instrument with a Supelcosil™ LC-18 semi-preparative reverse-phase silica gel (C18) HPLC column (dimension: 25 cm x 10 mm, 5 µm particle size). The eluent used was

composed of HPLC grade acetonitrile and 0.1 M KNO_3 aqueous solution with a ratio of 5:2. The progresses of bands were monitored with a UV detector at 269 nm and 309 nm simultaneously.

Another complication in the preparation and separation of these complexes was the unpredictable solubility of both **RuN2** and **RuNPh** in acetonitrile, where, depending on the sample history, some batches become less soluble in acetonitrile than the others. This may be explained by the possibility of forming π-π stacked dimer and/or oligomers due to the extended conjugated system involving the end nitro- group. Alternatively, interlocked structures may be formed with the help of acetonitrile solvent molecule. Interactions between the pendant aryl ring with the terpyridine ring in **RuPh2**·4MeCN crystal structure was earlier reported[9]. The extra nitro- substitution facilitated such interactions and brought in additional complication in the solubility. It has been found, however, both compounds dissolve well in acetonitrile with 10% ethanol.

3.3.2.2. RuNPh: Purity of the initial sample.

It is needed to point out that although HPLC is known to be the golden standard to establish purity of a sample, it is not the routine method for synthetic chemists. Instead, clean NMR and matched elemental analysis results are commonly relied upon as sufficient proof of purity. This routine method, however, turned out to be deceiving in this specific system: As the most probable impurities are the two relevant homoleptic

Table 3-2 ^1H NMR data for the Ru complexes in CD_3CN

	Phtpy								NO_2Phtpy						
	3	4	5	6	3′	o	m	p	3	4	5	6	3	O	m
RuPh2	8.68	7.99	7.22	7.47	9.05	8.24	7.82	7.73							
	4H	4H	4H	4H	4H	4H	4H	2H							
	d	dd	dd	d	s	d	t	t							
RuNPh	8.68	7.99	7.22	7.46	9.06	8.25	7.82	7.73	8.70	8.01	7.24	7.48	9.09	8.63	8.44
	2H	2H	2H	2H	2H	2H	2H	2H	2H	2H	2H	2H	2H	2H	2H
	d	dd	dd	d	s	s	t	t	d	dd	dd	d	s	d	t
RuN2									8.69	8.01	7.24	7.47	9.09	8.64	8.44
									4H	4H	4H	4H	4H	4H	4H
									d	dd	dd	d	s	d	t

complexes, an equal-molar mixture of which shall give exactly the same elemental composition as the desired pure complex. Considering the separations methods as well as its innate complication described above, it is very conceivable that equal amount of two homoleptic impurities are present at the same time. Similarly, the ^{1}H NMR spectrum of **RuNPh** can be expected to be almost the exact overlay of those from the two homoleptic complexes (Table 3-2), thus unable to differentiate between pure **RuNPh** versus **RuNPh** with equal amounts of **RuN2** and **RuPh2**. Therefore, even an exact match of peak positions as well as the integrations to the predicted values, may still not be taken as the definitive proof of the purity of the sample. It turned out that electrospray mass spectrometry was an effective definitive method to evaluate the purity of the sample in this situation.

Electrospray mass spectrometry (ESI-MS) is a very mild experimental technique, the molecular ions are not expected to fragment during the process. Therefore, provided that the ionizability of the heteroleptic complex and the two homoleptic complexes are very close to each other, the intensity of the detected molecular ion peaks shall track the concentration of that molecule within the sample. A typical ESI-MS spectrum is presented in Figure 3-11 (a). Contrary to my intuition, however, an equal-molar mixture of **RuPh2** and **RuN2** samples yielded two peaks with intensity ratios of 5:1, suggesting that the ionizability of these complexes are vastly different from each other and, as a result, simple evaluations of the concentrations based on the peak intensities will be misleading. In order to account for such differences, a reasonable assumption was

made that the heteroleptic complex has an ionizability of approximately the average of **RuPh2** and **RuN2**. Therefore, a sample with equal amount of the three complexes will yield molecular ion peaks in a pattern of 5 (**RuPh2**) : 3 (**RuNPh**) :1 (**RuN2**). The actual concentrations could then be obtained by normalizing peak intensities observed to these values. These evaluations of the purities of pre-HPLC **RuNPh** samples routinely gave values between 85 - 95% pure and that on the after-HPLC samples was confirmed to be > 99%. These estimates were corroborated with HPLC analysis.

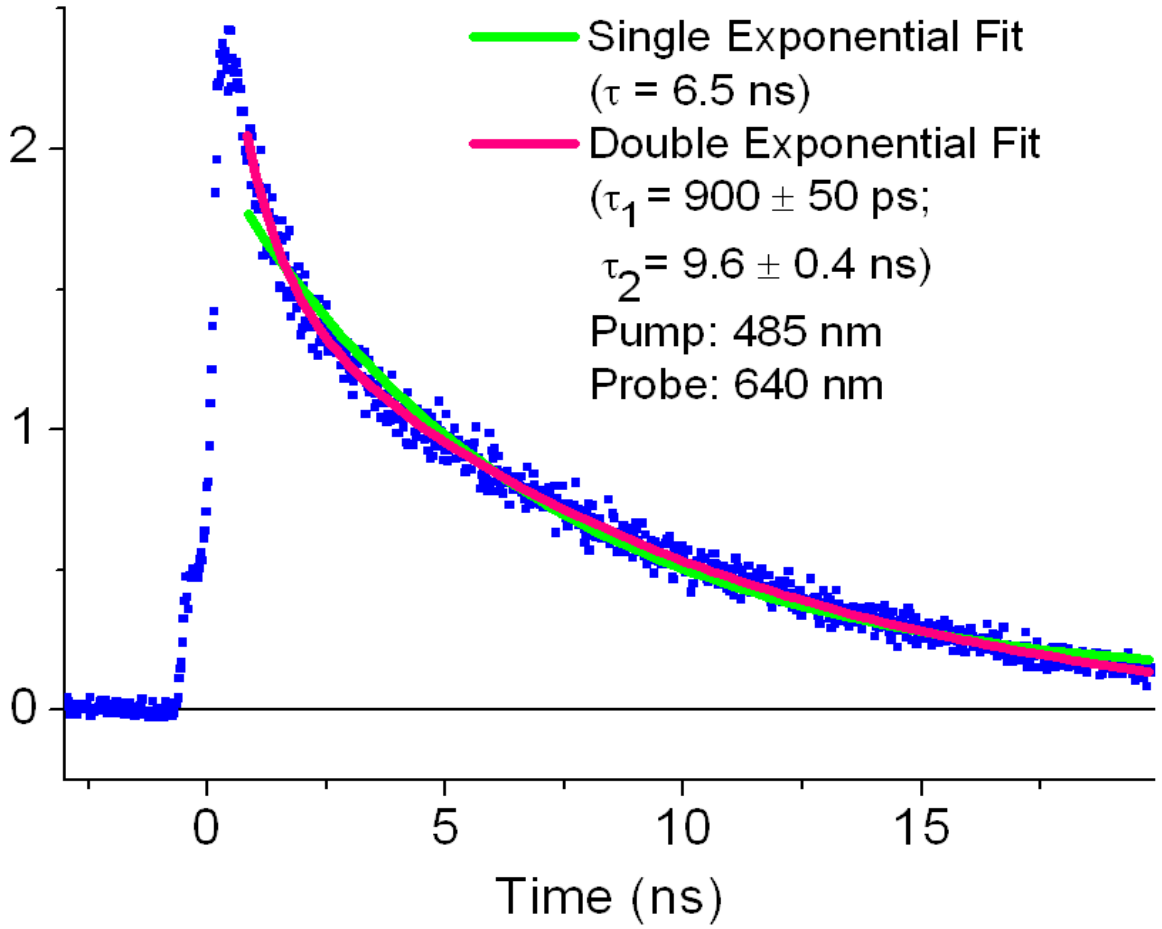

Figure 3-6 Representative TCPSC data for a **RuNPh** sample with less than ca. 10% impurities.The fit with single expoenential decay(green) shows wave-like discrepency; the fit with double exponential decay model (red) fits to a short (900 ± 50 ps) and a long (9.6 ± 0.4 ns) components.

It is worthwhile to emphasize that mass spectrometry is not generally intended to be a quantitative analysis method for purity. The method discussed above only applies when the identities of all impurities are known and can be tested accurately; and that the ionizability of the target molecule can be reasonably approximated from that of the impurities. These criteria are not always met for other classes of molecules, although it works nicely for the heteroleptic Ru bisterpyridyl complexes.

3.3.2.3. RuNPh: Time-resolved Emission Spectroscopy.

Time-correlated Single Photon Counting (TCSPC) spectroscopy was used to investigate the dynamics of the excited state decay(s) within HPLC-purified **RuNPh** complex following ^{1}MLCT excitation at 485 nm (Figure 3-5). Unlike **RuPh2** and **RuN2**, a single exponential model fit to the heteroleptic complex emission decay trace shows wave-like discrepancy at different time points (Figure 3-5, green trace), suggesting that the single exponential decay model was insufficient to faithfully reproduce the data being studied. This occurs at different pump/probe wavelength combinations, suggesting it being intrinsic to this system being interrogated. A double exponential model was therefore adopted to fit all the traces, according to the following formalism:

$$y=y_0+A_1e^{-x/\tau_1}+A_2e^{-x/\tau_2}$$

This model yielded two time components with lifetimes of 900 ps ± 50 ps and 9.6 ns ± 0.4 ns at room temperature respectively. These two lifetime constants are identical, within experimental error, to that of the two reference complexes (**RuPh2** and **RuN2**) resembling the two halves of the molecule respectively. Therefore, these two emission

components could be due to the decay of the two co-present ^{3}MLCT states localized on the two different ligands. This also means the ILET process in this complex is on a time scale comparable to the luminescence process of the higher ^{3}MLCT state based on 4'-phenyl-2,2':6':2”-terpyridyl (Phtpy) ligand. Considering the meridinal binding motif of this molecule, it can be argued that the orbitals on the two different ligands are orthogonal to each other as a consequence of molecular topology. Therefore, the interligand electronic communication will be hampered, ultimately leading to the presence of dual long-lived excited states, which, when emissive, present themselves as dual luminescence.

Despite of the reasonableness of this explanation from chemical intuition, dual luminescence is still a potentially dangerous model to present, due to luminescence being intrinsically very sensitive to small amount of impurities. Indeed, many previously reported[10] dual emission cases were refuted based on the purity criterion. Furthermore, it is crucial to note that, this result does not tell where these two emitting states are located. While it is possible that both states are present within one molecule, as suggested by the dual luminescence model; alternatively, they could also be from two homoleptic photoproducts produced exclusively during the laser interrogation, even though the initial purity of the sample was established from HPLC separation. This complication needs to be addressed before any conclusions being made.

3.3.2.4. RuNPh: Temperature-dependant TCSPC spectroscopy.

As explained earlier, the major deactivation pathway for the emissive ^{3}MLCT state is via thermally populating the higher-lying metal-centered state (MC). In other words, this is an activated decay processes with the MC state serving as the energy barrier. By doing variable temperature TCSPC measurements, the energy barriers associated with these processes can be determined from the slope of the Arrhenius plot (Figure 3-7). If the two emitting states are truly localized on the two halves of the same complex, the same lowest MC state shall serve as the common energy barrier for both long and short components. Although the energy for the MC state is hard to predict, the difference between these two energy gaps should be close to the energy separation between these two ^{3}MLCT states, which can be estimated from emission maxima of the two homoleptic complexes. Therefore, the match of energy barrier difference between the two deactivating process estimated from Arrhenius plot to that calculated from luminescence maxima energy will be a good support for the dual luminescence model.

To test this hypothesis, variable temperature TCSPC measurements were performed on a HPLC-purified **RuNPh** sample within the range of temperature between -4.4℃ and 45℃. All decay traces obtained required double exponential fits. The resulting time constants along with the pre-exponential factor ratios between the two time components are tabulated in Table 3-3. Representative decay traces are seen in Figure 3-7. It needs to be pointed out that due to instrumental resolution limitation, the absolute values of the pre-exponential terms are not accurate. Such a complication is especially clear for the

610 nm-probe data, where the early time spectra are dominated by peaks from instrumental artifacts (Figure 3-7). This point is especially important when comparing data at different probe wavelengths, where the contributions from the instrumental response functions varies significantly. Therefore, it is the trend of these ratios with the changing temperature that is meaningful: *i.e.*, at both 640 nm and 685 nm probe wavelengths, the contribution from the shorter component always grows with the growing temperature.

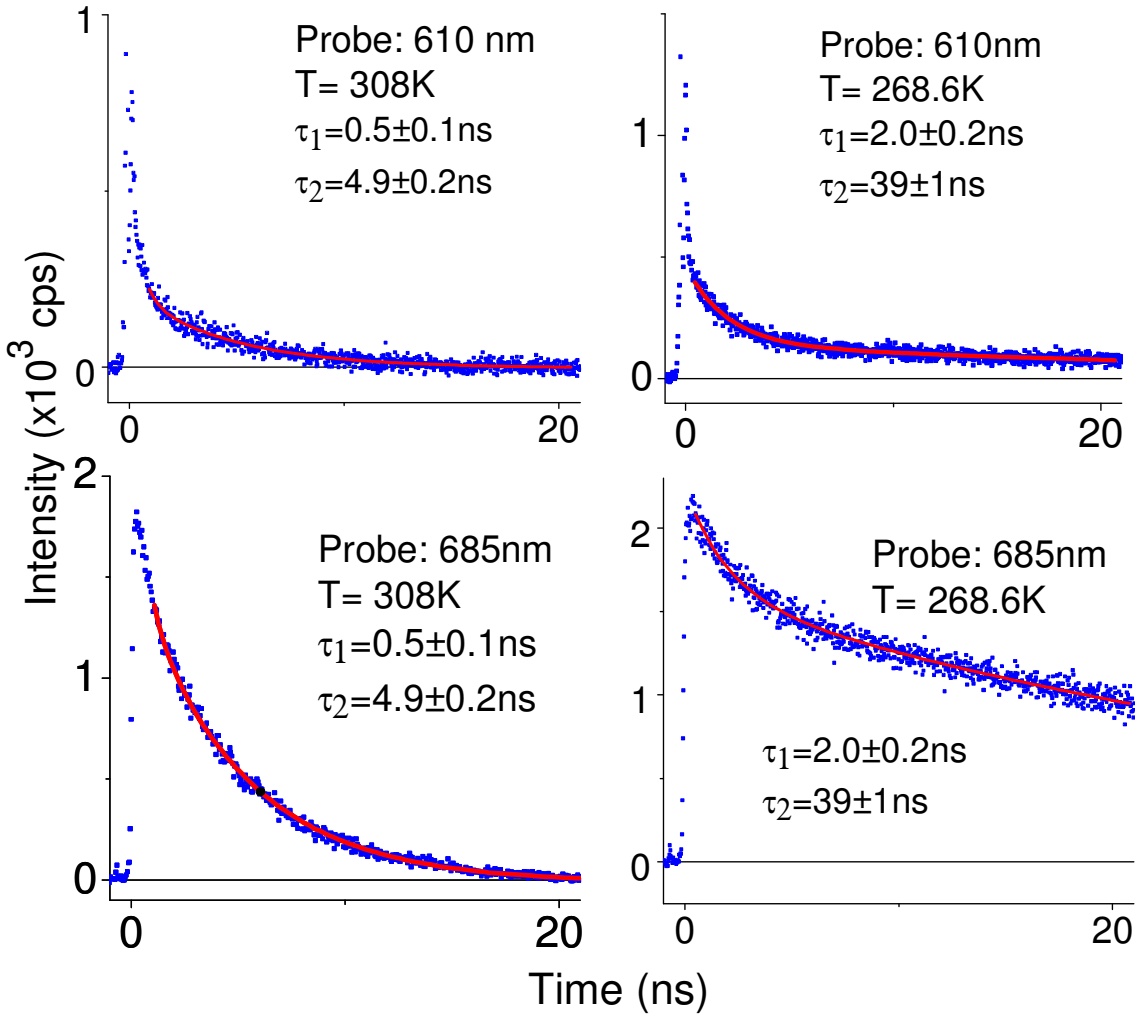

Figure 3-7 Representative dynamic traces of variable temperature time-resolved luminescence measurements.The red curve represents a fit with double exponential decay model.

While this change with temperature is consistent with the dual luminescence model discussed here, in that the higher temperature leads to a more populated higher-^{3}MLCT state, producing more signal manifested as the short component, the magnitude of such changes observed for a temperature increase of 50℃ (~ 2 fold change) is too big to be correct. In fact, based on the Boltzmann thermal distribution, such a contribution change should be on the order of 1%. This discrepancy therefore suggests that some other factor is leading to the change observed. In other words, dual luminescence may not be the correct model to explain the observations.

Table 3-3 Variable Temperature Time-Resolved Luminescence Data

Temperature (℃)	Lifetimes (ns) and Relative Amplitudes		
	610nm	640nm	685nm
-4.4	39.1:2.0 (0.41:1)	39.1:2.0 (2.4:1)	39.1:2.0 (2.7:1)
0.4	27.8:1.8 (0.56:1)	27.8:1.8 (2.0:1)	27.8:1.8 (2.0:1)
6.8	20.8:1.3 (0.59:1)	20.8:1.3 (0.9:1)	20.8:1.3 (2.3:1)
7.8	18.5:1.3 (0.59:1)	18.5:1.3 (1.3:1)	18.5:1.3 (2.2:1)
15.9	13.4:1.0 (0.62:1)	13.4:1.0 (1.1:1)	13.4:1.0 (1.9:1)
25.1	7.3:0.74 (0.71:1)	7.3:0.74 (0.9:1)	7.3:0.74 (1.6:1)
35.0	4.9:0.53 (0.76:1)	4.9:0.53 (0.9:1)	4.9:0.53 (1.3:1)
45.0		3.0:0.39	

Arrhenius plots for the variable temperature TCSPC measurements are shown in Figure 3-8. Two energy barriers were extracted out to be 0.25 eV for the short component and 0.38 eV for the longer component respectively. The magnitudes of both energy gaps are larger than that of $[Ru(H\text{-}tpy)]^{2+}$ complex (0.19 eV)[6], consistent with the delocalization effects discussed above. However, the difference between these two numbers is 0.13 eV, much larger than that estimated value from emission maxima (~0.04 eV). Therefore, the transition states for these two activated processes are *not* the same. Since the lowest MC state in the heteroleptic complex should be the most efficient deactivating pathway for both moieties, this is another evidence that more than one species exist in this system. Considering the initial purity of the sample, photodecomposition becomes the most reasonable explanation.

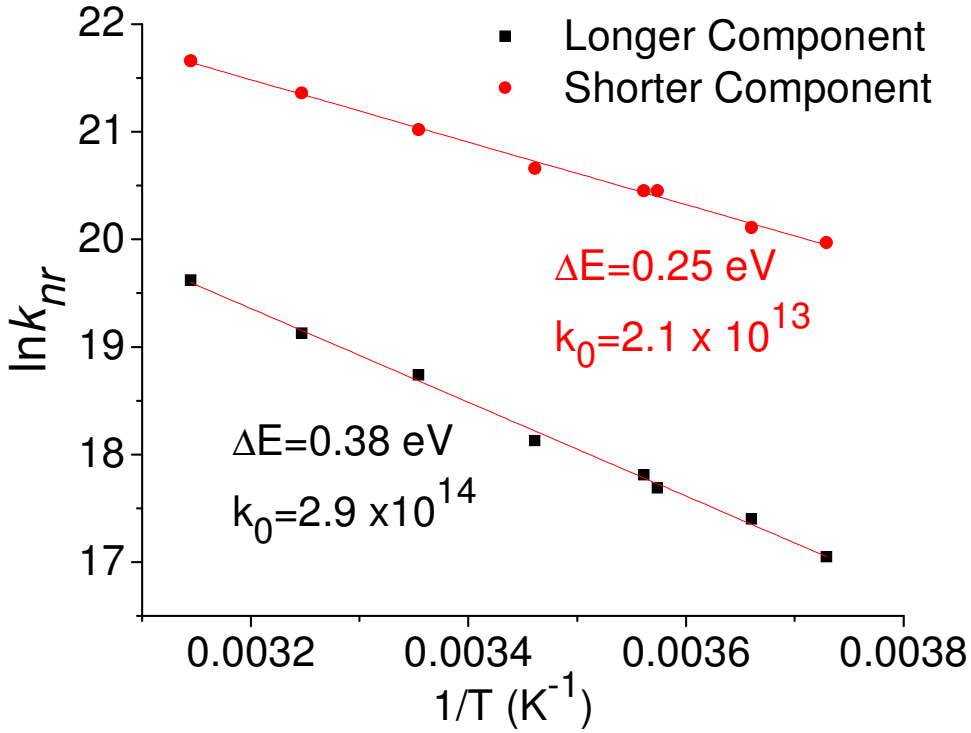

Figure 3-8 Arrhenius plot of temperature-dependent TCSPC measurements.

3.3.2.5. Femtosecond transient absorption:

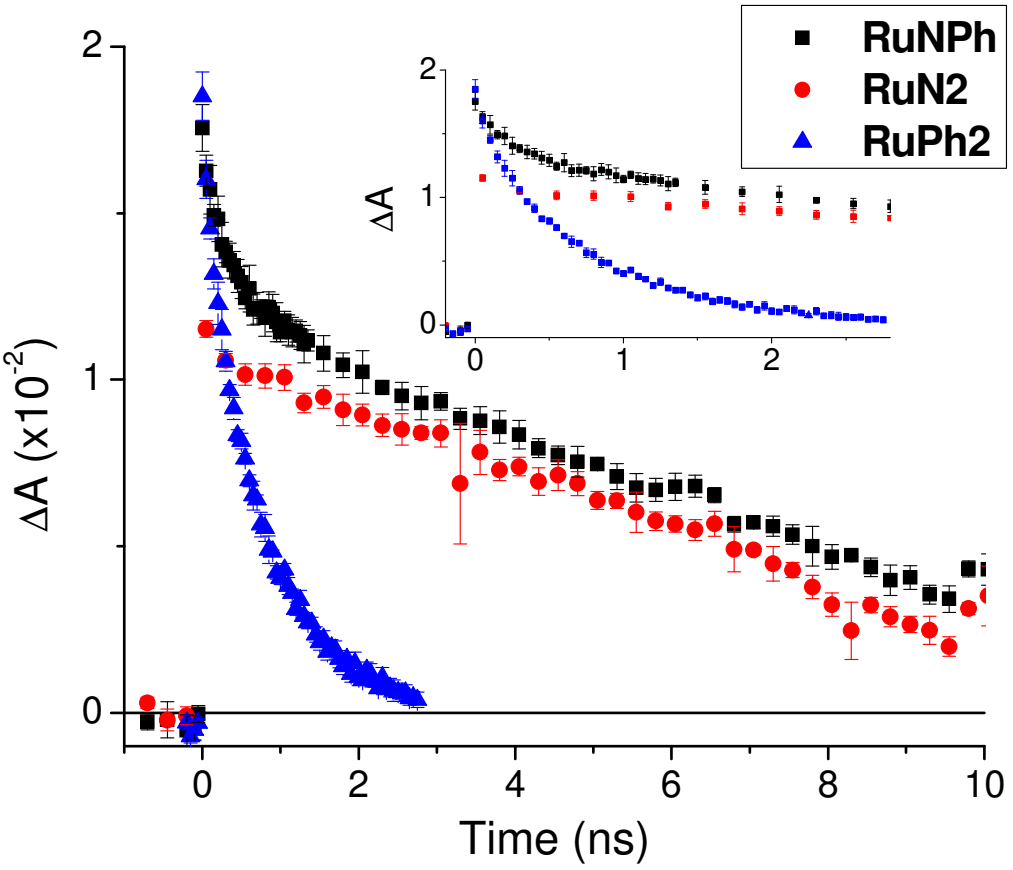

*Figure 3-9 Femtosecond TA single wavelength data of **RuNPh** (exposed to laser light for 4 hrs) observed at 570 nm following 485 nm excitation, overlaid on top of the two homoleptic **RuPh2** and **RuN2**.*

From a technical point of view, luminescence spectroscopy is the most straightforward way to disclose the number of long-lived excited states involved in the complex under investigation. But it is just one of the ways and has its intrinsic limitations: a lack of dual emission may be due to: 1) only one long-lived state being present, 2)

only one long-lived state being emissive or 3) indistinguishable emission signals out of the two long-lived states. On the other hand, the observation of dual emission may also be due to 1) emissive impurities, 2) photo-dissociated products[2], or 3) isomerization[3]. This highlights the necessity of another characterization method in addition to luminescence spectroscopy to fully understand these excited states. Transient absorption measurements were thus applied to further investigate the authenticity of such dual luminescence from photodecomposition explanation.

Evidences for the presence of dual long-lived states were again obtained repetitively with TA measurements (Figure 3-9) on different batches of samples, consistent with the TCSPC results. The lifetimes of these two components are also consistent with that observed for the two homoleptic complexes. Yet what is interesting is that the spectra of the same sample change over the course of TA measurements. In the very first data scan with femtosecond laser beam on a freshly prepared pure sample, where the illumination time was restricted to less than five minutes, a decay trace at 570 nm (Figure 3-10, black) was obtained. No short component was observed. Yet lengthening the time used for data collection hence the laser illumination time resulted in a gradual grow-in of the short component (Figure 3-10, blue). While the magnitude of amplitude change in this blue decay trace was not sufficient to give a clear time constant for this short component, subsequent decay traces obtained after longer laser-exposures (see, for example, Figure 3-9) all led to a time constant close to that of the $[Ru(Phtpy)_2]^{2+}$. This observation could only be explained by the *photodecomposition* which occurred

during the process of the laser spectroscopic measurements, which created *in situ* the two homoleptic complexes.

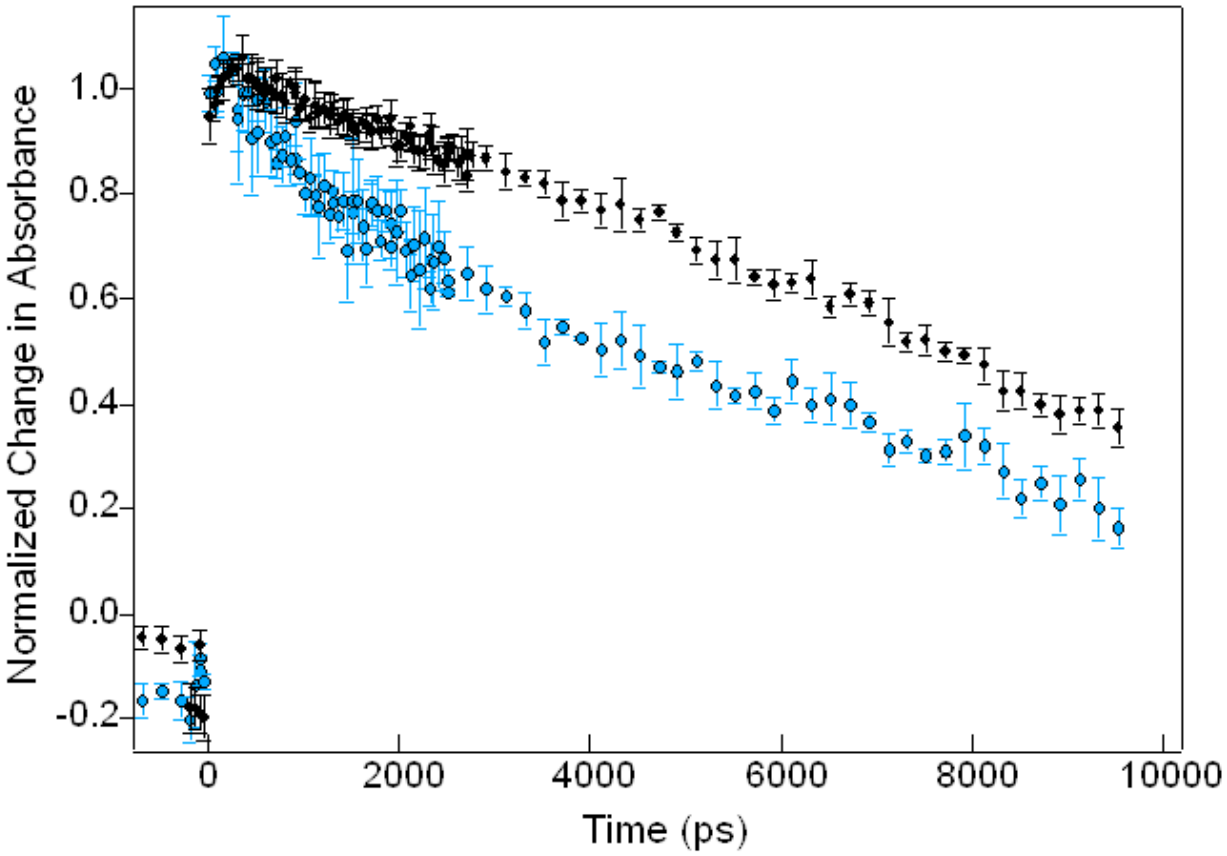

*Figure 3-10 Femtosecond TA measurements on the same **RuNPh** sample at early (black) and late (blue) times at 570 nm following 485 nm excitation.*

3.3.2.6. Mass Spectra

To further verify the photodecomposition explanation, ESI-MS was performed on exactly the same sample before and after femtosecond TA experiment. While the initial sample contains less than 5% impurities, with the ionization differences taken into

consideration (Figure 3-11 (a)), the concentration of both **RuPh2** and **RuN2** increased to approximately 20% each in the after-laser sample (Figure 3-11 (b)). Since the lowest ^{3}MLCT state in **RuNPh** should have properties very close to that in **RuN2**, only two components will be detected in laser spectroscopy. This model explains all the data observed so far.

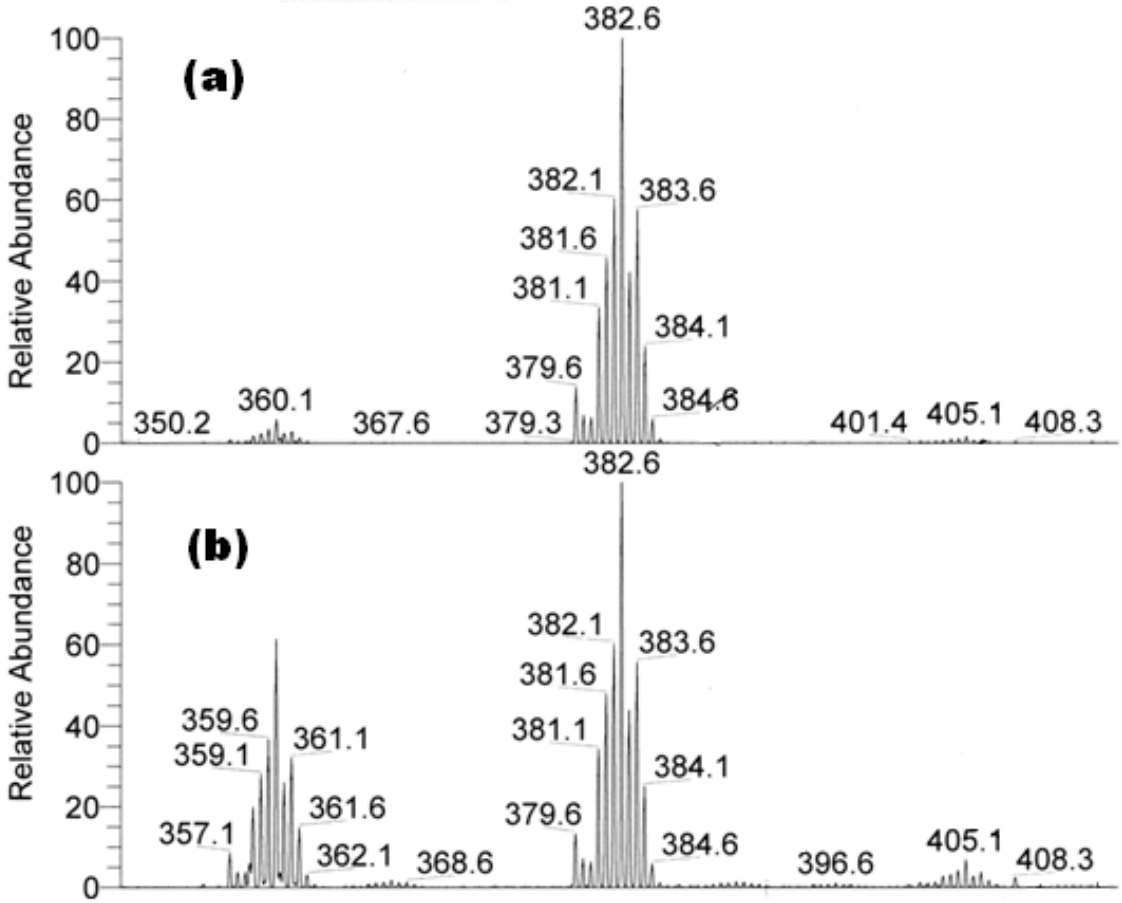

*Figure 3-11 Representative MS spectra of **RuNPh** before (a, top) and after (b, bottom) femtosecond TA experiments.*

3.3.2.7. Photostability

Like $[Ru(bpy)_3]^{2+}$-type complexes, $[Ru(tpy)_2]^{2+}$ is known to undergo scrambling at elevated temperatures. This appears to be a competition between the increased chelating binding strength of the tridentate ligand and the weaker ligand field strength due to the highly-strained pseudo-octahedral symmetry around the metal center. Isomerization were also reported to occur forming η^2-binding motif.[11] However, such scrambling effect was more considered as a precaution in the synthesis than any definitive spectroscopic proof in the literature. Explicit experimental observations of laser-induced photoscrambling of this magnitude has not been reported. This is not surprising, however, considering the high peak power of the femtosecond laser pulse and the high concentration of the sample (~0.15 mM) used in my TA measurements; as well as the prolonged time period the sample was exposed to nanosecond laser light in the variable-temperature TCSPC measurements, which amounted to over 100 hrs for the full length of experiment. In fact, going back to the variable temperature TCSPC results, the smaller contributions from the short component at lower temperatures are consistent with it being measured at earlier times, when less photodecomposition had happened. The growth of this contribution with temperature is in fact the indication of increasing amount of decomposition as the result of laser exposure.

3.3.2.8. Flow setup.

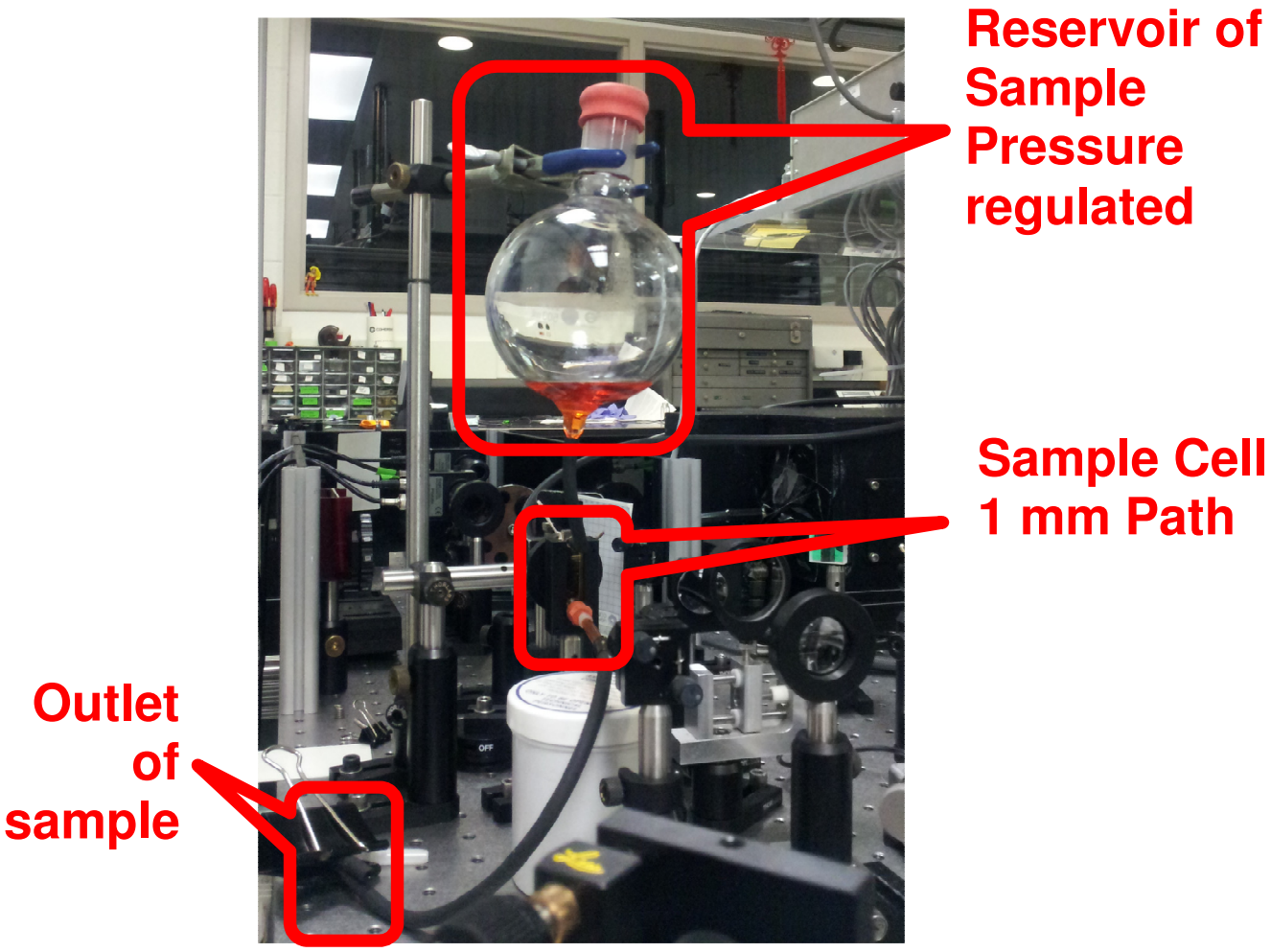

Figure 3-22 Flow setup for femtosecond TA measurements.

Clearly, to obtain faithful data to understand the behavior of these heteroleptic $[Ru(tpy)_2]^{2+}$ -based components, such photodecomposition problem has to be resolved, especially because photophysical measurements are the major characterization methods in this study. A one-pass flow cell setup was therefore custom-made, where

the sample flows through the laser spot and exits the system continuously. A graphic demonstration is shown in Figure 3-12, while the details were specified in the experimental section. In this setup, any potentially decomposed products exit the system and do not recirculate to give unwanted signals. The integrity of the sample can be closely monitored by comparing, before and after each laser spectroscopy measurement, the compositions via ESI-MS to confirm no decomposition.

3.3.3. Concluding Comments

The study presented in this chapter demonstrated a couple important issues involved in heteroleptic Ru complex studies. The first is methodological. Clear and definitive evidence for photodecomposition was observed only from ESI-MS measurements. Such decompositions lead to phenomena indistinguishable from a genuine dual luminescence photophysical behavior, at least for a pair of casual eyes. Similar processes may have been occurring in other heteroleptic complexes as well and the lack of careful sample-integrity check may have led to incorrect assignments. Therefore, a detailed evaluation of the photolability of this type of molecule will be crucial. A series of Ru heteroleptic bisterpyridyl complexes will be studied with ESI-MS methods to address this particular issue.

The second important observation from this study is the confirmation of non-existing dual emitting state in **RuNPh** as well as the presence of a slow ILET process. Unlike $[Ru(bpy)_2(L)]^{2+}$ systems[12, 13] (bpy is 2,2'-bipyridyl and L is another appropriately

selected bidentate polypyridyl ligand) where dual luminescence native to the same MLCT excited state nature were reported and mechanistically studied[12, 13], there have not been any reports on similar dual MLCT luminescent $[Ru(tpy)_2]^{2+}$-based complexes. This is somewhat counter-intuitive because, at least from the considerations of molecular topology, $[Ru(tpy)_2]^{2+}$-type complexes seem to possess very small inter-ligand interactions as a result of their orthogonal ligand alignment, and are expected to be more likely to dual luminescent. The explanation may simply be due to the difficulty associated with detecting and analyzing the intrinsically very weak luminescence signals from the $[Ru(tpy)_2]^{2+}$ molecules; or it could be due to a very fast interligand electron transfer process. Only if the ILET process is slowed down to a time scale close to that of the intrinsic decay of that state, dual luminescence could be detected. This is consistent with the magnitude difference between ILET (<100 ps) and the intrinsic decay rate of the higher-lying ^{3}MLCT state (700 ps) in this current system. The fact that this ILET rate is very close to that observed in $[Ru(bpy)_3]^{2+}$ (<50 ps) suggests the major interligand electronic communication is not via direct ligand-to-ligand interaction. A more possible pathway is via the scrambling of the hole created on the metal center upon photo excitation.

The biggest significance of this result, however, is not in the identification of such a time constant by itself, but rather it suggests a very limited electronic communication between the two states. These two states, due to their different redox chemistry, intrinsic lifetime as well as localization, could possess drastically different reactivities. The

traditional view on this problem is that, like $[Ru(bpy)_3]^{2+}$, only the lowest ^{3}MLCT state could be involved in intercomponent processes due to the fast relaxation of higher states. This may not be always correct in the light of discussed observations. In fact, the presence of the interligand electron transfer process, in itself, is a good indication that the two ^{3}MLCT states need to be addressed separately. The importance of such a concept will become much more evident when a dyad molecule containing this component is discussed in Chapter 4. This type of $[Ru(tpy)_2]^{2+}$ components have been commonly utilized in artificial photosynthesis and molecular electronic studies, due to its innate linear topology facilitating easier design and control of electron/energy flux. Therefore, such a clarification is expected to show profound impact on the further development of this field.

REFERENCES

REFERENCES

[1] Maestri, M.; Armaroli, N.; Balzani, V.; Constable, E. C.; Thompson, A. M. W. C., *Inorganic Chemistry*, (1995) **34**, 2759.

[2] Damrauer, N. H.; Boussie, T. R.; Devenney, M.; McCusker, J. K., *Journal of the American Chemical Society*, (1997) **119**, 8253.

[3] Malone, R. A.; Kelley, D. F., *The Journal of Chemical Physics*, (1991) **95**, 8970.

[4] Constable, E. C.; Lewis, J.; Liptrot, M. C.; Raithby, P. R., *Inorganica Chimica Acta*, (1990) **178**, 47.

[5] Das, S.; Incarvito, C. D.; Crabtree, R. H.; Brudvig, G. W., *Science*, (2006) **312**, 1941.

[6] Sauvage, J. P.; Collin, J. P.; Chambron, J. C.; Guillerez, S.; Coudret, C.; Balzani, V.; Barigelletti, F.; De Cola, L.; Flamigni, L., *Chem Rev*, (1994) **94**, 993.

[7] Thummel, R. P.; Hegde, V.; Jahng, Y., *Inorg Chem*, (1989) **28**, 3264.

[8] Presselt, M.; Dietzek, B.; Schmitt, M.; Rau, S.; Winter, A.; Jäger, M.; Schubert, U. S.; Popp, J. r., *The Journal of Physical Chemistry A*, (2010) **114**, 13163.

[9] Constable, E. C.; Housecroft, C. E.; Medlycott, E. A.; Neuburger, M.; Reinders, F.; Reymann, S.; Schaffner, S., *Inorg Chem Commun*, (2008) **11**, 805.

[10] Belser, P.; Von Zelewsky, A.; Juris, A.; Barigelletti, F.; Balzani, V., *Chem Phys Lett*, (1984) **104**, 100.

[11] Kirchhoff, J. R.; McMillin, D. R.; Marnot, P. A.; Sauvage, J. P., *Journal of the American Chemical Society*, (1985) **107**, 1138.

[12] Keyes, T. E.; O'Connor, C. M.; O'Dwyer, U.; Coates, C. G.; Callaghan, P.; McGarvey, J. J.; Vos, J. G., *The Journal of Physical Chemistry A*, (1999) **103**, 8915.

[13] Glazer, E. C.; Magde, D.; Tor, Y., *J Am Chem Soc*, (2007) **129**, 8544.

Chapter 4. Photoinduced Processes in Porphyrin – Ru Bisterpyridyl Donor-Acceptor Systems.

4.1. Introduction

As discussed in previous chapters, in an attempt to characterize biologically important electron transfer processes, the stepwise research protocol adopted here requires a detailed understanding of each component as well as their intercomponent interactions. A detailed study on the Ru bisterpyridyl moiety was presented in the previous chapter. In this chapter, interactions between porphyrin and Ru bisterpyridyl moieties will be investigated in the context of dyads. This allows a comprehensive understanding of this two-component system, laying the foundation for probing more complicated systems involving additional components. Especially important is the effect of remote substitution on these interactions, as such modification is required to include additional components, like iron-sulfur cluster or pyridinium moieties. This effect will be carefully analyzed during the discussions to follow.

The platform molecules for this study are seen in Figure 4-1, where substitution on the remote terpyridine alters the availability and energy of the charge-separated state, resulting in drastically different reactivities for compounds **1** versus **2**. In characterizing these dyads, the same model-to-assembly research protocol was used and a series of control molecules resembling the different components were synthesized and fully characterized. Steady-state and time-resolved spectroscopic measurements will be

applied as the major ways of characterizations. The novel feature observed in Chapter 3 will be seen as an important component to fully understand the current system.

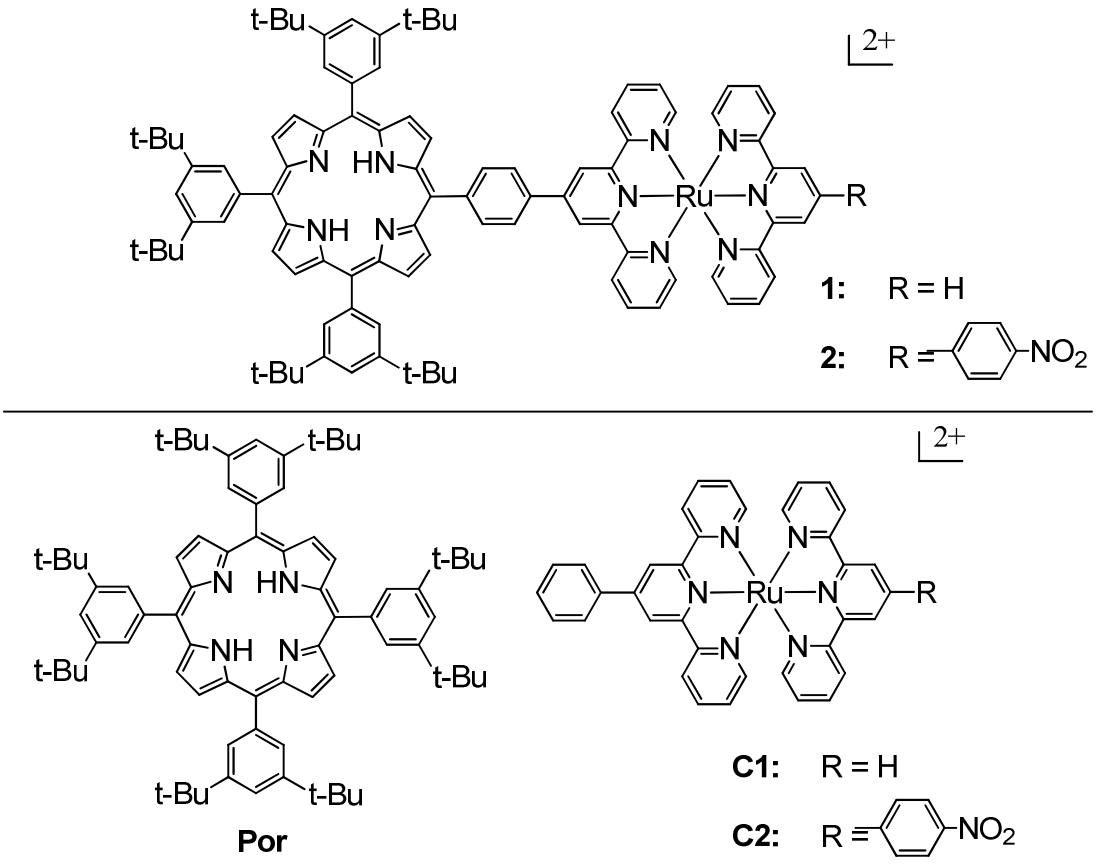

Figure 4-1. Illustration of the complexes investigated in this chapter.

4.2. Experimental Section

General. All reagents were obtained from commercial sources and used without further purification unless otherwise specified below. Solvents were purchased from

either Aldrich Chemical Company or Fisher Scientific and used as is for synthetic work. For all photophysical measurements, solvents were distilled and degassed via standard freeze-pump-thaw method. The ligands 4'-phenyl-2,2':6':2"-terpyridine[1] and 4'-nitrophenyl-2,2':6':2"-terpyridine[2], and the complexes $Ru(tpy)Cl_3$, $Ru(NO_2Phtpy)Cl_3$, and $Ru(tpy)(Phtpy)(PF_6)_2$ were prepared by reported literature methods[3]. $Ru(NO_2Phtpy)(Phtpy)(PF_6)_2$ was synthesized and purified as discussed in Chapter 2. The electrospray mass spectrometry (ESI-MS) data were acquired on a MS instrument from the Mass Spectrometry Facility at Michigan State University. ^1H NMR spectra were performed on either a Varian 300 MHz or 500 MHz spectrometer at the Max T. Rogers NMR Facility at Michigan State University.

3,5-di-*tert*-butylbenzaldehyde. The compound 3,5-di-*tert*-butylbenzaldehyde was prepared following a procedure modified from earlier literature[4]. 114 g of 3,5-Di-*tert*-butyltoluene (0.55 mol) along with 150 g *N*-bromosuccinimide (0.84 mol) were dissolved in 300 mL freshly distilled and thoroughly deoxygenated benzene. The solution was gently heated until all solids dissolved. 5 mL of a benzene solution containing 0.5 g of benzoyl peroxide (2 mmol) was then added via syringe. The solution was purged with five vacuum-nitrogen exchange cycles to ensure a strictly oxygen-free atmosphere. The solution was heated under reflux while rigorously stirring for another 4 hrs. The resulting mixture was opened to air and filtered over a fine frit and the filtrate was evaporated to dryness before being redissolved in a 300 mL of 1:1 ethanol-water mixture. 215 g (1.5 mol) of hexamethylenetetramine (HMTA) were added and the mixture was heated under

reflux for another 4 hrs. 100 mL of concentrated hydrochloric acid were added to the solution and the reflux continued for another 30 min. The product mixture was quenched into water at the end of the reaction and the desired product was then extracted into $CHCl_3$, washed thoroughly with distilled water, dried over anhydrous magnesium sulfate, concentrated and crystallized with petroleum ether. The yield was found to be 70%. ^{1}H NMR ($CDCl_3$): δ 10.00 (s, 1H), 7.62 (s, 3H), 1.35 (s, 18H).

4′-(4-methylphenyl)-2,2′:6′,2″-terpyridine. 2-acetylpyridine (30 mL, 0.24 mol) in 20 mL of methanol and 40 mL of 20% aqueous NaOH were simultaneously added dropwise very slowly to a stirring solution of *p*-tolualdehyde (10 mL, 0.1 mol) in 40 mL of methanol that had been cooled to -15℃ in an acetone solvent bath with dry ice. The reaction mixture was stirred for 3 hrs while the temperature was maintained between -10 ℃ and -15℃. It was then warmed to room temperature and filtered through a fine frit. The filtrate was refluxed with 40 g (0.5 mol) of ammonium acetate for 4 hrs before being filtered over a fine frit and washed with hot water and hot ethanol three times each. The crude product was recrystallized by slow evaporation in minimal amount of chloroform. The yield was 85%.

4′-(4-formylphenyl)-2,2′:6′,2″-terpyridine. The compound 4′-(4-formylphenyl)-2,2′:6′,2′′-terpyridine was synthesized from 4′-(4-methylphenyl)- 2,2′:6′,2′′-terpyridine via similar procedures as described above for 3,5-di-*tert*-butylbenzaldehyde, with modified stoichiometry as follows: 96 g (0.3 mol) 4′-(4-methylphenyl)-2,2':6',2"-terpyridine, 61 g (0.33 mol) *N*-bromosuccinimide and 2 g (8 mmol) benzoyl peroxide were dissolved in

500 mL of benzene. After refluxing for 4 hrs under oxygen-free environment, the product was evaporated to dryness and redissolved in 160 mL ethanol-water (1:1) mixture and refluxed with 114 g (0.8 mol) HMTA for 4 hrs, followed by the addition of 40 mL concentrated hydrochloric acid and further reflux for 30 min. The product mixture, after extraction into $CHCl_3$ and concentration, was passed through a short silica column and recrystallized. The product yield was found to be 60%. ^{1}H NMR ($CDCl_3$): δ 10.09 (s, 1H), 8.77 (s, 4H), 8.73 (d, 2H), 8.67 (d, 2H), 8.04 (dd, 2H), 7.88 (t, 2H), 7.37 (dd, 2H).

[5-(2,2′:6′,2′′-Terpyridine)-4′-ylphen-4-yl]-10,15,20-tris(3,5-di-*tert*-butylphenyl)porphyrin (aPor).[5] 62 g of 3,5-di(*tert*-butyl)phenyl aldehyde (0.28 mol) and 5.3 g of 4′-(4-formylphenyl)-2,2':6',2"-terpyridine (16 mmol) were dissolved in 2 L of neat propionic acid and heated to near boiling. 21 mL of freshly distilled pyrrole (0.30 mmol) was added quickly to the solution and refluxed for 30 min. The resulting solution was concentrated via vacuum distillation to approximately 1/3 of its original volume and was left undisturbed for two days for the porphyrin products to crystallize. The purple crystals were collected and redissolved in minimal amount of hexanes and loaded onto a short neutral alumina column. Using hexanes as the eluent the majority of the symmetric porphyrin (**sPor**) was brought out. Using hexanes saturated with dimethylformaldehyde, a mixture of **sPor**, **aPor** and polypyrrole was separated out. This mixture was evaporated, redissolved in hexanes and loaded onto a second neutral alumina column. A mixture of hexanes/ethyl acetate with a volumetric ratio between 99.9:0.1 and 99:1 was used to elute the product. The second purple band on the column

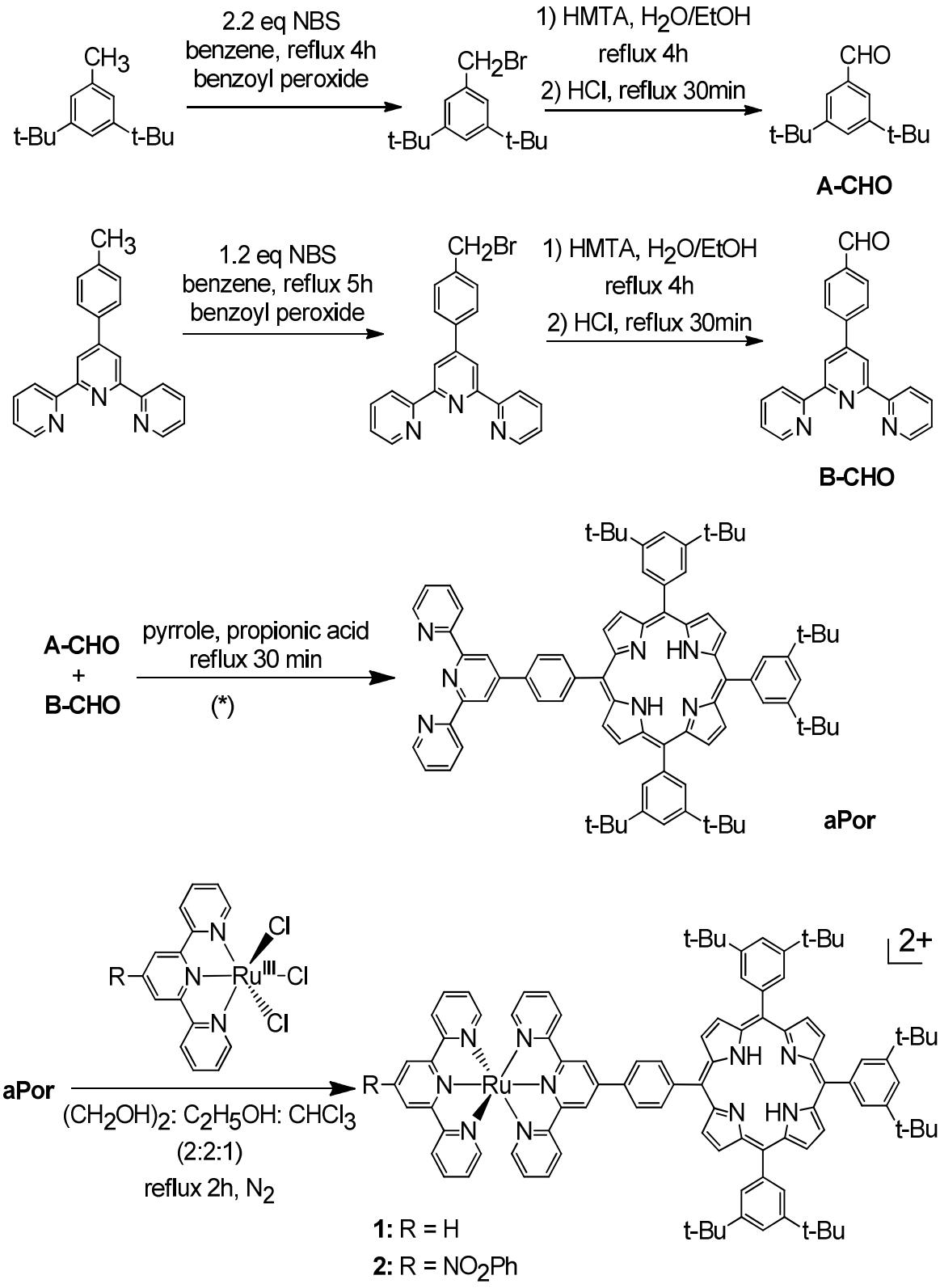

*Figure 4-2. Strategies to assemble dyads **1** and **2**. Stoichiometry used for the (*) step was A-CHO : B-CHO : pyrrole = 18 : 1 : 19.*

was collected and recrystallized in propionic acid before any further reactions. Yield: 5%. ^{1}H NMR (CD_2Cl_2): δ 9.10 (s, 2H), 8.95 (d, 2H), 8.94 (d, 2H), 8.91 (s, 4H); 8.80 (m, 2H); 8.78 (m, 2H); 8.42 (d, 2H), 8.24(d,2H), 8.12(d,4H), 8.10 (d, 2H), 7.96 (ddd, 2H), 7.86 (t, 3H), 7.43 (m, 2H), 1.54 (s, 54H), -2.71 (s, 2H). ES-MS ($CHCl_3$) m/z 1183.67 [**aPor** + H^+].

[5-(2,2′:6′,2′′-Terpyridine)-4′-ylphen-4-yl]-10,15,20-tris(3,5-di-*tert*-butylphenyl) porphyrinato 2,2′:6′,2′′-terpyridyl ruthenium (II) hexaflurophosphorate (1). $Ru(tpy)Cl_3$ (220 mg, 0.5 mmol), and **aPor** (590 mg, 0.5 mmol) were heated to reflux in 30 mL of a 2:2:1 solvent mixture of freshly distilled ethylene glycol, absolute ethanol and chloroform for 2 hours while stirring. The solution was cooled to room temperature and diluted with 30 mL of water and filtered over a fine frit to remove a fine black precipitate. The solution was concentrated to about half of its original volume via rotary evaporation and added dropwise to an aqueous solution of $NaPF_6$ (10 eq.), which resulted in the precipitation of a red-brown solid. The solid was collected on a fine frit, washed with three times with 20 mL aliquots of water and three times with 20 mL aliquots of diethyl ether. The crude product was dissolved in acetonitrile (2 mL) and chromatographed on silica gel stationary phase using acetonitrile with 0-10% saturated KNO_3 aqueous solution as the eluent. The main red-brown band containing the product was reduced in volume to 5 mL and treated with $NaPF_6$ to precipitate the product. The precipitate was filtered, washed with water and diethyl ether, three times with 20 mL aliquots each, and dried *in vacuo*. The yield was 50%. ^{1}H NMR (CD_3CN): δ 9.16 (s, 2H), 9.01 (4H, d), 8.93

(s, 4H), 8.64 (m, 4H), 8.53 (d, 2H); 8.42 (d, 4H), 8.12 (m, 6H), 7.98 (t, 2H), 7.93 (t, 2H), 7.86 (t, 4H), 7.51 (d, 4H), 7.35 (d, 2H), 7.27 (m, 4H), 1.54 (s, 54H), -2.69 (s, 2H). ESI-MS: m/z = 758.35 ([**1**-2PF_6]$^{2+}$). See Appendices B and C for spectra.

[5-(2,2′:6′,2′′-Terpyridine)-4′-ylphen-4-yl]-10,15,20-tris(3,5-di-*tert*-butylphenyl) porphyrinato 4′-(4-nitrophenyl)-2,2′:6′,2′′-terpyridyl ruthenium (II) hexafluro-phosphorate (2). Ru(NO_2Phtpy)Cl_3 (280 mg, 0.5 mmol), and **aPor** (590 mg, 0.5 mmol) were heated to reflux in 30 mL of a 2:2:1 solvent mixture of freshly distilled ethylene glycol, absolute ethanol and chloroform for 2 hrs while stirring. The solution was cooled to room temperature and diluted with 30 mL of water and filtered over a fine frit to remove a fine black precipitate. The solution was concentrated to about half of its original volume via rotary evaporation and added dropwise to an aqueous solution $NaPF_6$ (10 eq.), which resulted in the precipitation of a red-brown solid. The solid was collected on a fine frit, washed with three 20 mL aliquots of water and three 20 mL aliquots of diethyl ether. The crude product was dissolved in a minimal amount of CH_2Cl_2 and loaded onto a neutral alumina column. The dark red-brown band left at the top of the column was washed out with acetonitrile, concentrated to about 3 mL and re-chromatographed on silica gel stationary phase using acetonitrile with 0-10% saturated KNO_3 aqueous solution as the mobile phase. The main red-brown band containing the product was reduced in volume to 5 mL, and treated with $NaPF_6$ to precipitate the product. The precipitate was filtered, washed with water and diethyl ether, three 20 mL portions each, and dried *in vacuo*. The yield was 15%. ^{1}H NMR (CD_3CN): δ 9.43 (s,

2H), 9.17 (s, 2H), 9.01 (4H, d), 8.94 (s, 4H), 8.86 (d, 2H), 8.78 (d, 2H), 8.73 (d, 2H), 8.68 (d, 2H), 8.65 (d, 2H), 8.49 (d, 2H), 8.18 (m, 6H), 8.05 (t, 4H), 7.99 (s, 2H), 7.62 (d, 2H), 7.52 (d, 2H), 7.32 (t, 2H), 7.27 (t, 2H), 1.54 (s, 54H), -2.69 (s, 2H). ESI-MS: m/z = 819.0 ([**2**-2PF_6]$^{2+}$). See Appendices D and E for spectra.

Physical Measurements: Electrochemistry. Electrochemical measurements were performed with a CHI 630B electrochemical analyzer under Ar atmosphere in a glove box. A standard three-electrode electrochemical setup, consisting of a Pt working electrode, a graphite counter electrode and a Ag/AgCl reference electrode (from Cypress Systems) was used. Solutions of the compounds were dissolved in distilled spectrometric grade acetonitrile, which was degassed by freeze-pump-thaw method prior to the experiment. Tetrabutylammonium hexafluorophosphate ($TBAPF_6$, ca. 0.1 M) was used as supporting electrolyte.

Steady State Electronic Absorption and Emission Spectroscopy. Steady state electronic absorption and extinction coefficient measurements were done with a Cary 50 UV-visible spectrometer in spectral grade acetonitrile solutions unless otherwise noted. Steady-state emission spectra were obtained on a Spex Fluoromax fluorimeter with an instrumental response corrected against a NIST standard for spectral irradiance[6]. All samples were dissolved in spectral grade solvents distilled over CaH_2 and thoroughly degassed via standard freeze-pump-thaw method. Spectra were acquired in an argon filled air-free **1** cm path length quartz cuvette under optically dilute conditions with absorbance values between 0.1 and 0.15. The excitation slits on the fluorimeter varied

from 0.5 mm to 7 mm to obtain highest signal intensity without exceeding the instrumental limit of 10^6 counts per second, while emission slit widths were maintained at 0.5 mm.

Time-Resolved Luminescent Spectroscopy. All fluorescence lifetime data were acquired using a time-correlated single photon counting (TCPSC) instrument. The light source is a CW, diode-pumped Nd:YVO_4 laser (Spectra Physics Vanguard) that has been passively mode-locked to produce 2.5 W pulses at 355 nm or 2.5 W pulses at 532 nm. The rep rate is 80 MHz and the pulses are nominally the same 13 ps pulse width at both wavelengths. The output of the Nd:YVO_4 laser pumps a cavity-dumped dye laser (Coherent 702-2), which operates in the range of 430 nm to 850 nm, producing 5 ps pulses. The repetition rate of the dye laser is adjustable between 80 MHz and 80 kHz by means of the cavity dumping electronics (Gooch & Housego). For excitation of the $S_1 \leftarrow S_0$ transition, the dye laser was operated with Stilbene 420 dye (Exciton) to produce the excitation wavelength of *ca*. 435 nm. For the $S_2 \leftarrow S_0$ transition, Coumarin 500 dye (Exciton) was used to produce an excitation pulse of 520 nm. For both excitation wavelengths, the laser output is linearly polarized with a polarization extinction ratio of *ca.* 100. The 520 nm excitation pulses were frequency doubled using a Type I BBO crystal to produce a pulse of *ca.* 260 nm. The 260 nm pulse polarization was rotated to vertical using a UV-grade quartz polarization rotating Fresnel rhomb pair (CVI). The fundamental excitation pulse from the dye laser is divided, with one portion of the pulse directed to a reference photodiode (Becker & Hickl PHD-400-N), and the other portion

directed to the sample. Emission is collected using a 40x reflecting microscope objective (Ealing). The collected emission is separated into polarization components parallel (0^0) and perpendicular (90^0) to the vertically polarized excitation pulse using a polarizing cube beam splitter (Newport, extinction ratio ≥ 500:1). The parallel and perpendicular polarized signal components are detected simultaneously using micro channel plate photomultiplier tubes (MCP-PMT, Hamamatsu R3809U-50), each equipped with a subtractive double monochromator (Spectral Products CM-112) for wavelength selection. The detection electronics (Becker & Hickl SPC-132) resolve the parallel and perpendicular transients separately, yielding *ca*. 30 ps response functions for each detection channel. The detection electronics include a time-to-amplitude converter (TAC) and a constant fraction discriminator (CFD) that temporally resolves the fluorescence signal for each polarization component. Data are collected using multichannel analyzers (MCAs), which are integral components of the SPC-132 electronics. Data acquisition, detector bias, and collection wavelength are all controlled using an in-house written LabVIEW® (National Instruments) program on a PC. The sample temperature was regulated to ± 0.1^0C with a water-circulating bath (Neslab RTE-110) connected to a temperature-controlled brass cell jacket which held the sample cuvette. All samples were allowed to equilibrate thermally for 10 minutes prior to data acquisition.

Transient Absorption (TA) Spectroscopy. The spectra were taken on samples with absorbance values of approximately 0.35 for 485 nm excitation or 0.15 for 650 nm

excitation which were prepared inside a Ar filled glove box. The solvent used was spectral grade acetonitrile distilled over CaH_2.

For nanosecond TA, an air-free static cell with a 1 cm path length was used for all measurements. The instrumental set up has been previously described[6] and was used without further adjustments. Peak powers of were typically 3 mJ.

For femtosecond TA, the sample was held in a 1 mm path length flow cell which was connected to a bubbler-shaped reservoir via a special c-flex tubing (Masterflex®). This setup was used with a Masterflex® peristaltic pump, which circulates the sample solution at a flow rate between 0.5 to 1.5 mL/s. The major components of the femtosecond system have remained unchanged and are as previously described[7]. One major change to the system is the delay line which has been replaced with a 1.2 m LMAC series linear actuator from Aerotech driven by a Soloist controller (Aerotech). This delay line has been double passed to allow for the collection of kinetics out to approximately 13 ns. The powers used for both single-wavelength and full spectra measurements ranged from 3 μJ to 5 μJ. Full spectra data were collected with the pump beam defocused at the sample, while some single wavelength data were collected with a more focused pump beam. A check of single wavelength data collected at the same pump and probe combinations with a focused or defocused pump beam revealed no obvious discrepancies. The polarization was maintained at magic angle and confirmed to avoid potential drift by manually checking before collecting each set of data.

4.3. Results and Discussions

4.3.1. Consideration of Synthesis

The large flat conjugated macrocycle of porphyrin is known to undergo π-π stacking interaction. *tert*-butyl *meso*-substituted porphyrin was therefore selected to mitigate this issue and minimize unnecessary complexity in the subsequent photophysical characterizations. The stoichiometry for the aldehyde synthesis steps were optimized to give the highest yield of the product. It was found that the purity of the terpyridyltoluene starting material was critically important for the yield of the aldehyde product, and a strictly air-free environment was crucial for the first bromonization step.

The major synthetic challenge was the low yield of the asymmetrically substituted porphyrin ligand (**aPor**). In order to optimize the yield, a couple of different procedures were attempted: the Lindsey method and the Adler method. The Adler method is a one-pot reaction utilizing oxygen as the oxidizing agent in refluxing propionic acid. It was found that rather than mixing all three starting materials at once and heating after that, adding the pyrrole quickly to a near-boiling pre-mixed solution of the two aldehydes was more effective, giving a significantly higher yield of the desired asymmetric product. This method essentially allows formation of a dynamically controlled statistical mixture of various porphyrins with different substitutions, minimizing the thermodynamic preference for the symmetric products. Column chromatography was heavily relied upon to separate all these components. The selection of eluent was critical and a very

delicate balance for a successful separation. Previously, it has been reported[5] that a hexane/ethyl acetate mixture with a volumetric ratio of 99.9 : 0.1 on a neutral alumina stationary phase elutes out the symmetric porphyrin while that mixture with a ratio of 99 : 1 can be used to elute out the desired 3:1 asymmetric porphyrin. These ratios need to be fine-tuned for each new batch of asymmetric porphyrin synthesized, which means low reproducibility for these separation conditions.

The two major side products in this reaction were polypyrrole and symmetrically substituted *tetrakis-meso-3,5*-di-*tert*-butylphenylporphyrins. Polypyrroles are molecules in the shape of chains with various lengths. Although they mostly stayed on top of the stationary phase, some did elute along with the porphyrins. These chains may also entangle the desired products and either retain them on the stationary phase, or elute out along with the product. These complications led to the irreproducible results as well as very low yields.

In order to address these issues, two modifications were made: 1) instead of running a column on the neutralized product mixture immediately following its synthesis, the concentrated propionic acid solution was allowed to sit for a few days and crystallize. The crystals obtained were redissolved in hexanes and used to run the column; 2) instead of running repetitive columns with the above-mentioned eluent combinations, the very first eluent used was a mixture of hexanes saturated with dimethylformaldehyde. The crystallization step isolated most of the polypyrrole into the filtrate and this new eluent combination allowed quick elution of the porphyrins and left

any small amount of residual polypyrrole behind. The resultant mixture contained only symmetric and unsymmetric porphyrins. Two subtle points should be clarified: 1) the solubility of neither the porphyrin products are good in plain hexanes, the fact it can be used as an eluent is due to the residual propionic acid in the crystalline products obtained; addition of other solvents (for example, methylene chloride) obscures the differences between the two porphyrins on the column and leads to poor separation results. 2) The solvents hexanes and dimethylformaldehyde are usually considered to be immiscible, yet the tiny amount dimethylformaldehyde was able to alleviate the complications caused by the polypyrrole chains, leading to a better separation. A second column separation with the above-mentioned hexane/ethyl acetate eluents yielded the desired unsymmetric porphyrin **aPor**. With this procedure, the loss of product was mostly in the crystallization step and a total yield of 5% could be reproducibly obtained.

The Lindsey method is a milder synthesis protocol for delicate porphyrins with sensitive substituents and involves multiple steps. My attempt with this procedure showed only very slight improvement in yields and was therefore not routinely used.

The synthesis of the dyads was achieved following similar $[Ru(R_1\text{-tpy})(R_2\text{-tpy})]^{2+}$ preparation methods as discussed in Chapter 3. A portion of chloroform was used in the solvent mixture in order to solublize the porphyrin starting material which otherwise does not dissolve. It was notable that the yield for dyad **1** was significantly higher than that of dyad **2**. The major impurities for dyad **2** were identified as homoleptic Ru(II)

complexes with two **aPor** ligands, as well as NO_2Phtpy ligand. Apparently, the complex scrambled during the synthesis, resulting in the much lower yield. This difference in reactivity could be explained by the Ru(II) affinity for the terpyridyl ligands in the sequence of tpy > **aPor** >> NO_2Phtpy. The extent of delocalization as well as the electron withdrawing substituent on the NO_2Phtpy ligand presumably caused this ordering. Attempts to prepare Ru(**aPor**)Cl_3 as starting material failed due to low yield and extensive amount of unidentified side products.

4.3.2. Reference Compounds

Due to the intrinsic complexity of this system, a series of model complexes were synthesized and investigated in order to extract out the photophysical and electrochemical signatures for the individual components. Any new processes in the dyads must arise out of the interactions between these components. For a control molecule to faithfully report the behaviors of its corresponding component in the dyad, the structural and spectral differences have to be carefully evaluated.

4.3.2.1 *Porphyrin reference compounds*

For the purpose of modeling the behavior of porphyrin component, **aPor** is not an ideal reference. In the dyad, the nitrogen atoms of the terpyridine are bound to a metal center which significantly alters the energy levels involved. Therefore, the majority of the

porphyrin reference data was obtained on the symmetrically substituted porphyrin (**sPor**, see Figure 4-1) obtained as the side product in the synthesis discussed above. To ensure that the lower symmetry of the porphyrin core in the dyads did not cause energetic and spectroscopic consequences, **aPor** was also used to check the consistency. Fortuitously, both **sPor** and **aPor** produced very similar spectral profiles from 400 – 800 nm as well as dynamics in the time window of interest. Therefore, **sPor** was used as the reference molecule for convenience.

The absorption spectrum of porphyrin shows typical porphyrin features including a soret band at 420 nm and four Q bands in the visible region (see table 4-1). After excitation at 485 nm, the steady-state emission spectrum shows two emission peaks at 652 nm and 718 nm, the latter of which is a vibrational overtone. The quantum yield of emission was determined to be 0.048 by comparison to a $[Os(bpy)_3](PF_6)_2$ standard. Excitation at 650 nm produced identical results.

The triplet T state was the only species that can be observed on the nanosecond transient absorption (TA) system, which has an instrumental response function (IRF) of approximately 8 ns. The quantum yield for the formation of the T state is estimated from literature data[8-10] to be between 0.6 and 0.8. The profile registered at 20 μs following 650 nm excitation is shown in Figure 4-3 which has an intense 450 nm peak as well as lower peaks in the red region from 500 – 700 nm. The lifetime is determined to be 130 ± 20 μs with a 650 nm pump / 450 nm probe combination.

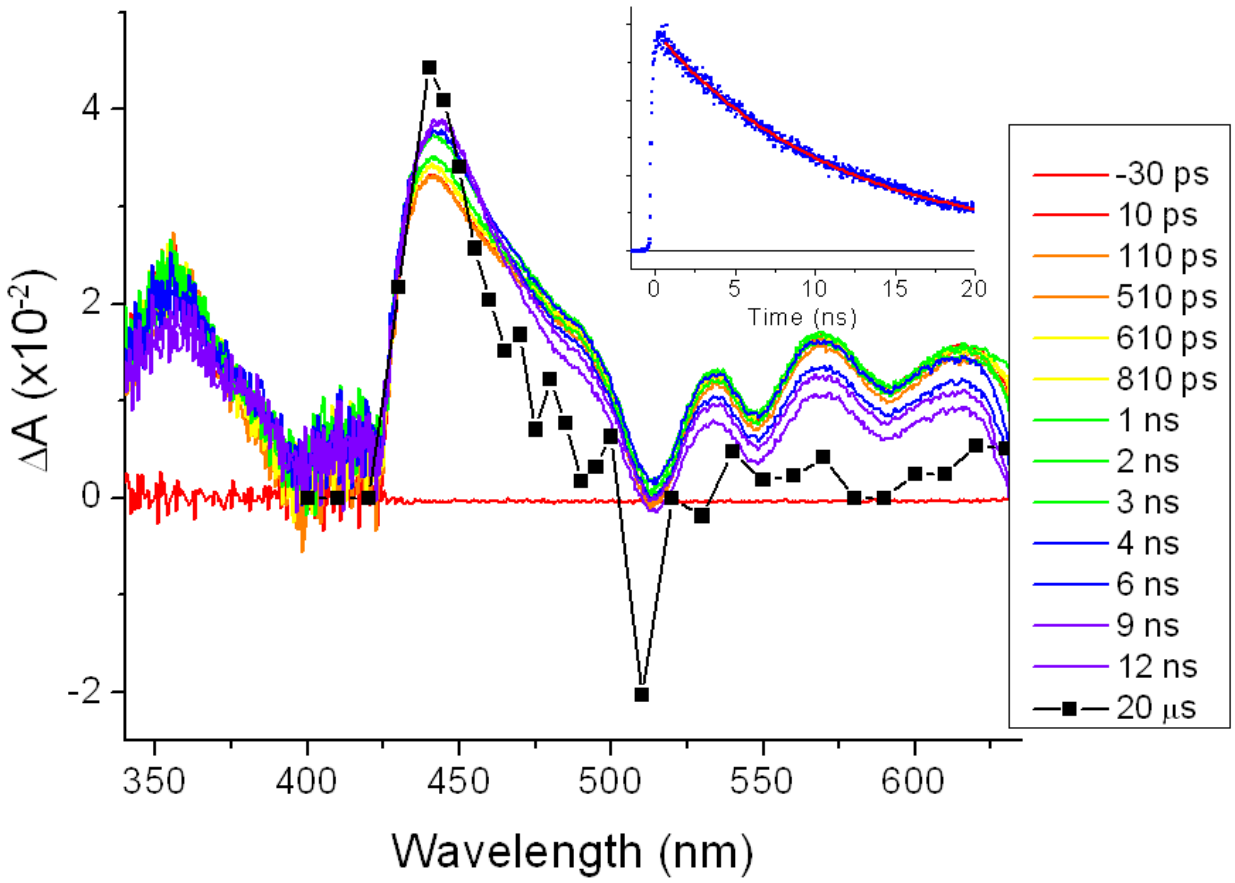

*Figure 4-3. Nanosecond (–■–) and femtosecond (—) TA spectra for porphyrin (**sPor**) following excitation at 650 nm. The solvent used was spectral grade acetonitrile with approximately 20% toluene which was strictly dearearated with freeze-pump-thaw method. Nanosecond spectrum was taken in a 10 mm path length cell; femtosecond spectra were taken in a 1 mm path length cell. The absorbance of both samples was approximately 0.14 at 650 nm. Inset shows typical TCSPC decay trace recorded at 660 nm following 650 nm excitation.*

The S_1 state decays via a combination of luminescence, internal conversion as well as intersystem crossing to form T state. Time-resolved luminescence spectroscopy revealed that the lifetime of S_1 is 10.6 ns in an acetonitrile solution with approximately 20% toluene. On the femtosecond transient absorption spectra, the S_1 state manifests

itself as a bleach in the Q band region overlaid on a broad absorptive feature extending from 500 nm to 700 nm resulting in weak absorption features in this region. As the time progress, the peak at 450 nm grows in while the peaks in the red region decay; and a shoulder feature around 485 nm goes away, leading to a characteristic profile for the T state. The peaks in the bluer region between 340 nm and 400 nm broaden at the same time.

4.3.2.2 *Ruthenium reference compounds*

Ruthenium complexes (**C1** and **C2**) were characterized as reference compounds in order to help identify dyad signatures relevant to the Ru components. Both **C1** and **C2** show typical sharp and strong ruthenium terpyridyl ^{1}MLCT absorption features at 480 nm and 490 nm respectively, along with terpyridine-based absorptions in the ultra-violet region. At least two ^{1}MLCT states, one localized on each terpyridyl ligand, shall contribute to the overall shape of the absorption envelop. The average energy of these two relevant ^{1}MLCT excited states can therefore be estimated from the MLCT maxima in the steady state absorption spectra. These energies are 2.58 eV for **C1** and 2.53 eV for **C2**. The emission spectra show very weak features centered at 645 nm and 685 nm for **C1** and **C2**, respectively, with a quantum yield on the order of 10^{-5} for both compounds (Table 4-1). These emission maxima and quantum yields are consistent with previous literature results[11] and the low quantum yields were attributed to the

small energy gap between the emissive ^{3}MLCT state and the higher lying metal-based ligand-field states (MC). These states are thermally accessible and serve as effective decay pathways, leading to strongly quenched emission. The slightly larger quantum yield of **C2** may be attributed to the electron withdrawing effect of the nitrophenyl substitution, lowering the energy of the ^{3}MLCT state thus increasing the aforementioned energy gap with upper deactivating levels.

The quenching effect of the higher-lying ligand field states also manifests itself in the lifetimes of the ^{3}MLCT state as revealed by TCSPC. Excitation at 485 nm reveals a lifetime of 450 ± 25 ps for **C1** and 9.6 ± 0.4 ns for **C2**. The 450 ps lifetime is in line with those for earlier reported ruthenium terpyridine complexes[11]. For example, $[Ru(tpy)_2]^{2+}$ was found to have a lifetime of 250 ps, while $[Ru(Phtpy)_2]^{2+}$ was measured to have a lifetime of 700 ± 10 ps. The much longer **C2** ^{3}MLCT lifetime is attributed to the same stabilization effect discussed above for the quantum yield.

It is important to note that these heteroleptic ruthenium bisterpyridyl complexes may undergo photo-induced scrambling to form the two relevant homoleptic complexes as discussed in the previous chapter. Initial time-resolved luminescence and absorption measurements indicated the presence of two ^{3}MLCT states within the same **C2** molecule. This was later attributed to the scrambled products produced during laser illumination when the sample was not flowed. In handling these heteroleptic complexes, it is crucial that the purity both before and after laser illumination is checked carefully. As precaution, all femtosecond data on the two dyads presented in this chapter were

obtained with a flow setup as described in the experimental section. The integrity of the samples were checked with ESI-MS before and after each experiment.

The general profiles for the femtosecond TA for both ruthenium complexes are similar including a bleach in the ground state absorption region as well as two broad absorption features in both the red and blue regions (see Figure 4-26 in appendix for **C1** and Chapter 3 for **C2**). However, isosbestic points of **C2**, (440 nm and 530 nm) were significantly red-shifted compared to that of **C1** (424 nm and 505 nm), which is attributed to the electro-withdrawing effect of nitro- group, lowering the energies for the radical anions in the **C2** case. For **C1**, the absorptive feature at 570 nm decays back to ground state with a lifetime of 505 ± 15 ps following 485 nm excitation, consistent with luminescence data (450 ± 25 ps). The same ground state recovery dynamics of **C2** observed at the same wavelength showed a very long component which cannot be accurately determined within the 13 ns time window available on this femtosecond instrument, but it is consistent with the 9.6 ns lifetime obtained from TCSPC. An additional short (75 ± 25 ps) rise is observed with **C2**, which was assigned to the interligand electron transfer processes (see Chapter 3).

4.3.3. Photophysical Processes in Dyads 1 and 2

The covalent linkage between the Ru and porphyrin leads to deviations of properties from the individual compounds. A Combination of electrochemistry, steady-state and transient spectroscopic measurements was utilized to interrogate such changes.

4.3.3.1 *Establishment of the energy level diagrams*

4.3.3.1.1 Ground State Absorption: Weak Coupling

The absorption spectra of the free-base porphyrin-ruthenium dyads **1** and **2**, seen in Figures 4-2 and 4-3, show very similar features as a combination of those for the individual components: the high intensity peak at 417 nm corresponds to the porphyrin soret band; the four more peaks in the range of 500 nm to 700 nm are assigned to the porphyrin Q-bands; the band peaking between 480 nm and 490 nm is characteristic to the ruthenium bisterpyridyl component. This indicates that the donor and acceptor are reasonably decoupled electronically, and both components possess their individual photophysical tags as if they were not connected. This justifies a component-to-assembly investigation strategy which only holds in the limit of weak electronic coupling. These absorption features, however, do not overlay *exactly* with the sum of the individual component spectra, which is especially obvious in the soret band region. The intensity of the dyad peak is significantly lower than the uncoordinated porphyrin and slightly blue shifted in both dyads (see table 4-1). This difference can be explained with an exciton coupling model[12] and results from the close positioning of two intensely absorbing chromophores. The magnitude of this mismatch is in line previous literature reports where intercomponent processes were clearly identified[13]. A much more drastic change in the absorption profiles was observed by Therein and coworkers in a similar system[14] yet with acetylene linkage, for which a strong coupling limit was

proposed. It is important to understand that the ground state absorption spectrum only tells about the electronic communication in the ground state of the dyads. The coupling in the excited states may be completely different and may produce new features associated with different processes.

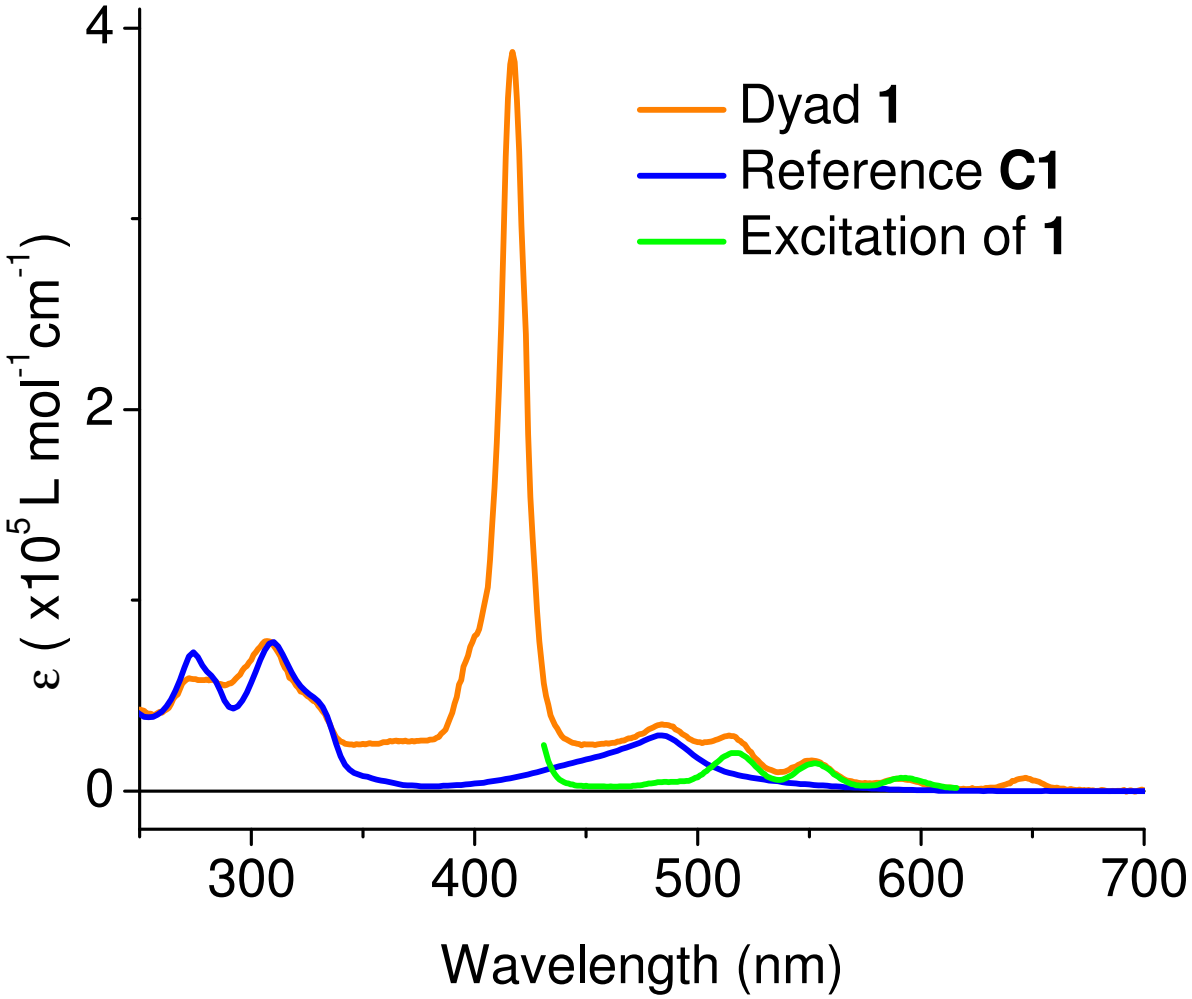

*Figure 4-4. Absorption spectra of dyad **1** and **C1**, and excitation spectrum of dyad **1**. Excitation spectrum was taken monitoring porphyrin emission at 650 nm.*

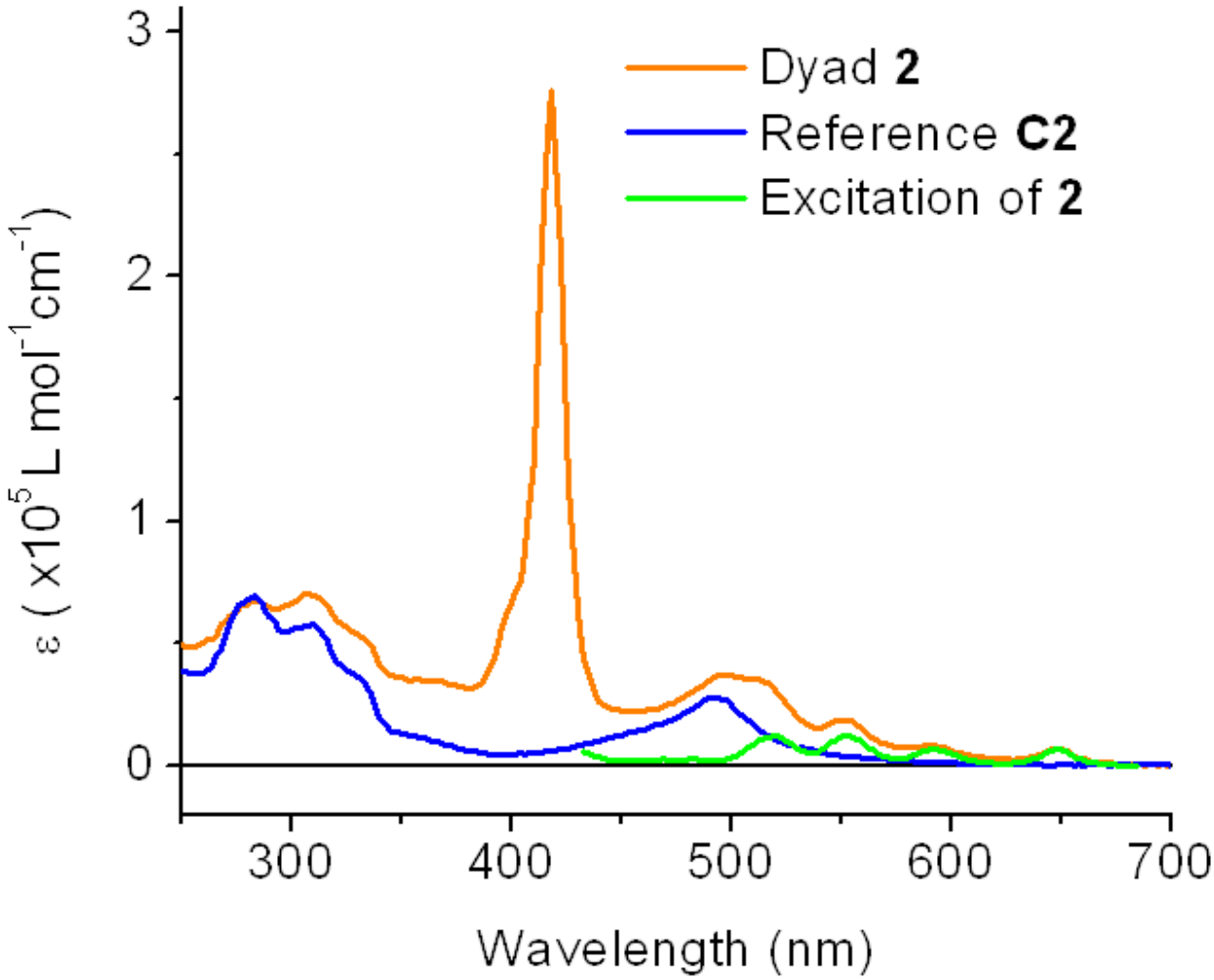

Figure 4-5 Absorption spectra of dyad **2**, **C2** and excitation spectrum of dyad **2**. Excitation spectrum was taken monitoring porphyrin emission at 718 nm.

To elucidate the mechanisms of photoinduced processes involved in the dyads, it is desired to independently probe features arising exclusively out of porphyrin excitation as well as Ru(II) bisterpyridyl excitation. As seen in Figures 4-2 and 4-3, the major ruthenium-based absorption band diminishes after 600 nm; therefore, excitation at 650 nm will lead to clean excitation of porphyrin-based S_1 state. However, clean excitation of ruthenium component is not possible due to residual porphyrin absorptions even in the 480-490 nm region where Ru(II) metal-to-ligand charge transfer feature peaks.

Despite the fact that porphyrin absorption only accounts for ~ 20% of the total photons absorbed, it is clearly not negligible. This becomes crucially important when emission properties are examined, because the emission quantum yield of porphyrin is orders of magnitude higher than that of the ruthenium bisterpyridyls in the same spectral region.

Table 4-1. Absorption and emission data for the dyads and the reference compounds.

Complexes	Absorption λ, nm (ε, x10^4 M^{-1} cm^{-1})						Emission τ, ns (Φ)	
	Soret	Q1	Q2	Q3	Q4	Ru	650 nm	485 nm
sPor	420 (37.0)	520 (1.8)	555 (1.1)	595 (0.7)	650 (0.7)		10.6 (0.048)	
C1						484 (2.9)		0.7 (2 x 10^{-5})
C2						492 (2.8)		9.6 (6 x 10^{-5})
1	417 (34.7)	514 (2.8)	551 (1.6)	590 (0.7)	646 (0.7)	485 (3.3)	4.8 (0.025)	4.8 (0.0038)
2	418 (27.6)	515 (3.5)	551 (1.9)	591 (0.8)	648 (0.7)	496 (3.7)	2.0 (0.0077)	2.0 (0.0014)

Comparing the spectra of **1** and **2**, the Ru peak in the dyad **2** is less clearly separated from the Q-band features. This is simply due to a 10 nm red shift as

compared to dyad **1**, thus blending into the first peak of porphyrin in the Q-band region more significantly. It is interesting to note that the color of this complex is sufficiently different that the human eye can detect this relatively subtle change, *i.e.* dyad **2** appears slightly more yellow-ish than dyad **1**. A similar effect is seen in the comparison between **C1** and **C2** where **C2** appears more purplish in color than **C1** as a result of this 10 nm red shift. The peak intensity of dyad **2** between 480 nm and 490 nm is also slightly higher due to a larger contribution from the porphyrin component at the redder wavelengths. The lower intensity of the soret band in dyad **2** suggests a stronger porphyrin-Ru interaction than that in dyad **1**, which will become more evident later.

Table 4-2. Cyclic Voltammetry Data, $E_{1/2}$/V vs Ag/AgCl

Complexes	Electrochemistry $E_{1/2}$, V				
	$Ru^{3+/2+}$	$P^{+/0}$	$P^{0/-}$	$tpy^{0/-}$	$tpy^{-/2-}$
sPor		+0.92	-1.33		
C1	+1.17			-1.34	-1.59
C2	+1.20			-1.04	-1.27

Conditions: collected in spectral grade acetonitrile containing $[Bu_4N][PF_6]$ (0.1 M) with a Pt working electrode, a graphite counter electrode and a Ag/AgCl reference electrode at 298 K under Ar atmosphere.

4.3.3.1.2 Energy level and redox potentials of dyads

The energy levels of the excited states in the dyad systems can be inferred from the steady state absorption and emission data and redox chemistry data. The position of the emissive porphyrin S_1 state relative to the ground state can be estimated from the intersection of the normalized absorption and emission profiles, which gives a value of 1.90 eV. ^{1}MLCT state for the Ru component can be estimated from the absorption spectra to be either 2.58 eV (dyad **1**) or 2.53 eV (dyad **2**). It is very important to understand that the absorption peaks of the two halves of the Ru complex are always extensively overlapped, therefore, these energetic numbers shall be considered as an average between the two ^{1}MLCT states co-present in the dyads, which are simultaneously populated with 485 nm excitation. The energy of the ^{3}MLCT state can be reasonably estimated from the 0-0 emission maxima of the Ru reference complexes at low temperature. The numerical sum of the donor oxidation potential and acceptor reduction potential can be considered as an approximation to the energy of charge separated (CS) excited state due to similar chemical compositions. Therefore, porphyrin-Ru dyad CS states can be estimated to be at approximately 2.26 eV (**1**, P^+-$Phtpy^-$), 2.51 eV (**1**, P^+-tpy^-), 2.50 eV (**1**, P^--Ru^+) and 1.96 eV (**2**, P^+-NO_2Phtpy^-), 2.19 eV (**2**, P^+-$Phtpy^-$), 2.53 eV (**2**, P^--Ru^+).

From the driving force point of view, it can be expected that energy transfer processes will be the only available intercomponent pathways in dyad **1** following 650 nm excitation yet electron transfer from non-thermalized ^{1}MLCT or hot ^{3}MLCT excited

state will be possible when excited at 485 nm. In dyad **2**, electron transfer processes are possible following excitation at either wavelength. In both dyads, the direction of the electron transfer should be from porphyrin to the Ru component based on thermodynamics arguments.

These measurements establish a basic energy level diagram for both dyads, which dictates the availability of intercomponent processes. Time resolved measurements were subsequently used in order to probe the processes arising out of the intercomponent interactions.

4.3.3.2 *Dynamics of intercomponent processes*

As explained earlier, in order to explicitly probe the intercomponent photoinduced processes in both dyads, 650 nm excitation was used to investigate the dynamics resulting explicitly from porphyrin excitation, while 485 nm excitation was used to largely excite the Ru(II) component and isolate its features by comparing to the 650 nm results. It can be estimated based on extinction coefficients of the reference compounds that 18% of the photons go into the porphyrin moiety following 485 nm excitation in both dyads.

As dyad **1** possesses less convoluted intramolecular processes, the discussion below will start from dyad **1**. The schemes for dyad **2** will be generated based on the similarities and differences as compared to dyad **1**. For both dyads, 650 nm excitation data will be presented first before the more complicated 485 nm data.

4.3.3.3 *P-RuH dyad (1)*

4.3.3.3.1 Exclusive Excitation of porphyrin component at 650nm:

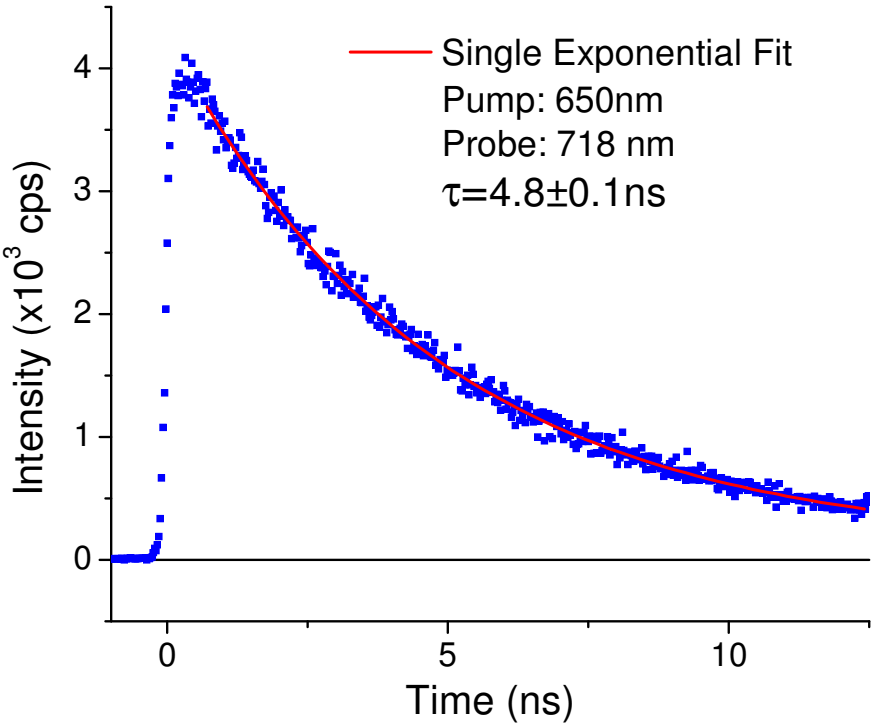

*Figure 4-6. Time-resolved luminescence data for lifetime characterization of dyad **1** following 650 nm excitation. Dynamics observed at other probe wavelengths gave the same time constants.*

4.3.3.3.1.1 *Quenching of S_1 state*

Steady state and time-resolved luminescence spectroscopy: When exciting at 650 nm, luminescence spectrum shows the typical porphyrin emission profile peaking at 652 nm with a 718 nm vibrational overtone. The quantum yield is approximately 50% of that

of porphyrin reference ($\Phi^{650}_{\mathbf{1}}$=0.025 *vs.* $\Phi^{650}_{\mathbf{sPor}}$=0.048), suggesting a quenching pathway brought in by the presence of Ru component.

This proposed quenching of the S_1 excited state is supported by the reduction in the S_1 lifetime from 10.6 ns to 4.8 ns in the dyad (see Figure 4-6).This is a 55% quenching efficiency, consistent with the quantum yield data. A quenching rate constant of 1.1 x 10^8 s^{-1} or $(8.8\ ns)^{-1}$ can therefore be deduced according to equation 1:

$$k_q = \frac{1}{\tau_{dyad}} - \frac{1}{\tau_{ref}} \quad (1)$$

where τ_{dyad} and τ_{ref} represents the lifetime of the dyad and the reference compound, respectively.

From a mechanistic point of view, the reduction in quantum yield and lifetime may be due to one of two processes: 1) catalyzed intersystem crossing from the S_1 state to the T state of porphyrin as a result of the heavy atom effect, 2) an additional decay pathway from the porphyrin S_1 state to transfer either energy or an electron to a ruthenium terpyridyl component, or more likely, a combination of both. The lack of characteristic Ru(II) emission at 645 nm does not exclude the possibility of energy transfer from porphyrin to ruthenium. Even if the ruthenium component is sensitized via energy transfer and emits, its signal may not manifest itself on top of the porphyrin emission due to its much lower quantum yield (see Table 4-1).

The relative contribution of pathway (1) can best be estimated from the formation quantum yield of the T state in the dyad as compared to that of the reference. Unfortunately, our current nanosecond TA instrument setup does not allow a clear

measurement of this quantity. While the sensitivity of S_1-to-T transition to the heavy atom effect may be different from that of T-to-GS (ground state), it is reasonable to assume that such a difference should not be very big considering the same singlet-triplet intersystem crossing nature. Therefore, the change in the lifetime of T state, determined exclusively by T-to-GS process, should be a good indication of the magnitude of heavy atom effect. Nanosecond TA measurements yield a lifetime of 130 ± 30 μs for dyad **1**, identical to that of the porphyrin reference compound, suggesting the heavy-atom effect is minimal and not the dominating quenching pathway. This leaves energy transfer as the major contributor to the effective S_1 quenching, and can be assigned a rate constant close to $(8.8\ ns)^{-1}$.

A more definitive assignment of the energy transfer pathway requires the observation of the ^{3}MLCT features with 650 nm excitation, where Ru(II) does not absorb. The intrinsically low quantum yield of ^{3}MLCT as well as the possible poor accumulation of this state, considering the much faster $(505\ ps)^{-1}$ intrinsic Ru ^{3}MLCT decay as compared to the relatively slow formation from S_1 $(8.8\ ns)^{-1}$, may preclude the direct observation of this state. Figure 4-7 shows the spectral profile of the Ru(II) emission scaled up by a factor of 1000 overlaid with porphyrin emission profile. As can be seen in the figure, probing at 718 nm, the emission intensity of the porphyrin component is approximately 1000 fold larger than that of Ru component, *i.e.* the emission signal will be completely dominated by porphyrin. Probing at 610 nm, the porphyrin feature is tailing out and the Ru(II) emission is still close to its maximum.

While the residual porphyrin emission signal is still 10 times higher than that of Ru(II), the Ru(II) signature could not be neglected at this wavelength. Therefore, the 610 nm probe will be relatively sensitive to the Ru(II) component for time-resolved luminescence spectroscopy measurements, and could potentially yield a Ru-signature when compared against the 718 nm probe data. Unfortunately, no Ru(II) ^{3}MLCT features were detected at 610 nm, leaving uncertainty in this ^{3}MLCT-to-T energy transfer pathway. No faithful conclusion can be made with these emission data.

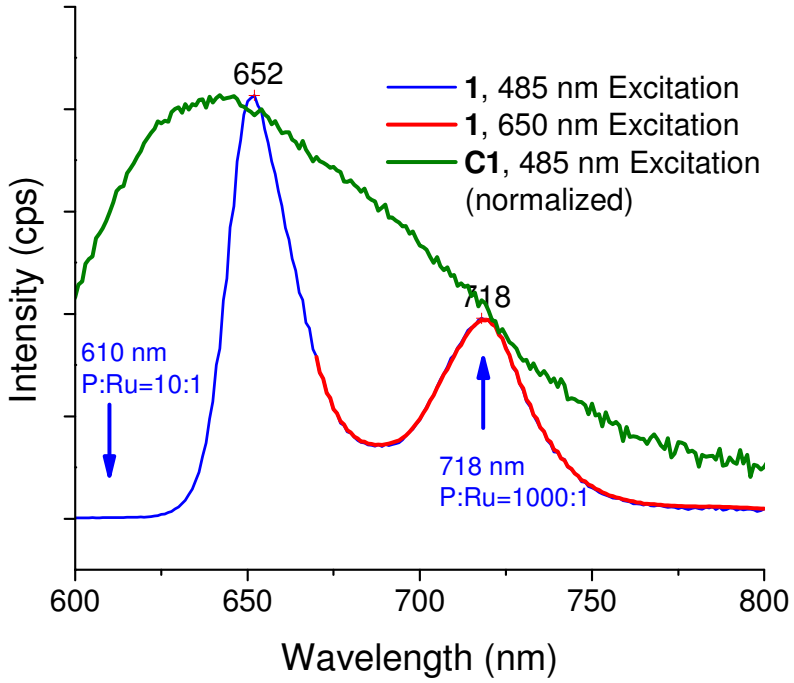

*Figure 4-7 Normalized emission profiles for dyad **1** at different excitation wavelengths as well as that of **C1** to the intensity at 718 nm. The **C1** profile was scaled up by a factor of 1000 to match the intensity at 718 nm following 485 nm excitation. The ratio between emission intensities of P:Ru following 485 nm excitation at 610 nm was approximately 10:1; and that at 718 nm was approximately 1000:1.*

The excitation spectrum obtained by monitoring the porphyrin emission intensity at either 650 nm or 718 nm, as shown in Figure 4-4, shows no Ru(II) MLCT related absorptions at around 485 nm, indicating no energy transfer from ruthenium to S_1 state.

4.3.3.3.1.2 *Sequential energy transfer: S_1-^{3}MLCT-T conversion*

Similar to the decay of S_1 state, the formation of the T state can proceed via two different pathways: enhanced intersystem crossing from the S_1 state, and back energy transfer from the Ru(II) ^{3}MLCT state to the T state. As the latter pathway relies on the formation of the ^{3}MLCT state from the S_1 state, it is essentially an sequential energy transfer originating from S_1. Therefore, the formation time constant for the T state will be exclusively limited by the lifetime of the S_1 state. Unfortunately, this process is too fast to be observed on the nanosecond TA instrument. Femtosecond TA spectra were recorded for further characterizations.

Femtosecond Transient Absorption (TA) Spectra: The full spectra of dyad **1** obtained following excitation at 650 nm is seen in Figure 4-8. The initial traces show features similar to that of the porphyrin S_1 state as observed in the reference porphyrin molecule (Figure 4-3). In the visible region, starting from 430 nm, a very broad absorption feature extends over to the red region. On top of the broad feature are the four valleys corresponding to the ground state porphyrin Q bands. The spectral profile of the final trace, taken at an 11.1 ns delay, is very close to the profile of the long-lived T state

observed in porphyrin nanosecond TA spectra, characterized by a stronger 450 nm absorption and less intense peaks in the region to the red of 480 nm. The peak profile in the blue region also showed the broadening with time as seen in the porphyrin reference compound. Therefore, the overall spectral profile change suggests a relatively simple time evolution and can be interpreted as a gradual conversion from S_1 to T.

The noise level of these spectra were relatively high due to the diminished white light background as the result of high absorbance in the bluer region (<430 nm) which is unavoidable given the ground state absorption spectral profile and an absorbance of 0.15 at 650 nm.

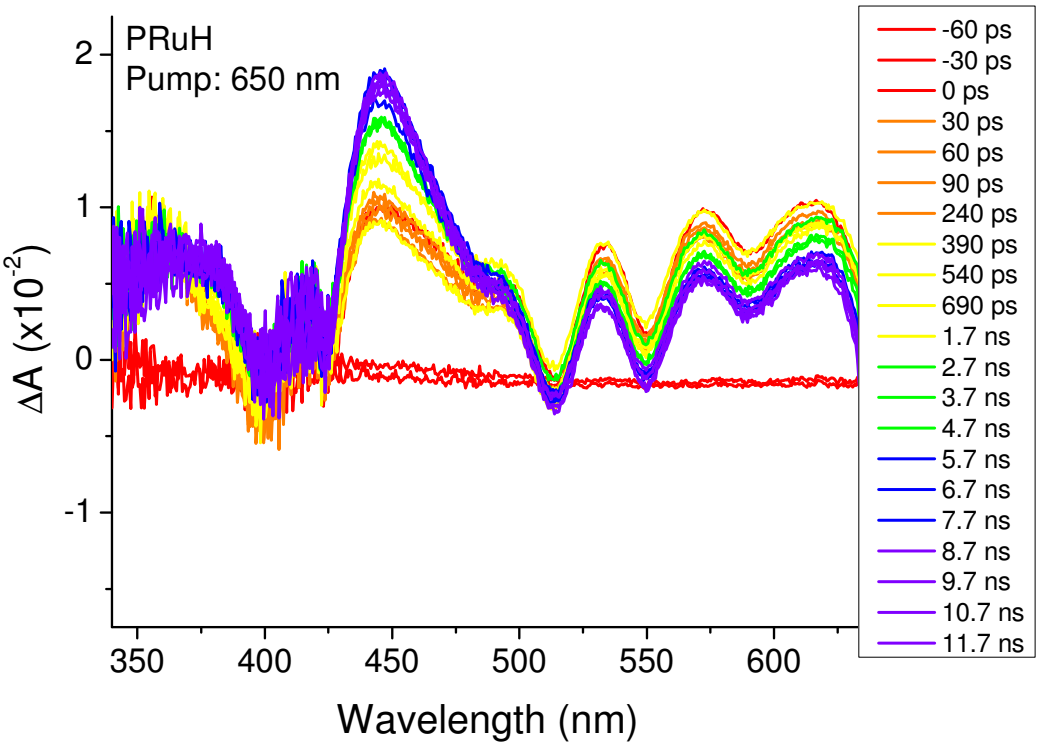

*Figure 4-8. Femtosecond TA Spectra of dyad **1** with 650 nm excitation wavelength. The sample was prepared as an acetonitrile solution with an absorbance of 0.15 in a flow cell connected to a peristaltic pump. The flow rate was set to be approximately 1 mL/s.*

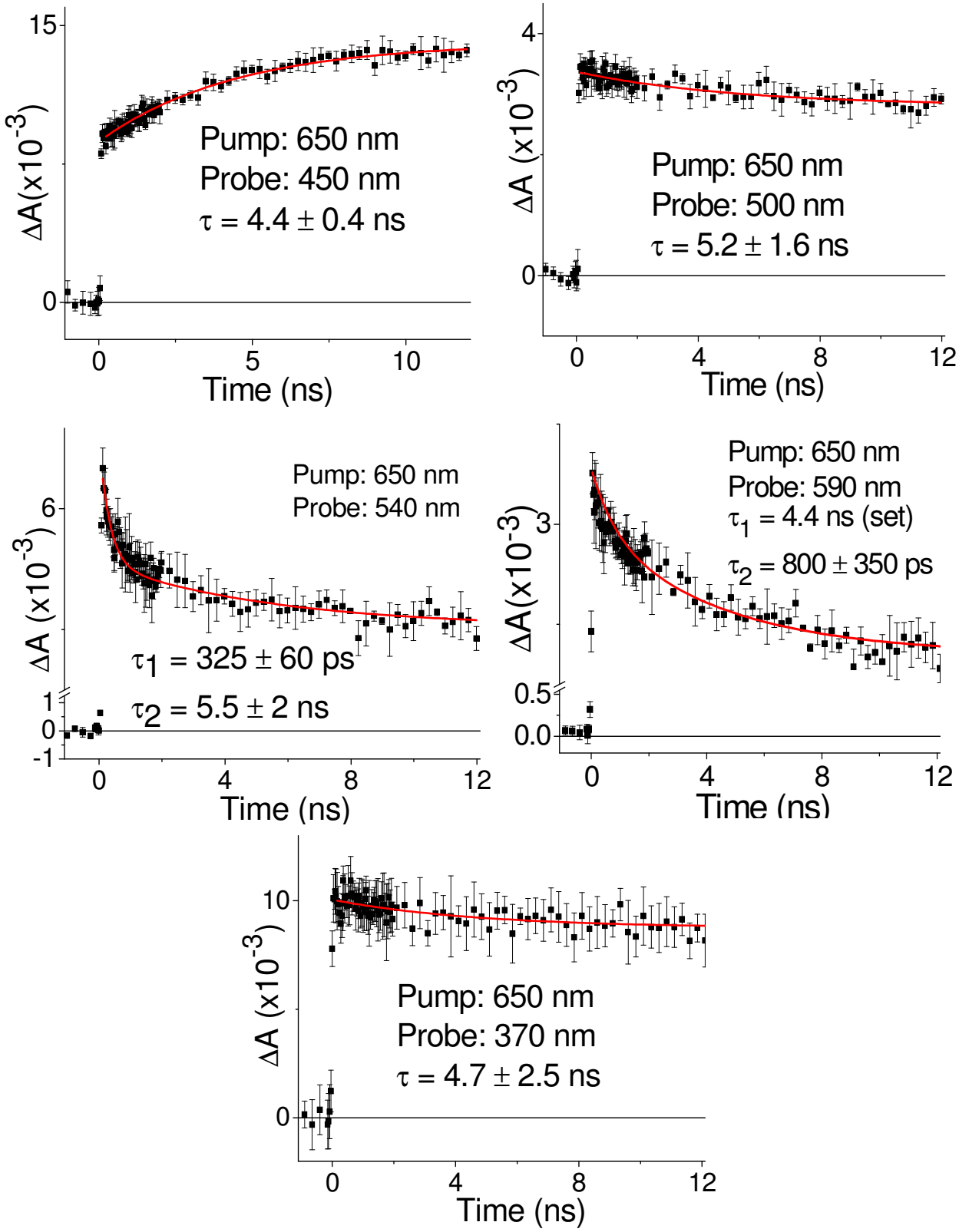

*Figure 4-9. Femtosecond TA: Single wavelength dynamics for Dyad **1** following 650 nm excitation.*

The kinetics of the S_1-to-T relaxation were monitored by single wavelength measurements, as seen in Figure 4-9. At 450 nm, a wavelength most characteristic to the formation of the porphyrin-based T state, a rise feature with a lifetime of 4.4 ns is observed. This is identical, within experimental error, to the 4.8 ns lifetime of the S_1 state determined from the TCSPC data. This time constant is therefore assigned to the S_1-to-T conversion. This 4.4 ns component is observed at all probe wavelengths in Figure 4-9.

4.3.3.3.1.3 *^{3}MLCT-to-T conversion*

When probing at 540 nm, in addition to the 4.4 ns component, a shorter component of approximately 325 ± 60 ps is also identified and tentatively assigned to the intrinsic decay of Ru(II) ^{3}MLCT state. This short component was not identified in TCSPC or femtosecond TA full spectra as a distinct spectral feature due to a combination of poor population accumulation as well as its small luminescence quantum yield. This feature may also be present at 590 nm probe wavelength, but the noise level does not allow for a meaningful time constant to be extracted. Similar to the luminescence situation, the ΔA of Ru(II) component is smaller than the porphyrin ΔA at most wavelengths, which explains the absence of the Ru feature at wavelengths other than 540 nm and 590 nm. These two wavelengths are relatively sensitive to the Ru(II) signature because the ΔA of

the porphyrin component is at its minimums yet that for the Ru(II) component is close to the maximum.

That a porphyrin absorption at 650 nm produces a Ru(II) ^{3}MLCT-based signature is the strongest evidence for the S_1-to-^{3}MLCT energy transfer pathway. Unfortunately, the high noise level did not allow a definitive time constant to be calculated for this ^{3}MLCT-to-T energy transfer. However, based on the lower and upper limit of these time constants, this rate can be calculated to be in between $(4\ ns)^{-1}$ and $(530\ ps)^{-1}$.

To summarize this section, excitation of dyad **1** at 650 nm yields a relatively simple picture: the S_1 state is formed immediately following excitation, which then decays via three parallel pathways: a quenched luminescence process with a quantum yield of 0.025; the intrinsic S_1 decay via a combination of intersystem crossing to T state as well as internal conversion; and an intercomponent energy transfer process to form Ru-based ^{3}MLCT state with an efficiency close to 50%. The S_1-to-T intersystem crossing may be slightly enhanced by the heavy atom effect, but the very close lifetime of the T state in dyad **1** as compared to that of porphyrin reference molecule suggests this effect is minimal. The ^{3}MLCT-to-S_1 energy transfer pathway should not account for any significant decay as evidenced by the absence of Ru(II) peak on excitation spectrum of porphyrin emission. Due to the small signal of Ru(II) in both absorption and luminescence measurements, as well as the poor accumulation, the ^{3}MLCT state is only detected in a couple of single-wavelength femtosecond TA measurements. The comparison of the lifetime of this state to that in reference complex (505 ± 10 ps)

indicates the presence of a reverse energy transfer process from ^{3}MLCT-to-T, yet no accurate rate constant can be extracted out.

4.3.3.3.2 Simultaneous excitation of Ru and porphyrin components at 485nm:

The excitation at 485 nm effectively creates two major photophysical pathways: the one initiated from Ru(II) ^{1}MLCT state which constitutes *ca.* 82% of the photon absorbed; and the one initiated from the S_1 porphyrin state via the *ca.* 18% absorption of porphyrin component. This latter pathway produces all of the features described above for 650nm excitation, only with attenuated signals. The extra energy from the 485 nm photons absorbed by porphyrin is expected to dissipate via vibrational cooling and/or other similar nonradiative pathways, and does not appear to introduce significant differences in either the spectral profile or the dynamics, as shown in reference porphyrin compound measurement.

4.3.3.3.2.1 *The isolation of Ru ^{3}MLCT signature and ^{3}MLCT-to-T conversion*

Steady-state and time-resolved luminescence: The emission profile of dyad **1** following 485 nm excitation is identical to that characteristic to porphyrin fluorescence. The quantum yield, formally $\Phi^{485}_{\mathbf{1}}$=0.0038, is within experimental error of that observed with 650 nm excitation, $\Phi^{650}_{\mathbf{1}}$=0.025, after correcting for porphyrin's relevant

absorbance at 485 nm. This suggests that the Ru-to-S_1 energy transfer is not a major S_1-forming pathway, consistent with the excitation spectrum result discussed earlier.

Since Ru(II) ^{1}MLCT is the dominant absorber at 485 nm, a significant amount of the Ru(II) ^{3}MLCT state is expected to be present due to the intrinsically fast intersystem crossing. Since time-resolved luminescence is a sensitive technique, TCSPC was used to look for such Ru(II) features. The same probe wavelength dependence study as that used with 650 nm excitation situation was performed here. As previously discussed, probing at 718 nm will be insensitive to the Ru-based excited states, and it therefore serves as a reference point when interpretating features at other probe wavelengths. As seen in Figure 4-10, probing at 718 nm following 485 nm excitation, a single exponential decay is observed, which can be fit with a lifetime of 4.8 ns, identical to that of porphyrin-based S_1 state. Probing at 610 nm, however, a second minor, but non-negligible component is observed on top of the same 4.8 ns S_1 emission. This shorter component can be fit with a lifetime of approximately 400 ± 100 ps and is attributed to the decay of the ^{3}MLCT state populated from the Frank-Condon state following direct excitation. Due to the relatively broad instrument response function, interpretation of the ratio between the pre-exponential terms is not meaningful. Yet it is clear that the weight of Ru(II) component decreases with redder probe wavelengths and finally diminishes when porphyrin emission peaks at 652 nm. This lifetime was not sufficiently different from that observed in the reference complex (505 ± 15 ps), yet was consistent with the 325 ± 60 ps component (^{3}MLCT-to-T energy transfer) observed in the 650 nm TA

results. The reason that it can now be detected via TCSPC can be explained by the much higher initial ^{3}MLCT concentration.

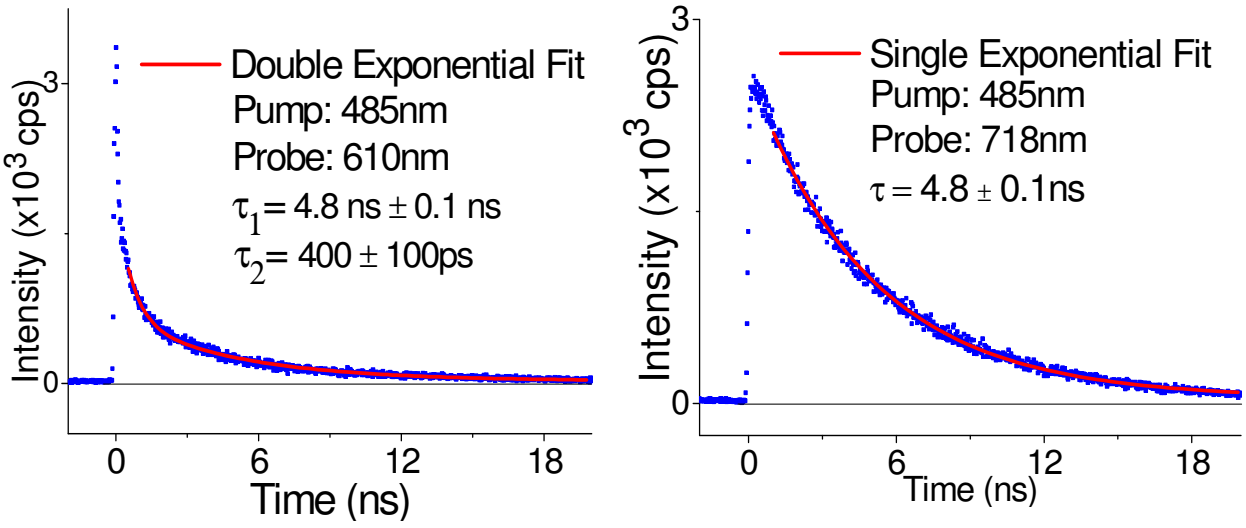

*Figure 4-10. Time-resolved luminescence spectra of dyad **1** following 485 nm excitation. This probe wavelength dependence study isolates Ru(II)-related time constant.*

Femtosecond Transient Absorption Spectra:

The full spectra of dyad **1** obtained following 485 nm excitation is much less noisy than the 650 nm excitation spectra. This is because 485 nm is an intense peak in the absorption profile, second only to the soret band, and is therefore a major absorber. Since the majority of light absorbed produces signal, a larger signal/noise ratio was obtained. As seen in Figure 4-11, a clear bleach feature between 390 nm to 430 nm is observed with a small absorption peak at 420 nm.

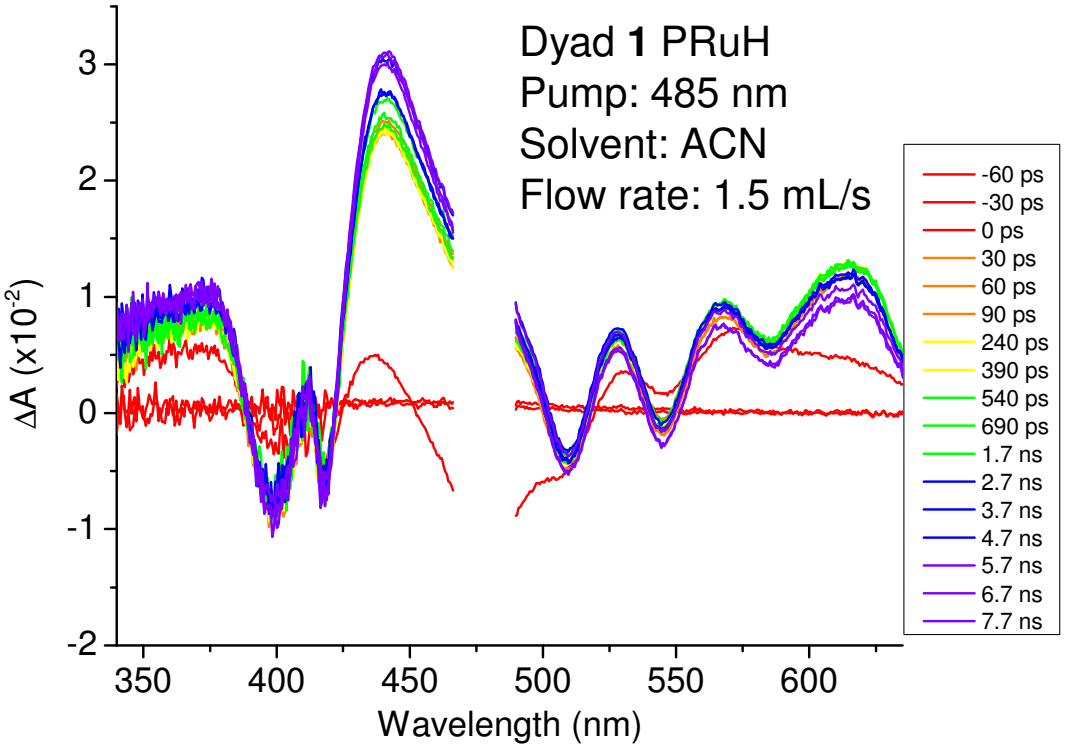

*Figure 4-11. Femtosecond Transient Absorption Spectra of Dyad **1** with 485 nm excitation wavelength. The sample was prepared as a acetonitrile solution with an absorbance of 0.35 in a flow cell connected to a peristaltic pump. The flow rate was set to be approximately 1 mL/s.*

A Ru(II) ^{1}MLCT-based bleach signal is present at time zero concurrent with excitation, and within a few picoseconds, it converts into a state characteristic of the porphyrin-based T state. This latter state grows on the timescale of a few nanoseconds. Unlike excitation at 650 nm, no obvious S_1 features were observed within the first 40 ps. Since the S_1 state has a lifetime of 4.8 ns, as already established via luminescence spectroscopic measurements, it could not have been populated within this short time window. Therefore, a direct Ru-to-T conversion pathway is present which does not

involve the population of the S_1 state. Such an assignment is consistent with the absence of a Ru(II)-based feature in the excitation spectrum when probing the S_1-based emission at 650 nm, as well as the absence of an S_1 quantum yield increase with 485 nm excitation compared to 650 nm. It has to be clarified here that the growth at 450 nm with time after the first 40 ps, also present in single-wavelength dynamics in Figure 4-12, does not show a process initiated from Ru(II)-excitation. Rather, it is assigned to the S_1-to-T transition originated from the other excitation pathway, *i.e.* S_1 state produced out of the porphyrin-based direct residual absorption at 485 nm. This accounts for the much smaller amplitude change at 450 nm as compared to that observed with 650 nm excitation as discussed above, since only 18% of photons absorbed will produce such dynamics. Such a small change in the amplitude of the ΔA signal over time also leads to a relatively large error bar in determining time constants.

The trace obtained at 590 nm seen in Figure 4-12, although very noisy, shows a fast component which can be fit to 390 ± 190 ps. This is reminiscent of the Ru(II) decay described above in TCSPC measurements (400 ± 100 ps) and that in 650 nm TA (325 ± 60 ps). Again, the noise level precludes a distinction between this number and that of the intrinsic ^{3}MLCT decay in the reference complex, 505 ± 15 ps. None of other probe wavelengths, *i.e.* 500 nm, 510 nm or 540 nm give a sufficiently large amplitude change to yield a reliable lifetime.

From the full spectra traces shown in Figure 4-11, it is clear that the T state is completely established from the Ru(II) excitation within <40 ps. This is a quite surprising

observation as the formation rate of the T state in similar systems is usually on the order of 10^8-10^9 s^{-1}, at least an order of magnitude less than that proposed here. Since the ^{3}MLCT-to-T energy transfer pathway is found to be slower than $(320\ ps)^{-1}$, another Ru-related state is populating T state at the same time.

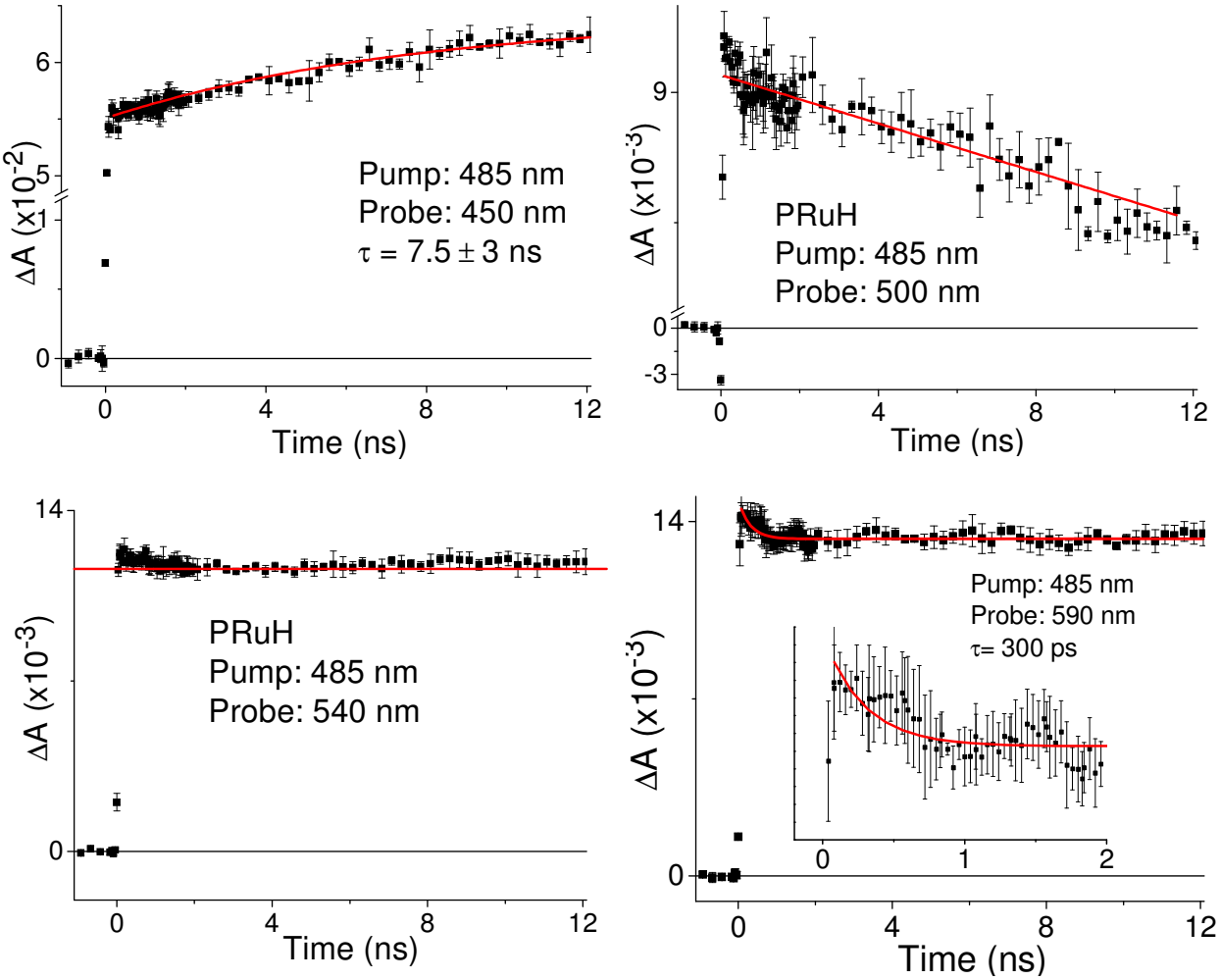

Figure 4-12*. Femtosecond TA of dyad* ***1****: Single wavelength dynamic following 485 nm excitation.*

4.3.3.3.2.2 *Fast formation of T state from Ru-based states*

This extremely fast rate forming the T state directly from a Ru(II)-based state has not been previously reported. It is too quick to originate from a thermally relaxed ^{3}MLCT state, which has an observed lifetime of a few hundred picoseconds, as discussed above. The only remaining possibility is a process out of either the initial ^{1}MLCT state or a hot ^{3}MLCT state. This T state forming process may be either an energy transfer process or a sequential electron transfer process mediated by a charge-separated species. Since the driving force for energy transfer directly into the T state is deep within the inverted region of the Marcus curve, the rate of energy transfer is not likely to be as fast as that observed here, which is larger than $(40\ ps)^{-1}$. Sequential electron transfer is, therefore, a more reasonable explanation.

This charge-separated state mediating this sequential electron transfer should be triplet in nature, considering it mediates the conversion from the high-energy Ru(II) state to the triplet T state much more efficiently than to the singlet S_1 state. From the electrochemical data discussed above in Table 4-2, the chemical composition of this charge separated state most likely consists of a formally oxidized porphyrin and reduced Ru(II) component, with an electron localized at the bridging terpyridyl group, *i.e.* a P^+-Ru^- CS state. The energy of this state, as discussed above, is estimated to be 2.26 eV, accessible from the ^{1}MLCT Frank Condon state which has an energy of 2.55 eV. Due to the moderate electronic coupling, as well as the short geometric distance between the proximally localized Ru(II) state and that of porphyrin, ultrafast electron

transfer is conceivable. A weak emission signal of ^{3}MLCT is observed in TCSPC, suggesting this Ru(II)-CS-T pathway is competitive with the thermalization of the initial Ru(II)-based state, and has a rate constant similar to that of vibrational cooling and solvent interactions, *i.e.* on the order of a few hundred femtoseconds to a few picoseconds. Femtosecond full spectra TA with 1 ps steps was performed in order to fill in between the time slices shown in Figure 4-11, and to further understand the ultrafast intercomponent sequential electron transfer.

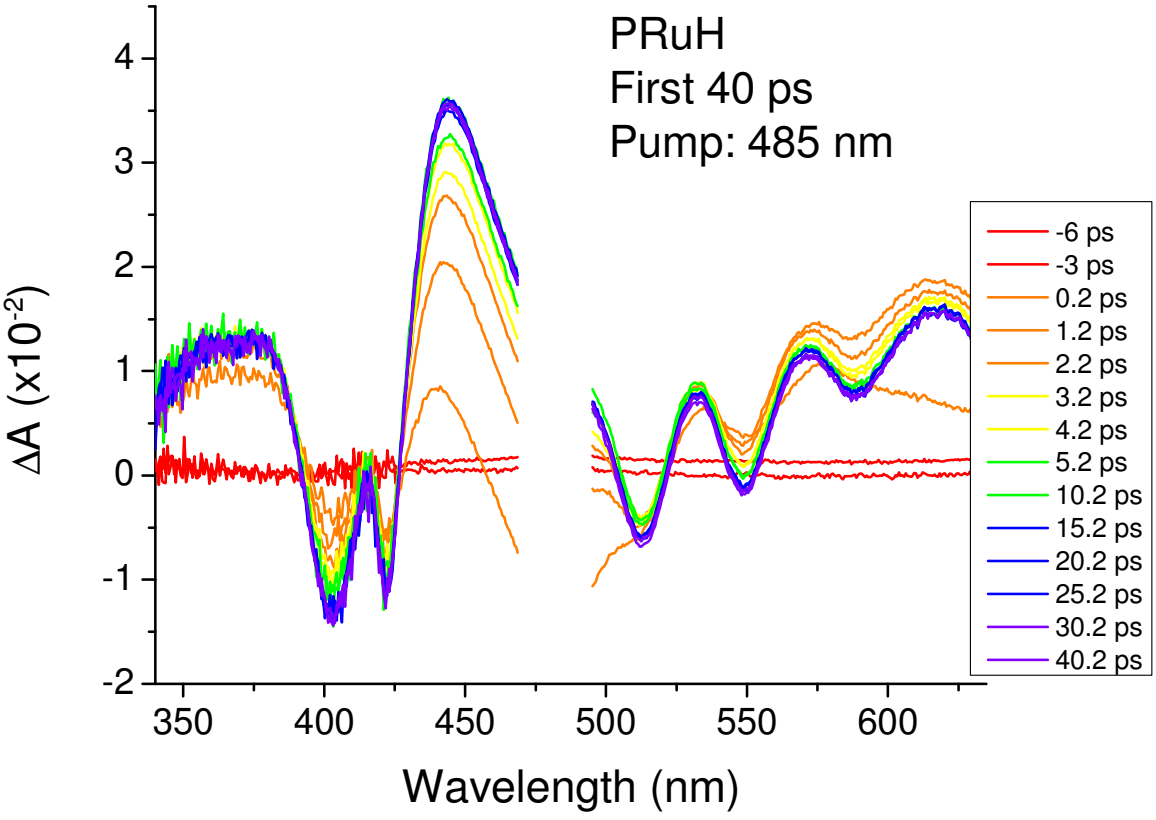

*Figure 4-13. Early time femtosecond Transient Absorption Spectra of Dyad **1** with 485 nm excitation. The sample was prepared as an acetonitrile solution with an absorbance of 0.15 in a flow cell connected to a peristaltic pump. The flow rate was set to be approximately 1 mL/s.*

The full spectra within the first 40 ps following 485 nm excitation are presented in Figure 4-13. A clearer grow in of the feature at 450 nm along with the decay of the Ru(II) bleach (the shoulder between 490 nm and 500 nm) can be related to the Ru(II)-to-T conversion. The spectral profile of the CS state can be reasonably approximated as the sum of the porphyrin cation features and the terpyridyl radical anion features. Therefore, the most characteristic change for the charge separation process will be the disappearance of the Ru(II) bleach, most obvious at 500 nm. The signature for the charge recombination process forming the T state will be the growth of the 450 nm feature since the porphyrin radical cation has a much smaller extinction coefficient than the T state. These processes are quite clear in single wavelength dynamic traces, seen in Figure 4-14. The trace obtained probing at 450 nm can be fit with a double exponential to yield time constants of 780 ± 10 fs and 4.6 ± 0.1 ps. The shorter 780 fs component is tentatively assigned to the Ru(II)-to-CS electron transfer process. The 4.6 ps component, however, can be confidently assigned to the rise of the T state from the CS state due to its major manifestation at 450 nm, a wavelength most sensitive to the T state formation. Probing at other wavelengths, such as 500 nm, 540 nm and 590 nm, another time constant between 1 and 2 ps is observed, slightly longer than the 780 fs attributed to the Ru disappearance. These time constants are assigned to a mixture between the 780 fs component and the 4.6 ps component. As the T state does have a broad spectral profile, it the 4.6 ps component also contributes to the time constants observed at these other wavelengths. As the probe wavelength moves away from 450

nm, the contribution of this 4.6 ns will be less and less, thus the observed 1-2 ps components in the redder region. The change in the sign of ΔA at 500 nm, occurring within the first few hundred femtoseconds, suggests the shorter component originates from the Ru(II) state which is a bleach at early times, consistent with the above assignments. The slower electron recombination than charge separation can be rationalized with a simple energy gap argument.

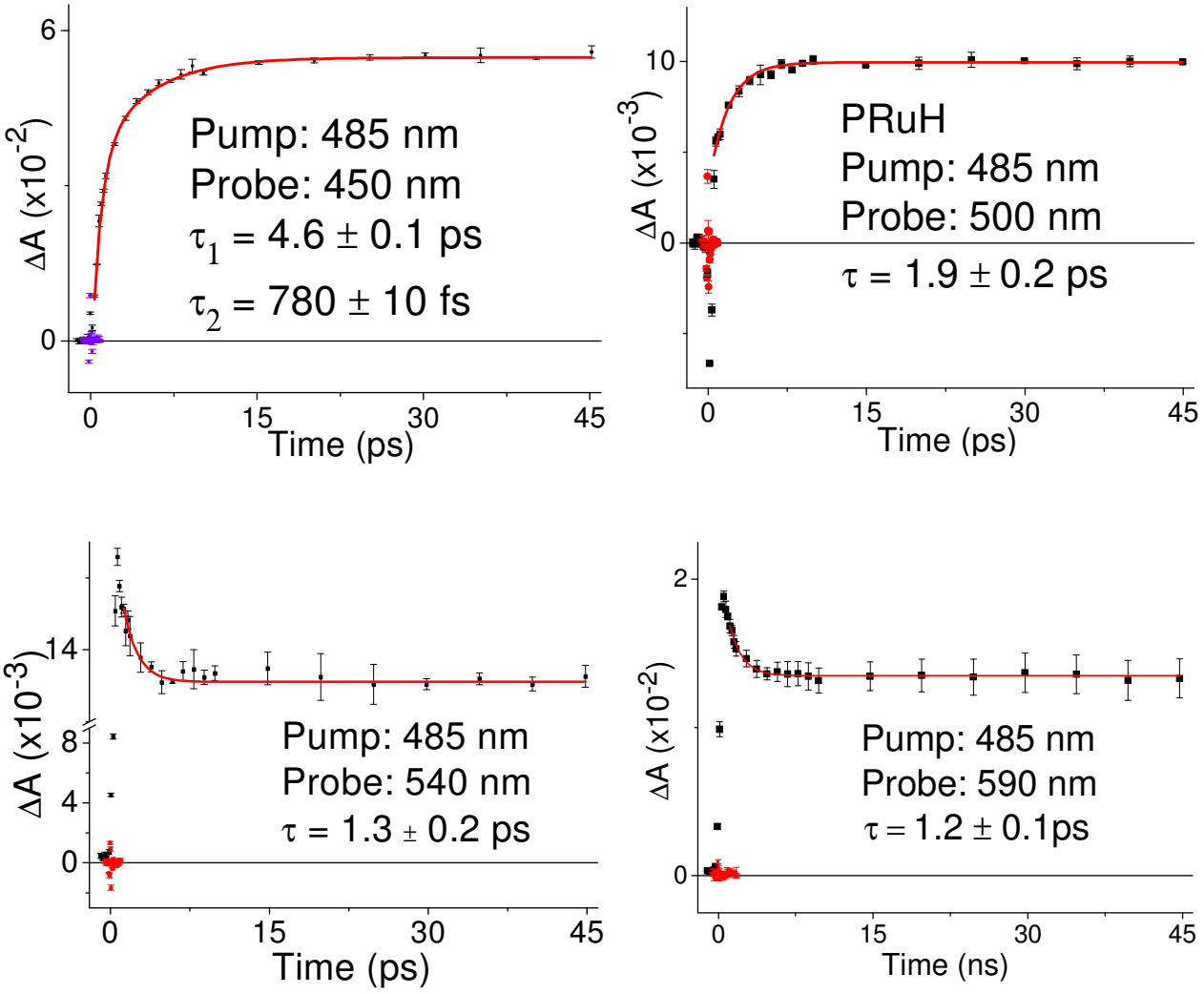

*Figure 4-14. Femtosecond transient absorption: Early time single wavelength dynamics for dyad **1** following 485 nm excitation.*

Now that the electron transfer (charge separation) rate is established, the identity of the native high-energy Ru(II) state can be better evaluated., Given the high quantum yield of the T state within the first few picoseconds, if the ^{1}MLCT state is the donor of the transferred electron then the electron transfer rate needs to be much faster than $(100\ fs)^{-1}$ in order for it to compete with the spin-flip process of the ^{1}MLCT. This rate has been assigned as sub-100 fs in the similar $[Ru(bpy)_3]^{2+}$ system for hot ^{1}MLCT-to-^{3}MLCT intersystem crossing[15]. The 780 fs process tentatively assigned as CS state formation certainly does not support this assumption.

Alternatively, if the electron transfer occurs out of the hot ^{3}MLCT state, following the intersystem crossing mentioned above, the coupling between these triplet states can be expected to be quite large, consistent with the sub-picosecond electron transfer rate. The competing process in this model will be the relaxation of the hot ^{3}MLCT state involving both solvent reorientation and vibrational cooling, which are typically on the order of 1-10 ps. These slower rates leave the ^{3}MLCT relaxation dominated by the 780 fs electron transfer process, resulting in the high quantum yield of the T state.

As a summary of this section, all of the photophysical processes discussed for dyad **1** with 485nm excitation are shown below in Figure 4-15. Initial excitation of the ^{1}MLCT on Ru(II) quickly goes through a spin-flip process within the first 100 fs. The resulting hot ^{3}MLCT state has a significant amount of vibrational energy and strongly couples to the porphyrin component, facilitated by its close geometric distance to the porphyrin. This electronic coupling results in the population of a CS state with the radical anion

located on the proximal terpyridyl ligand and a radical cation located on the porphyrin ring. This charge separation event proceeds with an unprecedented rate of $(780\ fs)^{-1}$. The charge recombination process produces the T state of the porphyrin with a time constant of 4.6 ps. This CS state should be mostly triplet in character as it interacts strongly with the T state yet does not interact with S_1 state. While the majority of the T state population is established via this sequential electron transfer pathway following Ru(II) excitation at 485 nm, the residual porphyrin absorption also directly populates the S_1 state, which decays via the same energy transfer pathways as observed with 650 nm excitation. This S_1 lifetime, as compared to the porphyrin reference compound, suggests a Ru(II) quenching efficiency of approximately 50%, consistent with the quantum yield data. The magnitude of amplitude change at 450 nm is consistent with the approximate 20% initial available S_1 state as compared to the rise at 450 nm seen with 650 nm excitation.

While various evidence points to the validity of the electron transfer model proposed here, it would be ideal if this could be compared to a similar process in different system. Unfortunately, to the best of our knowledge, no previous reports of fast process of the same order of magnitude exist. Yet as discussed in the next section, the self consistency of this model is also supported by comparing to dyad **2** in a slightly different model (vide infra).

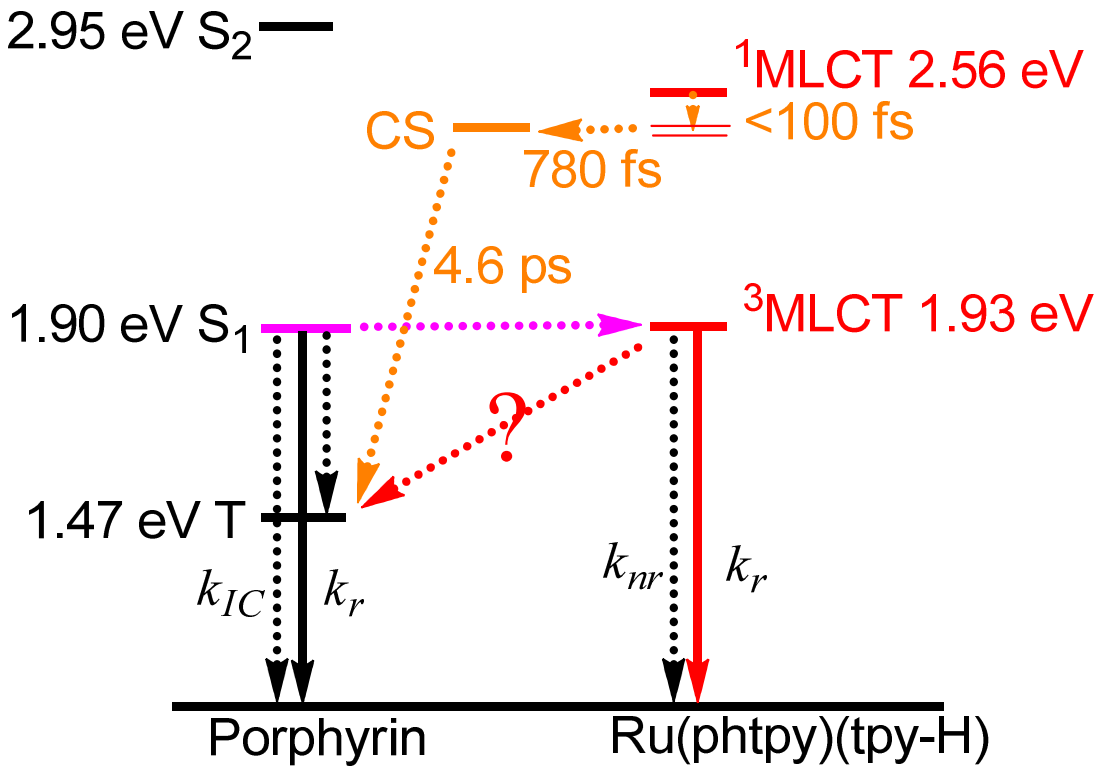

*Figure 4-15. Energy level diagram and dynamics for dyad **1**.*

4.3.3.3.2.3 *Role of peripheral terpyridyl ligand*

All above discussions omit the effect of the peripheral terpyridyl ligand. Since the absorption spectra of $[Ru(tpy)_2]^{2+}$ and $[Ru(Phtpy)_2]^{2+}$ are largely overlapped, the excitation of the Ru(II) component in the dyad **1** at 485 nm will in fact produce ^{1}MLCT states localized on both terpyridyl ligands. The unsubstituted terpyridyl-based ^{1}MLCT and ^{3}MLCT states were not discussed here because these states always lie energetically above the corresponding Phtpy-based states. The interligand electron transfer or electron randomization between these ligands should occur on a very competitive time scale, channeling the population to the Phtpy-based ^{3}MLCT state

before any other process can occur. Such a situation will be changed drastically if the peripheral ligand has a lower reduction potential and becomes a valid energy/electron acceptor. This effect will be discussed below in the context of dyad **2**.

4.3.3.4 *P-RuNO$_2$ dyad 2*

Considering the molecular structure of dyad **2**, the only difference with that of dyad **1** is the additional substitution on the backbone of the peripheral terpyridine. Since the peripheral ligand in dyad **1** was not obviously involved in any dynamics observed, all reactivities were associated with the rest of the molecule, which is present in its entirety in dyad **2**. Therefore, it is reasonable to assume that all pathways discussed above for **1** exist in dyad **2** as well. Thus, for the purpose of simplicity, dyad **1** will be used as the reference to model the interactions of the porphyrin and the proximal terpyridine, while additional processes associated with the peripheral nitrophenyl substituted ligand will be addressed separately. In other words, in studying dyad **2**, I base the interpretations on the energy level diagram derived for dyad **1** in Figure 4-15 and bring in modifications as needed. Any differences shall have their roots in the presence of the peripheral substitution.

Studies on the reference complex **C2** suggest a small enough inter-ligand electronic communication which slowed down the interligand electron transfer to the extent that it could be detected and identified with a time constant of 75 ± 25 ps (see Chapter 3). This

suggests that a separate treatment of the two terpyridyl ligand is appropriate when considering dynamic processes on the same or shorter time scales.

4.3.3.4.1 Exclusive Excitation of porphyrin component at 650nm:

4.3.3.4.1.1 *Quenching of S_1 state*

Steady-state and time-resolved luminescence spectroscopy: The steady-state emission data suggest that the energy of the porphyrin emissive S_1 state in dyad **2** is almost identical to that of dyad **1**. However, the quantum yield is much lower, $\Phi^{650}_{\mathbf{2}}$=0.0077, at approximately 16% of the reference porphyrin and approximately 31% of dyad **1**. The lifetime of the S_1 state was measured by time-resolved luminescence to be 2.0 ± 0.2 ns, representing an 80% quenching efficiency which is consistent with the quantum yield data (Figure 4-16). The quenching rate constant can be calculated from the inverse of the difference in S_1 lifetimes in dyads **2** and **1** according to equation (1); this results in a value of $(4.1\ ns)^{-1}$. Since the Ru moiety directly connected to the porphyrin is the same in both dyads, this quenching could only be attributed to the presence of the remote ligand. Three possible explanations exist for this increase in the quenching efficiency: 1) the increased S_1-to-$MLCT^{Ph}$ energy transfer; 2) the additional energy transfer pathway to the $^3MLCT^{NO_2Ph}$ state; 3) the additional electron transfer pathway to form a charge-separated state localized on the peripheral ligand, *i.e.* CS^{NO_2Ph}.

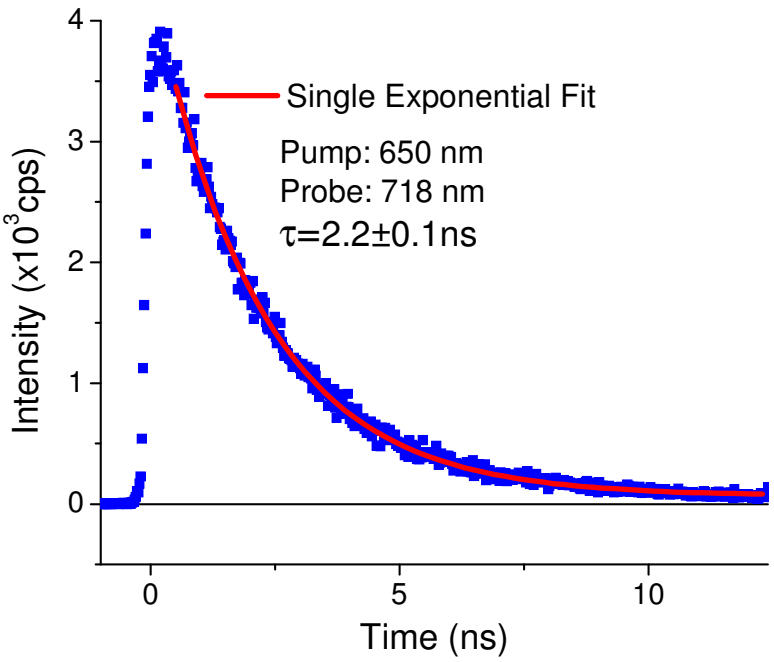

*Figure 4-16. Time-resolved luminescence measurement on dyad **2** following 650 nm excitation.*

The possibility of the first pathway being the dominating mechanism is low, when considering a driving force argument: since the nitrophenyl substituent pushes the oxidation potential of the Ru (III/II) couple up while leaving the reduction potential of the Phtpy ligand relatively unchanged, the energy of the $^3MLCT^{Ph}$ state should be slightly higher than that in dyad **1**, suggesting a slower rate. Differentiating between the latter two mechanisms is not as straightforward. An estimate of the rate of pathway (2) based on the comparison with the S_1-to-$^3MLCT^{Ph}$ process in dyad **1** was not successful. On one hand, the 120 mV larger driving force predicts a larger quenching rate, yet the larger donor-acceptor distance suggests otherwise. It is the competition between these

factors that determines the actual rate of energy transfer. However, a qualitative comparison between pathway (2) and (3) can be performed. The pathway (2) involves a Dexter-type two electron swap mechanism where one electron travels from the porphyrin to the periphery NO_2Phtpy, while a second electron goes from the Ru metal center to the porphyrin component at the same time. Pathway (3) involves only the first electron transfer step. Taking the typical reorganization energy of 1 eV for electron transfer and 0.14 eV[13] for energy transfer, the ratio between k/V^2 can be calculated from the equation

$$k=\frac{2\pi}{\hbar}V^2\frac{1}{\sqrt{4\pi k_B T\lambda}}exp\left(-\frac{\Delta G^{\neq}}{k_B T}\right) \quad (2)$$

$$\Delta G^{\neq}=\frac{(\Delta G^0+\lambda)^2}{4\lambda} \quad (3)$$

where V is the electronic coupling matrix element, $\Delta G^{\neq}$ is the activation energy, λ is the reorganization energy, and ΔG^0 is the free energy change for the process. The ratio is found to be 2.5, favoring electron transfer. Since Dexter energy transfer is an intrinsically two-electron simultaneous transfer mechanism, the electronic coupling matrix element V can be expected to be much smaller than that of electron transfer between the same donor-acceptor couple. Therefore, both pieces of evidence point to a larger contribution from pathway (3) than that from pathway (2). Using the lower limit of the rate difference of 2.5 fold, it can be estimated that electron transfer should account for at least 75% of the $(4.1\ ns)^{-1}$ quenching rate derived above.

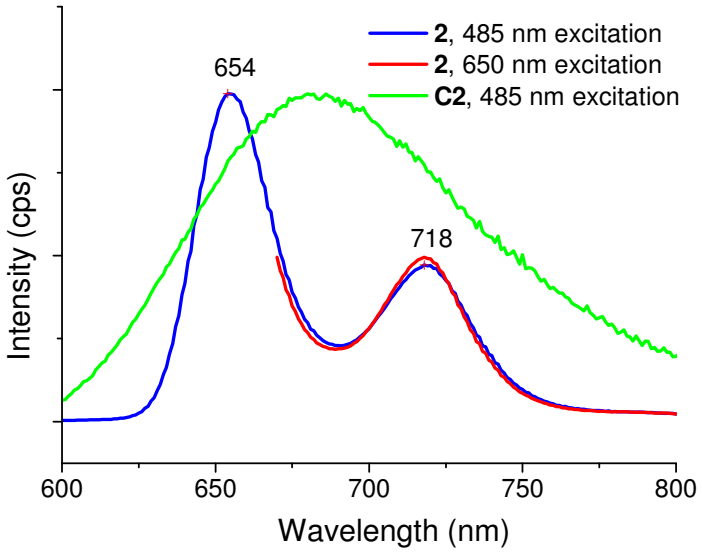

*Figure 4-17. Emission profiles for dyad **2** at different excitation wavelengths normalized to the intensity at 718 nm, as well as that of **C2** scaled up by a factor of 200. The ratio between emission intensities of P:Ru following 485 nm excitation at 610 nm is approximately 10:1; and that at 718 nm is approximately120:1.*

4.3.3.4.1.2 *Formation of T state*

Transient absorption spectra: The only species present on the timescale sensitive to our nanosecond TA setup is the porphyrin T state, which is identical to that in dyad **1** as well as the porphyrin reference, consistent with the expectation that all dynamic processes are completed within the first 10 ns. The lifetime of this state was found to be 100 ± 30 μs, which is within experimental error to the values found for dyad **1** and the porphyrin; this suggests a small, if any, heavy atom effect. In femtosecond TA spectra, the overall spectral shape of dyad **2** is quite similar to that of dyad **1**. However, the time evolution is completely different. The transition from the S_1 state to the T state exhibited a lifetime of 4.4 ns in dyad **1**; this same process was found to have a time constant of

1.8 ± 0.2 ns in dyad **2**. This dynamic was observed at 450 nm, 530 nm, and 570 nm. It is consistent with S_1 lifetime of 2 ns measured by TCSPC.

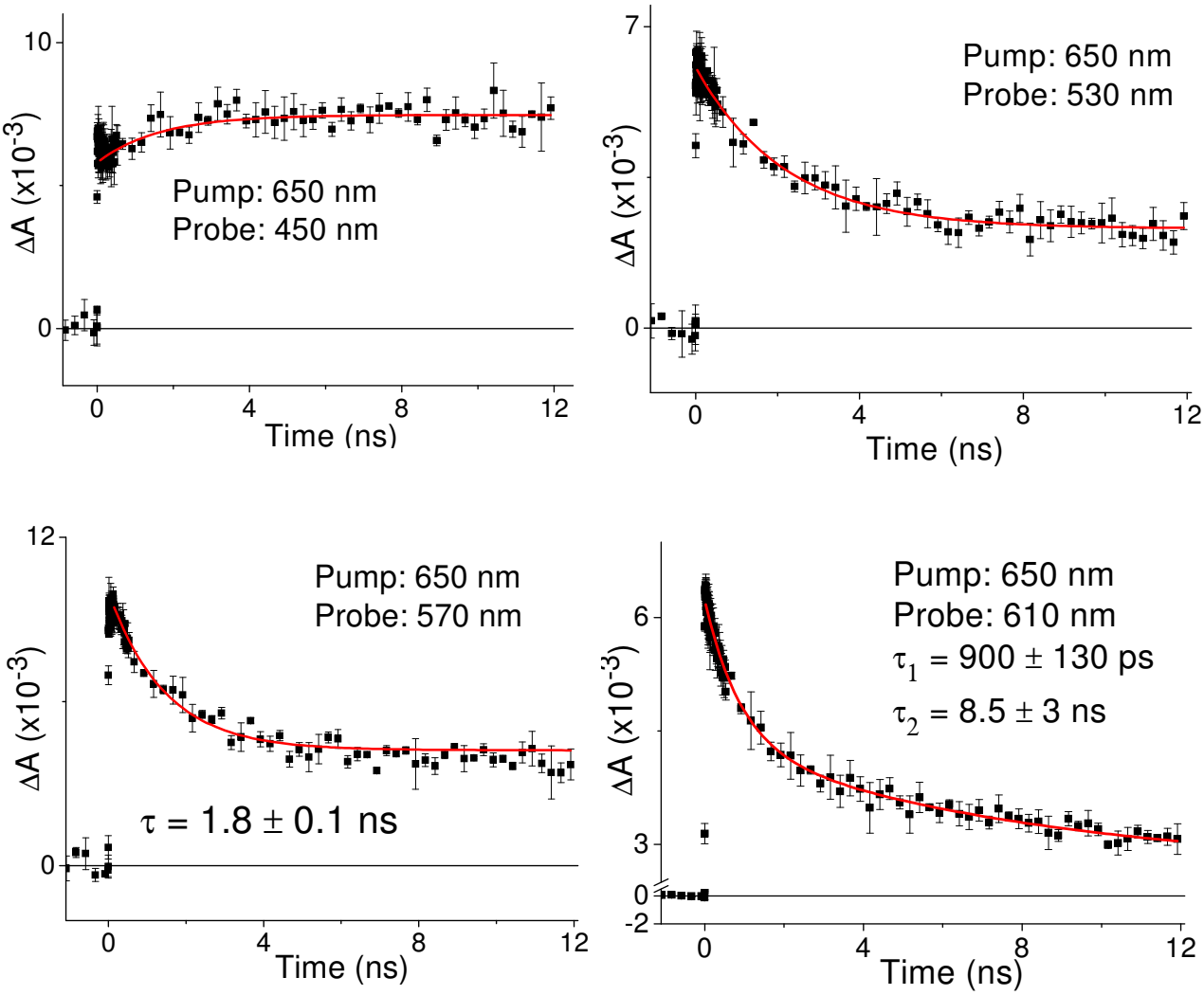

*Figure 4-18. Femtosecond transient absorption: Single wavelength dynamics for dyad **2** following 650 nm excitation.*

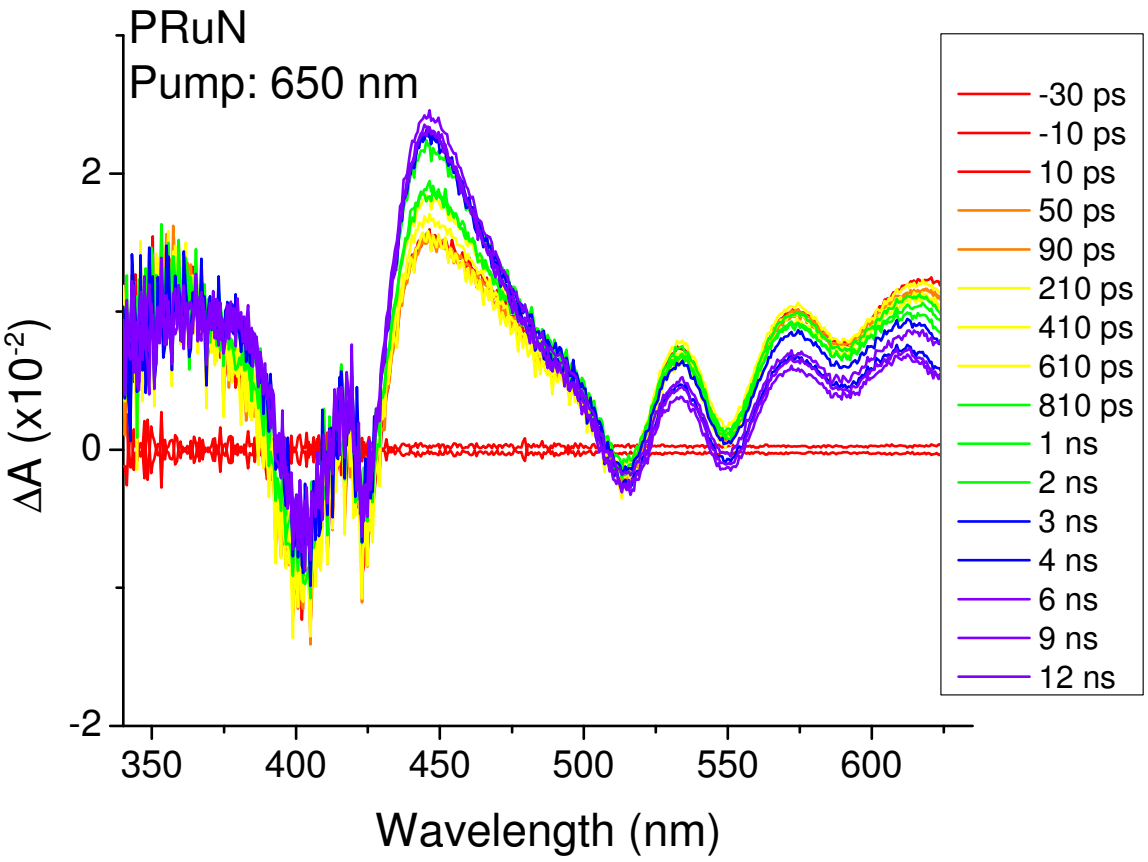

*Figure 4-19. Femtosecond transient absorption spectra of dyad **2** with 650 nm excitation. The sample was prepared in an acetonitrile solution with an absorbance of 0.15 in a flow cell connected to a peristaltic pump. The flow rate was set to be approximately 1 mL/s.*

From the data obtained at 610 nm, although noisy, it is reasonable to believe that a component much longer than 2 ns was present. This can be rationalized by the decay of the $^{3}MLCT^{NO2Ph}$ state formed from the S_1 state via the CS^{NO2Ph}, *i.e.* S_1-CS^{NO2Ph}-$^{3}MLCT^{NO2Ph}$. Similar to dyad **1**, there is no clean spectral evidence for the formation of the $^{3}MLCT^{Ph}$ state at 570 nm, 610 nm, or the 370 nm sensitive to the terpy radical anion, presumably due to its transient nature and a small ΔA change.

In summary of this section, the excited state evolution of dyad **2** following 650 nm excitation was very similar to that of dyad **1**, however, with a new electron transfer pathway with a time constant close to 4.1 ns. In addition to the presence of the $^3MLCT^{Ph}$ state as found in dyad **1**, a second Ru-based $^3MLCT^{NO2Ph}$ state was identified in the femtosecond TA spectra, which was populated via the S_1-CS^{NO2Ph}-$^3MLCT^{NO2Ph}$ pathway.

4.3.3.4.2 Simultaneous excitation of Ru and porphyrin components at 485 nm:

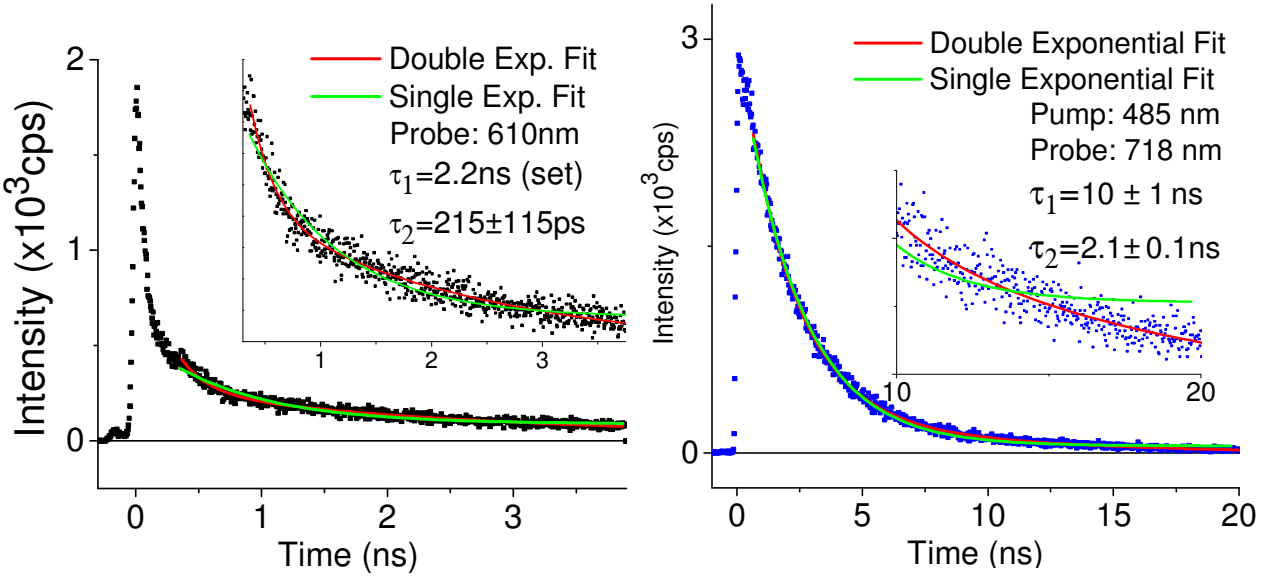

*Figure 4-20 TCSPC data for dyad **2** following 485 nm excitation.*

Similar to dyad **1**, the ratio of extinction coefficients of the two components following excitation at 485 nm are 5.5:1, favoring Ru component. The quantum yield of the observed emission ($\Phi^{485}_{\mathbf{2}}$=0.0016), when corrected with the porphyrin contributions at 485 nm, is identical to that observed when excited at 650 nm ($\Phi^{650}_{\mathbf{2}}$=0.0077). No Ru

peak was identified on the excitation spectrum probing at the S_1 state emission wavelength; thus, there is no Ru-to-S_1 conversion.

Following the 485 nm excitation, TCSPC gave the same approximately 2 ns lifetime as seen at the 650 nm excitation wavelength, although two more components were identified via the probe wavelength dependence study discussed above. An additional shorter component could be detected at 610 nm. A double exponential fit gave a value of 215 ± 115 ps, however, this number may have already been limited by the instrumental response, and hence not be reliable. The additional longer component observed at 718 nm could be fit to approximately a 10 ns lifetime. This longer component was assigned to the $^3MLCT^{NO2Ph}$ state which is consistent with that suggested by 650 nm excitation results. Since Ru is the dominant chromophore at 485 nm excitation, these data do not provide insights to the S_1-to-Ru pathways. However, the invariant $^3MLCT^{NO2Ph}$ lifetime as compared to the **C2** reference complex strongly supports the previous assumption of small electronic coupling between this peripheral ligand with the porphyrin component, hence minimal S_1-to-$^3MLCT^{NO2Ph}$ energy transfer. For the proximate $^3MLCT^{Ph}$ state, a competition exists between energy transfer, electron transfer to the porphyrin, as well as the interligand electron transfer to the peripheral ligand. A somewhat similar yet less complicated situation was observed in an Os-contained dyad studied by Bennison et al.[16], where it was found that interligand electron transfer can compete, when sufficient driving force is present, with energy transfer.

4.3.3.4.2.1 *Fast formation of T state: Sequential intercomponent electron transfer processes*

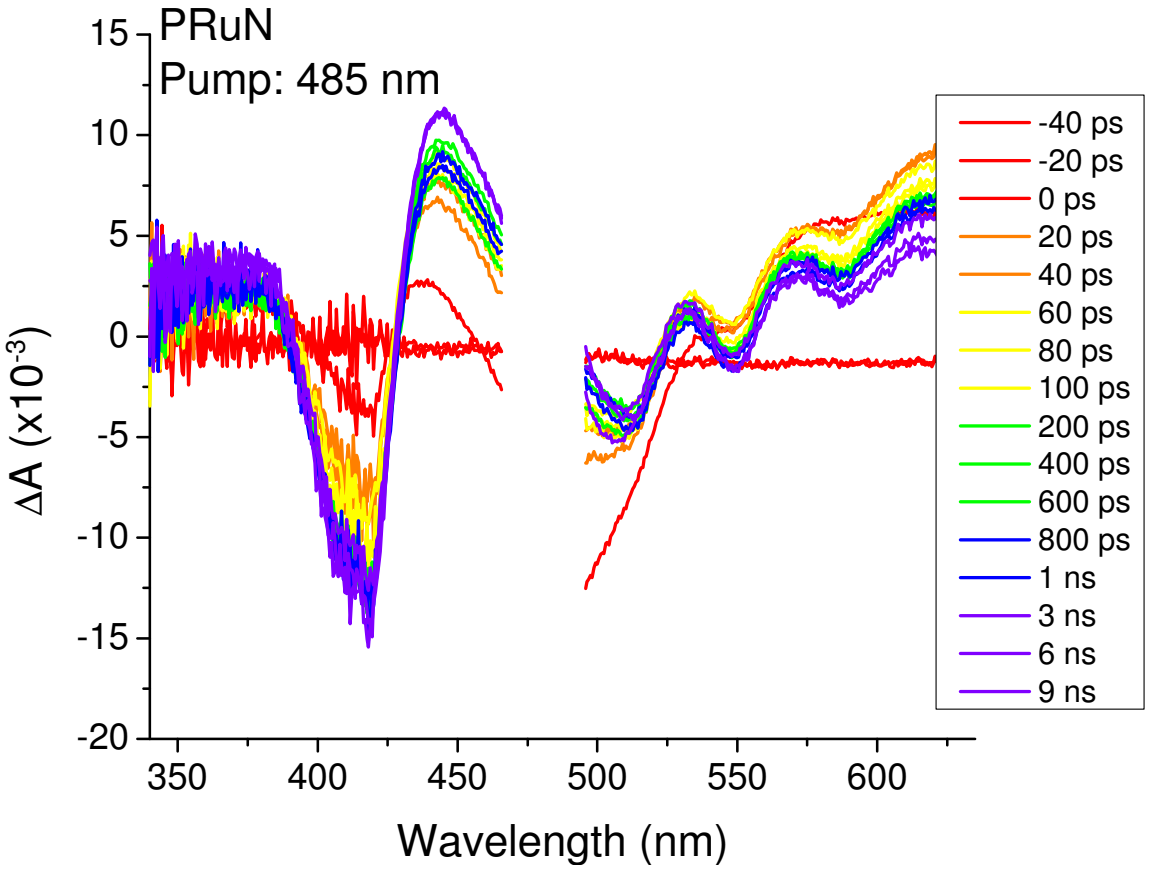

*Figure 4-21. Femtosecond transient absorption spectra of dyad **2** with 650 nm excitation. The sample was prepared in an acetonitrile solution with an absorbance of 0.15 in a flow cell connected to a peristaltic pump. The flow rate was set to approximately 1 mL/s.*

Transient Absorption spectra following 485 nm excitation: Following 485 nm excitation, nanosecond TA spectra gave a lifetime of 100 ± 20 μs, again supporting a small heavy atom effect. In the femtosecond spectra, a Ru-based bleach is present

immediately following the excitation, assigned to the Ru ^{1}MLCT state, and evolves to the T state of porphyrin within a few tens of picoseconds. Single wavelength dynamics at 450 nm yielded a lifetime of 70 ± 15 ps for this process. This spectral profile change is very similar to the CS^{Ph}-to-T transition observed in dyad **1**. Yet it cannot be associated with the same CS^{Ph} state due to the significantly smaller rate. As the CS^{NO2Ph} state exists close in energy, the most reasonable assignment is the CS^{NO2Ph}-to-T transition, which is expected to possess very similar profile change.

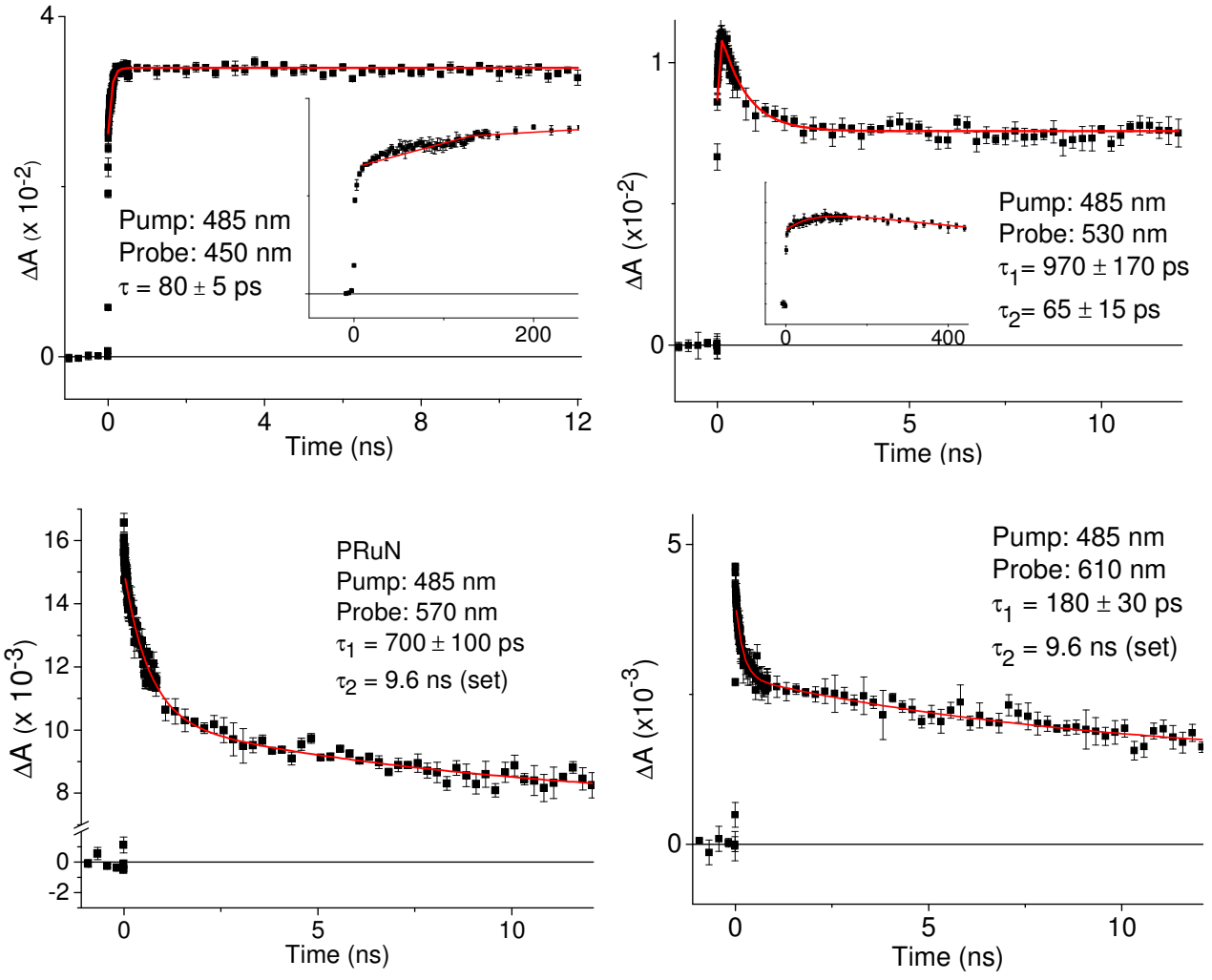

*Figure 4-22. Femtosecond transient absorption: Single wavelength dynamics for dyad **2** following 485 nm excitation.*

The fact that no CS^{Ph} state is populated to any significant extent can be explained by the availability of a lower lying $^1MLCT^{NO2Ph}$ state from the initial $^1MLCT^{Ph}$ state, which, via hot interligand electron transfer (ILET), quickly directs the electron to the periphery of the molecule, and converts into the $^3MLCT^{NO2Ph}$ state. The reasonably significant 10 ns Ru feature observed in both TCSPC and transient absorption spectra are strong support for this pathway.

While the peak at 450 nm stays invariant after the first 100 ps, the features in the red region show additional dynamics. At 530 nm, on top of the short component of 70 ps, an additional 970 ± 170 ps component is present. This time constant cannot be associated with any process originating from the $^3MLCT^{NO2Ph}$ state as that negates the possibility of seeing the ~10 ns intrinsic lifetime of that component. It is tentatively assigned to the CS^{NO2Ph}-to-$^3MLCT^{NO2Ph}$ process. At both 570 nm and 610 nm, in addition to the ~10 ns component of $^3MLCT^{NO2Ph}$, a shorter component also exists at both wavelengths although with different time constants, *i.e.* 700 ps at 570 nm and 180 ps at 610 nm. The same long component pollution argument can be invoked here to explain these coexisting multiple time constants: two distinct processes are actually present with time constants of 970 ps and 70 ps; while at 530 nm, the sign for ΔA is opposite in these two components, allowing for clear separations between these two components, the differentiation at the redder wavelengths where they exhibit the same sign of ΔA is much more difficult. Therefore, these two components may appear as an average of the long and short components due to limited resolution. Depending on the relative magnitude of

the ΔA associated with these two processes at different wavelengths, the average could be expected either to possess a bigger contribution from the 70 ps, leading to an observed shorter lifetime (*i.e.* 180 ps), or from the 970 ps, leading to the observed longer lifetime (*i.e.* 700 ps).

The formation of this CS^{NO2Ph} state should be faster than 80 ps in order for the T-forming step to not be limited by this rate. As mentioned earlier, it could not be due to a hole transfer from the $^{3}MLCT^{NO2Ph}$ state, as this results in strong quenching in the 10 ns lifetime of this state. It therefore is most likely due to a $^{3}MLCT^{Ph}$-to-CS^{NO2Ph} process which involves a simultaneous Ru-to-porphyrin hole transfer as well as an interligand electron transfer, much like a Dexter energy transfer mechanism. As the intrinsic ILET process pathway is still present, the decay of the $^{3}MLCT^{Ph}$ state should have a combined rate constant of both pathways, leading to a lifetime shorter than 40 ps; this is consistent with the IRF-limited short component observed in TCSPC.

These charge separation and recombination rates were much slower than that in the dyad **1**, 780 fs and 4.6 ps, respectively. This can be explained by the localization effect of the radical anion. Since the electron was localized on the periphery of the molecule in dyad **2**, the electronic coupling with the porphyrin component was much smaller than that present in dyad **1**. Because the electron transfer rate scales with the square of the electronic coupling matrix element, a much slower charge separation process can be expected. The charge recombination rate was slow presumably for the same reason.

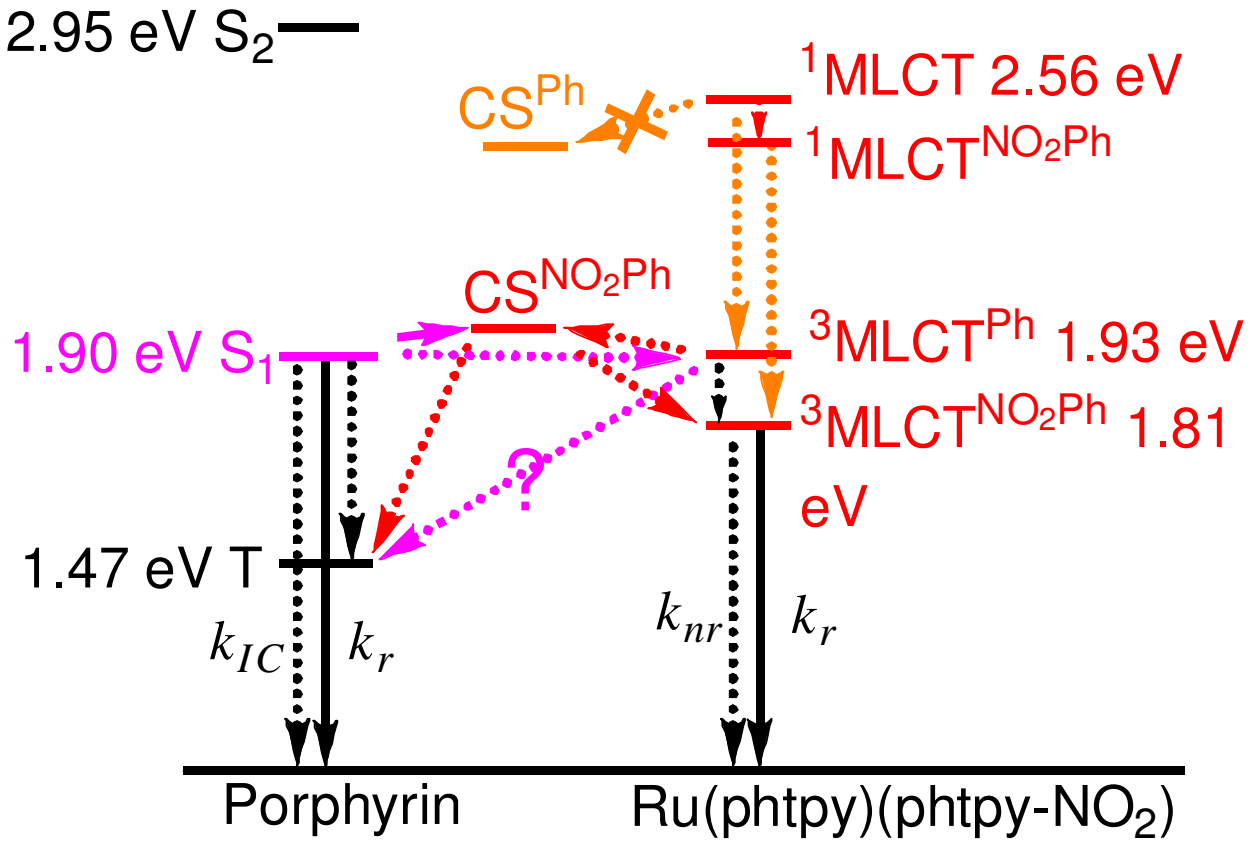

*Figure 4-23. Energy level diagram and dynamics for dyad **2**.*

4.3.3.4.3 Formation pathways of T state: A comparison between dyad 1 and 2.

It is interesting to compare the 485 nm excitation / 450 nm probe data between dyads **1** and **2**. Although neither S_1 state was produced from Ru absorption, there is a clear rise in dyad **1** associated with the S_1-to-T conversion as a result of residual porphyrin absorption. Such a rise is not present in dyad **2**. Considering the fact that the extinction coefficient ratios between the porphyrin and Ru components at 485 nm are very close in both dyads, this comparison suggests that a very small fraction of the T state formed in dyad **2** has its rate limited by the lifetime of S_1 state, leading to a

negligible change in ΔA for the T-forming step. This is consistent with the presence of the S_1-to-CS^{NO_2Ph} pathway. Since any molecules that end up in the CS^{NO_2Ph} state do not maintain a memory as to where they came from, this pathway in effect drains the population of S_1 state without asserting a dynamic consequence on the decaying processes thereafter. In this picture, only the intrinsic intersystem crossing on the porphyrin ring will have the $(2.0\ ns)^{-1}$ formation rate, which accounts for only *ca.* 4% of the total excited state produced, and thus the negligible change in ΔA for this process. This same percentage for dyad **1** shall be in the range of 10% to 20% depending on the branching ratios between decay pathways.

4.3.3.4.4 Accessibility of the CS state

While the CS^{NO_2Ph} is situated close to both the S_1 and the $^3MLCT^{Ph}$ states, the efficiencies of electron transfer from the two states were enormously different. Comparing the electron transfer rate from the S_1 state to the CS^{NO_2Ph} state versus that from the $^3MLCT^{Ph}$ state to the CS^{NO_2Ph} state, the latter is at least *ca.* 50 times larger, based on the upper limit of the $(4.1\ ns)^{-1}$ for the first process and the lower limit of $(80\ ps)^{-1}$ for the second process. Based on a calculation with the non-radiative decay rate equations (2) and (3), the 0.03 eV less negative driving force for the latter could only account for a *ca.* 2-fold increase in rate. To explain such a much larger difference, a spin-restriction argument can be invoked here, similar to that in dyad **1**: since this CS^{NO_2Ph} state is expected to be mostly triplet in nature, due to its lower energy, its

electronic coupling with triplet states will be much stronger than that with singlet states, leading to a much faster rate. Probably more importantly, however, is the excessive amount of vibrational energy needed to be released as the initial ^{1}MLCT state starts to decay. This provides a sufficiently high driving force to overcome the energy barrier to form the charge-separated state and also increases the charge separation rate. The initial excitation at 650 nm, on the other hand, puts the dyad in the porphyrin S_1 state without much vibrational energy. As the formation of the same CS state is slightly uphill and requires an electron transfer from the porphyrin to be transferred to the peripheral terpyridyl ligand, passing the proximal terpyridyl-based state *ca.* ~0.36 eV higher in energy, a much slower rate is not unexpected.

4.3.4. Photoinduced Chemical Processes in Dyads

Consideration of photostability. There have been no comments in the literature about the photostability issue of these porphyrin-Ru supramolecular complexes. In my own routine handling, storage, and characterizations of these dyads, including nanosecond time-resolved spectroscopic measurements, no indication of photolability is observed. However, the samples subjected to the femtosecond laser pulses suggested photodecomposition. In a static 1 mm path length air-free cuvette under normal conditions, the sample changed color from red-brown to brownish green following exposure to 485 nm laser beam for approximately 10 min. UV-Vis spectra before and after 485 nm laser spectroscopy show drastic changes to the spectra profiles, where

characteristic porphyrin radical anion features[17] at 490 nm and 756 nm were produced, and porphyrin soret band and Q bands diminished. These spectra gradually returned to genuine porphyrin features either when opened to air or over a prolonged period of time. The same setup used on both dyads as well as the plain porphyrin reference compound showed similar photoproducts, suggesting this phenomenon be not caused by the presence of the Ru component. The 650 nm laser exposure did not show significant changes with the same magnitude, yet a very small shoulder at 485 nm may be reminiscent of the start of a similar reduction process. Interestingly, the ESI-MS spectra before and after the laser exposure showed, within experimental error, identical sample compositions.

While photobleaching for porphyrin compounds is a known issue in the presence of oxygen, it is not likely to occur in our strictly controlled air-free atmosphere throughout the full length of characterization. However, as opposed to 1 cm path length cuvettes, we use a 1 mm path length cuvette that still requires an absorbance of 0.4 at the excitation wavelength in order to ensure a sufficient amount of excited state produced. This means that the concentration of the sample, *ca.* 0.5 mM for 650 nm excitation and 0.1 mM for 485 nm excitation, is 10 times larger than what is typically used for similar experiments with a laser beam in the picosecond or nanosecond domains. Further, the spot size we initially used was as tight as it could be, which may be smaller than common picosecond laser beams as well and potentially may lead to a higher power density. Both of these factors may contribute to unprecedented photobleaches.

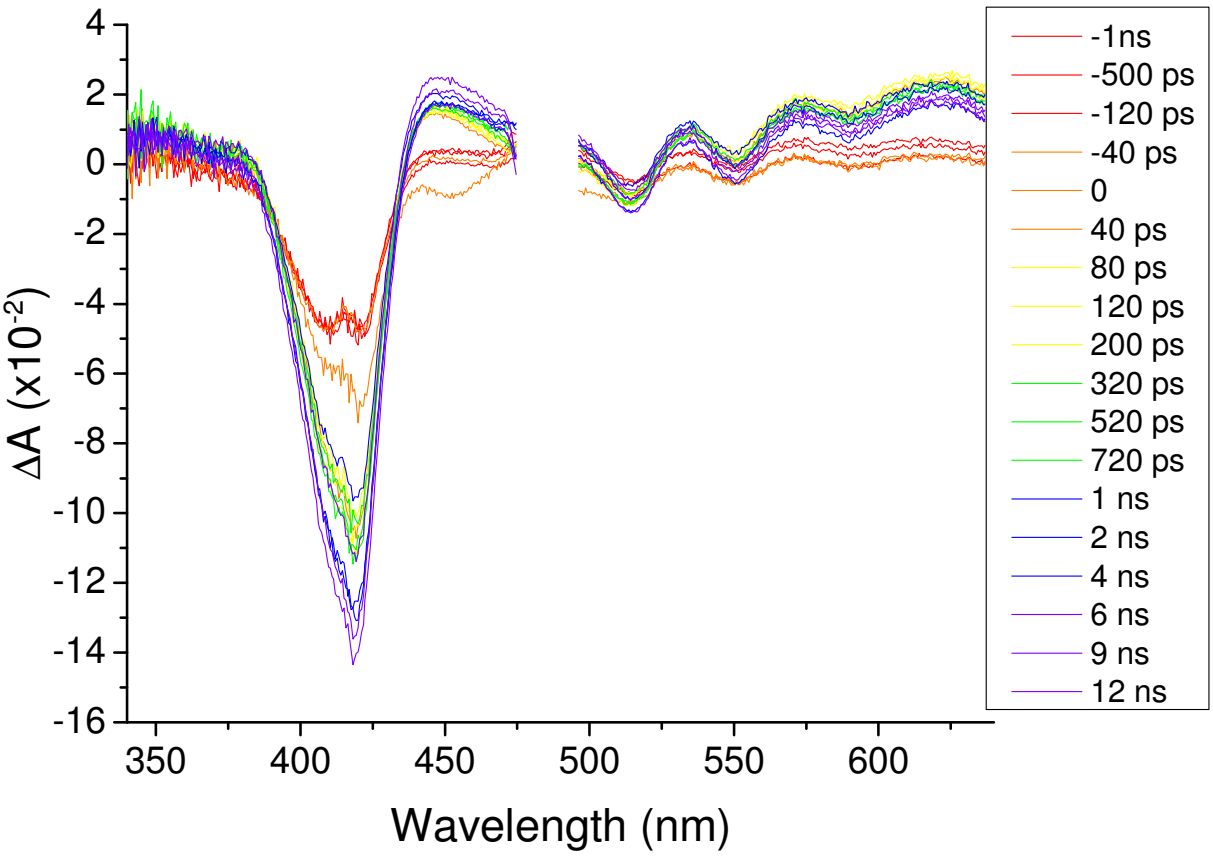

*Figure 4-24 Representative femtosecond TA for dyad **1** to illustrate the negative time abnormaly following excitation at 485 nm.*

One possible explanation to this abnormally observed is the intermolecular charge transfer product, *i.e.* Por^{+}-Por^{-}, produced following 485 nm excitation. This species recombines given enough relaxation time leading to self-restoration of the UV-Vis spectra, at which point it displays no permanent change in ESI-MS results. The fact that the only reduced porphyrin feature was observed in a UV-Vis spectrum for a sample in a static cell may be explained by a much smaller spectral feature of the porphyrin cation than the porphyrin anion. The fact that such a charge-separated state requires an

estimated energy input of approximately 2 eV from the redox chemistry data, suggests that 485 nm excitation beam will be a lot more efficient in inducing such changes than the 650 nm beam.

In order to prevent photobleaching, a single-flow setup was used where the sample solution passed the laser spot at a rate of *ca.* 0.003 mL/s. The slow rate is adopted because of the limited amount of sample available. Yet to ensure the flow rate is not an issue, a different circulating-flow set-up with a peristaltic pump was also used, where the flow rate was as high as 3 mL/s. This second setup ensured that each molecule sees laser light only once before it exits the laser spot. For both of these setups, no photobleaching was observed over the course of the femtosecond TA measurements following 485 nm excitation. However, some unexpected features (Figure 4-24) were present even before the pump and probe laser beams overlap to create and measure the excited state; since this occurred prior to time zero, it is referred to as *negative time*. Lowering the concentration of the sample to an absorbance between 0.15 to 0.20 results in a smaller magnitude of these negative time features, but does not completely remove them.

These odd negative time features also exist in the spectra following 650 nm excitation (Figure 4-25). However, due to the low I_0, the bleach at 420 nm can no longer be observed. The spectral profile at negative time seems to be jumping around the baseline, presumably due to the its changing amplitude on top of less than ideal laser signal stability. Comparing the magnitude of the negative time features to those at

positive time, the amplitude seems to in fact be larger at 650 nm excitation than that observed at 485 nm, consistent with the higher concentration (0.1 mM at 485 nm excitation *vs.* 0.5 mM at 650 nm excitation). The intensity of the amplitude does not scale linear with the concentration of the sample probably due to the higher excitation energy providing a larger driving force for such processes to occur.

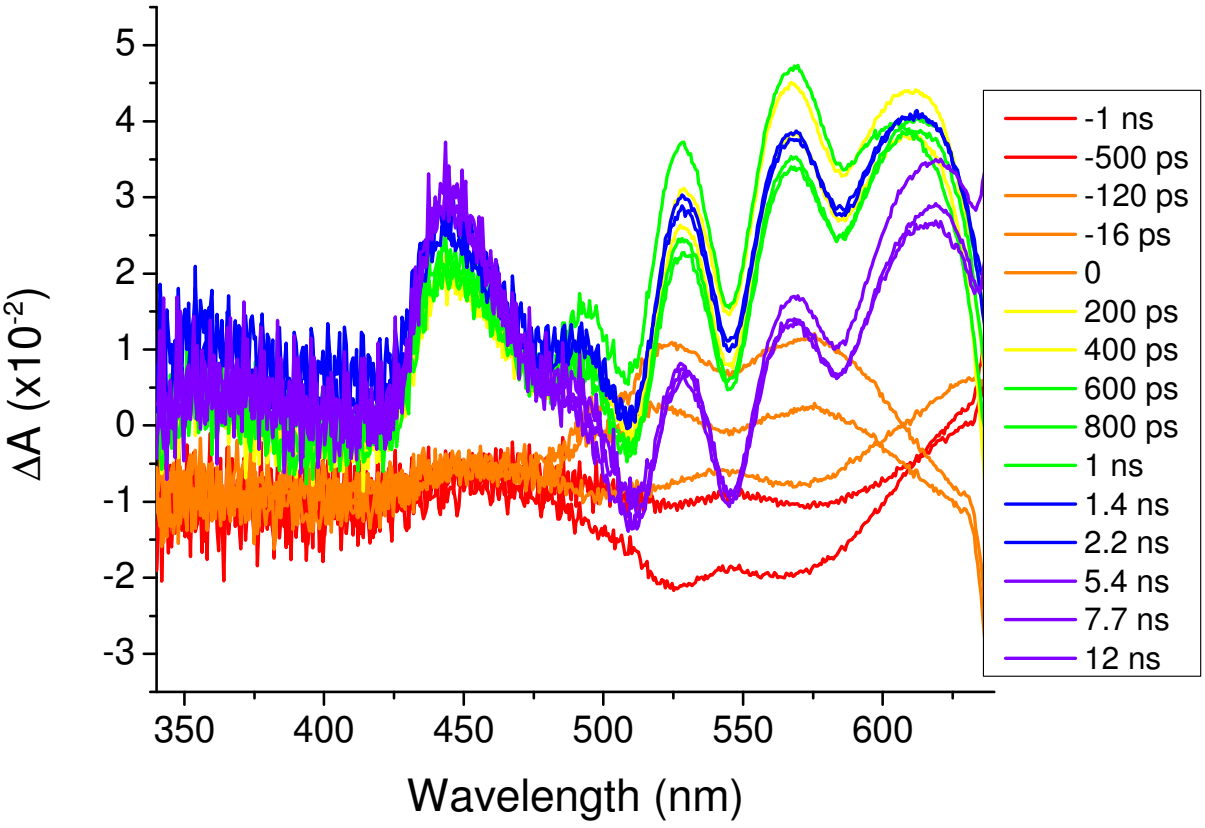

*Figure 4-25 Representative femtosecond TA for dyad **1** to illustrate the negative time abnormally following excitation at 650 nm.*

Such negative time features can only be explained by a very long-lived species with a lifetime beyond the laser pump intervals, which is approximately 1 ms in our setup. Since the triplet state of porphyrin lasts on the order of 100 μs (*vide infra*), it is not likely to be a result of that. It could be argued that there may be the same charge-transfer complex as discussed above, yet the amount was much smaller in these two setups and only showed up in the intrinsically more sensitive ΔA spectra. The absence of distinct features for the porphyrin radical anion, however, makes such a proposal less convincing.

An alternative explanation is the upconversion mechanism by triplet-triplet annihilation, which is also a high concentration-facilitated intermolecular process. A similar triplet-triplet annihilation was observed by Castellano and coworkers[18] in an anthracene-$Ru(bpy)_3$ system, where such an upconversion manifested as delayed fluorescence. The concentration at which triplet-triplet annihilation was observed was as low as 10 μM. Admittedly, the power of the laser Castellano used was much higher than this current investigation, although a spot size was not reported. Also the much longer lifetime of anthracene may relax the concentration requirement for these annihilation processes to occur, which may be needed for triplet states with shorter lifetimes (for example the T state discussed here). Nevertheless, this remains the most probable explanation for the photochemical reactivity observed. The supporting evidence for this proposal is the fact that the negative spectral traces observed at 485 nm excitation were in general agreement with the positive time profiles, although with reduced amplitudes

(Figure 4-24), which suggests the very long-lived species is S_1 in nature. This could only be produced as a photoproduct of triplet-triplet annihilation at such long time delays.

These features at negative times were not present when a larger pump beam spot size was used. This was attributed to the lowered peak power per unit area. Therefore, all femtosecond transient absorption data reported in the previous sections were performed with a larger, defocused spot size.

*Table 4-3 Lifetimes of different states involved in dyads **1** and **2**.*

Complex	States	τ, ns
1	^{3}MLCT	0.4 ± 0.1
	S_1	4.8 ± 0.4
	T	(130 ± 30) x 10^3
	CS^{Ph}	(4.6 ± 0.1) x 10^{-3}
2	$^3MLCT^{NO2Ph}$	10 ± 1
	$^3MLCT^{Ph}$	< 40 x 10^{-3}
	S_1	2.0 ± 0.2
	T	(100 ± 20) x 10^3
	CS^{NO2Ph}	< 80 x 10^{-3}

4.4. Conclusions and Comments

To conclude, I have hopefully demonstrated that these porphyrin-Ru bisterpyridyl complexes are very interesting systems with a plethora of photophysical and photochemical properties. The major excited states involved were listed in Table 4-3 along with their associated dynamic constants. Especially interesting is the fact that a simple substitution on the periphery of the system introduces a drastic change in the reactivity on the other end of the system. Low-energy charge transfer states are not the only states that can effectively quench the initial excited states, the much higher-in-energy charge-separated (CS) state can also play an important role in the early-time dynamics.

It is worthwhile to point out that the current study is not only meaningful for enhancing our fundamental knowledge in complicated biomimetic system as the one described in chapter 1; they are also critically important to provide guidance to the molecular system design and engineering in contemporary technological applications, like solar energy conversion[19] and molecular electronics[20]. For example, in terms of dye-sensitized solar cell (DSSC), porphyrin-ruthenium polypyridyl dyes can be superior to smaller molecular dyes in that they combine the large absorption cross-section and broad spectral coverage of porphyrin with the charge-transfer character of the Ru MLCT features.[21] Such an application requires an electron transfer pathway in a specifically defined direction, favorably from porphyrin to the semiconductor-bound ruthenium component in order to ensure the photoelectron moves in the desired direction. While

electron transfer in metalloporphyrin-transition metal supramolecules has been extensively studied[13, 14, 22-24], see Chapter 2 as a brief review, direct evidence for electron transfer in free-base porphyrin-Ru bisterpyridyl supramolecules has eluded researchers. There have been a few reports[24] where a charge-separated state (ET product) was invoked in order to better explain the spectroscopic results, yet no distinct spectral profile or dynamic process could be attributed to this specific species. The 780 fs and 4.6 ps components identified in dyad **1** are the first dynamic evidences for such charge-separated states.

Furthermore, within those limited number of literature examples[24] where the presence of CS state was inferred, the Ru component unanimously includes a ligand with either a significant electron-withdrawing substituent or strong delocalization effect, lowering the energy of charge-separated state sufficiently for it to be accessible from the lowest Ru-based ^{3}MLCT state. Yet from the viewpoint of energy conversion applications, such a significant lowering in potential reduces the energy content of the system and is an unwanted waste of energy. From an argument of driving forces, the ^{1}MLCT state formed immediately following the Ru(II) excitation typically has an energy close to 2.5 eV. This state could in principle populate most charge-separated states which are usually lower in energy in these porphyrin-Ru supramolecules. This *hot* electron transfer process was demonstrated in dyad **1** for the very first time and has significant meaning to the DSSC field. The studies on dyad **2** provided further insights into factors affecting the ET processes and their role in changing the overall reactivity.

Admittedly, these molecules may not be directly applicable in dye-sensitized solar cell due to the still fast back-electron transfer, they provided the first example to show such potential and the direction to look for such applications.

APPENDICES

APPENDIX A

Femtosecond TA of reference compound **C1**

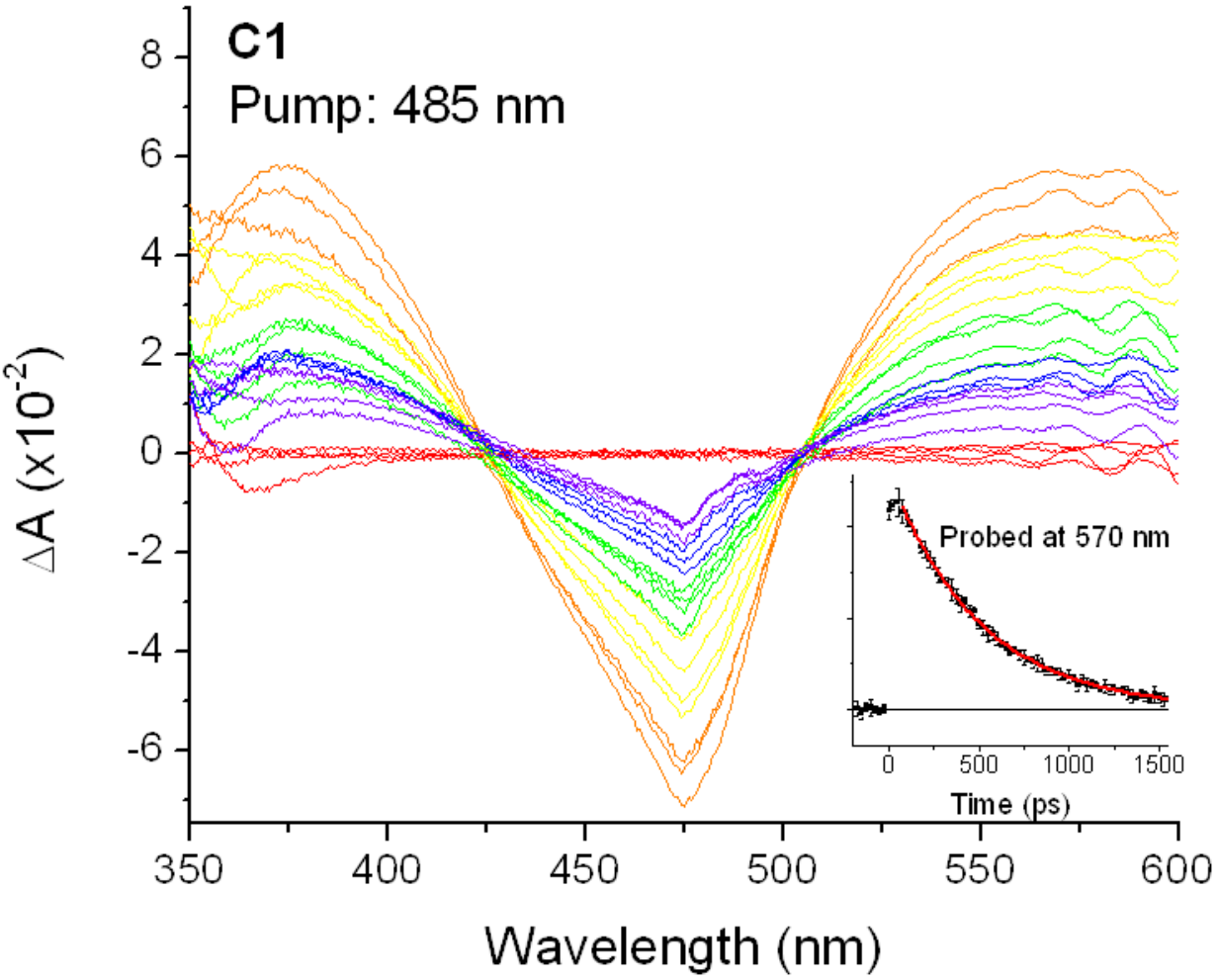

*Figure 4-26. Femtosecond TA of reference compound **C1**. The dynamic trace probed at 570 nm (inset) was fit to a single exponential decay model to be 505 ± 10 ps.*

APPENDIX B

ESI-MS of dyad **1**

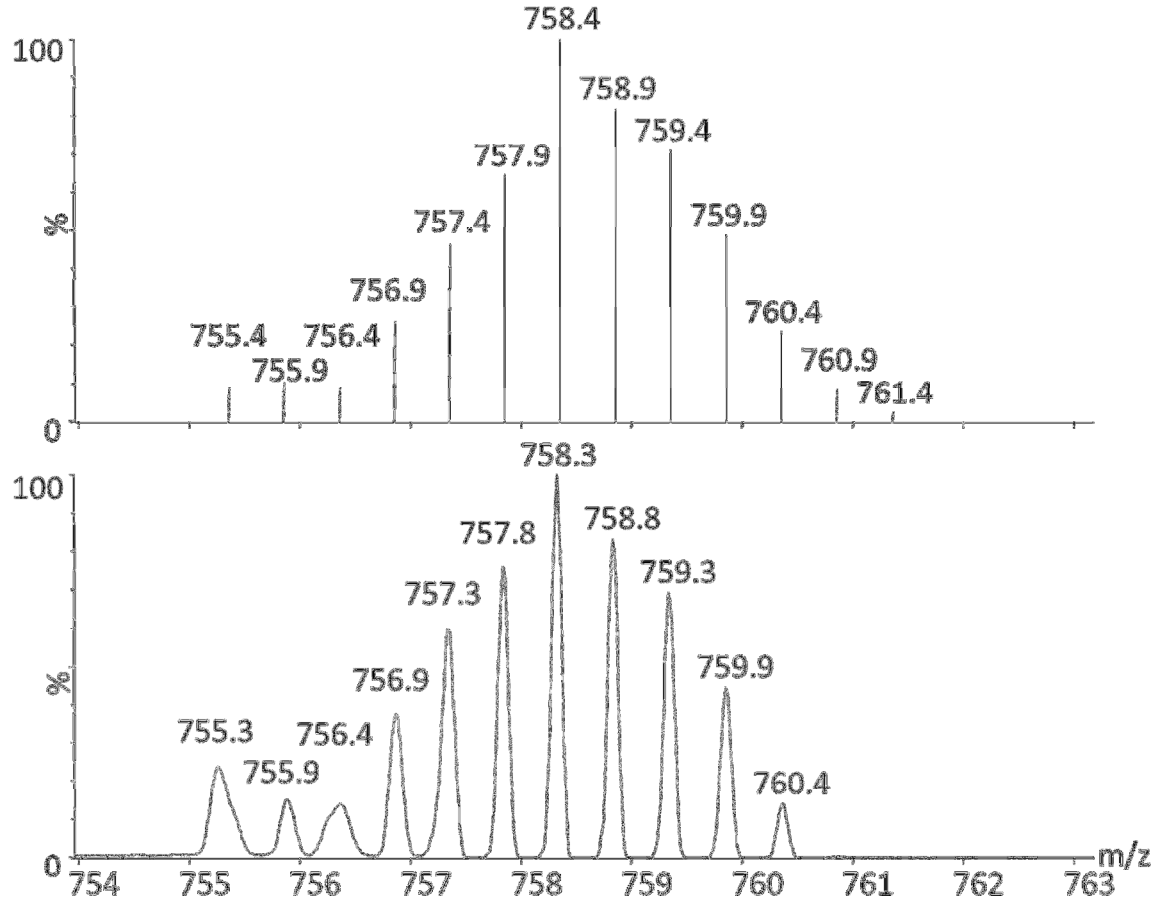

*Figure 4-27. ESI-MS of dyad **1**. The top panel shows the theoretical isotope pattern for molecular ion [**1**-2PF$_6$]$^{2+}$; the bottom panel shows experimental result obtained in acetonitrile solution.*

APPENDIX C

^{1}H NMR of dyad **1** and assignments

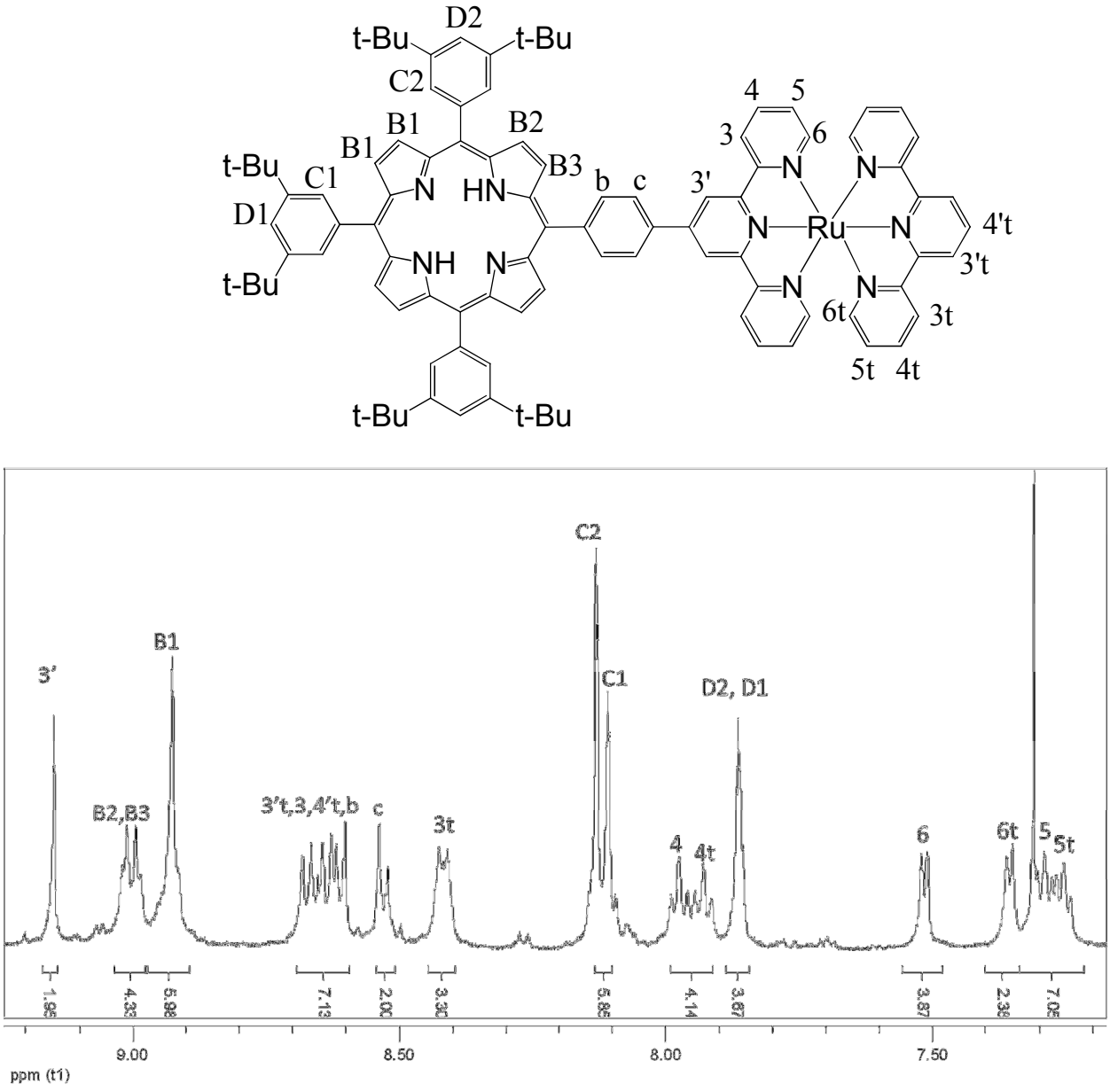

*Figure 4-28. ^{1}H NMR (aromatic region) of dyad **1** in CD_3CN. The top panel shows the labeling of the H atom positions; the bottom panel shows the spectrum along with peak assignments. Note aliphatic region was omitted for clarity purpose. See experimental section for details.*

APPENDIX D

ESI-MS of dyad **2**

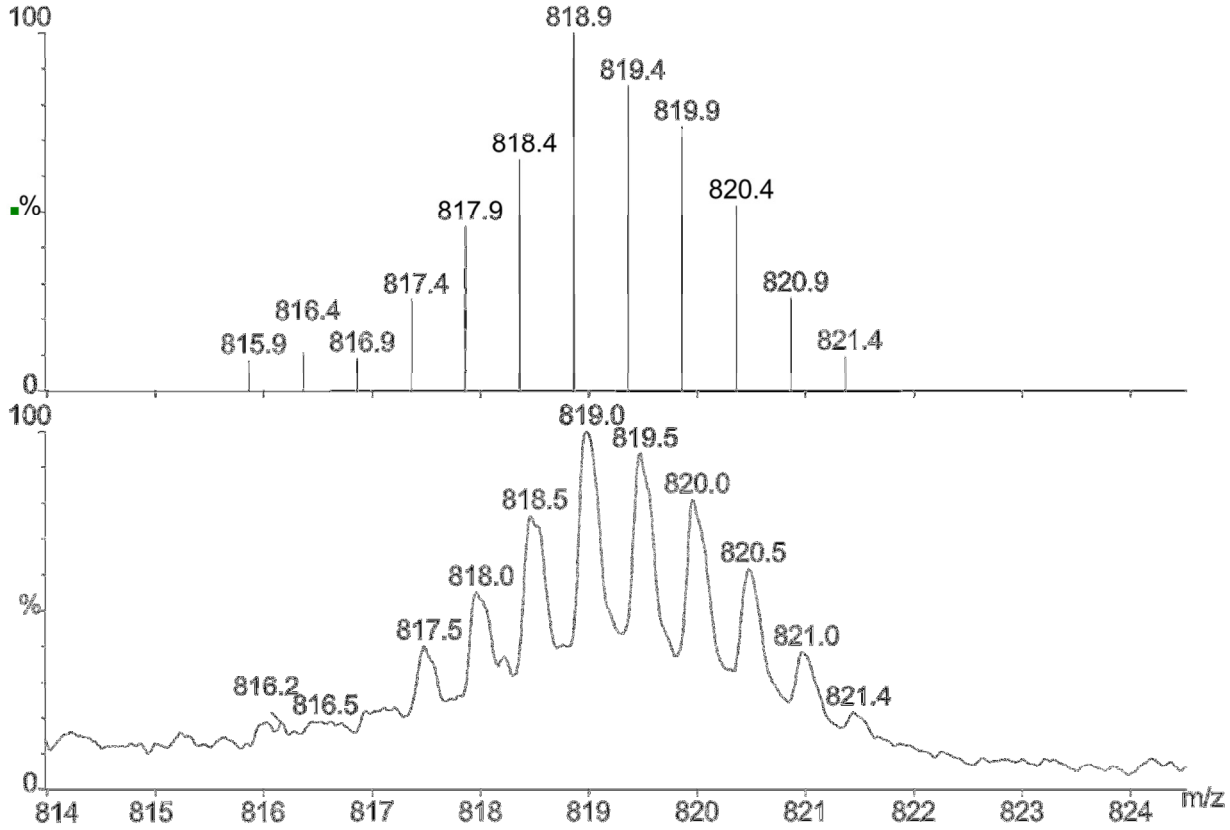

*Figure 4-29. ESI-MS of dyad **2**. The top panel shows the theoretical isotope pattern for molecular ion [**2**-2PF$_6$]$^{2+}$; the bottom panel shows experimental result obtained in acetonitrile solution.*

APPENDIX E

^{1}H NMR of dyad **2**

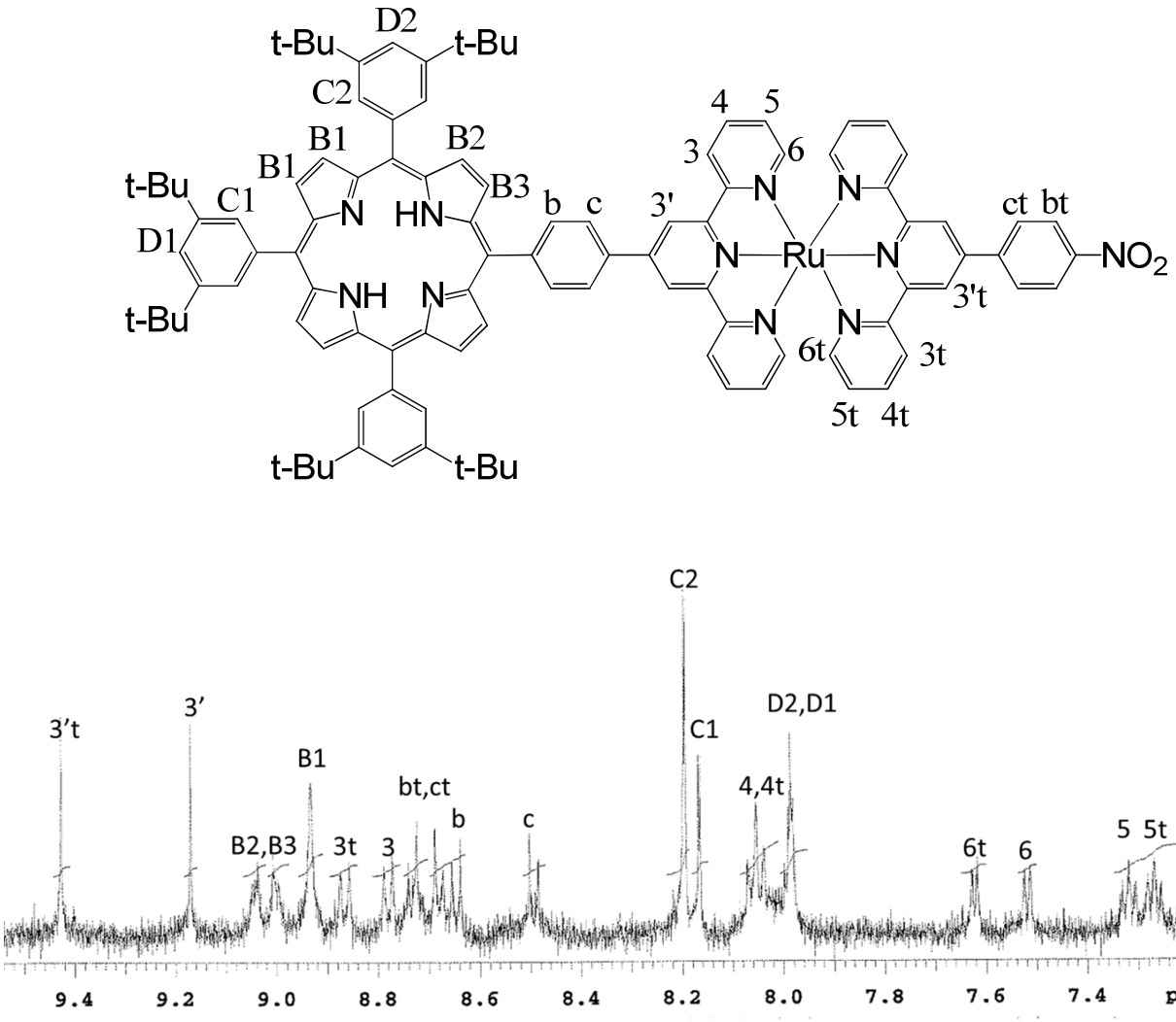

*Figure 4-30. ^{1}H NMR (aromatic region) of dyad **2** in CD_3CN. The top panel shows the labeling of the H atom positions; the bottom panel shows the spectrum along with peak assignments. Note aliphatic region was omitted for clarity purpose. See experimental section for details.*

REFERENCES

REFERENCES

[1] Constable, E. C.; Lewis, J.; Liptrot, M. C.; Raithby, P. R., *Inorganica Chimica Acta*, (1990) **178**, 47.

[2] Das, S.; Incarvito, C. D.; Crabtree, R. H.; Brudvig, G. W., *Science*, (2006) **312**, 1941.

[3] Metcalfe, C.; Spey, S.; Adams, H.; Thomas, J. A., *Journal of the Chemical Society, Dalton Transactions*, (2002), 4732.

[4] Newman, M. S.; Lee, L. F., *The Journal of Organic Chemistry*, (1972) **37**, 4468.

[5] Harriman, A.; Odobel, F.; Sauvage, J. P., *Journal of the American Chemical Society*, (1995) **117**, 9461.

[6] Damrauer, N. H.; Boussie, T. R.; Devenney, M.; McCusker, J. K., *Journal of the American Chemical Society*, (1997) **119**, 8253.

[7] Juban, E. A.; McCusker, J. K., *Journal of the American Chemical Society*, (2005) **127**, 6857.

[8] Pineiro, M.; Carvalho, A. L.; Pereira, M. M.; Gonsalves, A. M. d. A. R.; Arnaut, L. G.; Formosinho, S. J., *Chemistry – A European Journal*, (1998) **4**, 2299.

[9] Bonnett, R.; McGarvey, D. J.; Harriman, A.; Land, E. J.; Truscott, T. G.; Winfield, U. J., *Photochemistry and Photobiology*, (1988) **48**, 271.

[10] Dudkowiak, A.; Teslak, E.; Habdas, J., *Journal of Molecular Structure*, (2006) **792-793**, 93.

[11] Maestri, M.; Armaroli, N.; Balzani, V.; Constable, E. C.; Thompson, A. M. W. C., *Inorganic Chemistry*, (1995) **34**, 2759.

[12] Telfer, S. G.; McLean, T. M.; Waterland, M. R., *Dalton Transactions*, (2011) **40**, 3097.

[13] Benniston, A. C.; Harriman, A.; Pariani, C.; Sams, C. A., *Phys Chem Chem Phys*, (2006) **8**, 2051.

[14] Uyeda, H. T.; Zhao, Y. X.; Wostyn, K.; Asselberghs, I.; Clays, K.; Persoons, A.; Therien, M. J., *Journal of the American Chemical Society*, (2002) **124**, 13806.

[15] Cannizzo, A.; van Mourik, F.; Gawelda, W.; Zgrablic, G.; Bressler, C.; Chergui, M., *Angewandte Chemie International Edition*, (2006) **45**, 3174.

[16] Benniston, A. C.; Harriman, A.; Pariani, C.; Sams, C. A., *J Phys Chem A*, (2007) **111**, 8918.

[17] Araki, K.; Toma, H. E., *Journal of Photochemistry and Photobiology A: Chemistry*, (1994) **83**, 245.

[18] Kozlov, D. V.; Castellano, F. N., *Chemical Communications*, (2004), 2860.

[19] Nogueira, A. F.; Furtado, L. F. O.; Formiga, A. L. B.; Nakamura, M.; Araki, K.; Toma, H. E., *Inorganic Chemistry*, (2003) **43**, 396.

[20] Nemykin, V. N.; Barrett, C. D.; Hadt, R. G.; Subbotin, R. I.; Maximov, A. Y.; Polshin, E. V.; Koposov, A. Y., *Dalton Transactions*, (2007), 3378.

[21] Odobel, F.; Zabri, H., *Inorganic Chemistry*, (2005) **44**, 5600.

[22] Harriman, A.; Hissler, M.; Trompette, O.; Ziessel, R., *Journal of the American Chemical Society*, (1999) **121**, 2516.

[23] Flamigni, L.; Marconi, G.; Dixon, I. M.; Collin, J.-P.; Sauvage, J.-P., *The Journal of Physical Chemistry B*, (2002) **106**, 6663.

[24] Flamigni, L.; Armaroli, N.; Barigelletti, F.; Balzani, V.; Collin, J.-P.; et al., *Journal of Physical Chemistry B: Condensed Matter, Materials, Surfaces, Interfaces, & Biophysical Chemistry*, (1997) **101**, 5936

Chapter 5. Iron Porphyrin-Chromophore Dyad via Axial σ-bond Coordination: Alternative Binding Motifs and Chromophores

5.1. Introduction

For the purpose of realizing the global system design described in Chapter 1, the core problem from a synthetic perspective is the preparation of an $[Fe_4S_4\text{-}S\text{-}FeP]^{2-}$-chromophore triad. In view of the complexity involved in $[Fe_4S_4]$ cluster derivatizations, a chemistry-on-the-complex approach on $[Fe_4S_4\text{-}S\text{-}FeP]^{2-}$ to introduce the third component of chromophore can be expected to be difficult, if not impossible. The linkage between the iron porphyrin and the chromophore needs to be attained first. To this end, Chapter 4 described one way to obtain such a construct. The dyad obtained was reasonably stable when appropriate precautions were used. The photobleaching complication discussed at the end of Chapter 4 can be expected to be less of a problem when the redox active metal center, *i.e.* iron, is incorporated. Further modification on the iron porphyrin moiety could afford the desired complex.

Considering the other binding motif available for metalloporphyrins, *i.e.* axial coordinations, an alternative route to assemble such a triad is by connecting the chromophore directly to iron center via σ-type of bonding. Indeed, a few more benefits for this second design could be envisioned. 1) It is a more faithful mimetic system towards the protein active site as described in Chapter 1, where the substrate binding at

the metal center serves as the initiate mechanism. Similar effect could be achieved by a photo-induced redox event at the phototrigger in this design. 2) By avoiding the need for an asymmetric porphyrin core, the synthetic difficultness could be significantly reduced. 3) The choice of chromophore will be expanded enormously considering the only synthetic requirement will be one monodentate ligation site to the iron center.

The potential complication in this alternatively design, however, resides in the stability of such systems. Indeed, the system design is limited by a couple of factors: the iron-chromophore affinity cannot be very weak so that the complex obtained does not survive the method of interrogations; such an affinity could not be too strong either, due to the need for an empty axial binding site for the upcoming [Fe_4S_4] cluster. Such a balance may not be easily achieved. Therefore, research conducted in this design will go by trial-and-errors.

In this chapter, the preparation methods of various chromophore complexes along with preliminary characterizations will be presented. The strengths and disadvantages of these chromophores will be discussed in the context of the global design of the system as described in chapter 1. Attempts to synthesize the iron porphyrin-chromophore adduct via an axial σ-bond coordination motif will also be described briefly.

5.2. Selection of Chromophores

The selection of the chromophore needs to satisfy a few criteria. It has to 1) be photostable and survive prolonged laser illumination used for photophysical and photochemical measurements; 2) be able to provide a sufficiently large absorption cross-section to fulfill its role as a phototrigger; 3) possess unique and sensitive spectroscopic features in order to report changes of the structure and/or environments as the result of excited state dynamics; 4) possess a low-lying excited state, charge transfer in nature, in order for the electron transfer cascade to be initiated; 5) this charge transfer excited state has to have reducing or oxidizing powers at least on the order of 1 eV, in view of the redox potential of its electron transfer partner[1] ; and 6) given the complexity of the whole system, ideally the synthesis of the chromophore should be relatively straightforward.

Based on these criteria, two classes of chromophores, *i.e.* rhenium bipyridyl tricarbonyl complexes and ruthenium polypyridyls were selected as the initial candidates. Both these two class of molecules are known to possess metal-to-ligand charge transfer excited states that absorb strongly in the UV-Vis region, and also possess the desired redox potentials. The rhenium bipyridyl tricarbonyl complex provides a few additional benefits: 1) very facile syntheses and high yields; 2) the three carbonyl groups directly attached to the metal center have sensitive infrared spectroscopic tags which allow for unequivocal detection of the evolution of the excited state as a function of time and hence the reactivity of the ET processes. On the other hand, the ruthenium complexes

are some of the most studied inorganic complexes in the past decade, and a vast amount of literature exists for quick reference to aid the current investigation.

5.3. Synthesis

General. All reagents and materials were purchased from Aldrich Chemical Co. and used as received without further purification unless otherwise stated. $RuCl_3 \cdot xH_2O$ was purchased from Strem Chemicals, Inc. All syntheses were performed under a N_2 inert atmosphere unless otherwise specified. ^1H NMR spectra were recorded on either Varian UnityPlus-500 (500 MHz) or Varian Inova-300 (300 MHz) spectrometers. Mass spectra were obtained on either an electrospray MS instrument from the Mass Spectrometry Core of the Research Technology Support Facility, or a GC-MS spectrometer at Michigan State University. Elemental analyses and FT-IR data were obtained through the analytical facilities at Michigan State University. Absorption spectra were obtained on a Cary 50 UV-Vis Spectrometer.

5.3.1 Rhenium polypyridyl-based chromophores

$Re(CO)_3(dmb)Cl$ $Re(CO)_5Cl$ (180 mg, 0.5 mmol) and 4,4'-dimethyl-2,2'-bipyridine (dmb, 92 mg, 0.5 mmol) were dissolved in 20 mL of toluene and refluxed under N_2 for 1 hr. The color of the solution changed from colorless to pale yellow, then yellow to orange, and finally reached bright orange. The solid was washed with Et_2O

and dried in vacuo. The solid obtained was recrystallized in acetonitrile (ACN) by solvent evaporation. Yield: 233.6 mg (95%). Anal. Calcd. for $C_{13}H_8N_2O_3ClRe \cdot 1/2(CH_3CN)$: C, 37.65; H, 2.67; N, 6.86. Found: C, 37.65; H, 2.73; N, 7.01.

$[Re(CO)_3(dmb)(CH_3CN)](PF_6)$ $Re(CO)_3(dmb)Cl$ (254 mg, 0.4 mmol) was dissolved in 80 mL of ACN. $AgPF_6$ (110 mg, 0.44 mmol) was added to the solution and refluxed in the dark under N_2 for 2 hrs. The grey solid was filtered through celite, and the solvent was evaporated. Quantitative yield was obtained.

$[Re(CO)_3(dmb)(4\text{-}Etpy)](PF_6)$ $[Re(CO)_3(dmb)(CH_3CN)](PF_6)$ (256 mg, 0.4 mmol) was redissolved in 20 mL tetrahydrofuran (THF) and degassed with N_2 bubbling for 10 minutes. 4-ethylpyridine (47 mg, 0.44 mmol) was added to the solution, which was then heated and stirred at reflux for 2 hrs under N_2. Pentane was added dropwise to the solution to form an oil-like product. The oil was redissolved in THF. Crystals formed upon slow addition of ether. Yield: 90%. Anal. Calcd. for $C_{22}H_{21}PF_6N_3O_3Re$: C, 37.40; H, 3.00; N, 5.95. Found: C, 37.19; H, 2.74; N, 5.94.

$[Re(CO)_3(dmb)(pyz)](PF_6)$ $[Re(CO)_3(dmb)(CH_3CN)](PF_6)$ (256 mg, 0.4 mmol) was dissolved in 20 mL of tetrahydrofuran (THF) and degassed for 10 minutes. Pyrazine (pyz, 0.44 mmol) was added to the solution and heated to reflux and stirred for 3 hrs under N_2. Pentane was added dropwise to the solution to form an oil-like product. The oil was redissolved in THF, and slow solvent evaporation yielded microcrystalline product. Yield: 70%.

5.3.2 Ruthenium (II) bipyridyl complexes

$Ru(DMSO)_4Cl_2$[2] $RuCl_3 \cdot 3H_2O$ (0.9 g, 3.5 mmol) was heated to reflux in dimethyl sulfoxide (DMSO) (50 ml) under nitrogen for 1 h. The solution was quenched into 500 mL of acetone and kept in the freezer overnight. The crystals were collected on the frit and washed with ether. Yield: 90%.

$Ru(bpy)_2Cl_2$ *Route 1* $Ru(DMSO)_4Cl_2$ (0.55 g, 1.1 mmol), 2,2'-bipyridine (bpy, 0.36 g, 2.3 mmol) and LiCl (1 g, 23 mmol) were dissolved in 125 mL of dimethylformamide (DMF) and heated to reflux under nitrogen for 4 hrs. The resulting solution was rotovap-ed until dry and then washed with water. The residue was redissolved in a minimal amount of ethanol and run through a silica column with ethanol as the eluent. The purple band was collected.

Route 2 $RuCl_3$ (7.8 g, 15.6 mmol), bpy (9.4 g, 60 mmol) and LiCl (8.4 g, 190 mmol) were dissolved in 50 mL of DMF and refluxed under nitrogen for 8 hrs. The resulting solution was quenched in 500 mL of acetone and kept in the freezer overnight. A dark-green solid was collected and washed with water and ether. Yield: 80%. Anal. Calcd. for $C_{20}H_{16}Cl_2N_4Ru \cdot 1.4(H_2O)$: C, 47.14; H, 3.72; N, 10.99. Found: C, 47.44; H, 3.37; N, 10.95.

$[Ru(bpy)_2(4,4'\text{-}bpy)Cl]PF_6$ $Ru(bpy)_2Cl_2$ (184 mg, 0.38 mmol) was dissolved in a mixture containing 10 mL of water and 15 mL of ethanol and was stirred with 1.9 mmol of 4,4'-bipyridine (4,4'-bpy, 300 mg) under nitrogen for 45 mins. The solution was then condensed to approximately 10 mL. The crystals were collected and redissolved in a

minimal amount of ethanol; the solution was then added dropwise to an aqueous solution containing a 10-fold excess of NH_4PF_6 salt while vigorous stirring was maintained with a magnetic stir bar. The solid precipitation was collected on the frit.

5.3.3 Ruthenium terpyridyl complexes with cyano ligands

4'-pyridyl-2,2':6',2''-terpyridine (pytpy): *Route 1*[3] 4-pyridyl-carboxyaldehyde (3.0 mL, 0.032 mol) and 2-acetylpyridine (8.4 mL, 0.074 mol) were dissolved in a mixture containing NaOH (2.0 g), water (25 mL), and methanol (35 mL) and stirred at room temperature for 1h. Water (30 mL) was added slowly and a yellow gum was obtained. After addition of a small amount of methanol followed by trituration, a white precipitate formed. This precipitate was then dissolved in ethanol and refluxed under air with a large excess of NH_4Ac. Crystals were collected and characterized. The yield was approximately 10%.

Route 2[4] 2-acetylpyridine (3 mL, 24.2 mmol) in 2 mL of methanol and 4 mL of 20% aqueous NaOH were simultaneously added dropwise to a stirring solution of 4-pyridinecarboxyaldehyde (1 mL, 10.5 mmol) in 4 mL of methanol cooled to -15℃. The reaction mixture was stirred for 3h, maintaining a temperature between -10 ℃ to -15℃. It was then warmed to room temperature and filtered. The filtrate was refluxed with 4 g of ammonium acetate for 4 h, filtered, and washed with hot water and hot ethanol three times each. The crude product was recrystallized in a minimal amount of chloroform by

slow evaporation. The yield was 85%, mp=227-228°C. ^{1}H NMR (300 MHz, $CDCl_3$, δ): 8.75 (2H, s), 8.74 (2H, s), 8.72 (2H, d), 8.66 (2H, d), 7.88 (2H, t), 7.79 (2H, d), 7.36 (2H, t). Elemental analysis: Calc. for $C_{20}H_{14}N_4$: C, 77.40; H, 4.55; N, 18.06. Found: C, 77.14; H, 4.61; N, 17.96. Infrared: 1581 cm^{-1}, 1564 cm^{-1}, 1536 cm^{-1}, 1500 cm^{-1}, 1469 cm^{-1}, 1390 cm^{-1}, 790 cm^{-1}, 617 cm^{-1}.

Ru(tpy)Cl$_3$[5]: 262 mg of $RuCl_3 \cdot 3H_2O$ (1 mmol) and 233 mg of 2,2':6',2''-terpyridine (1 mmol) was added to 125 mL of absolute ethanol in a 200 mL round-bottom flask. The mixture was heated at reflux for 3 hrs while vigorous magnetic stirring was maintained. The reaction mixture was cooled to room temperature, and the fine brown powder was filtered and collected from the reddish-yellow solution. The powder was washed with 30 mL portions of absolute ethanol three times followed by three 30 mL portions of diethyl ether, and air-dried. The yield was 80%. Elemental analysis: Calc. for $C_{15}H_{11}Cl_3N_3Ru$: C, 40.88; H, 2.52; N, 9.53. Found: C, 41.02; H, 2.70; N, 9.55.

Ru(tpy)(acetone)$_3$(PF$_6$)$_2$ $AgPF_6$ (84 mg, 0.33 mmol) was added to a $Ru(tpy)Cl_3$ (44 mg, 0.1 mmol) suspension in acetone (40 mL) and heated to reflux under argon for 2h. The dark green solution was characterized by a GC-MS spectrum and was identified to be $[Ru(tpy)(acetone)_3]^{2+}$ with a peak at *m/z*=167.0 assigned to $[M\text{-}3(CH_3)_2CO]^{2+}$.

Ru(tpy)(DMSO)Cl$_2$[6] $Ru(DMSO)_4Cl_2$ (24 mg, 0.05 mmol) and terpyridine (13 mg, 0.055 mmol) were dissolved in DMF and refluxed under N_2 for 1 h. The resultant solution was dried and re-dissoved in methanol and ran through a silica column. Two

bands were observed, a purplish band and a yellow band that remained at the top of the column. The first purplish band was collected for further reactions.

$KRu(tpy)(CN)_3$ The $Ru(tpy)(acetone)_3(PF_6)_2$ solution obtained above was evaporated to dryness. A 10-fold excess of KCN dissolved in 4 mL of methanol was added. The mixture was heated at reflux for 19h. The resulting solution was concentrated to approximately 3 mL and filtered through a frit. The solid was redissolved in water and extracted with CH_2Cl_2 at least 10 times. The extracted CH_2Cl_2 solution was dried over sodium sulfate overnight and ran through a basic alumina column. Only one band was observed and ether diffusion yielded nice crystals. ^1H NMR ($(CD_3)CO$): δ 9.16 (H_b), 8.35 (H_3'), 8.31 (H_3), 7.82 (H_4), 7.825 (H_4'), 7.39 (H_5). IR: 2134.29 cm^{-1} (m), 2093.32 cm^{-1} (m), 2071.60 cm^{-1}(s).

5.3.4 Ruthenium complexes with pyridyl-appended bisterpyridyl

$[Ru(tpy)(pytpy)](PF_6)_2$ *Route 1*[7]: A mixture of $Ru(tpy)Cl_3$ (50 mg, 0.113 mmol) and $TlPF_6$ (125 mg, 0.36 mmol) in acetone (50 mL) was heated to reflux under N_2 atmosphere for 2 hrs. After filtering out a solid residue of TlCl, the solution was concentrated to 10 mL and transferred through a cannula to a degassed chloroform (40 mL) solution containing the pytpy ligand (40 mg, 0.13 mmol). The solution was then stirred for 3 hrs at reflux. After cooling and filtration, the solvent was evaporated under vacuum. The remaining residue was then dissolved in CH_3CN (2 mL) and added

dropwise to an aqueous solution (100 mL) with NH_4PF_6 (500 mg). The red-brown precipitate was collected and washed with water and diethyl ether. Chromatography on a silica gel with acetonitrile-H_2O/KNO_3 (saturated aqueous solution) =7:1 (v/v) as the eluent gave a red-brown major band. It was collected and metathesized with an NH_4PF_6 aqueous solution. The precipitate was recrystallized in acetonitrile by the ether diffusion method. The yield was 10%. Elemental Analysis: Calc. for $C_{35}H_{25}N_7RuP_2F_{12}$: C, 44.97; H, 2.69; N, 10.49. Found: C, 44.87; H, 2.61; N, 10.08.

Route 2[8]: $Ru(tpy)Cl_3$ (220 mg, 0.50 mmol) and pytpy (310 mg, 1.0 mmol) were heated to reflux in a 1:1 solvent mixture of freshly distilled ethylene glycol and absolute ethanol (15 mL) for 2h while being stirred. The purple solution was cooled to room temperature and diluted with water (20 mL) and filtered to remove a fine black precipitate. The solution was the treated with NH_4PF_6 (3 eq.), which resulted in the precipitation of a red-brown solid. This solid was collected on a frit, washed with water (2 × 20 mL) and diethyl ether (2 × 20 mL) and air dried. The crude product was dissolved in acetonitrile (2 mL) and chromatographed on silica eluted with 7:1 acetonitrile–H_2O/KNO_3 (sat.). The main red-brown band containing the product was reduced in volume to 5 mL, and treated with NH_4PF_6 to precipitate the product. The precipitate was filtered, washed with water (2 × 20 mL), diethyl ether (2 × 20 mL) and dried *in vacuo*. The yield was 304 mg (65%). ESI-MS; *m*/*z* (%): 791(2) $[M–PF_6]^+$, 323(100) $[M–2PF_6]^{2+}$. IR (KBr, cm^{-1}): 3430m, 3105w, 1635w, 1601m, 1475w, 1465w, 1448m, 1429w, 1408m, 1387m, 1030w, 839s, 791w, 766m, 557s. ^1H NMR (500MHz,

CD_3CN, δ): 9.08 (2H, s), 9.00 (2H, m), 8.79 (2H, d), 8.68 (2H, d), 8.53 (2H, d), 8.46 (1H, t), 8.16 (2H, m), 7.98 (4H, m), 7.43 (4H, m), 7.22 (4H, m). Elemental analysis: Calc. for $C_{35}H_{25}N_7RuP_2F_{12}$: C, 44.97; H, 2.69; N, 10.49. Found: C, 44.97; H, 2.70; N, 10.68.

5.4. Results and Discussions

5.4.1 Chromophores

A. *Chromophores based on rhenium tricarbonyl bipyridyl complexes*

A rhenium tricarbonyl bipyridyl complex is advantageous over the ruthenium complex due to better synthetic accessibility. Typical syntheses start from heating the starting material $Re(CO)_5Cl$ to reflux along with appropriate ligand in a nonpolar solvent under inert atmosphere for an hour; this is done to replace two of the five carbonyls with a bipyridyl ligand. The chlorine ligand is then removed and replaced with a solvent molecule by reacting the complex with a silver salt in a polar solvent like acetonitrile. After filtering out AgCl, the filtrate is refluxed with a monodentate ligand in tetrahydrofuran (THF) to afford the desired chromophore molecule with near-quantitative yields. The products can typically be purified via recrystallizations. These reactions were all performed in the dark to prevent light-induced ligand loss.

The products were characterized by elemental analysis, ^1H NMR, infrared absorption spectroscopy and UV-Vis absorption spectroscopy. Electrochemistry data

shows that $Re(dmb)(CO)_3Cl$ undergoes a reversible one-electron reduction but an irreversible first oxidation, consistent with literature data[9]. The overall electrochemical behavior is quite complex, involving ligand dissociations.

The infrared absorption measurement is a very useful tool for this class of compound because of the presence of carbonyl infrared tags. The stretching bands of the carbonyl group lie in the range between 1670 cm^{-1} and 1820 cm^{-1} and are very sensitive to the electronic structures the Re metal they attached to. It has been shown that electron-withdrawing substituents on the bipyridyl rings lead to a decrease in the amount of electron density on the metal center. Back bonding from the –CO π* orbital contributes to the lower amount of electron density, raising the bond order of the carbonyl and hence the vibrational frequencies which then exhibit a blue shift in the IR spectra. Likewise, the electron-donating substituents cause an increase in electron density on the metal center and decrease the carbonyl bond order resulting in a red shift of the corresponding bands. Such modulations are also applicable to the excited state behaviors. In the event of photo-excitation, the formation of a charge-to-ligand excited state shifts the electron density from the rhenium metal center to the bipyridyl ligands. The lower electron density on the Re center leads to less π-back bonding to the carbonyls and manifests itself as a blue shift in the CO- stretching bands. Such changes can be detected by time-resolved infrared measurements[10] (TRIR). Further, TRIR has been used to interpret the orbital origins of the excited state, identify the acceptor ligand

involved in the charge transfer transitions and help evaluate the influence of various factors on the electronic structures.

An example of typical absorption spectra for [Re(R-bpy)(py-R′)$(CO)_3$]Cl complexes is shown in Figure 5-1. The peaks in the UV region are assigned to the ligand-based π to π* transitions localized on the bipyridyl ligand, based on the similarity of the profile to the uncoordinated ligand. The two broad peaks at 370 nm and 510 nm are assigned to the first and second $Re^{I}\rightarrow$dmb ^{1}MLCT bands. The energies of these bands reasonably match those estimated from electrochemistry measurements, *i.e.* approximately 3 eV. The extinction coefficient is measured to be 4 x10^{3} $M^{-1}cm^{-1}$ at λ_{max} (510 nm).

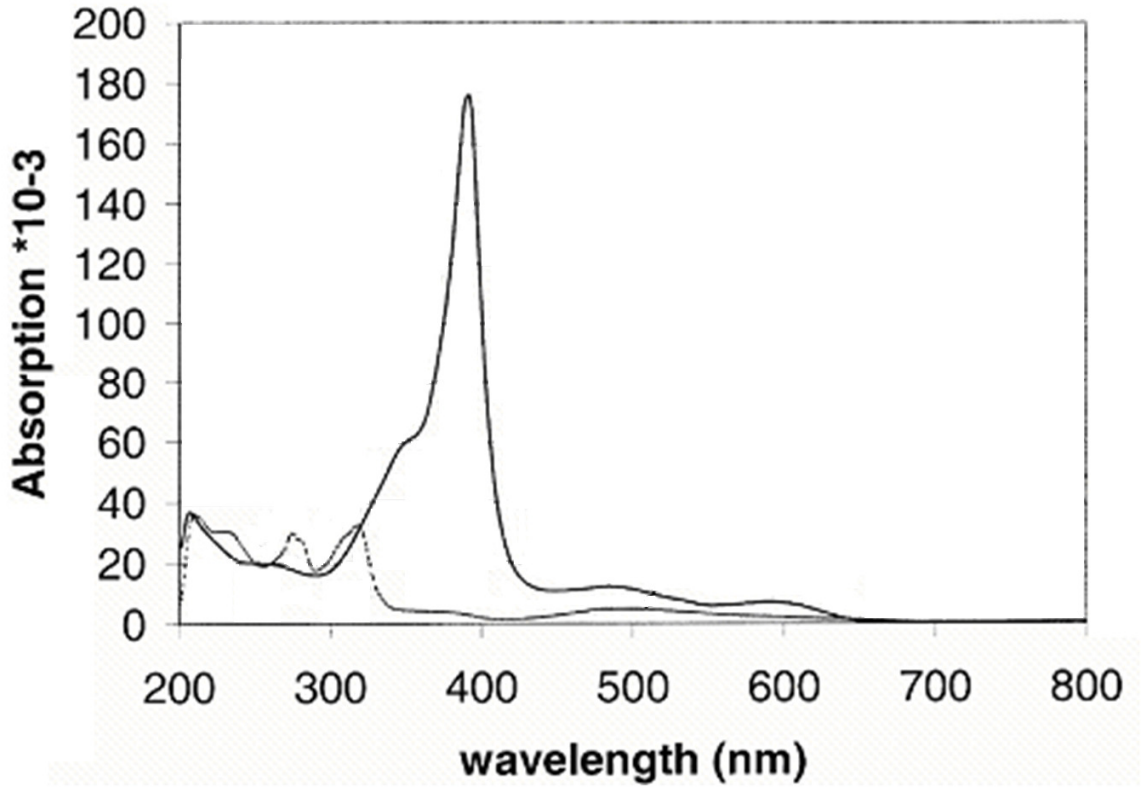

Figure 5-1. Absorption spectra of [Re(dmb)(4-Etpy)$(CO)_3$]Cl and Fe(OEP)Cl of equal concentration in absolute ethanol.

It is important to note that the purpose of these chromophores is to serve as the phototrigger which, upon excitation, initiates a cascade of electron transfer steps to be monitored by photophysical means. For a clean interpretation of the data, the phototrigger should be the dominant light absorber at the excitation wavelength. In other words, the extinction coefficient of the phototrigger should be significantly higher than the other components in the assembly, *i.e.* porphyrin, iron sulfur cluster and whichever additional components incorporated to achieve the overall design (see Chapter 1). Unfortunately, in comparison to the iron porphyrin spectrum, both of the ^{1}MLCT bands are buried beneath the porphyrin Q-bands. Therefore, selective excitation of the chromophore cannot be achieved. This is less than ideal as the large absorption by the iron porphyrin component will produce strong signals which may dominate the spectra and make clear assignments problematic. Nevertheless, utilizing time-resolved infrared (TRIR) technique, we may still be able to reveal the desired information.

Photostability

During the characterization process, the UV-Vis absorption spectra of the rhenium complex in acetonitrile changed slightly over time. Similar changes were absent in dichloromethane solution. There had been a limited number of reports indicating a photostability issue for this type of complex at the time. It was speculated that the excitation of the complex into the long-lived ^{3}MLCT excited state allows for the possibility of thermally populating the anti-bonding π* orbital. This weakens the bond between the metal center and the carbonyl ligands, leading to dissociation.

Sato and coworkers later reported a detailed investigation on the photostability of these mono-ligated rhenium complexes[11], which is consistent with my earlier speculations. They further found via TRIR measurements that such a photodissociation is a solvent-induced reaction with a sub-picosecond rate constant. In other words, it is a very competitive process in comparing to other photophysical or photochemical pathways. Fortuitously, the dissociation seems to only occur when higher-energy excitation wavelength was used. By exciting at the lower energy tail of the MLCT band, no indication for photodissociation was observed. Therefore, further investigation on systems with similar chromophores requires a lower-energy excitation at the tail of the MLCT band in less polar solvents.

B. Chromophores based on Ruthenium Cyano Polypyridyls:

The complications in the photostability of rhenium complexes suggested a potential need for alternative chromophore molecules. Ruthenium polypyridyls were therefore investigated considering their well-established synthetic methodology as well as detailed understandings.

The initial design of Ru-based chromophores incorporate a $[Ru(CN)_x]^{2-x}$ moiety. It was known in literature that such a motif leads to significant solvatochromism, *i.e.* large solvent dependence of the ^{1}MLCT excited state energies. This is a feature strongly desired for the purpose of rational designs in that perturbations on the driving force could potentially be conveniently achieved via simple change of solvents. This could

also be helpful in selecting the appropriate excitation wavelength to cleanly excite the chromophore. Furthermore, the –CN group is another efficient infrared phototag, which can be utilized to report the electronic environment changes at the metal center as discussed above.

The synthesis of the ruthenium bipyridyl-based chromophores follows literature methods[12-14]. The intermediate $Ru(bpy)_2Cl_2$ can be obtained either with Ru^{II} or Ru^{III} as a starting material. Further reaction with 5 eq. of 4,4′-bipyridine yields fine crystalline of $[Ru(bpy)_2(4,4'\text{-bpy})Cl]^+$, which can then be converted into $[Ru(bpy)_2(4,4'\text{-bpy})CN]^+$ upon refluxing with excess KCN. Unfortunately, a similar color change of the resulting acetonitrile solution was observed as manifested in shifts and intensity decays of the ^{1}MLCT bands within a couple of hours in light. Such photostability issues in monoligated ruthenium complexes has been reported by other groups[15] as well. The same argument can be used as that for rhenium-based chromophores, referring to the accessibility of the ligand field states from the ^{3}MLCT excited state, only these Ru complexes are even more light-sensitive since the energy gap between the lowest long-lived excited state ^{3}MLCT and the anti-bonding metal-centered orbitals are smaller than that in its rhenium counterpart. This is a result of a smaller ligand field strength in the case of Ru metal, as suggested by the Tanabe-Sugano diagram shown in Figure 5-2.

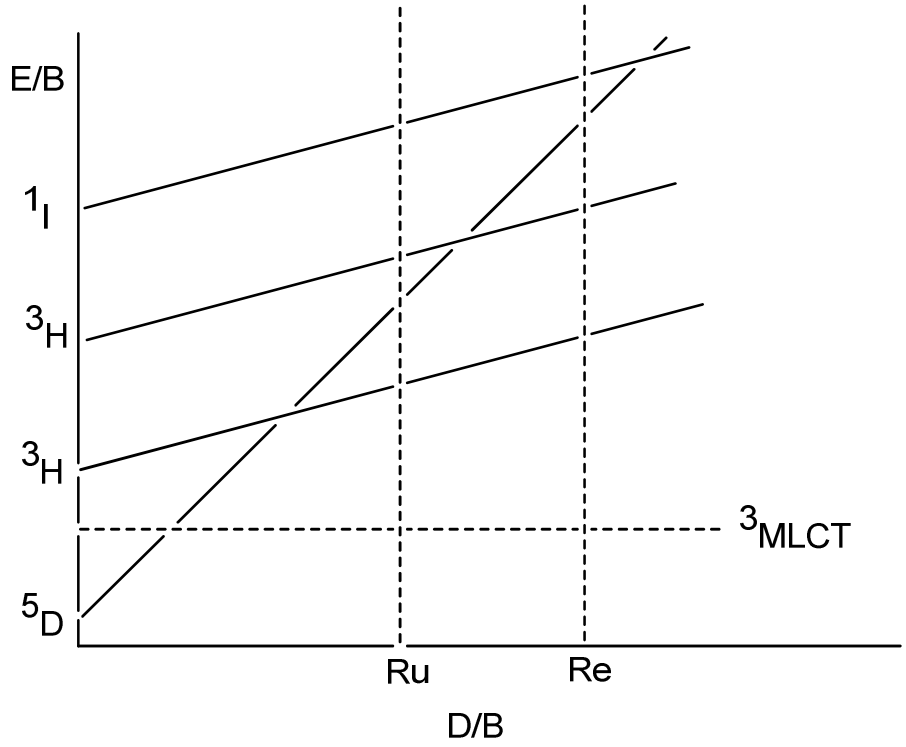

Figure 5-2. Tanabe-Sugano Diagram for d^6 metal ions. The ^{3}MLCT state energy of Ru and Re polypyridyls are relatively close. The ligand-field state in the Ru complex is significantly lower due to smaller ligand field strength. This reduced the energy gap between the ^{3}MLCT state and that of MC state, leading to potential stability problem. This is a similar effect as that discussed in Chapter 3, which leads to weak emission in $[Ru(tpy)_2]^{2+}$-type complexes.

To alleviate these complications, a different ligand design, 4'-pyridyl-2,2':6',2''-terpyridine (pytpy), was chosen with the hope that the stronger chelating effect of the terpyridyl group may help prevent ligand loss. From a thermodynamic point of view, more ligands are liberated from the metal center to form the $[Ru(terpy)L_3]^{2+}$ unit as that to form $[Ru(bpy)L_4]^{2+}$. The larger gain in entropy drives the reaction towards completion and keeps the product stable. As the bridging group pyridyl is attached via a covalent bond to the chromophore, no dissociation should be expected. This new bridging ligand also provides a larger absorption cross-section than its bipyridine counterpart.

The synthesis of the 4′-pyridyl-2,2′:6′,2″-terpyridine (pytpy) ligand following the most commonly cited procedures[16] yielded only a very small amount of product. Better results were obtained using a different method[4]. The reaction between 2-acetylpyridine and 4-pyridyl-carboxyaldehyde was carried out at low temperature in methanol. After the formation of the diketone intermediate, excess NH_4Ac was added *in situ* to produce the desired pytpy ligand. ^1H NMR data and determination of the melting point verified its identity.

To prepare the tricyano complex, ruthenium trichloride was first refluxed with 1 eq. of the substituted terpyridine ligand in ethanol for 3 hrs to yield Ru(R-terpy)Cl_3. Refluxing with 3 eq. of $AgPF_6$ in the dark for 2 hrs produced the *tri*-acetone solvato-complex. It was then converted into the final product by refluxing with 10-fold excess of KCN. ^1H NMR, IR, UV-Vis and elemental analysis were used to characterize this complex. The yield for this reaction was very low. This may be due to the incomplete dechlorination of Ru(R-terpy)Cl_3, reoxidation of the Ru^{II} center, or both. The length of the reaction time and the amount of $AgPF_6$ used was limited due to the potential oxidation of Ru^{II}. This problem is very likely considering the electrode potentials of Ag salt. Collecting the UV-Vis absorption spectrum at different points in the reaction and when reacted under different stoichiometries displayed shifts in the MLCT band peak positions. Meanwhile, the oxidation of Ru causes further difficulty in displacing the chloride ligand by strengthening the Ru-Cl bond; this is due to a better match of orbital energies between the Ru t_{2g} orbital and the Cl p orbital, which interacts and forms a π-back bond. Similar

problems have been identified in the literature and also by the other members of our group working on different projects. $TlPF_6$ was therefore used as a low-oxidation-potential displacing agent where the product TlCl has a K_{sp} smaller than that of AgCl in most solvents, while maintaining a low redox potential (-0.34 vs. SHE).

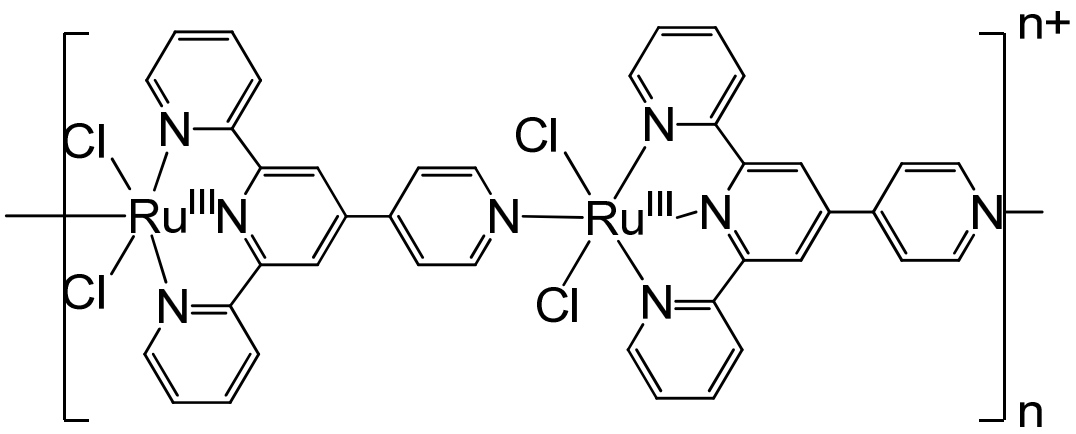

Figure 5-3. A one-dimensional polymer may form during the reaction between $RuCl_3$ and pytpy.

The synthesis of the chromophore bearing a monodentate bridging pyridyl group, *i.e.* $KRu(pytpy)(CN)_3$, experiences a lower yield due to the presence of an additional nitrogen donor. In the dechlorination step, unlike its H-terpy analogue where the majority of the black suspension disappeared to yield a deep colored solution, only a lightly pink-colored solution along with a significant amount of black powder remains. The black solid did not dissolve in any solvent and was not further characterized. This black powder was observed by other groups[17] as well, suggesting the possibility that it be a one-dimensional polymer (Figure 5-3). Alternatively, it can also be the Tl-

molecular adduct to the nitrogen donor atom. Due to its insoluble nature, no further identifications were explored with this black powder. The pale-pink filtrate was identified to be $[Ru(pytpy)(acetone)_3]^{2+}$ by GC-MS. Due to the very low yield, further reaction with cyanide salt did not yield sufficient amount of product to be characterized.

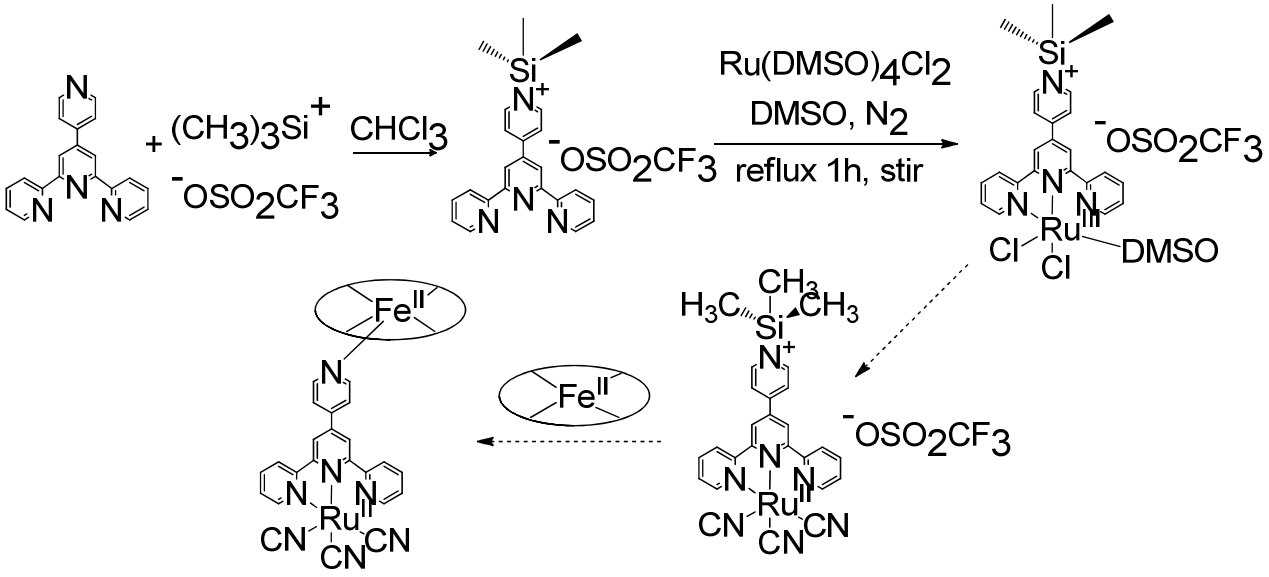

Figure 5-4. Protecting and deprotecting scheme of the 4'-pyridyl nitrogen atom.

To avoid the attack on the pyridyl nitrogen by either the Ru(III), Tl(I) or CN^- ion in the next reaction step, it is necessary to protect this nitrogen donor until the coordination of Ru as well as the binding of –CN groups are completed. A good protecting group needs to satisfy a couple of criteria. The interaction between the protecting group and the nitrogen donor atom should be stronger than the that between ruthenium or thallium and the donor nitrogen, yet smaller than the chelating interaction between all three pyridyl nitrogens towards the ruthenium metal. Meanwhile, the deprotection procedure should

be reasonably facile. A trimethyl silyl (TMS) group was used in the first trial attempt, according to a prep in the literature on TMS-pyridine.[18]

The first step (Figure 5-4) did occur under inert atmosphere as indicated by solids precipitating out of the initially clear chloroform solution. Yet the protecting group falls off as soon as it sees air, presumably due to the strong oxygen affinity of the TMS group. This may have occurred while being transferred into the GC-MS instrument. The spectrum obtained looked identical to that of the pure pytpy ligand. A detailed mechanism or retrial with more strictly controlled conditions was not pursued in light of the stability issue as described later. The second step of the reaction yielded $Ru(pytpy)(DMSO)Cl_2$, instead of the TMS-appended complex. The product was reaonably soluble in acetonitrile as well as a few other solvents, confirming that the presence of the protecting group prevented the formation of a one-dimentional polymer. The TMS protecting group was speculated to have fallen off during the transfer process, yet a proton was left behind on the nitrogen atom it initially bound to, which effectively serves as the protecting group. A similar situation was observed in the deprotection reaction of TMS-py with either ketone or acid.[18, 19]

Other possible protecting group include BPh_4^-, although high oxygen sensitivity issue remains. A more interesting protecting group is the Fe-porphyrin component itself, as it was designed as one of the directly connected component initially. This approach will be discussed briefly in the last section.

C. Chromophores based on Ruthenium Pyridyl-appended Bisterpyridyl:

The major reason that the cyano groups were incorporated in the ruthenium chromophore design was to retain infrared phototags. Given the complexity of the synthesis, especially the likelihood of a cyano group attacking the bridging nitrogen site, alternatives were pursued. Given the stability issue for most other monoligated ruthenium-ligand bonds, a second 2,2':6',2''-terpyridine (tpy) ligand was incorporated into the design. In other words, a ruthenium bisterpyridyl with a pyridine attached to the 4'-position of one of the terpyridines, *i.e.* $[Ru(pytpy)(tpy)]^{2+}$, was chosen as the chromophore. Chemical modification on its 4'-position is facile if needed.

The UV-Vis absorption spectrum of $[Ru(pytpy)(tpy)]^{2+}$ showed a strong MLCT band at 484 nm with an extinction coefficient of 28,000 $M^{-1}\cdot cm^{-1}$. Two ligand-centered $\pi \rightarrow \pi^*$ transitions are at 310 nm (78000 $M^{-1}\cdot cm^{-1}$) and 274 nm (72700 $M^{-1}\cdot cm^{-1}$) respectively. The absorption spectrum was overlaid with that of Holm's complex $[Fe_4S_4\text{-}FeP]^{2-}$, as shown in Figure 5-5. It is clear that at an excitation wavelength of 484 nm, the ruthenium chromophore absorption dominates over the $[Fe_4S_4\text{-}FeP]^{2-}$ assembly, appropriate for my purpose as a chromophore. Nevertheless, the porphyrin signatures could not be neglected and have to be treated with care as have shown in the previous chapter.

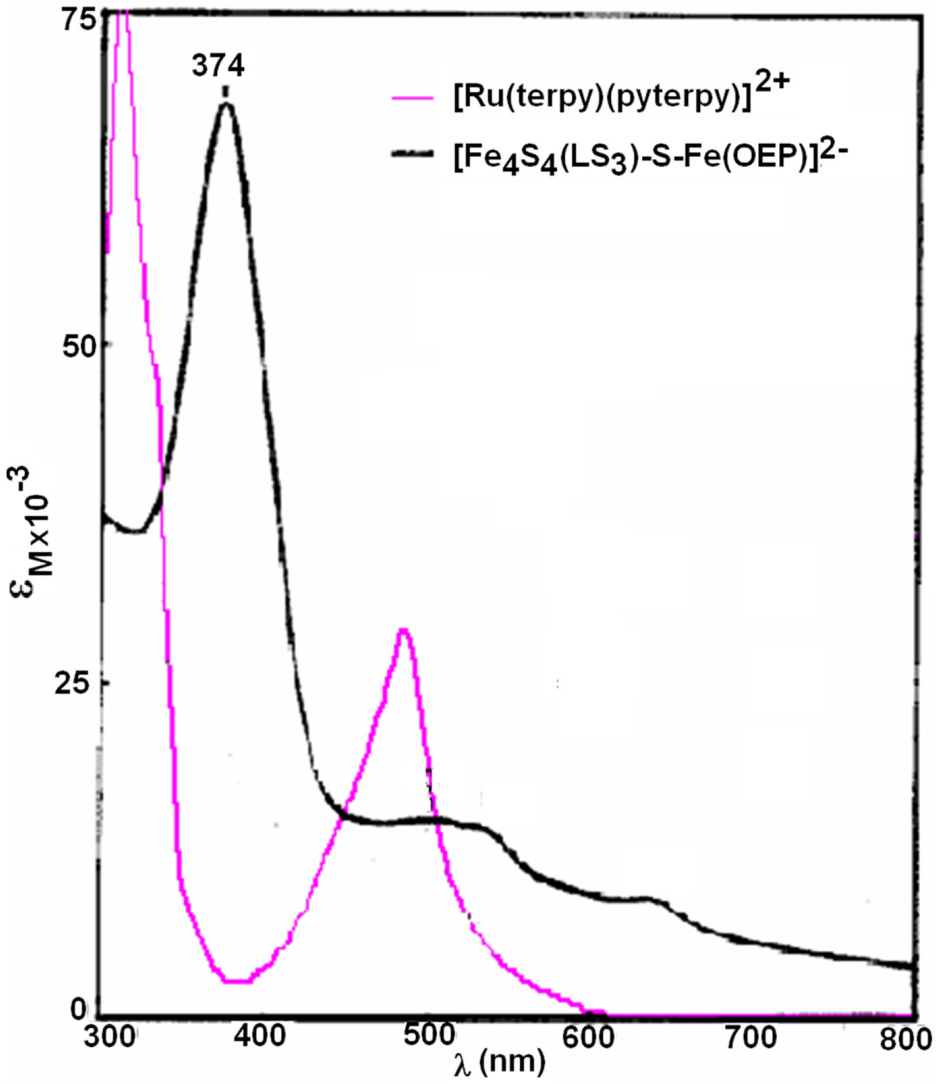

Figure 5-5. Overlay of the absorption spectrum of $[Ru(tpy)(pytpy)]^{2+}$ on top of Holm's complex[1] $[Fe_4S_4\text{-}FeP]^{2-}$.

Electrochemistry data are shown in Table 5-1. The reversible oxidation peak at 0.96 eV was assigned to the oxidation of Ru^{II} to Ru^{III}. Three reduction peaks for the ligands occurred at -1.54 eV, -1.82 eV and -2.22 eV and were assigned by comparing to those of $[Ru(tpy)_2]^{2+}$ and $[Ru(pytpy)]^{2+}$reference compounds. The assignments were consistent with reported literature data[20].

Table 5-1. The redox potential of [Ru(tpy)(pytpy)]$(PF_6)_2$

	$Ru^{III/II}$	$pyterpy^{-/0}$	$terpy^{-/0}$	$pyterpy^{-/2-}$
$E_{1/2}$ (V) vs. Fc^+/Fc	0.96	-1.54	-1.82	-2.22

5.4.2 **Synthesis of iron porphyrin-chromophore adducts**

Both the road map outlined in chapter 1 and the need for a protecting group discussed above suggested the need to prepare [FeP-pytpy-$RuCl_3$] adduct.

A. Iron porphyrin-pyridyl-chromophore adduct

From the vast majority of literature, the Fe^{III}-py bond is known to be unstable. This was confirmed by the unsuccessful reaction of iron (III) porphyrins with 1 eq. of pytpy ligand. Either iron meso-tetrapheynyl porphyrin chloride (Fe(TPP)Cl) or iron octaethylporphyrin chloride (Fe(OEP)Cl), refluxed with pytpy respectively in chloroform solution for two days, yielded no significant changes in the absorption spectra, which is expected as the ligand field strength changes with the binding of the axial ligand. This was true even with 100 eq. of pytpy ligand reacting with 1 eq. of Fe^{III} porphyrin. Such an instability of Fe^{III}-py linkage may prevent us from investigating the *reverse* electron transfer process as described in Chapter 1, which is from iron porphyrin to the iron sulfur cluster. But if the Fe^{II}-py bond is strong enough, the *forward* electron transfer process could still be measured, which, from the biological point of view, the more

interesting pathway. Initial titration experiments suggested significant binding with large excess of pyridyl ligands. Further investigation in this direction is planned. Depending on the Fe^{II}-Py bond strength, low temperature measurements in glassy matrix may be required in order to avoid of the Fe-py bond lability issues.

B. ***Iron porphyrin-phenyl-chromophore adduct***

The initial concern about the Fe-py bond stability problem directed me to look for alternatives for the iron porphyrin-chromophore linkage. A possible choice is 4'-Phenyl-2,2':6',2''-terpyridine (phtpy) ligand, which has been synthesized via the same procedures used for pytpy ligand. This type of Fe-C bond was supposed to be strong enough and eliminate the kinetic problem for the Fe-py connection. Synthesis of the phenyl analogue, Fe^{III}TPPph, through Grignard reaction was attempted according to the literature methods.[21, 22] The successful preparation of the Grignard reagent was proved by the formation of benzhydrol at the addition of benzaldehyde, which was identified in both ^{1}H NMR spectrum and IR spectrum. It was then reacted with iron(III) *meso*-tertraphenylporphyrin chloride with the Grignard reagent followed. The ^{1}H NMR peaks of the product at -82 ppm, -35 ppm suggested the formation of the compound. But due to the complexity caused by the paramagnetic iron (III) center, the ^{1}H NMR spectrum was complicated and a detailed interpretation of the spectrum was not attempted.

Ultimately, Grignard reagent of the ruthenium chromophore, [Ru(tpy)(Phtpy)]MgBr will be required to connect to the iron porphyrin in this design. A potential problem is that the magnesium turnings ($E^{\theta}_{1/2}$= -2.36V vs. NHE) used in such reactions may reduce the ruthenium (II) center to the zero oxidation state and decompose the chromophore. To circumvent this problem, a milder version of the Grignard reaction[23] was followed, where the Grignard reagent of isopropyl (*i*PrMgCl·LiCl) was made initially followed by a Br/Mg exchange reaction to afford the target Grignard reagent of ruthenium chromophore. With this method, the reduction of magnesium is moved one step away from the introduction of ruthenium(II), preventing the decomposition of the chromophore. This synthesis turned out to suffer from very low yield.

5.5. Conclusions

From the various trials and errors described in this chapter, it is clear that the general theme for axial-coordination to the iron porphyrin center suffers stability issues. For the purpose of fundamental research, initial insights of electron transfer between a porphyrin with d^6 metal in the ring and an [Fe_4S_4] cluster could be achieved utilizing alternative metal ions including Ru, Os, Re, etc, which afford more stable axial σ-bonds with ligands. Further, although a stable complex is desirable for the purpose of such characterizations, investigations on systems containing an equilibrium is not impossible. By using the same model-to-assembly approach as described in Chapter 4, the

signatures of the non-coordinated species may be isolated allowing the features related to the complex to be determined. The recent development of solution phase X-ray scattering methodology[24] provides additional characterization tool in identifying the integrity of the complexes being probed. Low temperature solid state characterization is another way to probe the system without the complication from stability.

REFERENCES

REFERENCES

[1] Cai, L.; Holm, R. H., *J Am Chem Soc*, (1994) **116**, 7177.

[2] Evans, I. P.; Spencer, A.; Wilkinson, G., *Journal of the Chemical Society, Dalton Transactions*, (1973), 204.

[3] Moya, S. A.; Pastene, R.; Le Bozec, H.; Baricelli, P. J.; Pardey, A. J.; Gimeno, J., *Inorg Chim Acta*, (2001) **312**, 7.

[4] Persaud, L.; Barbiero, G., *Canadian Journal of Chemistry*, (1991) **69**, 315.

[5] Sullivan, B. P.; Calvert, J. M.; Meyer, T. J., *Inorg Chem*, (1980) **19**, 1404.

[6] Ziessel, R.; Grosshenny, V.; Hissler, M.; Stroh, C., *Inorg Chem*, (2004) **43**, 4262.

[7] Gourdon, A.; Launay, J.-P., *Inorg Chem*, (1998) **37**, 5336.

[8] Metcalfe, C.; Spey, S.; Adams, H.; Thomas, J. A., *Journal of the Chemical Society, Dalton Transactions*, (2002), 4732.

[9] Breikss, A. I.; Abruna, H. D., *J Electroanal Chem*, (1986) **201**, 347.

[10] Dattelbaum, D. M.; Omberg, K. M.; Schoonover, J. R.; Martin, R. L.; Meyer, T. J., *Inorg Chem*, (2002) **41**, 6071.

[11] Sato, S.; Sekine, A.; Ohashi, Y.; Ishitani, O.; Blanco-Rodríguez, A. M.; Vlček, A.; Unno, T.; Koike, K., *Inorganic Chemistry*, (2007) **46**, 3531.

[12] Sullivan, B. P.; Salmon, D. J.; Meyer, T. J., *Inorg Chem*, (1978) **17**, 3334.

[13] Nikolaou, S.; Toma, H. E., *Polyhedron*, (2001) **20**, 253.

[14] Nikolaou, S.; Toma, H. E., *Journal of the Chemical Society, Dalton Transactions*, (2002), 352.

[15] Coe, B. J.; Friesen, D. A.; Thompson, D. W.; Meyer, T. J., *Inorganic Chemistry*, (1996) **35**, 4575.

[16] Constable, E. C.; Thompson, A. M. W. C., *Journal of the Chemical Society, Dalton Transactions*, (1992), 2947.

[17] Constable, E. C.; Thompson, A. M. W. C., *Journal of the Chemical Society, Dalton Transactions*, (1994), 1409.

[18] Anders, E.; Stankowiak, A.; Riemer, R., *Synthesis*, (1987) **1987**, 931.

[19] Weiss, R.; Roth, R., *Journal of the Chemical Society, Chemical Communications*, (1987), 317.

[20] Figgemeier, E.; Merz, L.; Hermann, B. A.; Zimmermann, Y. C.; Housecroft, C. E.; Güntherodt, H. J.; Constable, E. C., *The Journal of Physical Chemistry B*, (2003) **107**, 1157.

[21] Cocolios, P.; Lagrange, G.; Guilard, R., *J Organomet Chem*, (1983) **253**, 65.

[22] Guilard, R.; Boisselier-Cocolios, B.; Tabard, A.; Cocolios, P.; Simonet, B.; Kadish, K. M., *Inorganic Chemistry*, (1985) **24**, 2509.

[23] Krasovskiy, A.; Knochel, P., *Angewandte Chemie International Edition*, (2004) **43**, 3333.

[24] Mulfort, K. L.; Tiede, D. M., *The Journal of Physical Chemistry B*, (2010) **114**, 14572.

Chapter 6. Future Work and Broader Perspective

Described in previous chapters are the major synthetic efforts as well as spectroscopic investigations on sub-systems of the global design outlined in chapter 1. These progresses allow the initiation process for the electron transfer cascade to be studied explicitly. Subsequent incorporation of additional components is expected to bring in significantly more complications. In this chapter, current synthetic progresses, immediate future work and the way this study fits into a larger project evaluating the effect of electronic structure on the reactivity will be briefly described. Considering the better progress on the ring-connected dyads as described in Chapter 4, the discussion below will be based on this design.

The *forward* electron transfer from $[Fe_4S_4]^{n+}$ cluster to iron porphyrin proposed in Chapter 1 requires an iron(III) porphyrin to be produced *in situ* to allow electron transfer event to be initiated from the $[Fe_4S_4]^{+}$ cluster. This can be realized by using an internal acceptor attached to the chromophore. In such systems, selective excitation of chromophore will result in an initial excited state on the $[Ru(tpy)_2]^{2+}$ core. If energetically favorable, the first electron transfer event will bring one electron from the MLCT excited state to the remote acceptor. The charge separated state created thereafter has to have a sufficiently long lifetime to allow secondary electron transfer from iron(II) porphyrin to happen. This requirement precludes the use of simple nitro-

type substituents as an acceptor, as described as dyad **2** in Chapter 4. This was due to the very efficient charge recombination to form ground state. In fact, the charge recombination process observed in this system was faster than $(100\ ps)^{-1}$. In order to slow down this process, a pyridinium motif was chosen to serve as the internal acceptor. This was targeted to bring the pair of charge one more step away from each other for the purpose of increasing the its lifetime, allowing sequential electron transfer involving the iron porphyrin component to occur. Commercially available triphenylpyridinium salt ($[P_3Py]^+$) was initially chosen for convenience. A few versions of acceptors with different substituents were also synthesized and evaluated for electrochemical performances. A brief synthetic scheme is seen in Figure 6-1.

As discussed in Chapter 3 and 4, excitation of the Ru component essentially creates two excited states immediately following the laser pulse, which are localized on the two terpyridyl ligands respectively. Interligand electron transfer process will follow along with other intercomponent processes. Apparently, to reduce the level of complexity as seen in Chapter 4, it is desired that interligand electron transfer (ILET) is much faster than any other intercomponent processes. Such competition occurs at the very early stage of the time evolution, which involves ^{1}MLCT, hot ^{3}MLCT and charge separated states.

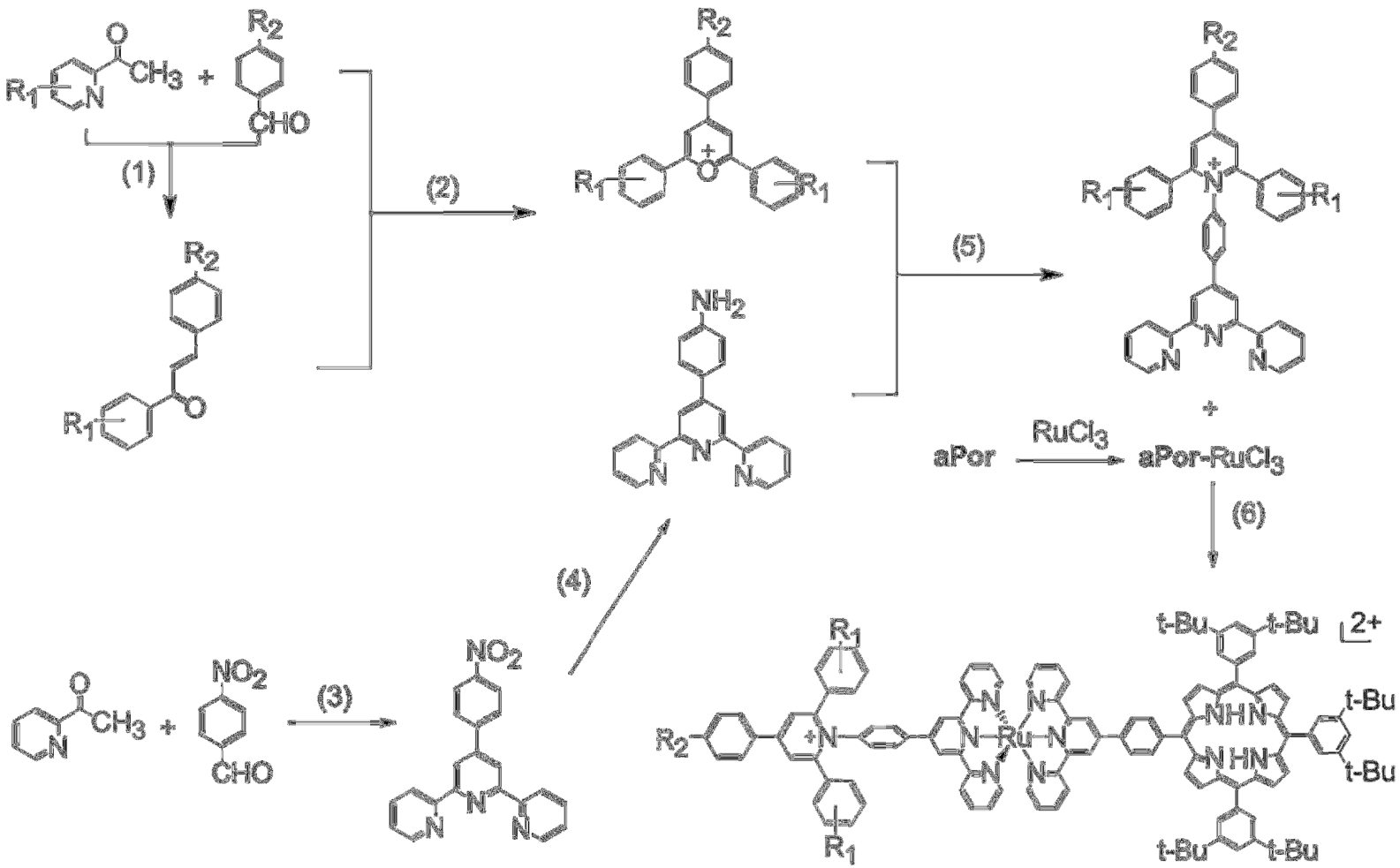

Conditions: (1) ice-cold KOH, H_2O/EtOH, 1h, RT; (2) $HClO_4$ in H_2O 70%, added in at 80°C, kept at 92-94°C, 2h; (3) MeOH, KOH, NH4OH, RT, 3 days; (4)Pd/C, Ar, 1h, EtOH, reflux, then, add in N_2H_4, dropwise, Ar, reflux 0.5h; (5) anhydrous NaAC, EtOH, reflux 20h; (6) EtOH/Ethylene Glyco/$CHCl_3$,N_2, reflux 2h

Figure 6-1 Synthetic scheme for acceptor appended porphyrin-Ru systems[1-3]

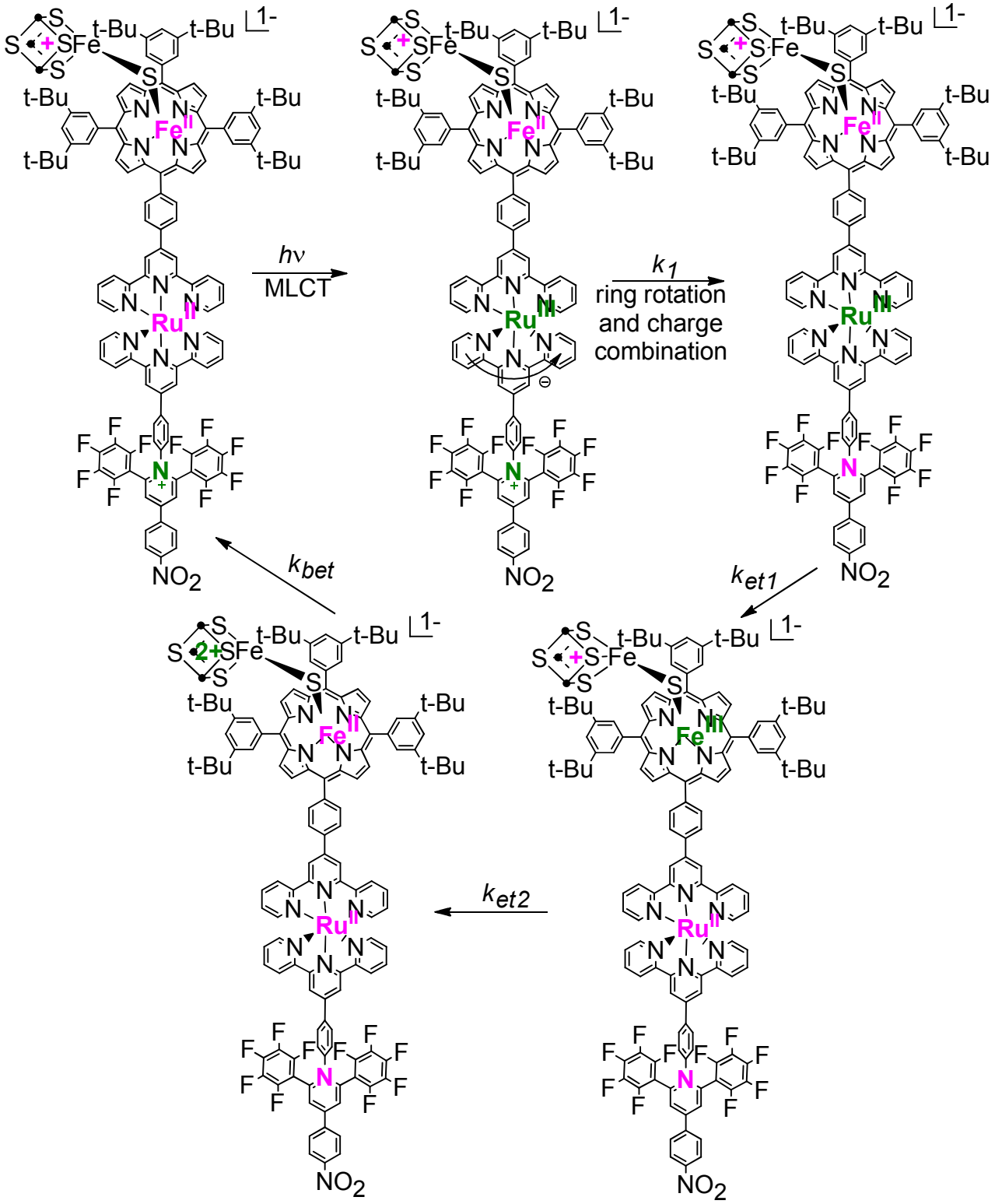

Figure 6-2 Anticipated reaction sequence following photoexcitation of a $[Fe_4S_4]^+$-Fe^{II} porphyrin-Ru^{II}-pyridinium$^+$ assembly. Green color illustrates oxidized state and purple stands for reduced state.

From the situation of dyad **1**, we know that the electron transfer process from the proximal terpyridyl to the porphyrin has a time constant of 780 fs. For the ILET to compete with this process, sufficient driving force has to be present. Therefore, the different modifications on the pyridinium moiety proposed in Figure 6-1 were designed to evaluate this aspect of the problem. From basic electrochemistry measurements as well as estimates from literature data[2, 4-6], the driving force differences between these different versions of acceptor-appended chromophores can be calculated. From the unsubstituted acceptor $[P_3Py]^+$ to the one with both nitro- and fluoro- substitutions $[NF_2P_3Py]^+$, the driving force shall span a range of 400-500 mV, allowing us to extract the driving force dependence of such ILET processes. Whether the pyridinium motif allows such fast ILET is not yet clear to us, especially due to complications from conformation changes and others. Nevertheless, they should serve as a good starting point to increase the lifetime of these CT states.

It is worth pointed out that trinitrophenyl-substituted pyridinium component $[N_3P_3Py]^+$ is a natural extension from what I already have in hand. This molecule was not pursued among my initial attempts partially because of its completely different synthetic route from what my established protocols (Figure 6-2). But more importantly, the preliminary DFT calculation shows that unlike 4'-(4-nitrophenyl)- substituent, the 2- and 6- phenyl rings with nitro- substituents are canted by as much as 70 degrees from the pyridinium plane where conjugation (presumably the dominating factor) will not be very effective. Therefore, it is not clear whether or not these two additional nitro- groups

will be more beneficial in regards to lowering the reduction potential of acceptor than the pentafluorinated phenyl version. It should still be considered as an alternative if the driving force requirement is still not fulfilled with the current acceptor design.

The above-discussed chromophore and acceptor combination allows the first electron transfer from chromophore to the acceptor to occur in the desired direction. The transiently generated Ru^{III} center has an estimated redox power of about 1.30 eV (vs. SCE), which will be sufficient to oxidize iron(II) porphyrin, which has a reduction potential of 1.05 eV (vs. SCE) in the $[Fe_4S_4]^{2+}$-$Fe^{III}P$ dyad[7]. Further estimate and calculations have shown that electron transfer driving from $[Fe_4S_4]^{+}$ cluster into iron(III) porphyrin is energetically favorable. Therefore, a scheme of electron transfer process can be described as in Figure 6-2. It needs to be noted that the complex prepared by Holm group is in its fully oxidized state ($[Fe_4S_4]^{2+}$-$Fe^{III}P$). The synthetic accessibility of the currently designed system is based on the reversibility of the second reduction process in the reported complex[7], but is yet to be experimentally proved.

Due to the complexity involved in this system, systematic photophysical studies will be conducted on (metallo-)porphyrin-chromophore-acceptor triad system before the exchange-coupled $[Fe_4S_4]^{+}$ cluster is incorporated. Even for this triad system, a complete understanding requires that two types of model complexes to be synthesized and fully characterized, i.e. chromophore-acceptor dyad and (metallo-)porphyrin-chromophore dyad. Lainé and coworkers[4, 6, 8, 9] have done systematic investigations on chromophore-acceptor dyads. They observed electron transfer events only in

geometrically constrained osmium system. Ruthenium chromophore-acceptor assembly does not undergo electron transfer due to its endothermic nature. Unfortunately, osmium(III) does not provide high enough oxidation power to oxidize iron(II) porphyrin and initiate the desired electron transfer process. Therefore, as discussed above, the only viable way appears to be derivatizing the acceptor group on the ruthenium chromophore.

Electrochemistry will be taken to carefully estimate the driving force of ET event. DFT calculations will be performed to help us elucidate both the conformational effects and the energetics of the system. In terms of iron porphyrin-chromophore dyad, initial characterization showed heavier quenching when iron(III) is inserted into the porphyrin ring, presumably due to the additional electron transfer quenching pathway. The driving force of electron transfer involving iron center is estimated to be -0.3 eV. It is not yet clear, without information from transient absorption experiments, whether electron goes into the d-manifold of iron center directly or goes through the bridging terpy-appended porphyrin ligand via LMCT. Extensive studies have been performed, as reviewed in Chapter 2, on other metalloporphyrins by Harriman and Sauvage[10-14], which shall also provide guidance in this regard. Synthetically, I have obtained free-base porphyrin-chromophore-acceptor triads where acceptor is either $[P_3Py]^+$or $[F_2P_3Py]^+$ and are working on the purifications.

Therefore, my subsequent approach to understand this very complicated tetrad system as designed is stepwise: first, understand comprehensively the behaviors of

dyads (H_2P-Ru(tpy-R) and Ru(tpy-R)-A'^+) by modulating the substitutions and therefore the electron density distribution in the molecule; second, with the informations gleaned from the first stage, explicitly understand the properties of H_2P-Rutpy-A^+ triad; third, a comparison between H_2P-Rutpy-A^+ and $Fe^{II}P$-Rutpy-A^+ should allow unequivocal investigation of the effect of iron ion and the additional excited state decay pathways I am interested in; finally, the $[Fe_4S_4]^{2+/+}$ cluster will be incorporated by collaboration and start to understand the effect of spin polarization in the electron transfer dynamics, where cluster serves as electron donor. Similar to that described in Chapter 4, a series of steady state and time-resolved luminescence and absorption spectroscopy measurements will be performed on all the target and control molecules. For example, intermediate charge separated states will be identified with a combination of transient absorption spectroscopy and spectroelectrochemistry: the concurrent appearances of Fe(II) signature and reduced pyridinium signature will be indicative of the charge separated species produced after the first electron transfer, etc. Such assignments will be supported by low temperature studies where charge separation will be inhibited by the solid matrix. Decay kinetics of the intermediate states will be analyzed to extract out relevant lifetimes and rate constants which are important concerns in sequential electron transfer system. Complicated as this system is, a stepwise approach like this will allow us to explore the various excited state behaviors rationally.

The last step of incorporating the $[Fe_4S_4]^{n+}$ cluster can be envisioned to be achievable by either attaching my iron porphyrin-ruthenium chromophore-acceptor

assembly to the cluster[15] or by attaching the [Fe_4S_4-S-FeP] complexes to my ruthenium chromophore-acceptor dyads. At first glance, it is expected that the second approach should be more challenging synthetically due to the harsh condition required to form the asymmetric porphyrin and ruthenium bisterpyridyl complexes, which the iron sulfur cluster may or may not survive. However, the synthetic challenges require us to be open towards all possible alternatives. It is also possible that the axial-binding motif as described in chapter 5 will be a better approach in the context of the whole assembly.

As electron transfer process I am looking at is largely dependent on the electronic structures of both the donor and acceptor, this project fits into a larger research program in examining the correlations between the electronic structure and the chemical reactivity of transition metal complexes. More specifically, to what extent spin polarization in a transition metal cluster will affect the dynamics of the electron transfer process.

Qualitatively, spin can affect the chemical reactivity in various ways. Looking at the Marcus equation,

$$k_{ET}=\frac{8\pi^2}{\hbar^2}|H_{ab}|^2\left(\frac{1}{4\pi\lambda k_B T}\right)^{1/2} exp\left[-\frac{(\Delta G^\circ+\lambda)^2}{4\lambda k_B T}\right]$$

every variable can be affected by the spin change in one way or another: ΔG^0 is changed with the energy separation which is determined by J value, the exchange coupling constant for the spin interaction; λ is affected when double exchange effect is taken into consideration, which decreases the amount of structural change through

delocalizing; H_{ab} is the extent to which the redox pairs are interacting. When $2|H_{ab}|=0$, the reactant will not be aware of the existence of the product potential surface and will not go; when $2|H_{ab}|<<k_BT$, the reaction will be nonadiabatic and the probability of reaction will be finite; when $2|H_{ab}|>>k_{BT}$, the reaction will be adiabatic and the probability of reaction approaches to 1.

Experimentally, spin polarization can affect the electron transfer by modulating the electronic structures of the donor component, bridging ligand or acceptor component. With this specific project, the spin effect of either donor cluster as in the *forward* ET design (Figure 1-2, right panel, Chapter 1) or accept cluster as in the *reverse* ET design (Figure 1-2, left panel, Chapter 1) can be studied. One potential problem, though, is that the innate complexity of spin structure of the iron-sulfur cluster may prevent us from separating the spin effects cleanly from the other factors. The stability of its derivatives may also limit the modifications we can make on the cluster for the purpose of tuning the electronic structure. Theoretically, selenium analog $[Fe_4Se_4]^{n+}$ can be built to obtain a different spin structure, or temperature can be adjusted to modulate the distribution of the population in different spin states. Nevertheless, the difficulty in doing so cannot be underestimated.

REFERENCES

REFERENCES

[1] Das, S.; Incarvito, C. D.; Crabtree, R. H.; Brudvig, G. W., *Science*, (2006) **312**, 1941.

[2] Lainé, P.; Bedioui, F.; Ochsenbein, P.; Marvaud, V.; Bonin, M.; Amouyal, E., *J Am Chem Soc*, (2002) **124**, 1364.

[3] Reichardt, C.; Eschner, M.; Schäfer, G., *J Phys Org Chem*, (2001) **14**, 737.

[4] Laine, P. P.; Ciofini, I.; Ochsenbein, P.; Amouyal, E.; Adamo, C.; Bedioui, F., *Chem-Eur J*, (2005) **11**, 3711.

[5] Laine, P. P.; Bedioui, F.; Loiseau, F.; Chiorboli, C.; Campagna, S., *J Am Chem Soc*, (2006) **128**, 7510.

[6] Laine, P. P.; Loiseau, F.; Campagna, S.; Ciofini, I.; Adamo, C., *Inorg Chem*, (2006) **45**, 5538.

[7] Cai, L.; Holm, R. H., *J Am Chem Soc*, (1994) **116**, 7177.

[8] Ciofini, I.; Laine, P. P.; Bedioui, F.; Adamo, C., *J Am Chem Soc*, (2004) **126**, 10763.

[9] Laine, P. P.; Campagna, S.; Loiseau, F., *Conformationally gated photoinduced processes within photosensitizer-acceptor dyads based on ruthenium(II) and osmium(II) polypyridyl complexes with an appended pyridinium group*, Elsevier: Kidlington, ROYAUME-UNI, (2008); Vol. 252, p 20.

[10] Benniston, A. C.; Harriman, A.; Pariani, C.; Sams, C. A., *Phys Chem Chem Phys*, (2006) **8**, 2051.

[11] Benniston, A. C.; Chapman, G. M.; Harriman, A.; Mehrabi, M., *J Phys Chem A*, (2004) **108**, 9026.

[12] Harriman, A.; Odobel, F.; Sauvage, J. P., *Journal of the American Chemical Society*, (1995) **117**, 9461.

[13] Harriman, A.; Odobel, F.; Sauvage, J. P., *J Am Chem Soc*, (1994) **116**, 5481.

[14] Collin, J. P.; Harriman, A.; Heitz, V.; Odobel, F.; Sauvage, J. P., *J Am Chem Soc*, (1994) **116**, 5679.

[15] Zhou, C.; Cai, L.; Holm, R. H., *Inorg Chem*, (1996) **35**, 2767.